MICROLAYER FORMATION, EVAPORATION AND BUBBLE GROWTH IN NUCLEATE BOILING

By

© HASSAN EL-BANNA SAAD FATH

B.Sc., Mech. Eng., Alexandria Univ.
M.Sc., Mech. Eng., Alexandria Univ.
M.Eng., Mech. Eng., McMaster Univ.

A Thesis

Submitted to the School of Graduate Studies

in Partial Fullfilment of the Requirements

for the Degree

Doctor of Philosophy

McMaster University

1981

DOCTOR OF PHILOSOPHY (1981) McMaster University
Mechanical Engineering Hamilton, Ontario, Canada

TITLE: Microlayer Formation, Evaporation and Bubble Growth in Nucleate Boiling

AUTHOR: Hassan El-Banna Saad Fath
B.Sc., Alexandria University,
M.Sc., Alexandria University,
M.Eng., McMaster University.

SUPERVISOR: Dr. Ross L. Judd

NUMBER OF PAGES: (xix), 214

ABSTRACT

A numerical study of microlayer formation and evaporation is reported in which computer programs developed in order to predict the isothermal (initial) and the instantaneous microlayer thicknesses as well as the time varying mass evaporated from the microlayer for any specified bubble growth rate are presented. The results of these programs show that the isothermal microlayer thickness $\delta_o(r)$ is of the order of 1-5 μm and its profile agrees with the author's experimental data. The results of the microlayer evaporation show that the microlayer may contribute up to 100% of the bubble mass and that the instantaneous microlayer profile $\delta(r,t)$ agrees with some photographically measured data from the same reference for certain selected bubbles.

Another computer program was developed to solve the Navier-Stokes equations, which account for all forces in the liquid acting on the bubble, in conjunction with the energy equation in order to study the entire hydrodynamic and thermodynamic fields around a growing bubble on a heating surface. The velocity, pressure and temperature distributions were analysed and the time varying mass evaporated from the bubble cap was computed. The results show that the mass evaporated from the bubble cap is less by an order of magnitude than the mass evaporated from the microlayer.

Finally, a numerical model for bubble growth was constructed using the programs mentioned above, assuming

the mass transfer across the liquid-vapour interface from both the microlayer and bubble cap to be the predominant mechanism for bubble growth. Some aspects of bubble growth are discussed including the time varying bubble mass, vapour pressure, bubble growth rate and bubble growth relationship. A comparison between this numerical model and the author's experimental data for the instantaneous microlayer thickness shows good agreement.

ACKNOWLEDGEMENTS

It is a pleasure to acknowledge my gratitude to my research supervisor Dr. R. L. Judd. His encouragement and guidance made this research successful.

I am indebted to Dr. S. Banerjee for his advice on various aspects of the numerical approaches and I would also like to express my appreciation to Dr. J. H. T. Wade, Chairman of the Mechanical Engineering Department and Dr. D. S. Weaver, the members of the Ph.D Supervisory Committee, for their continuing guidance during the course of this investigation.

Financial assistance from McMaster University and the Natural Sciences and Engineering Research Council of Canada and the moral support of my family are gratefully appreciated.

TABLE OF CONTENTS

NOMENCLATURE

SYMBOL	DESCRIPTION	UNITS
A	Area	m^2
B	Ratio defined in equation (5.21)	
C	Specific heat	J/kg C^o
C_0	Constant in the equation $R = C_0 t^n$	
C_1	Evaporation rate defined in equation (5.20)	
DMML	Microlayer incremental mass ΔM_{ML}	kg
D	Divergence defined by equation (6.3)	$\frac{m/s}{m}$
$\bar{f}$	Average frequency of bubble emission	1/s
g	Gravitational acceleration	m/s^2
h_{fg}	Latent heat of evaporation	J/kg
i	Subscript representing the radial direction	
IBL	Column defining the beginning of the boundary layer	
IML	Column defining the beginning of the microlayer	
II	Number of nodes or cells along the radial direction	
j	Subscript representing the axial direction	
JJ	Number of nodes or cells along the axial direction	
k	Thermal conductivity	W/m ^oC
M	Mass	kg

SYMBOL	DESCRIPTION	UNITS
n	Superscript representing time	
N	Number of active sites	
P	Pressure	N/m^2
P*	The ratio P/ρ_ℓ	m^2/s^2
P_r	Prandtl number ν/α	
Q	Heat transfer rate	W
r	Radial coordinate	
R	Bubble radius	m
$\dot{R}$	Bubble growth rate dR/dt	m/s
$\ddot{R}$	Bubble acceleration d^2R/dt^2	m/s^2
R_e	Reynolds number $R\dot{R}/\nu$	
t	Time	s
T	Temperature	^oK
u	Radial velocity component	m/s
U*	Potential flow radial velocity outside the bubble = $R\dot{R}^2/r^2$	m/s
v	Axial velocity component	m/s
$\bar{V}_{ML}$	Average volume of microlayer	m^3
y	Axial coordinate	
Y	Parameter defined in equation (5.14)	

Greek Letters

α	Thermal diffusivity	m^2/s
β	Parameter defined by equation (6.27)	
γ	Parameter defined by equation (5.10)	
$\delta(r,t)$	Instantaneous microlayer thickness	m
$\delta_o(r)$	Initial microlayer thickness	m
Δ	Incremental step size	
ε	Convergence accuracy	
θ	Temperature difference $T-T_{sat}$	K^o
μ	Dynamic viscosity	Ns/m^2
ν	Kinematic viscosity	m^2/s
π	Constant	
ρ	Density	kg/m^3
σ	Surface tension	N/m
τ	Penetration time δ_o^2/α_ℓ	s
ϕ	Hydrodynamic boundary layer thickness	m
ω	Accelerating coefficient	

Subscripts

b	Bulk
B	Bubble
CAP	Bubble Cap
d	Dry area under the bubble
g	Growth
k	Marker
ℓ	Liquid
ML	Microlayer

o	Initial
s	Solid
sat	Saturation
sup	Superheat
v	Vapour
w	Wall

LIST OF FIGURES

LIST OF TABLES

CHAPTER 1

INTRODUCTION

The transfer of heat from a heated surface to a liquid by boiling has attained wide importance for two main reasons. Firstly, evaporation of liquids as occurs in boilers and distillation equipment is highly dependent upon the rate of heat transfer associated with boiling. Secondly, boiling liquids are very effective cooling media and as a consequence are essential to cool devices producing high heat transfer rates such as nuclear reactors. These facts have been realized for a long time and numerous studies have been carried out to investigate the mechanisms governing the process.

Nucleate boiling is a complex heat transfer phenomenon that has been the subject of much research in the last three decades. The problems which stand out among those encountered in nucleate boiling and which contribute to its complexity concern the nucleation, growth, and detachment of individual bubbles, and their collective behaviour. The work described in this thesis will be restricted to the problem of the individual bubble on a heating surface for which there is no interference between bubbles originating from neighbouring nucleation sites.

The ability to predict the nucleate boiling heat

transfer rate for any surface-liquid combination is dependent upon three factors which are most likely interdependent, the number of active sites on the surface, the frequency of bubble emission at these sites and the heat transfer associated with the nucleation, growth and detachment of individual bubbles. As a consequence, the analysis of bubble dynamics is of great importance. In addition, several other mechanisms have been suggested to explain the increased heat transfer rate associated with nucleate boiling, among which is the formation and evaporation of the microlayer under the bubble.

The goals of the present investigation are to apply a theoretical approach to the analysis of the formation and evaporation of the microlayer underneath a bubble and to utilize the predictions to develop a bubble growth model which involves microlayer evaporation. A numerical approach to the formation of the isothermal microlayer on a surface under a growing bubble is presented in Chapter 4 in which the momentum and continuity equations for the liquid boundary layer outside the bubble and the liquid microlayer left under the bubble are solved simultaneously using a finite difference method. Chapter 5 presents a model for the microlayer evaporation in which the instantaneous microlayer thickness and mass evaporated from the microlayer were evaluated. As a vapour bubble grows, it sets the surrounding liquid in motion and the flow and thermal fields determine the shape of the bubble and the rate of the bubble growth. For this purpose, Chapter 6

presents a complete solution of the continuity, momentum and energy equations utilizing the Marker And Cell (MAC) technique in its modified version (SOLA) with some modifications to suit the particular bubble growth problem. A computer program was developed and the entire flow and thermal fields were analysed enabling evaporation from the bubble cap to be evaluated. A combination of the programs developed in Chapters 4, 5 and 6 is presented in Chapter 7 resulting in a bubble growth model which incorporates microlayer evaporation at the bubble base and evaporation from the bubble cap. This model assumes that the mass transfer across the liquid vapour interface is the predominent mechanism governing bubble growth. Concluding remarks with some recommendations for future work are presented in Chapter 8.

CHAPTER 2

LITERATURE SURVEY

2.1 Introduction

Bubble nucleation, growth and departure play an important role in determining the mechanisms responsible for increasing the heat flux during boiling. The nucleation of a bubble occurs during the waiting period where natural convection is the mechanism transferring heat. Bubble departure occurs during a relatively short period of time and as a consequence, the analysis of the bubble growth period is of great importance. During the bubble growth, a mechanism for transferring heat known as the "microlayer evaporation phenomenon" is assumed to be present. The evaporation of the microlayer is responsible for the transfer of a large amount of heat from the heating surface, thereby enhancing the overall heat transfer.

The present chapter presents a review of bubble growth and the formation and evaporation of the microlayer.

2.2 Bubble Growth

2.2.1 Introduction

The growth of a vapour bubble in a liquid has been studied by many investigators, both theoretically and experimentally since 1917 when Rayleigh [2] computed the pressure developed in the liquid when a spherical bubble collapsed

due to external pressure. Rayleigh's solution considered only the inertia of the liquid to be important and did not consider the effect of heat and mass transfer across the liquid vapour interface. A complete solution to the bubble growth problem requires that the continuity, momentum and energy equations for both vapour and liquid be solved simultaneously and coupled with the mass and energy exchange across the interface. However, practically speaking, any analytical solution requires some assumptions to simplify the problem. From the literature, it is well known that various phases can be distinguished in the growth history of a bubble, each of which is applicable to a certain period of bubble growth life. The main phases distinguished are (1) the "inertia controlled" phase, during which the inertia of the surrounding liquid controls the process, predominantly in the early stages of the bubble life, (2) the "diffusion controlled" phase, during which the process is controlled by the rate at which heat can be supplied from the surroundings to the bubble interface causing vaporization of the bubble interfacial liquid, predominantly in the later stages of the bubble life. Recent studies have been more concerned about developing a so called "complete solution" in the sense that it will be applicable for the entire growth period. Generally speaking, the growth of a vapour bubble is a function of the effects of liquid inertia, surface tension, viscosity and the difference between pressure within the bubble and the external pressure as well as the rate at which the bubble exchanges

heat with the surrounding fluid.

Several papers have been published solving the problem of spherical bubble growth in an infinite superheated liquid. The presence of the solid liquid interface imposes boundary conditions which lead to more complicated temperature and flow fields, and causes the formation and evaporation of the microlayer which adds another complexity to the problem.

The following sections discuss bubble growth in an infinite superheated liquid, bubble growth on heating surface, and some parameters which are assotiated with the bubble growth phenomenon.

2.2.2 Bubble Growth in Infinite Superheated Liquid

At the inception of bubble growth in an infinite superheated liquid, it is assumed that the pressure and temperature of the bubble and its liquid envelope can be represented by point A, Figure (2.1), while the surrounding liquid is represented by point D. If the liquid-vapour interface is in thermodynamic equilibrium during the growth, point A will move down the saturation line towards point C. At point A, the early stage of bubble growth, the driving force is the excess vapour pressure $\Delta P_v = P_v(0) - P_\infty$. This force will overcome inertia, surface tension and viscous forces. After a short period of growth, the surface tension force will vanish and the viscous forces in the infinite liquid

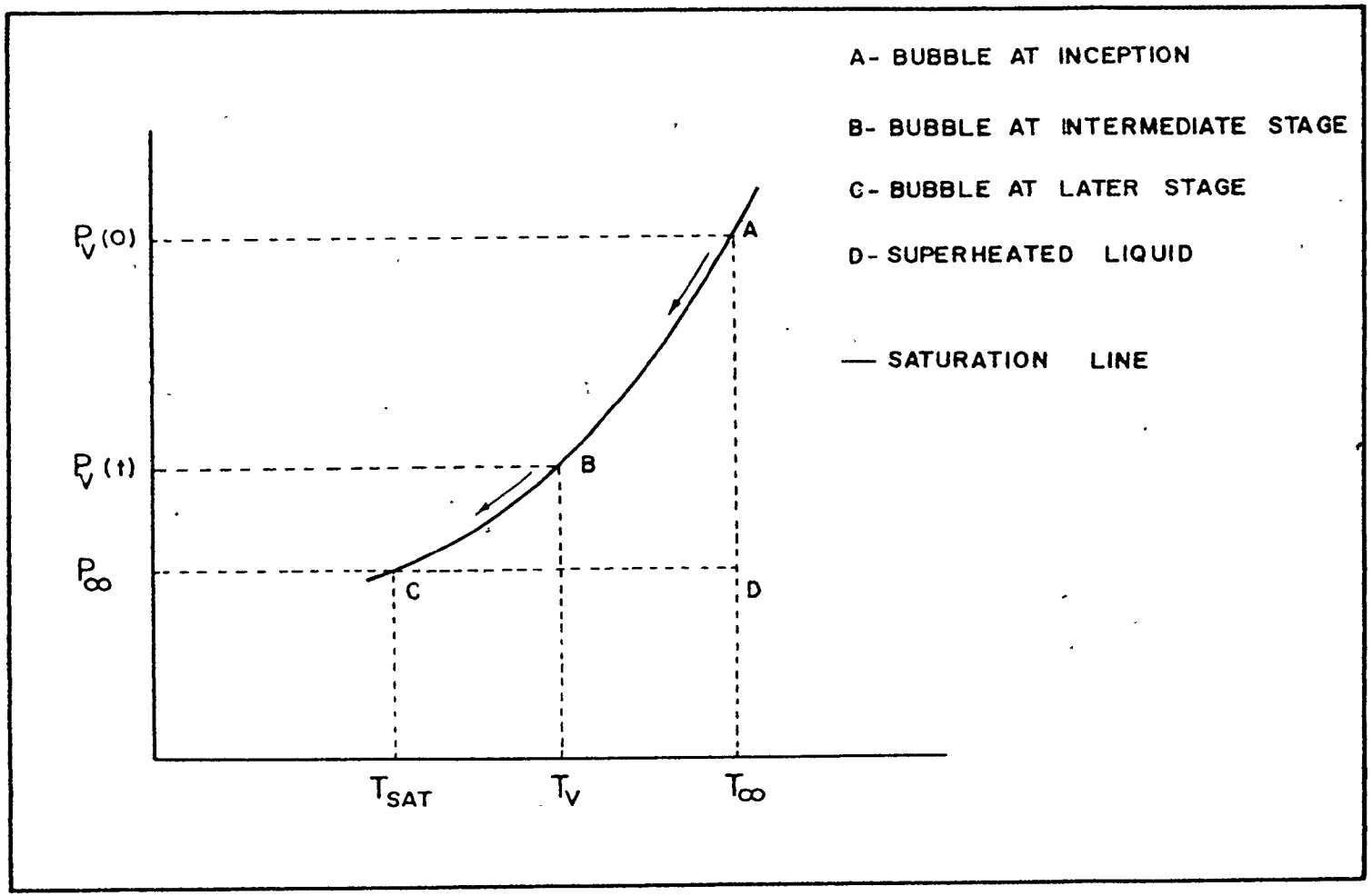

FIGURE (2.1) BUBBLE GROWTH HISTORY

will be small compared to the inertia forces. Accordingly, the "early stage" of bubble growth is "inertia controlled". At the other extreme, as point C is approached, the excess vapour pressure ΔP_v decreases while the temperature difference $\Delta T_v = T_\infty - T_v$ increases. As a consequence heat will diffuse to the liquid-vapour interface, where it will evaporate the liquid surrounding the bubble, increase the bubble mass and raise the vapour pressure which drives the bubble to grow. Accordingly the "later stage" of the bubble growth is "heat diffusion" controlled. In between these two stages (point B) both inertia and heat diffusion are relatively important. Early solutions for the bubble growth were obtained by solving either the momentum equation, where inertia forces controlled the growth or the energy equation, where heat diffusion controlled the growth. Later studies have been more concerned about the complete solution which exists during the entire bubble growth period.

(i) Inertia Controlled Stage

The solution of the continuity and momentum equations for the fluid outside the bubble leads to the general differential equation for the bubble growth, known as the modified Rayleigh equation, written as:

$$R\ddot{R} + \frac{3}{2}\dot{R}^2 = \frac{1}{\rho_\ell}\left[(P_v(t) - P_\infty) - \frac{2\sigma}{R} - \frac{4\mu\dot{R}}{R}\right] \qquad (2.1)$$

If in the right hand side of the above equation, the surface tension and viscosity effect were ignored as well

as considering $(P_v(t) - P_\infty)$ to be a constant, integration of the resultant equation leads to Rayleigh's solution [2]:

$$\dot{R}(t) = \left[\frac{2}{3}\frac{P_v - P_\infty}{\rho_\ell}\right]^{1/2} \tag{2.2}$$

Integration of equation (2.2) again gives:

$$R(t) = \left[\frac{2}{3}\frac{P_v - P_\infty}{\rho_\ell}\right]^{1/2} t \tag{2.3}$$

When the surface tension is to be introduced, the resultant growth rate is given by:

$$\dot{R}(t)^2 = \frac{2}{3}\frac{P_v - P_\infty}{\rho_\ell}\left[1 - \frac{3}{2}\frac{R_c}{R} + \frac{1}{2}\left(\frac{R_c}{R}\right)^3\right] \tag{2.4}$$

With increasing bubble radius R, the growth rate will approach the constant value in equation (2.3) since R_c/R will decrease. All these results are obtained with the assumption of constant $P_v(t)$ which is not correct.

(ii) Intermediate Stage

During growth, evaporation at the liquid vapour interface will withdraw heat from the adjacent liquid and consequently the temperature around the bubble and the vapour temperature will drop. This will lead to decreasing vapour pressure and decreasing rate of bubble growth. Ultimately the vapour temperature will be the saturation value and the heat diffusion equation will determine the bubble growth rate.

(iii) Heat Diffusion Controlled Stage

Several investigators including Scriven [3] and Plesset and Zwick [4] attempted to solve for the so called "asymptotic growth rate" where heat diffusion is the controlling factor. Solution of the energy equation for the temperature distribution around the bubble, and subsequent applications of the heat balance equation at the interface given by:

$$k_\ell \frac{\partial T(R,t)}{\partial r} = \rho_v h_{fg} \dot{R}(t),$$

gives the bubble growth rate $\dot{R}(t)$ expressed as:

$$\dot{R}(t) = C_o/2\sqrt{t} \tag{2.5}$$

and the growth relationship $R(t) = C_o\sqrt{t}$ (2.6)

where C_o is a constant (function of the liquid conditions and properties). The constant C_o given by Plesset and Zwick solution [4] is:

$$C_o = \frac{2\kappa_\ell (T_{sup} - T_{sat})}{h_{fg} \rho_v \sqrt{\frac{\pi}{3} \alpha_\ell}} \tag{2.7}$$

(iv) Complete Solution

It is clear from equation (2.3) and (2.6) that for the two limiting cases (inertia and heat diffusion), the bubble growth relationship varies with t when the liquid inertia is controlling and with $\sqrt{t}$ when heat diffusion is controlling. Accordingly it is expected that a complete

solution will fall between these two limits.

More recently Theofanous et al. [5], Board and Duffey [6] and Mikic et al. [7] attempted to derive a complete solution for bubble growth in a uniform superheated liquid, which took into account inertia, viscous, surface tension, and heat transfer effects. Moreover, Theofanous et al. [5] introduced the effect of non-equilibrium at the liquid-vapour interface by assuming a quadratic temperature distribution in the thermal boundary layer around the bubble. Board and Duffey [6] also allowed for the variation of vapour density with time. The analysis of Theofanous et al. [5] is the most rigorous, but the more simple analyses of Board and Duffey [6], and Mikic et al. [7] give results in close agreement with those of Theofanous et al. [5].

2.2.3 Bubble Growth on a Heating Surface

Bubble growth on a heating surface is much more realistic and more complex than bubble growth in a superheated liquid. However the basic knowledge of the relative importance of various factors affecting bubble dynamics is almost the same and could be obtained from the later case. The main difference between the two cases is the existence of the heating surface which leads to:

1. The presence of non-uniform temperature field surrounding the bubble.
2. The formation and evaporation of the microlayer

during the growth period.

The bubble growth on a heating surface, however, passes through the same inertia controlled, intermediate and heat transfer controlled stages, similar to the bubble growing in a superheated liquid.

Mikic et al. [7] presented a model in which they considered the existence of non-uniform temperature distribution near the heating surface, but they did not account for microlayer evaporation. To predict the growth of bubbles allowing for the microlayer evaporation, it is necessary to know the thickness of that layer. Based upon experimental measurement, Cooper and Lloyd [8] have taken $\delta_o = 0.8 \sqrt{\nu\, t_g}$. A simple computer program was written allowing for evaporation from the bubble cap, adding the net evaporation to that of the microlayer to get the instantaneous vapour bubble volume. Assuming the bubble to be a hemisphere, an equivalent bubble radius was obtained which showed good agreement with their experimental results. Cooper and Lloyd found that:

$$R(t) = \frac{4}{\sqrt{\pi}} \frac{\rho_\ell C_\ell \Delta T}{\rho_v h_{fg}} \sqrt{\nu t} = \frac{4}{\sqrt{\pi}} J_a \sqrt{\alpha t} \qquad (2.7)$$

Later, Van Ouwerkerk [9] presented a detailed analysis of a bubble growing on a heating surface including the evaporation of the microlayer which resulted in:

$$R(t) = \frac{2}{\sqrt{\pi}} \frac{\rho_\ell\, \ell \Delta T}{\rho_v\, h_{fg}} \sqrt{\alpha t} = \frac{2}{\sqrt{\pi}} J_a \sqrt{\alpha t} \qquad (2.8)$$

Note that the Cooper and Lloyd [8] and Van Ouwerkerk [9] theoretical solutions were based on the premise that $R \alpha \sqrt{t}$ which generally has been indicated by experimental results implying that the bubble growth was predominantly controlled by the rate of heat diffusion. In other words, their theoretical relationships do not represent complete solutions that cover the entire bubble life time. Bubbles growing at low pressures spend a considerable portion of their lifetime in the inertia controlled stage.

A numerical approach by Guy and Ledwidge [10] was developed using an explicit finite difference marching technique. Imposing a sudden temperature disturbance, the temperature distribution in the liquid was solved; and evaporation at the bubble cap was computed. The evaporation from the microlayer was incorporated assuming the Cooper and Lloyd [8] relationship for the initial microlayer thickness, i.e., $\delta_o = 0.8 \sqrt{\nu t}$, and that the thickness of the thermal boundary layer was the mean value of the microlayer thickness $(\delta_o/2)$, i.e., the evaporation mass rate was:

$$\frac{dm}{dt} = \frac{2kA}{h_{fg}\delta_o} (T_\ell - T_\omega)$$

The incremental change of vapour mass changed the vapour pressure in the bubble which grew according to the modified Rayleigh equation:

$$\frac{P_v(t)-P_\infty}{\rho_\ell} = R\ddot{R} + \frac{3}{2}\dot{R}^2 + \frac{2\sigma}{\rho_\ell R} + 4\nu\frac{\dot{R}}{R} \qquad (2.9)$$

2.2.4 Parameters Associated with Bubble Growth

During the growth period, there are some parameters which in one way or another influence the behaviour of the bubble growth. These parameters include the vapour pressure, the temperature inside and outside the bubble, and the bubble shape. These parameters will be discussed in the following sections.

(i) Vapour Pressure

The vapour pressure inside the bubble was assumed to be invariant with time by Rayleigh [2]. Comparing the experimental data of Bankoff and Mikesell [12] with the theoretical solution for bubble growth and collapse by Rayleigh [2], it was found that the pressure inside the bubble increases with time and therefore the assumption of constant vapour pressure by Rayleigh was found to be incorrect.

By means of a force balance at the bubble departure time and an energy balance during bubble growth, the excess vapour pressure ΔP_v was calculated by Hahne [13], which showed that ΔP_v decreases from about 100 N/m^2 in the early stages of bubble growth to about 10-20 N/m^2 at the moment of departure.

Pressure variation in the fluid and at the liquid-vapour

interface were acquired using bubble growth data obtained from the high speed camera motion pictures of Schmidt et al. [14]. The momentum equation used for determining vapour pressure was:

$$P_\ell (R,t) - P_\infty = \rho_\ell [R \ddot{R} + \frac{3}{2} \dot{R}^2] \qquad (2.10)$$

The resulting vapour pressure prediction of equation (2.10) shows that $\Delta P_v(t)$ increases from zero to a maximum value and then drops back asymptotically to about 20 N/m^2. In addition it was found that a larger superheat resulted in an increase in the maximum pressure as well as a more rapid pressure rise.

The results presented above showed that the vapour pressure difference ($\Delta P_v(t) = P_v(t) - P_\infty$) increases from zero (due to static equilibrium when the surface tension effect is ignored) to a maximum and then drops back, approaching zero again.

(ii) Temperature Inside and Outside the Bubble

Knowledge of the temperature inside and outside the bubble is important in order to evaluate the amount of heat conducted from or to the bubble and accordingly the amount of liquid condensed or evaporated at the bubble cap.

(A) Temperature Inside the Bubble

The vapour temperature inside the bubble was measured by means of a microthermocouple inserted into the bubble

from above by Hahne [13]. The thermocouple response observed showed that the liquid adjacent to the heating surface heats exponentially during the waiting period. As soon as the bubble starts to grow and rises to the thermocouple junction, the temperature drops to the (constant) vapour temperature which was found to be superheated by 0.3-0.4 ^{o}C.

An analysis based on the experimental measurements of the temperature inside the bubble and its liquid environment was presented by Ganic and Afgan [15] using a fast response thermocouple and high speed camera. The analysis showed that as the bubble approaches the thermocouple, the thermocouple comes into contact with the superheated liquid around the bubble which shows a temperature jump to a maximum value T_{max}. As the thermocouple probe pierces the bubble, the temperature suddenly drops to the saturation temperature T_{sat}.

(B) Temperature Outside the Bubble

The analysis presented by Ganic and Afgan [15] showed that there is a superheated liquid layer around the bubble and the temperature increases from T_{sat} at the liquid vapour interface to a maximum temperature T_{max} then drops down to the bulk temperature T_{∞}.

Wiebe and Judd [16] reported an experimental study of the temperature distribution near the heating surface. The analysis indicated that increasing heat flux and decreasing subcooling resulted in a decreasing extrapolated superheated

layer thickness, defined as the height of the intersection between the tangent to the temperature profile at the surface and the constant liquid bulk temperature.

These results showed that the liquid surrounding the bubble is at a higher temperature than both the vapour temperature inside the bubble and the bulk temperature. Such a temperature difference helps the evaporation of liquid surrounding the bubble as well as the diffusion of heat to the bulk liquid. At the same time these results showed that a more quantitative analysis is needed and a theoretical study is of great help.

(iii) Bubble Shape

Johnson et al. [17] presented photographs of bubbles produced under a wide range of conditions, which were classified as spherical, hemispherical and oblate. The authors suggested that the shape of a bubble at a particular instant is determined by the relative size of the contribution of inertia and surface tension forces in the equation for the excess pressure inside the bubble. If the former term predominates as in a rapidly growing bubble , the bubble growth will be nearly hemispherical. If the later term predominates, the bubble will tend towards the spherical shape. Note that, however, all bubbles no matter what their initial shape, finally approach a spherical shape before lift off because of the eventual dominance of surface tension over inertia effects.

Cooper and Lloyd [8] attempted a quantitative

verification of Johnson's et al. [17] suggestions. The terms had been evaluated as follows

Inertia term $$P_i = \rho_\ell \left(R \ddot{R} + \frac{3}{2} \dot{R}^2\right) \quad (2.11)$$

Surface tension term $$P_\sigma = \frac{2\sigma}{R} \quad (2.12)$$

Gravity term $$P_g = (\rho_\ell - \rho_v)\, gR \quad (2.13)$$

Viscous term $$P_v = 4\, \mu \frac{\dot{R}}{R} \quad (2.14)$$

These terms were evaluated as functions of time (for $R \propto t^{1/2}$) for two different cases. In both cases, the viscous term P_v was found to be much smaller than the predominant term, and Johnson's suggestions were confirmed. Also it was suggested that factors tending to make bubbles grow rapidly to large size will tend to encourage formation of a microlayer and also make the bubble of hemispherical shape with large area of contact at the wall, hence a large microlayer area.

Much of what has been said about this point was summarized by Dywer [18] in Table [1] below. Spherical and hemispherical bubbles are the two limits of bubble shape and there can be intermediate shapes between them, depending on the thermodynamic and hydrodynamic conditions that exist. Finally, it must be remembered that the conditions assumed are idealized to the extent that there is no interference between bubbles from neighbouring nucleation sites and no large scale turbulence. These conditions are seldom fully met.

Table (1)

Summary of Parameters Affecting Bubble Shape

	Shape of Vapour Bubble	
Independent Parameters	Tending to be spherical	Tending to be hemispherical
Temperature of heating surface and liquid	low	high
System pressure	high	low
Heat flux	low	high
Thermal conductivity of liquid	low	high
Degree of wetting	moderately good	very good
Heating surface topography	less smooth	smoother (polished)
Dependent Parameters		
Initial bubble growth rate	low	high
Bubble size	small	large
Length of waiting period	short	long
Area of microlayer	smaller	larger
Thickness of microlayer	greater	less
Fluctuations of heating surface temperature	smaller	larger
Forces Acting on Bubble		
Inertia	low	high
Surface tension	high	low
Viscous	high	low
Gravitational (surface facing upward)	higher	lower

Madhavan and Mesler [11] studied the shape of a growing bubble on a surface. They used the Marker And Cell (MAC) method to solve the Navier-Stokes equation which accounts

for all forces in the liquid acting on the growing bubble. The effect of the surface tension force was included as a boundary condition at the liquid-vapour interface. A chosen time dependent vapour pressure function $P_v(t)$ was used to match the bubble growth rates experimentally observed. The calculated shape agreed with the experimental shape and the results indicated that the inertia force affects the bubble shape significantly. The surface tension force was found to be a dominant factor causing the bubble detachment and the buoyancy force contribution to bubble detachment was relatively small. These results are in contrast with previous investigators who suggested that buoyancy and inertia of a growing bubble promotes bubble detachment, the effect of the surface tension is to hold the bubble down to the surface.

2.3 Microlayer Formation

2.3.1 Introduction

Because of viscosity and the no-slip condition at the heating surface, a growing bubble has thin superheated liquid layer known as the "microlayer" associated with it. When the microlayer comes in contact with the vapour, evaporation from the microlayer occurs rapidly and a considerable amount of heat is withdrawn from the heating surface. The percentage contribution of the microlayer evaporation heat flux to the total heat flux was found (by the author's research and others) to be as much as 40% at subatmospheric pressure. The initial and instantaneous thickness of the microlayer

plays an important role and has been the subject of several investigations. In the following sections, a summary of the research carried out to confirm the existence of the microlayer and to measure its thickness will be presented followed by a review of the models derived in order to calculate the initial microlayer thickness.

2.3.2 Confirmation and Measurements of the Microlayer

The existence of a liquid microlayer under a vapour bubble formed during nucleate boiling heat transfer was first hypothesized by Snyder and Edwards [19]. Qualitative verification followed through experimental work by Moore and Mesler [20]. They observed a local surface temperature drop during bubble growth which could only be attributed to evaporation of a liquid microlayer beneath the bubble. Further qualitative evidence of the liquid microlayer existence was provided by Hendricks and Sharp [21]. The first actual verification of the presence of the microlayer was done by Sharp [22] using interferometric techniques coupled with high speed photography. Jawurek [23] performed another interferometric photographic investigation in which he found that the instantaneous microlayer thickness $\delta(r,t)$ for methanol boiling on a glass surface was less than 1 μm. Cooper and Lloyd [8] calculated the initial microlayer thickness $\delta_o(r)$ from their thermal data using three independent methods. They found that $\delta_o(r)$ varied from 5 μm to 30 μm at very low pressures.

Similarly using the temperature measurements of the heating surface Foltz and Mesler [24] deduced that the microlayer thickness ranged from 3 μm to 9 μm. Katto et al. [25] found that the microlayer thickness $\delta_o(r)$ was of the order of 11 μm. Voutsinos and Judd [26] and Fath and Judd [27] presented experimental investigations in which the growth and evaporation of the microlayer underlying a bubble forming on a glass heating surface was measured using laser interferometry and high speed photography. Their results indicated that the microlayer thickness $\delta_o(r)$ is of the order of 2-7 μm and varies from bubble to bubble. In conclusion, the existence of the liquid microlayer under a growing bubble on a surface has been confirmed by many researchers with an initial thickness of the order of 5-10 μm.

2.3.3 Initial Microlayer Thickness

(i) Models Based on Theoretical Analysis

As far as the theoretical formulation is concerned, in the literature two fundamentally different approaches have appeared to analyse the microlayer formation and its thickness. One group of investigators has a common understanding that the phenomenon is concerned with the flow of liquid within the conventional range of hydrodynamics in spite of individual interpretations put in their studies. Another group considered that the formation of the microlayer is a local phenomenon related to the flow of liquid near the front meniscus of the bubble and that the liquid microlayer is subject

to positional change of pressure due to the effect of surface tension whereby the liquid layer is driven to flow against viscous forces.

It has been assumed that the initial thickness of a microlayer $\delta_o(r)$ under a bubble is equal to the displacement thickness of the hydrodynamic boundary layer outside the bubble base.

Cooper and Lloyd [8] considered plane two dimensional flow outside the bubble. Assuming $R \alpha t^{1/2}$, they found that the initial thickness of the microlayer was equal to

$$\delta_o(r) = 0.8 \sqrt{\nu t_g} \tag{2.15}$$

Under the assumption of axial symmetric spherical coordinates, Olander and Watts [28] neglected the convective terms in the momentum equation and in conjunction with the assumption that $R \alpha t^{1/2}$ reached a similar result that

$$\delta_o(R) = \frac{\sqrt{\pi \nu}}{4 A_o} R \tag{2.16}$$

where

$$A_o = \sqrt{\frac{3}{\pi}} \frac{(T_w - T_{sat}) \rho_\ell C_\ell}{\rho_v h_{fg}} \sqrt{\alpha_\ell} = C_o/2 \tag{2.17}$$

Dwyer and Hsu [29] reexamined the model of Cooper and Lloyd with a different method and considered that $R \alpha t^n$ where n is variable. Their result for the initial thickness of the microlayer was,

$$\delta_o = k \sqrt{\nu t} \tag{2.18}$$

where

$$k = \frac{\Gamma(3n)}{\Gamma(1/2+3n)}$$

and Γ is the gamma function.

An elaborate analysis of the boundary layer equations was carried out by Van Ouwerkerk [9] using a self-similar solution. A hemispherical bubble with growth relationship $R \sim \sqrt{t}$ was assumed. The initial microlayer thickness was found to be:

$$\delta_o(r) = 1.26 \sqrt{\nu t} \tag{2.19}$$

Van Stralen et al. [30] introduced the displacement thickness of the Blasius boundary layer assuming $R \alpha t^n$ to obtain the microlayer thickness in accordance with:

$$\delta_o(r) = 3.012 \left(\frac{r}{R}\right)^{1/2n} \left(\frac{\nu R}{R}\right)^{1/2} \tag{2.20}$$

Katto and Shoji [31] concluded from their study that the liquid microlayer between a bubble and a solid surface is subject to positional change of pressure due to the effect of surface tension. Hence, the liquid layer is driven to flow against the viscous force leaving a microlayer with a thickness of the order of microns behind. Theoretical analysis was attempted by the authors to study the flow of a liquid layer in which surface tension played an important role. The results of the thickness when an interface moves between two narrow plates with uniform velocity V_o was found to be:

$$\frac{d\delta_o}{dr} = K_o \left(\frac{3\mu V_o}{\sigma}\right)^{1/3} \frac{H}{r} \qquad (2.21)$$

where K_o = a numerical constant

H = half the distance between the two plates.

Zijl [32] proposed a modification of the Landau and Levich model [33] for the free coating problem to calculate both the thickness of the microlayer δ_o and the radius of curvature in the meniscus region. The dimensionless microlayer thickness $h_\infty(t) = \delta_o/\sqrt{\nu t}$ was found to be:

$$h_\infty(t) = \frac{\delta_o}{\sqrt{\nu t}} = 1.15 \left(\frac{\sigma^2 t}{Ja^4 P_r \rho_\ell^2 \alpha_\ell^3}\right)^{-1/6} \qquad (2.22)$$

for a hemispherical bubble which grew according to $R = 2Ja(\ell t)^{1/2}$ and,

$$h_\infty = \frac{\delta_o}{\sqrt{\nu t}} = \frac{4}{3} \frac{n^{1/6}}{\sqrt{2-2n}} \left(\frac{\sigma t^{1-n}}{2C_o P_r \rho_\ell \alpha_\ell^{1+n}}\right)^{-1/6} \qquad (2.23)$$

for a hemispherical bubble which grew according to $R = 2C_o(\alpha_\ell t)^n$.

The results of these models were compared with the experimental data of Fath [1] and none of them fitted the data. As a consequence it was felt that a more elaborate analysis of the boundary layer equations for both the liquid outside the bubble and inside the microlayer should be carried out taking into consideration some of the parameters which were ignored in the previous studies, including:

a) Introduction of any growth relationship $R(t)$ with no restriction on the functional form $R(t) \sim t^n$.

b) Consideration of the residual flow inside the microlayer especially near the boundary layer outside the bubble.

c) Incorporation of other definitions of the microlayer with no restriction on the displacement thickness of the boundary layer.

d) The possibility of inclusion of the surface tension effect.

(ii) Models Based on Experimental Analysis

Many experiments have been carried out to measure or estimate the microlayer thickness. Some of the investigators tried to correlate data to get an experimental expression for the variation of the microlayer thickness with time or with radial coordinate. In the earliest attempts, the initial microlayer thickness δ_o was estimated by several methods from the measurements of heating surface temperature variation with time and position by Cooper and Lloyd [8]. The agreement between the results of different methods of calculation was not perfect but it was sufficiently close. The authors found that

$$\delta_o = C_2\sqrt{\nu t} \qquad (2.24)$$

where the constant C_2 varied between 0.5-1.0. The above equation was based on the interpretation that the formation of the microlayer is determined by the unsteady flow of viscous liquid near the solid wall.

More recently Cooper et al. [34] used the techniques established before, applying dimensional analysis to obtain

δ_o at zero gravity taking into account the liquid surface tension. The results showed that the thickness of the micro-layer depended on the surface tension so that $\delta_o/\sqrt{\nu t_g}$ falls as t^* increases where $t^* = t_g\sigma^2/b^6\rho^2$, $b = \sqrt{\nu/Pr}$ Ja and t_g refers to the time when the base grows past the point considered.

Van Beek and Vennekens [35] started from the heat flux balance:

$$q_w(t) = -\rho_\ell h_{pg} \dot{d} = k\, \theta_w(t)/d \qquad (2.25)$$

where d = the thermal boundary layer thickness beneath the hemispherical bubble. Integration over the time interval required for complete evaporation of the microlayer yielded an expression for the initial thickness of the thermal layer. This model was based upon the common assumption that the liquid in the microlayer was at rest, giving rise to a linear temperature profile in the direction perpendicular to the surface and that the vapour temperature remained constant throughout the growth period at the saturation temperature. The final results for the thermal and hydrodynamic layers were given as

$$d_o(r) = 3.5^* \; 10^{-5}\; r^{1/2} \qquad (2.26)$$

and

$$\delta_o(r) = 0.48\sqrt{\nu t_r} \qquad (2.27)$$

Note that $\delta_o(r)$ is only 38% of Van Ouwerkerk's experimental

result ($\delta_o = 1.26\sqrt{\nu t}$).

According to the experiments by Katto and Shoji [31], the formation of the microlayer was regarded as a local phenomenon related to the flow of liquid near the front meniscus of bubble. The local profile of the microlayer for bubbles forming between two parallel plates was given by the following experimental equation within the region of $r/H >> 1$:

$$\frac{d\delta_o}{dr} = 0.8 \left(\frac{\mu U_o}{\sigma}\right)^{2/3} \frac{H}{r} \tag{2.28}$$

where U_o = spreading velocity of the bubble

and H = half of the normal distance between the parallel plates.

Katto et al. [25] measured the thickness of the microlayer from the evaporating velocity of the liquid layer for a bubble in saturated boiling of water at pressure of 0.11 kN/m^2 from which the following empirical formula was derived:

$$\frac{d\delta_o}{dr} = 0.65 \left(\frac{\mu U_o}{\sigma}\right)^{1/6} \frac{1}{\left(\frac{U_o r}{\nu}\right)^{1/2}} \tag{2.29}$$

where

$U_o = \frac{dr_b}{dt}$ = local velocity of the bubble front

It was also found from their experiment that $r_b = B\ t^n$.

Finally after substitution:

$$\frac{\delta_o}{r} \approx \left(\frac{\mu U_o}{\sigma}\right)^{1/6} \frac{1}{\left(\frac{U_o r}{\nu}\right)^{1/2}} \qquad (2.30)$$

2.4 Microlayer Evaporation

2.4.1 Introduction

As soon as the superheated microlayer under a growing bubble is formed and comes in contact with the vapour inside the bubble, evaporation starts. Initially, heat needed for the evaporation will be obtained from the heat content of the microlayer and then after the penetration depth of the transient cooling process reaches the heating surface, heat will be withdrawn from the solid surface.

Early analyses of the microlayer evaporation phenomenon have used one or more of the following simplifications:

a) Neglecting the thermal capacity of the microlayer

b) Neglecting the variation of the wall temperature during evaporation

c) Neglecting the applied system heat flux

d) Assuming a very "thick" or very "thin" microlayer thickness

e) Considering initial microlayer thickness with no residual flow and using one of the models mentioned in Section 2.3.

The following sections review some aspects of the microlayer evaporation phenomenon, including the instantaneous microlayer thickness, volume of microlayer evaporated, dry

area under the bubble, and finally microlayer evaporation and nucleate boiling heat transfer.

2.4.2 Instantaneous Microlayer Thickness

Sharp [22] was the first to measure the instantaneous microlayer thickness (for water) using optical techniques. Further measurements were carried out later by Jawurek [23] who used an optical technique which permitted simultaneous determination of the microlayer geometry and bubble profile. Both authors found that the microlayer thickness was less than 1 μm for all cases studied. Voutsinos and Judd [26], and Fath [1] investigated boiling dichloromethane (methylene chloride) on an oxide coated glass surface using laser interferometry and high speed photography at different levels of subcooling, system pressure and heat flux. Their results show that the microlayer thickness was of the order of 2-7 μm and decreased with increasing system pressure, subcooling and heat flux. Comparison between the above mentioned results is shown in figure (2.2)

2.4.3 Volume of Microlayer Evaporated

At any time during the growth of a vapour bubble, the total volume evaporated from the microlayer $\overline{\forall}_{ML}$ can be expressed as:

$$\overline{\forall}_{ML} = 2\pi \left[\int_{o}^{R_d} \delta_o(r)\, r\, dr + \int_{R_d}^{R_b} [\delta_o(r) - \delta(r,t)]\, r\, dr \right] \qquad (2.31)$$

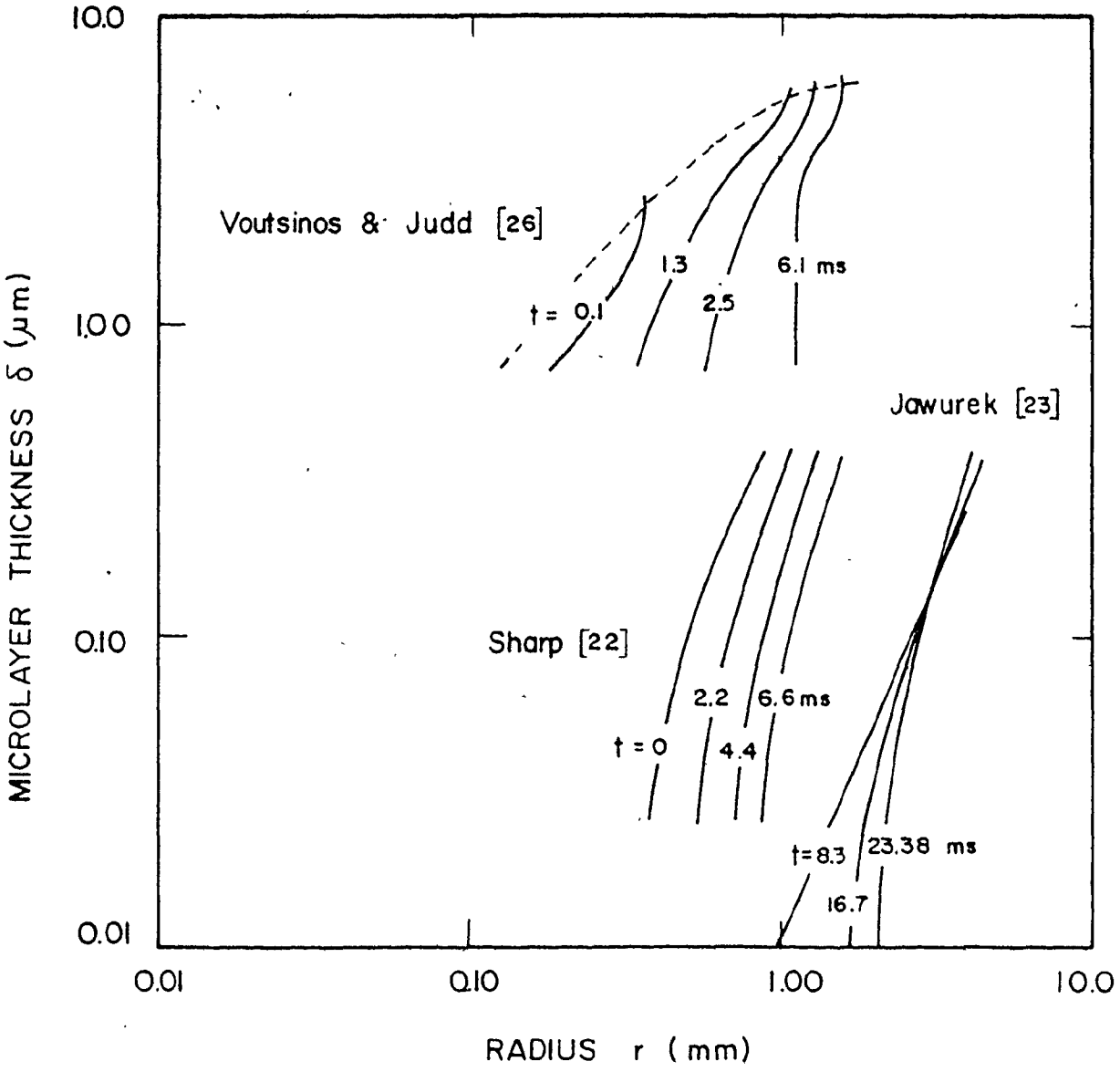

FIGURE (2.2) MICROLAYER THICKNESS RESULTS

This volume was evaluated by Voutsinos and Judd [26] and expressed as:

$$\bar{V}_{ML} = \frac{2}{3} \pi R^3 \frac{\rho_v}{\rho_\ell} \left[1 + \sqrt{\frac{3}{\pi}} \frac{\rho_\ell C_\ell \theta_{sat}}{\rho_v h_{fg} A_o}\right] \quad (2.32)$$

where A_o = the constant in the assumed growth relationship $R = 2 A_o \sqrt{\alpha t}$ obtained experimentally. Note that the term

$$\sqrt{\frac{3}{\pi}} \frac{\rho_\ell C_\ell \theta_{sat}}{\rho_v h_{fg} A_o}$$

represents the fraction of the bubble volume condensed at the liquid vapour interface.

In the experimental research by Fath [1], the effect of both system pressure and heat flux on the volume evaporated from the microlayer was computed as presented in figure (2.3). It is clear that $\bar{V}_{ML}$ decreases with increasing system pressure and heat flux. Similarly Hwang and Judd [37] found that $\bar{V}_{ML}$ decreases with increasing system subcooling.

2.4.4 Dry Area Under the Bubble

Sharp [22] was the first investigator who observed the existence of the dry area in the center of the microlayer. This author also pointed out that the degree of wettability is a factor which influences the size and growth rate of the dry area. Similarly, Jawurek [23] showed that the dry area grows with time. Cooper and Lloyd [8] indicated that the dry area is small relative to that of the microlayer and varies from 0.5% in the initial growth period to 4% at the end of

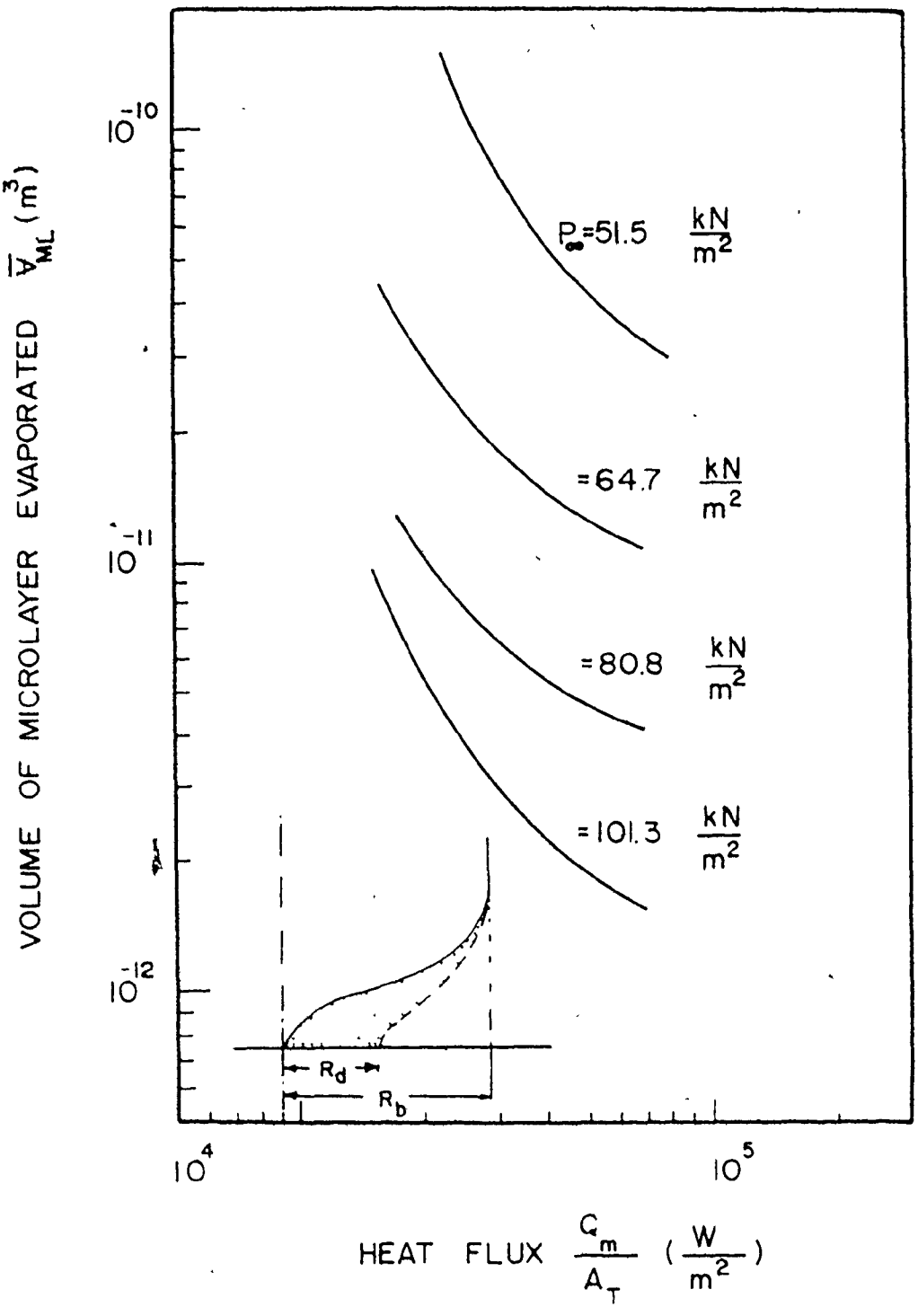

FIGURE (2.3) VOLUME OF MICROLAYER EVAPORATED PER BUBBLE ACCORDING TO FATH [1]

the growth period. On the contrary, Voutsinos and Judd [26] showed that the microlayer may evaporate completely and that the ratio R_d/R_b is close to unity at the end of the bubble growth period as indicated in figure (2.4). More recently, Fath [1] found that the complete evaporation of the microlayer observed by Voutsinos and Judd [26] is valid for most bubbles. A plot of the ratio of the dry patch radius to bubble radius with time is shown in figure (2.5).

2.4.5 Microlayer Evaporation and Nucleate Boiling Heat Flux

Although there are many models proposed to explain the nucleate boiling phenomenon, none of these models can adequately predict nucleate boiling heat transfer under all the parameters of heat flux, subcooling and pressure for different combinations of surface and fluid conditions. Also, in the models which exist in the literature, little attention has been given to the existence of the microlayer evaporation mechanism as a significant contributor to the total heat transfer. Fath [1] obtained the rate of heat transfer by microlayer evaporation Q_{ME}/A_T by multiplying the average energy transferred per bubble due to microlayer evaporation ($\rho_\ell h_{fg} \bar{V}_{ML}$) by bubble flux density ($\phi = \frac{N}{A_T} \bar{f}$):

$$Q_{ME}/A_T = \rho_\ell h_{fg} \bar{V}_{ML} \phi = \rho_\ell h_{fg} \bar{V}_{ML} \frac{N}{A_T} \bar{f} \qquad (2.33)$$

The results of equation (2.33) are shown here in figure (2.6). From this figure it is clear that increasing heat flux and

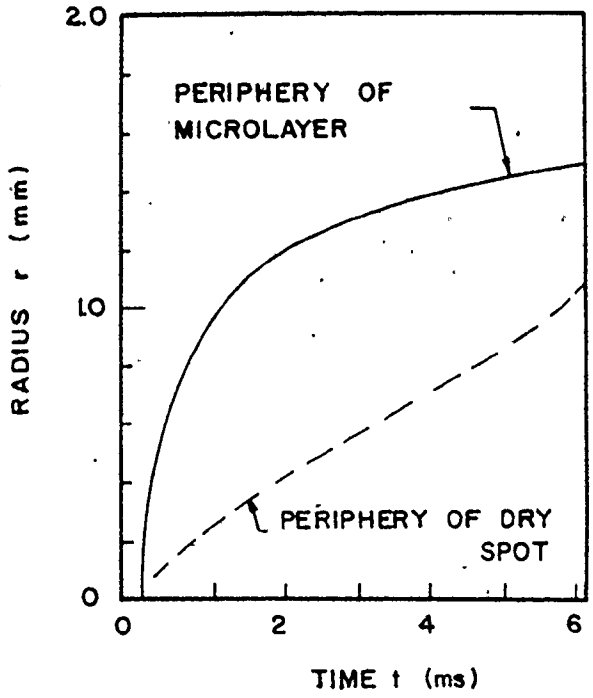

FIGURE (2.4) MICROLAYER HISTORY ACCORDING TO [26]

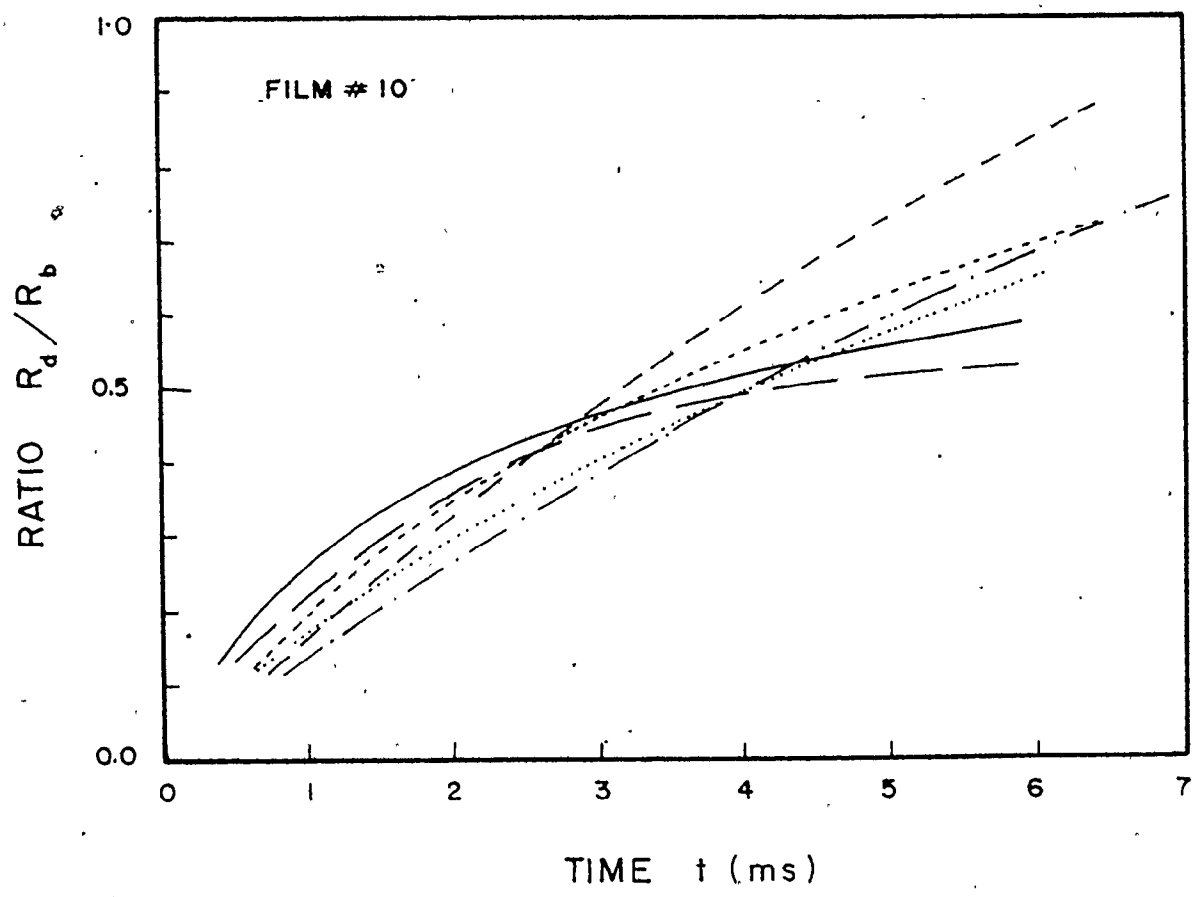

FIGURE (2.5) DRY TO BUBBLE RADIUS RATIO ACCORDING TO FATH [1]

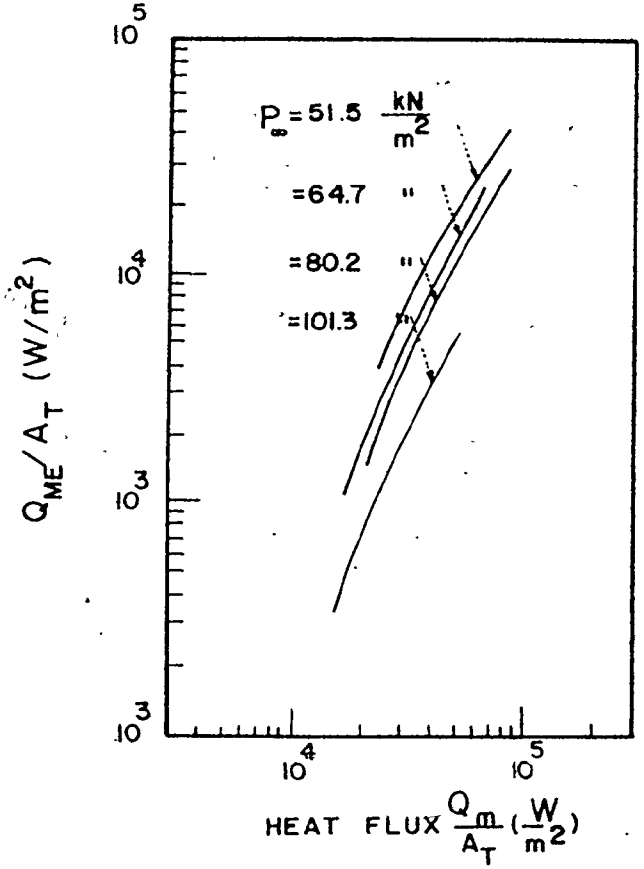

FIGURE (2.6) MICROLAYER EVAPORATION HEAT TRANSFER ACCORDING TO FATH [1]

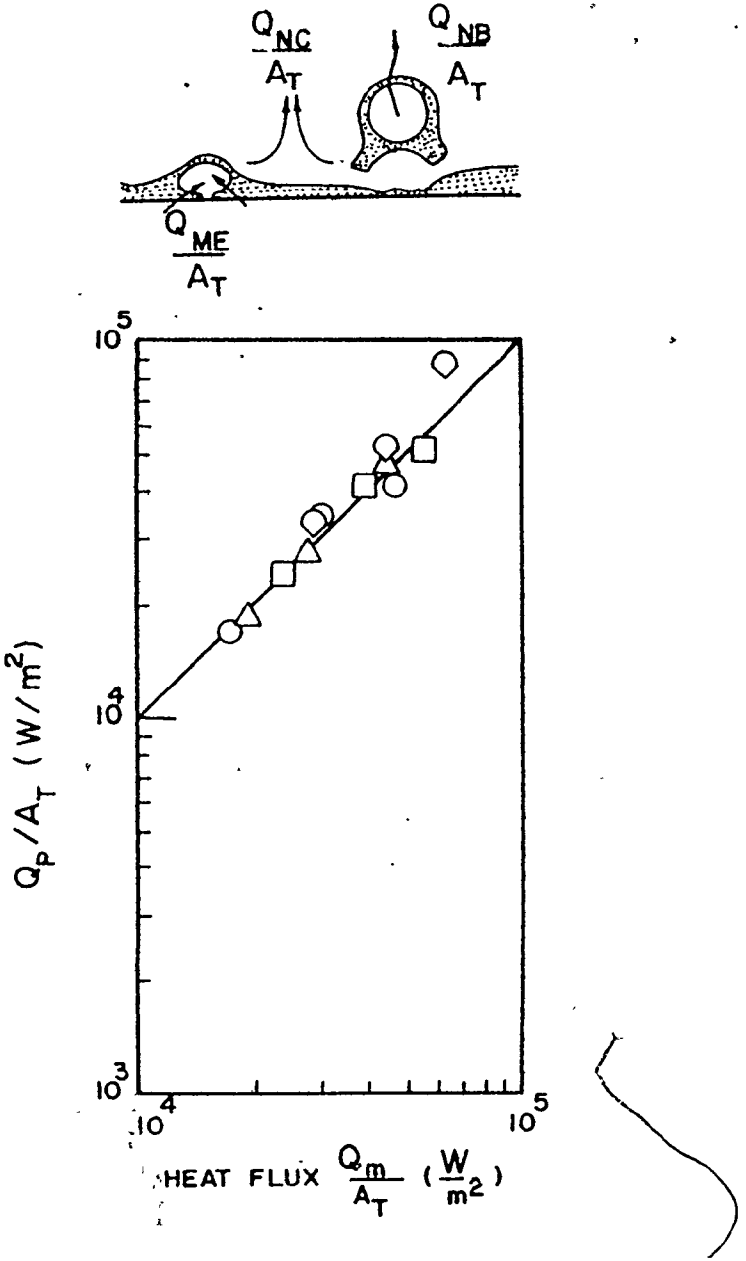

FIGURE (2.7) VERIFICATION OF HEAT TRANSFER MODEL ACCORDING TO FATH [1]

and decreasing system pressure leads to increasing microlayer evaporation heat transfer contribution. Hwang and Judd [37] proposed a model which gives an indication of the significance of the microlayer heat transfer contribution to the total boiling heat flux. The authors considered the predicted heat flux Q_P/A_T to be comprised of three components, microlayer evaporation Q_{ME}/A_T, transient conduction to the superheated layer (nucleate boiling) Q_{NB}/A_T and natural convection Q_{NC}/A_T. The natural convection component occurs in the regions uninvolved in bubble nucleation, whereas the microlayer evaporation component as well as the transient conduction to the superheated layer component occurs in the region of bubble influence. However, the heat transfer associated with the displacement of the superheated layer occurs during the waiting period, whereas the heat transfer associated with the microlayer evaporation occurs in the growth period and so the two mechanisms complement each other. Figure (2.7) presents a verification of the above mentioned model using the measurements reported by Fath [1].

CHAPTER 3

PROBLEM STATEMENT

The objective of the present work is to supplement the body of knowledge of nucleate boiling heat transfer with theoretical analyses of the following: (1) the formation of the isothermal microlayer under a growing bubble, (2) the microlayer evaporation, (3) the bubble growth on a heating surface, and finally (4) the microlayer evaporation and bubble growth. The goal is to develop computer programs which could take advantage of the speed and storage capabilities of present day computers as well as recent advances in numerical methods to establish numerical codes capable of analysing the problems of microlayer formation, evaporation and bubble growth. The numerical approaches to be adapted for this purpose and the programs developed should be simple, flexible and capable of overcoming the disadvantages of previous analyses particularly,

1. The numerous simplifying assumptions which sometimes lead to a hypothetical problem rather than the real problem.
2. The inflexibility of the previous analyses in which one might be forced to restart the formulation from the beginning if changes were made or a new effect was added.

The first part of the present work is a study of the microlayer formation and evaporation underneath a bubble of

a known growth rate. A finite difference approach was used to study the microlayer formation with massless markers located at the liquid-vapour interface which move with the liquid flow field to define the isothermal microlayer profile and bubble front. A model for transient heat transfer was adapted to solve for microlayer evaporation using the markers which could continuously move due to evaporation to define the instantaneous microlayer profile.

The second part of the present work deals with the analysis of bubble growth on a heating surface. A numerical technique was adapted to solve the continuity, momentum and energy equations to position massless markers which were used to define the liquid vapour interface. The flow and thermal fields around the growing bubble were analysed enabling evaporation from the bubble cap to be evaluated.

The third part of the present work is a combination of the two previous parts concerning evaporation from the microlayer and the bubble cap to develop a bubble growth model assuming the mass transfer across the liquid-vapour interface to be the predominant mechanism for the bubble growth.

CHAPTER 4

ISOTHERMAL MICROLAYER FORMATION

4.1 Introduction

A bubble grows on a wall while a thin layer of liquid is left on the surface under the bubble (due to the no-slip condition at the wall). This layer is called the microlayer. The isothermal (initial) thickness of the microlayer $\delta_o(r)$ is that thickness of liquid left on the wall during an isothermal bubble growth with no microlayer evaporation occurring. The present chapter deals with the formation of such an isothermal microlayer and its thickness $\delta_o(r)$. The following sections present the proposed model for the microlayer formation, the theoretical analysis, the numerical solution, the results of the initial microlayer thickness and finally the discussion of these results in comparison with those published in the literature.

4.2 The Proposed Model

As a bubble grows on a wall, a boundary layer will be established in the liquid outside the bubble near the wall (bubble front). The bubble front will pass over the growing boundary layer and an amount of liquid will be captured under the bubble (microlayer). This microlayer liquid must be related to the boundary layer outside the bubble in a continuous manner and hence the microlayer liquid ought to flow

with a considerable velocity (residual flow) in the neighbourhood of the boundary layer. This "pumping" of liquid microlayer will continue until the flow ceases. When this occurs, the thickness of liquid left will be the initial thickness of the microlayer $\delta_o(r)$, Figure (4.1).

4.3 Theoretical Analysis

The formulation of the liquid microlayer will be analysed by considering both the dynamics of the liquid outside and under the bubble. The boundary layer equations of continuity and momentum will be solved with some simplifications related to the bubble growth problem, for both the liquid flow outside the bubble and the liquid flow under the bubble.

4.3.1 Liquid Flow Outside the Bubble Base Near the Wall

Consider the motion of the bubble front in a region near to the wall with a growth rate $\dot{R}(t)$. The flow can be divided into two regions, Figure (4.1):

1. A region very near to the wall (Boundary Layer Region) where the effect of viscosity in the momentum equation is significant.
2. A region sufficiently far from the wall (Potential Flow Region) where the effect of viscosity in the momentum equation can be neglected.

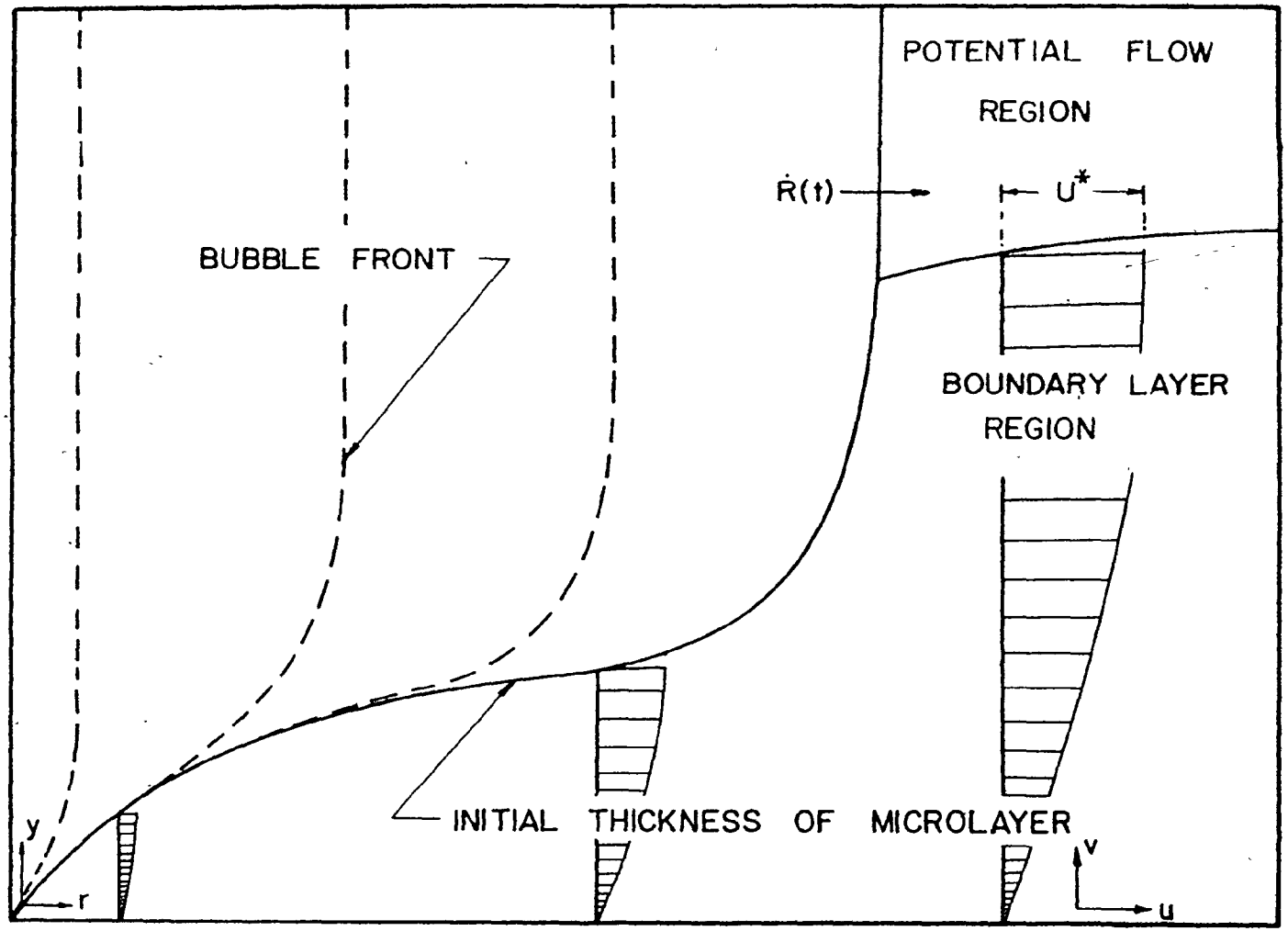

FIGURE (4.1) INITIAL MICROLAYER THICKNESS (Proposed Model)

Region 1 (Boundary Layer Region)

For axi-symmetrical flow using the cylindrical polar coordinates the boundary layer equations of continuity and momentum can be written as:

Continuity

$$\frac{1}{r}\frac{\partial}{\partial r}(ru) + \frac{\partial v}{\partial y} = 0 \tag{4.1}$$

Momentum

$$\frac{\partial u}{\partial t} + u\frac{\partial u}{\partial r} + v\frac{\partial u}{\partial y} = -\frac{1}{\rho_\ell}\frac{\partial P}{\partial r} + \nu\frac{\partial^2 u}{\partial y^2} \tag{4.2}$$

$$\frac{\partial P}{\partial y} = 0 \tag{4.3}$$

Equations (4.1) to (4.3) prescribe the motion of the liquid in the boundary layer region around the bubble base with the constraints,

Initial Condition

$$u(o,r,y) = v(o,r,y) = 0 \tag{4.4}$$

Boundary Conditions

$$u(t,r,o) = v(t,r,o) = 0 \tag{4.5}$$

$$u(t,r,\phi) = U^* \tag{4.6}$$

where U^* is the potential flow velocity.

At the liquid-vapour interface, the shear stress will be zero if the surface tension effect is ignored.

Region 2 (Potential Flow Region)

Since the bubble grows as a spherical shape (sphere or hemisphere - see Section 2.2.4), the spherical coordinate system will be the most appropriate to express the motion in the potential flow region. The continuity and momentum equations can be written as:

Continuity

$$\frac{\partial}{\partial r}\left(r^2 U^*\right) = 0 \tag{4.7}$$

Momentum

$$\frac{\partial U^*}{\partial t} + U^* \frac{\partial U^*}{\partial r} = -\frac{1}{\rho_\ell}\frac{\partial P}{\partial r} \tag{4.8}$$

The initial and boundary conditions are:

Initial Condition

$$U^*(o,r) = 0 \tag{4.9}$$

Boundary Conditions

$$U^*(t,R) = \dot{R}(t) \tag{4.10}$$

$$U^*(t,\infty) = 0 \tag{4.11}$$

Specific Formulation for Bubble Growth

If the bubble grows with a known growth rate $\dot{R}(t)$, one can integrate equation (4.7) with the aid of equation (4.10) to get,

$$U^*(t,r) = \frac{\dot{R}(t)\, R^2(t)}{r^2} \tag{4.12}$$

Then, the pressure term in equation (4.8) becomes:

$$\frac{1}{\rho_\ell}\frac{\partial P}{\partial r} = -\frac{\ddot{R}\,R^2+2\dot{R}^2\,R}{r^2} + \frac{2\,\dot{R}^2\,R^4}{r^5} \qquad (4.13)$$

The potential flow velocity, equation (4.12), will be used in the boundary condition, equation (4.6), and the pressure terms, equation (4.13), will be used in the momentum equation (4.2).

4.3.2 Liquid Flow Inside the Microlayer

Equations similar to (4.1) to (4.6) will be used for the microlayer liquid flow and can be written as:

Continuity

$$\frac{1}{r}\frac{\partial}{\partial r}(ru) + \frac{\partial v}{\partial y} = 0 \qquad (4.14)$$

Momentum

$$\frac{\partial u}{\partial t} + u\frac{\partial u}{\partial r} + v\frac{\partial u}{\partial y} = -\frac{1}{\rho_\ell}\frac{\partial P}{\partial r} + \nu\frac{\partial^2 u}{\partial y^2} \qquad (4.15)$$

$$\frac{\partial P}{\partial y} = 0 \qquad (4.16)$$

Initial Conditions

$$u(o,r,v) = 0 \qquad (4.17)$$

Boundary Conditions

$$u(t,r,o) = v(t,r,o) = 0 \qquad (4.18)$$

$$\mu\frac{\partial[u(t,r,\delta_o)]}{\partial y} = 0 \qquad (4.19)$$

4.3.3 Problem Statement

For a known bubble growth rate $\dot{R}(t)$, it is required to solve the momentum equation (4.2) for the radial velocity component $u(t,r,y)$ in the boundary layer (the pressure term is defined in equation (4.13)), then to solve the continuity equation (4.1) for the boundary layer axial velocity $v(t,r,y)$ using the initial and boundary conditions specified in equations (4.4), (4.5), (4.6) and (4.12). As soon as the liquid is captured under the bubble, the momentum equation (4.15) has to be solved for the microlayer radial velocity component $u(t,r,y)$ and the continuity equation (4.14) has to be solved for the microlayer axial velocity component $v(t,r,y)$ using the initial and boundary conditions equations (4.17) to (4.19). It is also required to identify the interface of the bubble in order to identify the regions outside and under the bubble as well as applying the interface boundary condition (4.19).

4.4 Numerical Solution

4.4.1 Introduction

The momentum equations for both the boundary layer outside the bubble and the microlayer under the bubble are similar and therefore the method of solution is similar except for the difference in handling the initial and boundary conditions.

Recent publications concerning the solution of unsteady

boundary layer problems have indicated that finite difference techniques are a powerful tool for obtaining numerical solution to such nonlinear partial differential equations [38]. Once it had been decided to solve the equations described in the last section using the finite difference technique, the choice between explicit and implicit procedures remained. The explicit method allows the solution to proceed directly, solving explicitly for one unknown at a time. In the implicit technique, a set of simultaneous algebraic equations must be solved at each step. The difficulty with the explicit procedures is that small steps must usually be taken in the "Marching" direction, otherwise instability problems arise. Implicit methods, on the other hand, are stable even with relatively large steps. Since the handling of large sets of simultaneous equations by matrix techniques is not a problem with modern computers especially if library subroutines are available, implicit methods are usually used.

A finite difference grid was superimposed on the flow field as illustrated in figure (4.2). Values of velocity components were calculated at the nodal points of the grid by replacing the derivatives in the conservation equations with the appropriate finite difference approximations, and then solving these difference equations at each node. In the explicit method, the difference equations are solved one node at a time for all the nodes in the grid. In the implicit method, two possibilities exist. The equations for an entire column of nodes can be solved simultaneously, in which case progress

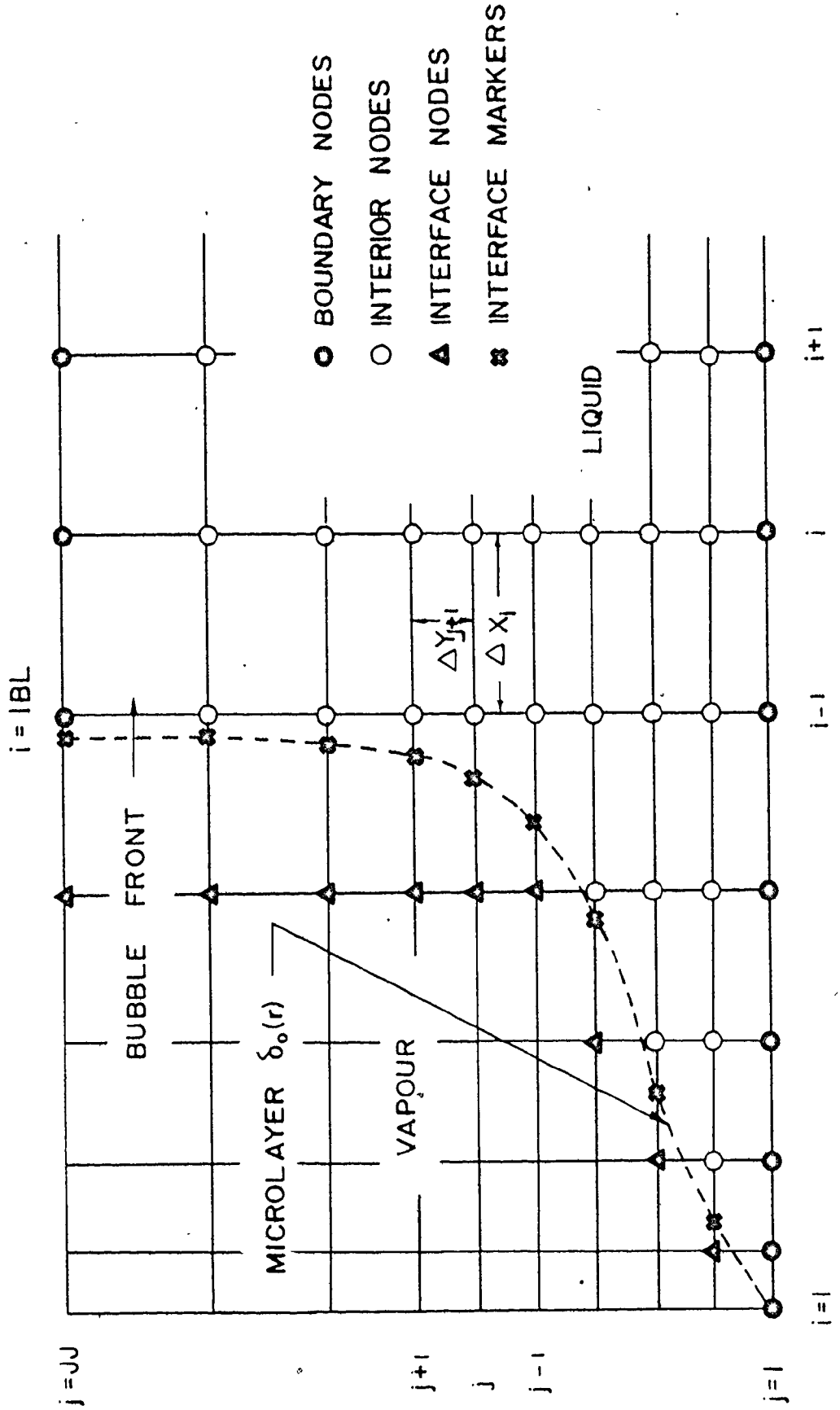

FIGURE(4.2) FINITE DIFFERENCE NODAL REPRESENTATION

through the grid is made by "marching" downstream column by column. This marching procedure is applied when the system of equations is parabolic, i.e. when boundary conditions are specified at three of the four boundaries of the flow field. Alternatively, the equations at each node in the grid can be solved simultaneously when the system of equations is elliptic, i.e., when the boundary conditions are specified at all four boundaries. The former procedure of "marching" was applied to the present problem.

4.4.2 Nodal Structure, Interface Markers and Node Flagging

The nodal structure of part of the computational region is shown in figure (4.2). The "filled circular" nodes represent the boundaries where the velocity values are known from the boundary conditions. The "blank circular" nodes represent the nodes whose values are unknown. The "triangular" nodes represent the liquid-vapour interface where the known interface conditions have to be applied.

The interface can be defined by massless markers which move with the flow field according to a simple kinematic relation between the surface geometry and the fluid velocity. The "cross" markers in figure (4.2) identify the interface and move along the radial lines. The interface marker coordinates (r,y) are related to the marker velocity components u_k and v_k by:

$$r^{n+1} = r^n + u_k.\Delta t - v_k.\Delta t.\ \frac{\Delta r}{\Delta y} \qquad (4.22)$$

The marker velocity components u_k and v_k were extrapolated from the surrounding node velocities.

According to the position of the interface markers, liquid and vapour regions could be easily defined. Every node was "flagged" by a number defining its condition. Vapour nodes were given number 1, interface nodes number 2 and liquid nodes number 3.

4.4.3 Finite Difference Representation

(i) Boundary Layer Outside the Bubble

A. Radial Velocity Component

An implicit finite difference method was used to solve the boundary layer momentum equation (4.2) with the aid of the initial and boundary conditions (4.4) to (4.6). Equation (4.2) was rewritten as:

$$\left(\frac{\partial u}{\partial t}\right)_{ij}^{n+1} = -u_{ij}^n \left(\frac{\partial u}{\partial r}\right)_{ij}^{n+1} - v_{ij}^n \left(\frac{\partial u}{\partial y}\right)_{ij}^{n+1} - \frac{i}{\rho_\ell}\left(\frac{\partial P}{\partial r}\right)_{ij}^{n+1} + \nu\left(\frac{\partial^2 u}{\partial y^2}\right)_{ij}^{n+1} \qquad (4.23)$$

Applying the finite difference approximations (discussed in Appendix B), equation (4.23) reduced to:

$$A_j\, u_{i,j-1} + B_j\, u_{ij} + C_j\, u_{i,j+1} = D_j \qquad (4.24)$$

where

$$A_j = \left[- \frac{v^n_{ij}}{(\Delta y_j + \Delta y_{j+1})} \cdot \left(\frac{\Delta y_{j+1}}{\Delta y_j}\right) - \frac{\nu}{\Delta y_1 \cdot \Delta y_j} \right]$$

$$B_j = \left[\frac{1}{\Delta t} + \frac{u^n_{ij}}{\Delta r_i} + \frac{v^n_{ij}}{(\Delta y_j + \Delta y_{j+1})} \left(\frac{\Delta y_{j+1}}{\Delta y_j} - \frac{\Delta y_j}{\Delta y_{j+1}}\right) + \frac{\nu}{\Delta y_1}\left(\frac{1}{\Delta y_{j+1}} + \frac{1}{\Delta y_j}\right) \right]$$

$$C_j = \left[\frac{v^n_{ij}}{\Delta y_j + \Delta y_{j+1}} \left(\frac{\Delta y_i}{\Delta y_{j+1}}\right) - \frac{\nu}{(\Delta y_1)(\Delta y_{j+1})} \right]$$

$$D_j = \frac{u^n_{ij}}{\Delta t} + u^n_{ij} \left(\frac{u^{n+1}_{i=1,j}}{\Delta r_i}\right) - DPDX$$

Thus for column i, a tridiagonal system of (JJ-2) equations with (JJ-2) unknowns was obtained. The equations were written as:

$$A_2 u_{i,1} + B_2 u_{i,2} + C_2 u_{i,3} = D_2 \quad (u_{i,1} = 0)$$

$$A_3 u_{i,2} + B_3 u_{i,3} + C_3 u_{i,4} = D_3$$

$$A_{(JJ-1)} u_{i(JJ-2)} + B_{(JJ-1)} u_{i(JJ-1)} + C_{JJ-1} u_{iJJ} = D_{(JJ-1)}$$

(u_{iJJ} known)

(4.25)

where $u_{i,1} = 0$, Equation (4.4)

$u_{i,JJ} = U^* = \frac{\dot{R} R^2}{r^2}$ Equation (4.6)

or in matrix form:

$$\begin{bmatrix} B_2 & C_2 & & & & & \\ A_3 & B_3 & C_3 & & & 0 & \\ & A_4 & B_4 & C_4 & & & \\ & & & & & & \\ & & & & & & \\ & 0 & & A_{JJ-2} & B_{JJ-2} & C_{JJ-2} & \\ & & & & A_{JJ-1} & B_{JJ-1} & \end{bmatrix} \begin{bmatrix} u_{i,2} \\ u_{i,2} \\ u_{i,4} \\ \\ \\ u_{i,JJ-2} \\ u_{i,JJ-1} \end{bmatrix} = \begin{bmatrix} D_2 \\ D_3 \\ D_4 \\ \\ \\ D_{JJ-2} \\ D_{JJ-1} \end{bmatrix} \qquad (4.26)$$

or

$$[A]\ [u] = [XB] \qquad (4.27)$$

This system of equations was solved for the radial velocity component u_{ij} at column i using McMaster Library Subroutine DIAG3.

B. Axial Velocity Component

Having determined the values of the radial velocity component u_{ij}^{n+1} for all values of i and j, the solution proceeded to compute the values of the axial velocity component v_{ij}^{n+1} from the continuity equation (4.1). Equation (4.1) was rewritten as:

$$\left(\frac{\partial v}{\partial y}\right)_{ij}^{n+1} = -\left(\frac{\partial u}{\partial r}\right)_{ij}^{n+1} - \left(\frac{u}{r}\right)_{ij}^{n+1} \tag{4.28}$$

or in finite difference form.

$$v_{ij}^{n+1} = v_{i,j-1}^{n+1} - \frac{\Delta y_j}{2}\left[(\text{DUDRJ}+\text{DUDRJJ}) + \left(\frac{u_{ij}^{n+1}+u_{i,j-1}^{n+1}}{r_i}\right)\right] \tag{4.29}$$

where

$$\text{DUDRJ} = \frac{(u_{i+1,j}^{n+1} - u_{ij}^{n+1})}{\Delta r_{i+1}}$$

$$\text{DUDRJJ} = \frac{(u_{i+1,j-1}^{n+1} - u_{i,j-1}^{n+1})}{\Delta r_{i+1}}$$

The solution of equation (4.29) starts at the wall where $v_{i,1}^{n+1} = 0$ (equation (4.4)). Since r and u are known across the boundary layer at every node, it is possible to determine v_{ij}^{n+1} one step away from the wall then at two steps, etc. This procedure was continued up to the top boundary

(j=JJ) and continued "marching" downstream up to the right hand (i=II) boundary .

C. Initial and Boundary Conditions

The velocity components u_{ij}^n and v_{ij}^n were represented by U(I,J,N) and V(I,J,N) respectively in the computer program where I defines the column, J defines the row and N defines the time increment, Figure (4.3.a).

Initial Conditions

$$U(I,J,1) = V(I,J,1) = 0 \tag{4.30}$$

Boundary Conditions

The boundary layer outside the liquid-vapour interface starts from column i = IBL. Accordingly, equations (4.5) and (4.6) will be:

$$U(I,1,N+1) = V(I,1,N+1) = 0 \tag{4.31}$$

$$U(I,JJ,N+1) = \dot{R}(t)\ R^2/r^2$$

$$= \dot{R}(t)\ R^2/\left(\sum_{m=2}^{i} \Delta r_m\right)^2 \tag{4.32}$$

The interface condition was applied at column i = IBL-1. This condition was simplified by setting the shear stress equal to zero

$$U(IBL-1,\ J,N+1) = U(IBL,\ J,N+1) \tag{4.33}$$

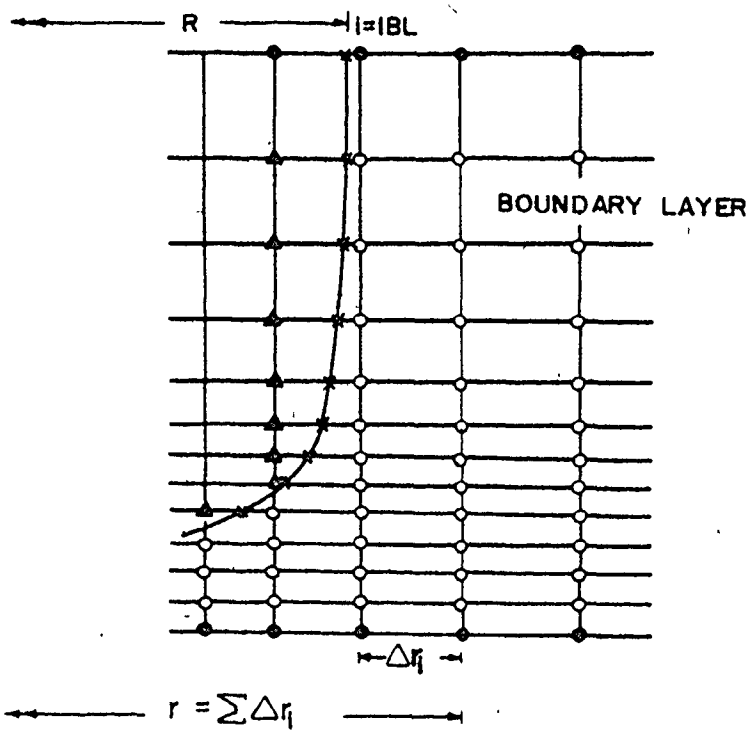

(a) BOUNDARY LAYER

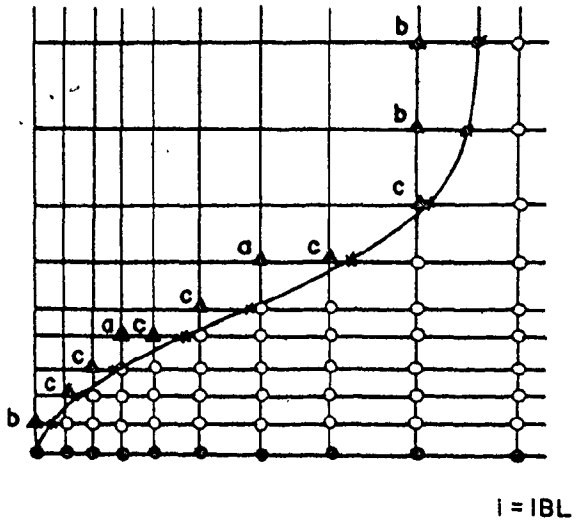

(b) MICROLAYER

FIGURE (4.3) INITIAL AND BOUNDARY CONDITIONS

(ii) Microlayer Under the Bubble

For the flow of liquid inside the microlayer (under the bubble), an explicit finite difference method was used to solve both momentum and continuity equations (4.15) and (4.14). This explicit method was found to suit the microlayer analysis better since the interface boundary is moving and the fluid nodes move with the fluid flow as time goes on, Figure (4.3.b).

A. Radial Velocity Component

The momentum equation for the microlayer flow (4.15) can be written as

$$\left(\frac{\partial u}{\partial t}\right)_{ij}^{n+1} = -u_{ij}^{n}\left(\frac{\partial u}{\partial r}\right)_{ij}^{n} - v_{ij}^{n}\left(\frac{\partial u}{\partial y}\right)_{ij}^{n} - \frac{1}{\rho_{\ell}}\left(\frac{\partial P}{\partial r}\right)_{ij}^{n} + \nu\left(\frac{\partial^2 u}{\partial y^2}\right)_{ij}^{n} \tag{4.34}$$

Using finite difference approximation (see Appendix B) equation (4.34) can be approximated by:

$$u_{ij}^{n+1} = u_{ij}^{n} - \Delta t\,(FUX+FUY) - \Delta t(DPDX) + \Delta t^{*}\nu^{*}\,VISCOX \tag{4.35}$$

where FUX, FUY, DPDX and VISCOX are defined in Appendix B.

B. Axial Velocity Components

Similar to the boundary layer outside the bubble, the microlayer continuity equation was solved explicitly for the axial velocity component v using the relationship:

$$v_{ij}^{n+1} = v_{i,j-1}^{n+1} - \frac{\Delta y_j}{2}\left[DUDRJ+DUDRJJ + \frac{u_{ij}^{n+1}+u_{i,j-1}^{n+1}}{r_i}\right] \quad (4.36)$$

C. Boundary Conditions

The velocity components at the wall are zero, i.e.,

$$U(I,1,N+1) = V(I,1,N+1) = 0 \quad (4.37)$$

At the interface (triangular nodes), the shear stress must be zero. According to the location of the interface node with respect to the fluid nodes, the interface node velocity will be defined, i.e., according to figure (4.3.b),

$U(I,J,N+1) = U(I,J-1,N)$ for interface nodes with number a

$U(I,J,N+1) = U(I+1,J,N)$ for interface nodes with number b

$U(I,J,N+1) = \frac{1}{2}[U(I,J-1,N) + U(I+1,J,N)]$ for interface nodes with number c

4.4.4 Computation Procedure

Figure (4.4) illustrates the computation procedure in a diagrammatic way. The computation steps are summarized as follows, but a detailed listing of the program is available in reference [39].

1. All fixed and know parameters (time steps, step sizes, number of nodes,... and density, viscosity,... etc.) are supplied (Subroutine DATAML).

2. The initial condition provides the starting values of u and v, the initial position of the bubble interface markers and the initial node flagging (Subroutine ICML).
3. Making use of the marker positions, the column which separates the boundary layer and the microlayer is defined (i=IBL).
4. The nodes are flagged (Subroutine FLAGML).
5. The boundary conditions are set up to define the new values of u and v at the boundaries (Subroutine BCML).
6. The new microlayer velocity components u and v are calculated, starting only after the markers pass over one column at least (Subroutine ML).
7. The new boundary layer velocity components u and v are calculated (Subroutine BL).
8. Marker velocities are calculated and marker positions r_k and y_k are defined (Subroutine MARKERML).
9. The new values of u, v, r_k and y_k are stored (Subroutine ADVANCML).
10. Results are printed if needed (Subroutine PRINTML).
11. The time is increased by time increment DT.
12. The procedure is repeated from step number 3 unless the time exceeds the prespecified growth time.

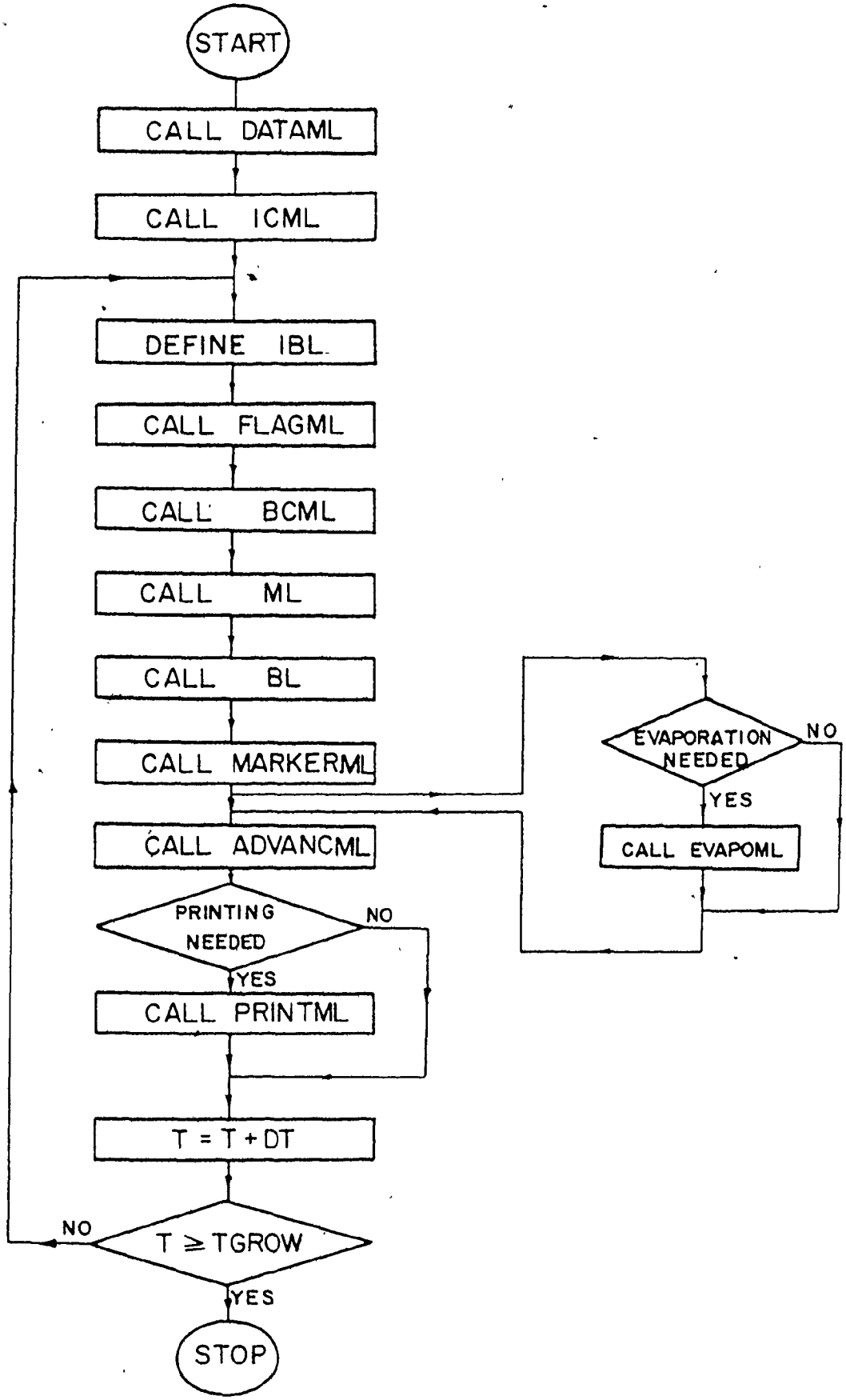

FIGURE (4.4) COMPUTATION PROCEDURE

4.4.5 Numerical Stability

The problem of numerical stability arises with the substitution of finite difference approximations in the differential equations. Stability means that errors made at one stage of the calculation do not grow as the computations continue but instead die out. These errors result from round off error and the choice of a finite step size. Specification of the step size varies from one problem to another. Smaller step sizes produce more accurate results. However in selecting the step size, it should be remembered that the computing time increases in inverse proportion to step size. Once the step sizes along and across the flow field have been chosen, the choice of time step in the explicit methods is governed by two restrictions. First, the fluid cannot move through more than one spatial step in one time step. This constraint is the Courant stability condition written as:

$$\text{Courant Number} = \max\left(\left|\frac{u\Delta t}{\Delta r}\right|, \left|\frac{v\Delta t}{\Delta y}\right|\right) < 1 \qquad (4.40)$$

Second, the momentum must not diffuse more than one spatial step in one time step. This constraint is the diffusion stability condition written as:

$$\Delta t < \frac{1}{2\nu}\left(\frac{\Delta r^2\ \Delta y^2}{\Delta r^2+\Delta y^2}\right) \qquad (4.41)$$

4.5 Prediction of the Isothermal (Initial) Microlayer Thickness

4.5.1 Introduction

The problem under consideration concerns a static bubble nucleus of radius R_c (represented by markers) growing from time zero to the growth time t_g with a known growth rate $\dot{R}(t)$. The final position of the markers after the liquid microlayer development ceases (or the growth time t_g is reached) will define the microlayer profile and its isothermal (initial) thickness $\delta_o(r)$. Figure (4.5) illustrates the formation of the isothermal microlayer with time. For this particular growth rate, the microlayer thickness is of the order of 0-5 μm. In the following sections, the effect of varying some computational and physical parameters are studied, including the spatial step size across the surface Δy, the cavity radius R_c, the boundary layer thickness ϕ, the bubble growth rate $\dot{R}(t)$, the residual flow and the kinematic viscosity ν. Three arbitrary growth rates were specified as depicted in figure (4.6) in order to exercise the computer program. A discussion of these results will also be presented in the last section.

4.5.2 Computational Parameters

(i) The Effect of the Step Size Δy

For the same bubble growth rate $\dot{R}(t)$, increasing the number of nodes near the wall (i.e. decreasing Δy near the wall) causes a decrease in the thickness. The rate of the decrease diminishes and the curves converge, giving a limiting value (3 μm at 0.4 mm from the bubble center) as

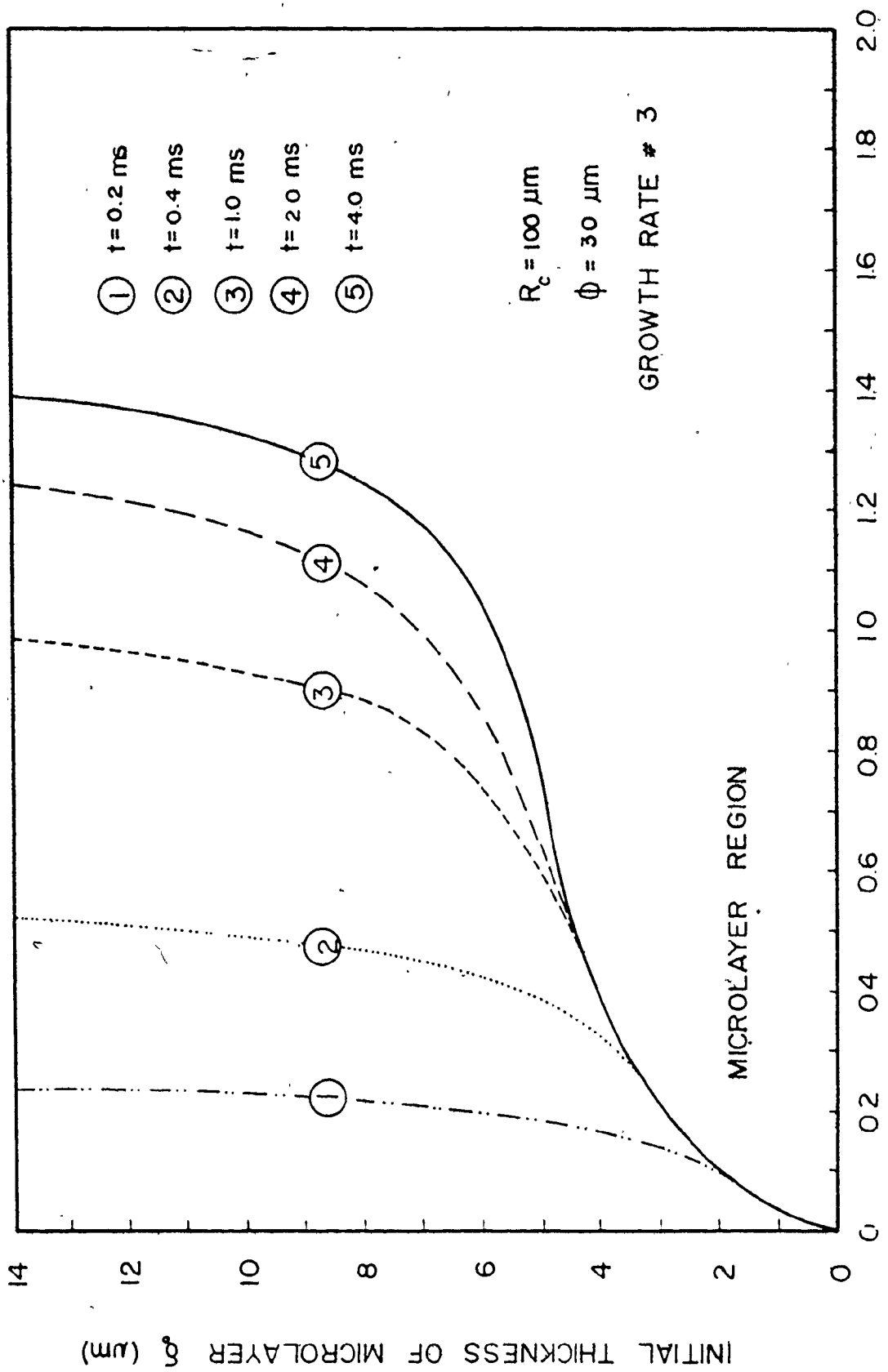

FIGURE(4.5) MICROLAYER FORMATION

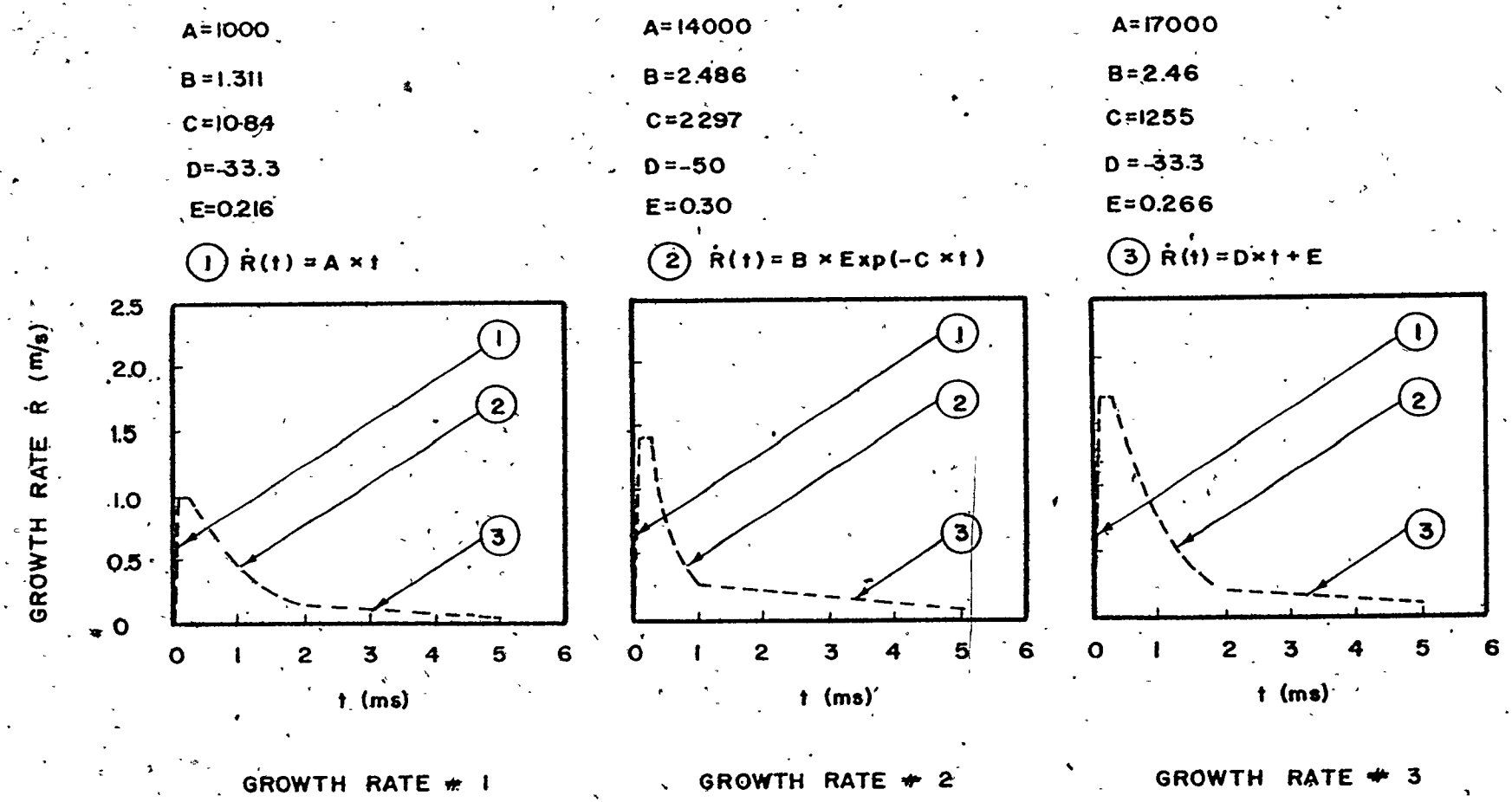

FIGURE(4.6) ASSUMED GROWTH RATES

shown in figures (4.7) and (4.8). As the number of nodes near the wall increases, the solution approaches a convergent solution; however the time step must decrease due to stability conditions and cost constraints assume preeminence.

(ii) The Effect of the Cavity Radius R_c

The effect of the cavity radius R_c is shown in figure (4.9) from which it is clear that increasing R_c four times increases δ_o by only (5-10)%. Consequently, it may be concluded that the computation procedure is relatively insensitive to the value specified for the cavity radius.

(iii) The Effect of the Boundary Layer Thickness ϕ

The bubble growth rate $\dot{R}(t)$, the potential flow velocity $U^*(r,t) = \frac{\dot{R}(t)R^2(t)}{r^2}$ and the pressure gradient $\frac{\partial P}{\partial r}$ have to be supplied at the upper boundary of the computational field ϕ (i.e., in the potential flow region). Accordingly, the assumed value of ϕ should always be bigger than or equal to the boundary layer thickness. A value of ϕ = 50 μm was assumed and checked by assuming larger values to see whether or not this parameter had a significant effect. Figure (4.10) shows the outcome which implies no significant influence on the microlayer results.

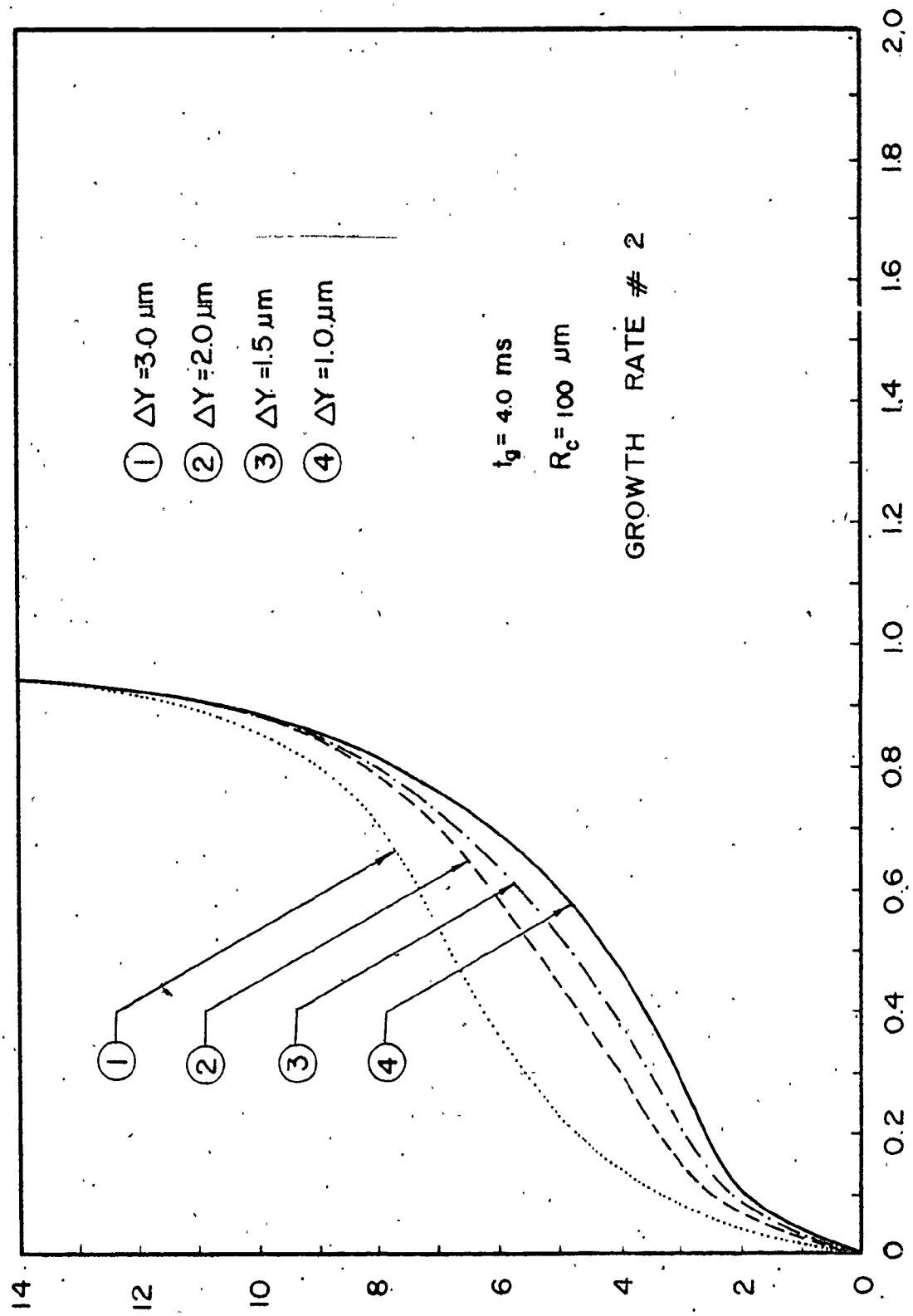

FIGURE(4.7) EFFECT OF STEP SIZE ΔY

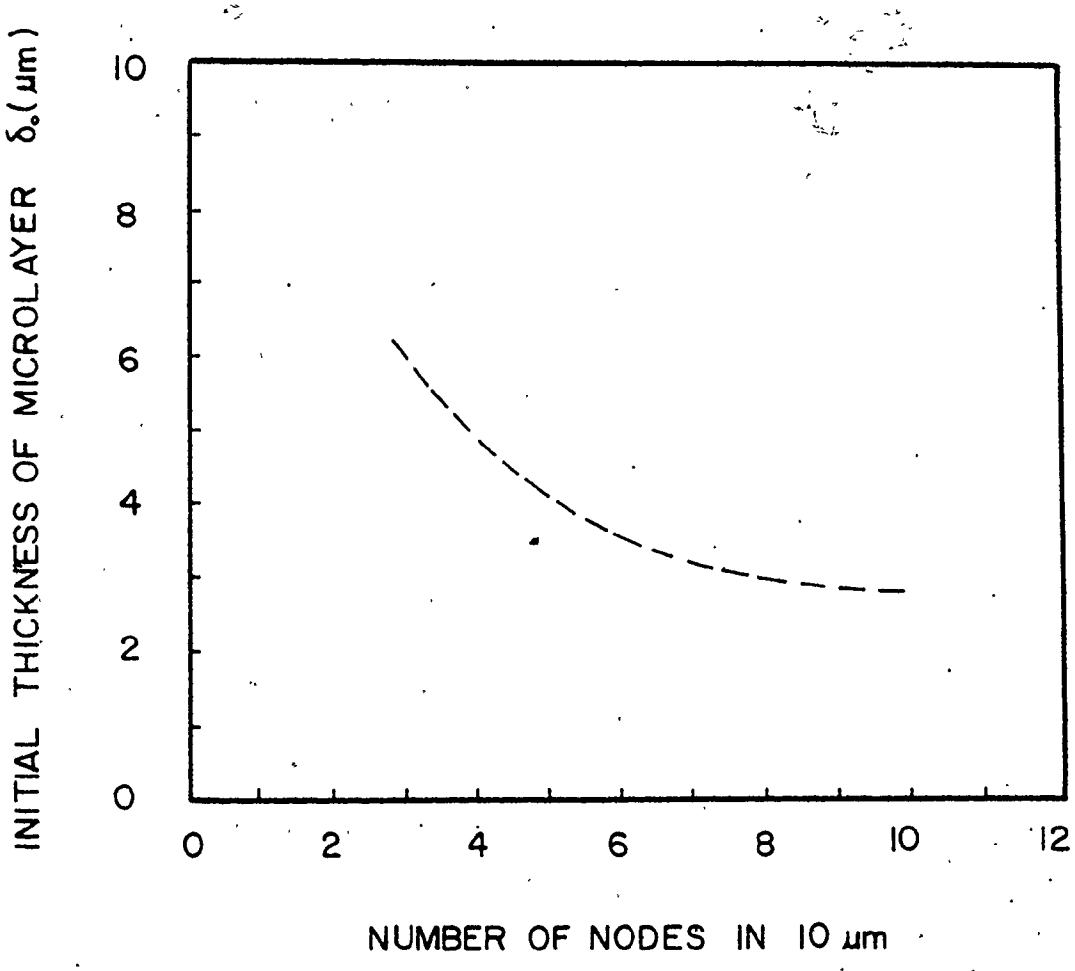

FIGURE (4.8) SOLUTION CONVERGENCE

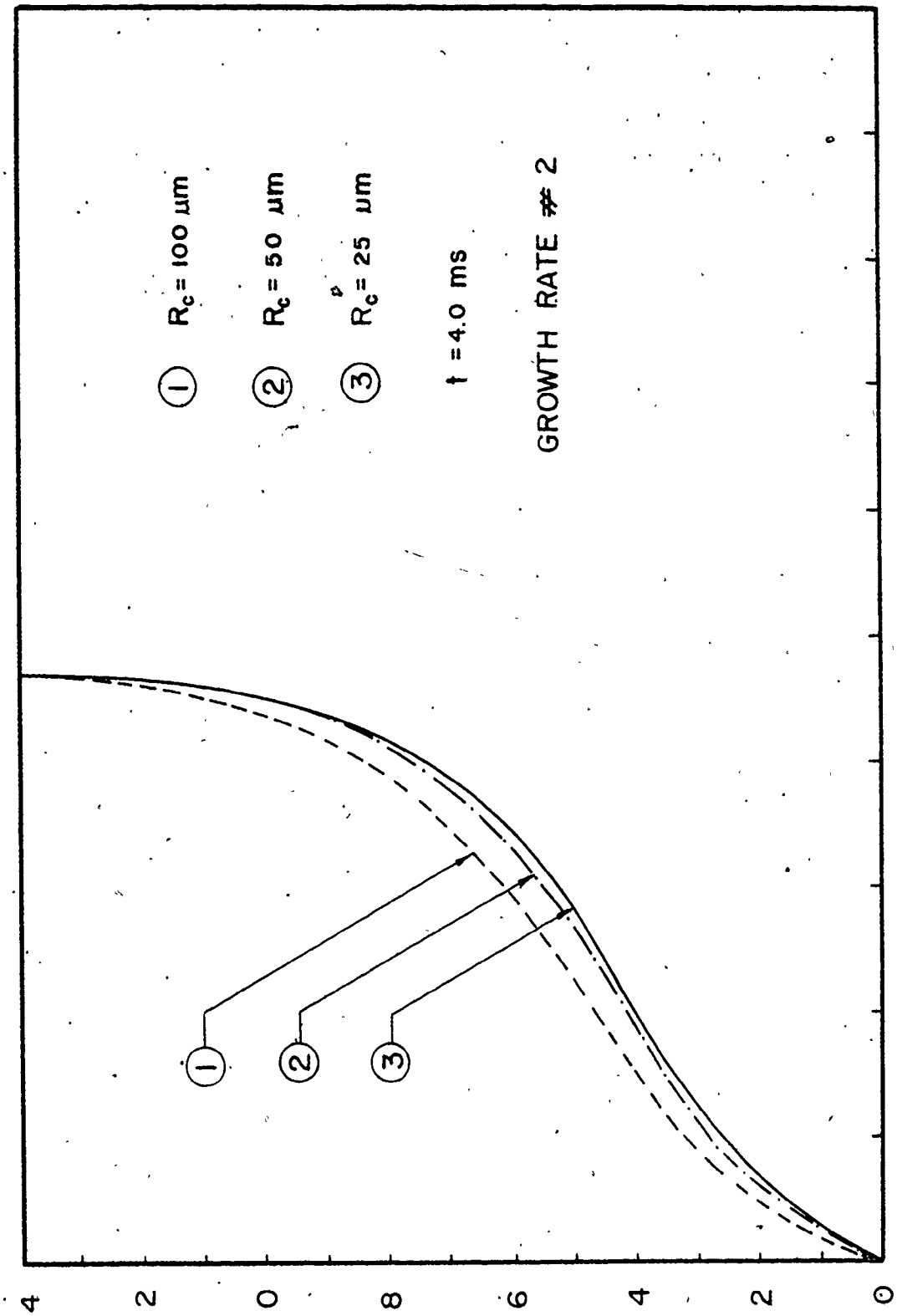

FIGURE (4.9) EFFECT OF CAVITY RADIUS R_c

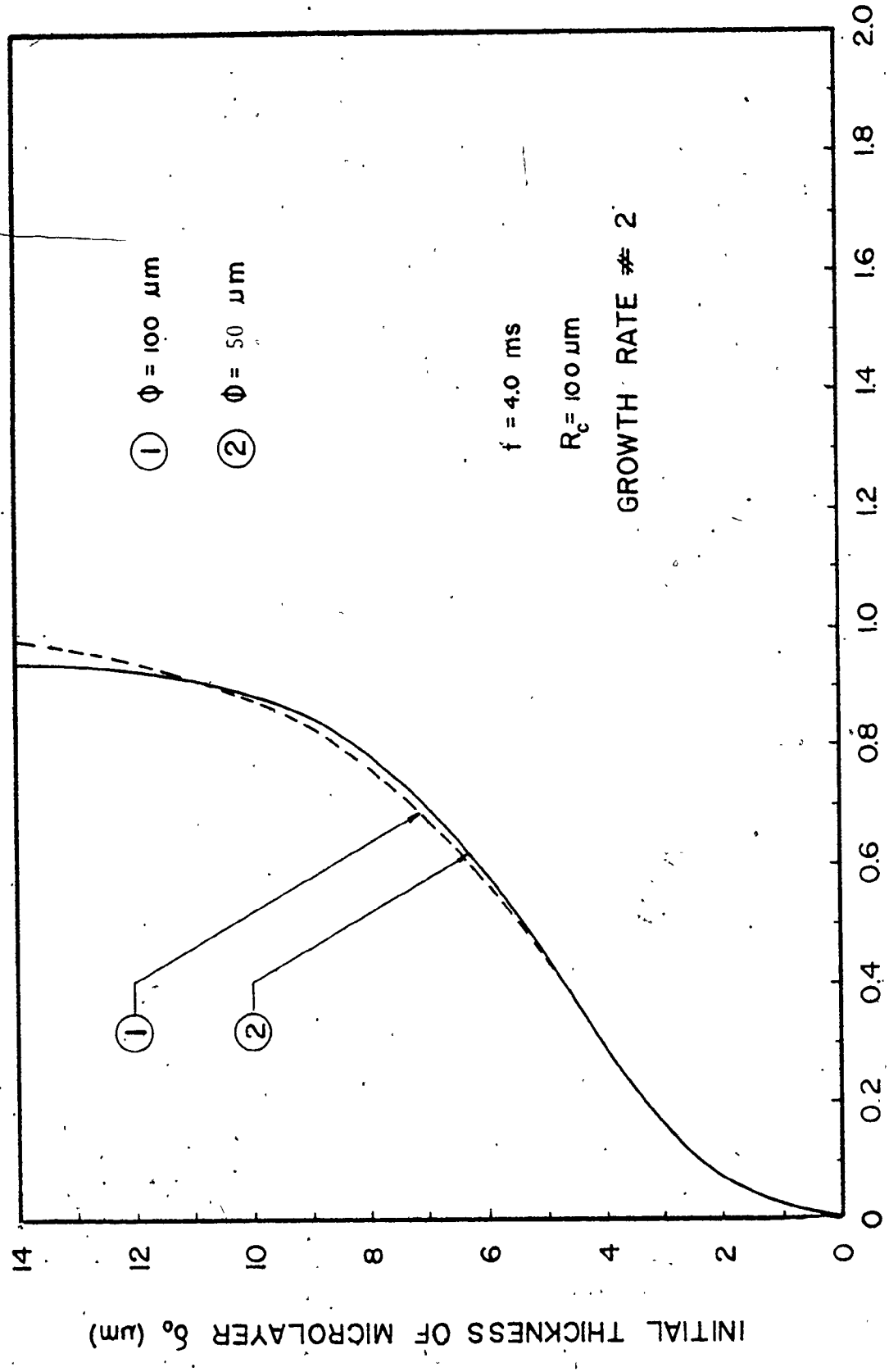

FIGURE (4.10) EFFECT OF BOUNDARY LAYER THICKNESS Φ

4.5.3 Physical Parameters

(i) The Effect of the Bubble Growth Rate $\dot{R}(t)$

The effect of the bubble growth rate $\dot{R}(t)$ is illustrated in figure (4.11). Increasing the growth rate causes larger bubbles to be formed and more liquid to be captured under the bubble. On the other hand, the increased potential flow velocity ($U^* = \dot{R}^* R^2/r^2$) corresponding to higher growth rates causes higher residual flow which pumps more liquid to the surroundings resulting in a thinner microlayer thickness.

(ii) The Effect of Residual Flow

If the microlayer velocity (residual flow) were neglected, there would be no "pumping" of the liquid towards the outside and the microlayer thickness would be bigger as shown in figure (4.12).

(iii) The Effect of Liquid Properties

Thermophysical properties vary from one liquid to another and for a single liquid they change with the system conditions (mainly system pressure and temperature). So it is of some interest to determine the effect of liquid properties (mainly density and viscosity) on the initial thickness of the microlayer. Figure (4.13) shows this effect for various conditions for the single growth rate distribution $\dot{R}(t)$ indicated in the same figure. From this illustration it can be seen that the effect of the system pressure is

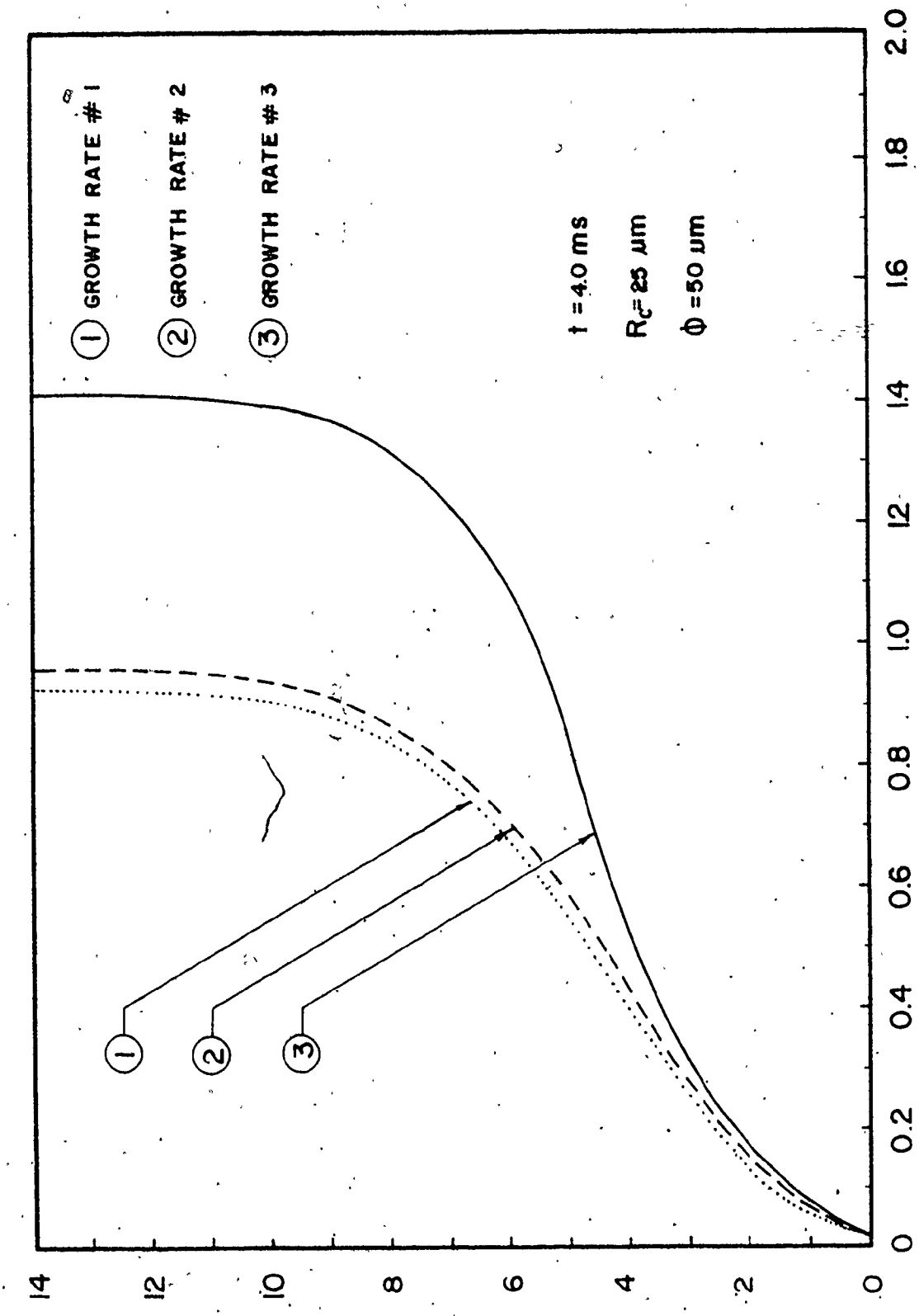

FIGURE (4.11) EFFECT OF GROWTH RATE $\dot{R}(t)$

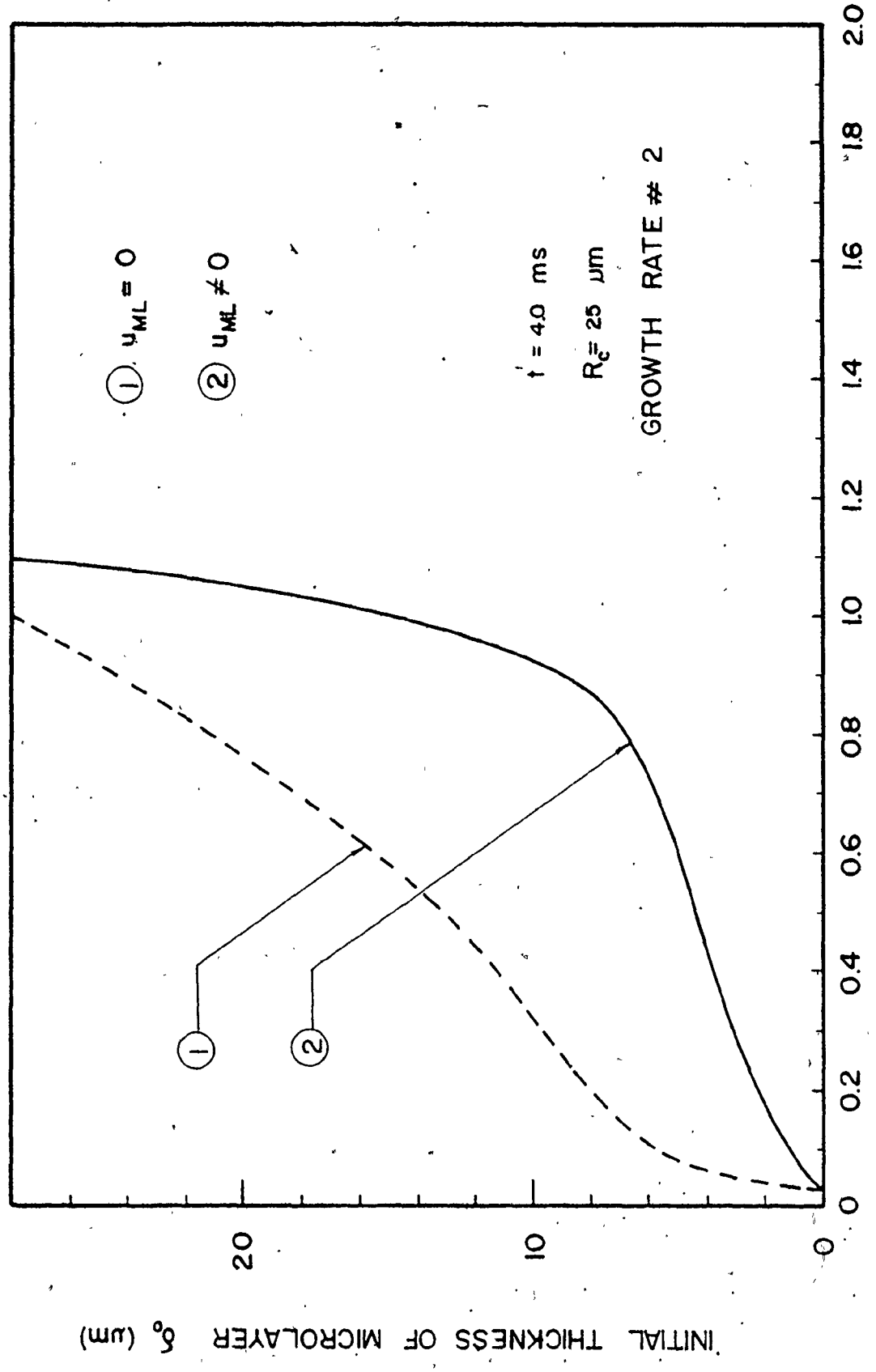

FIGURE (4.12) EFFECT OF RESIDUAL FLOW u_{ML}

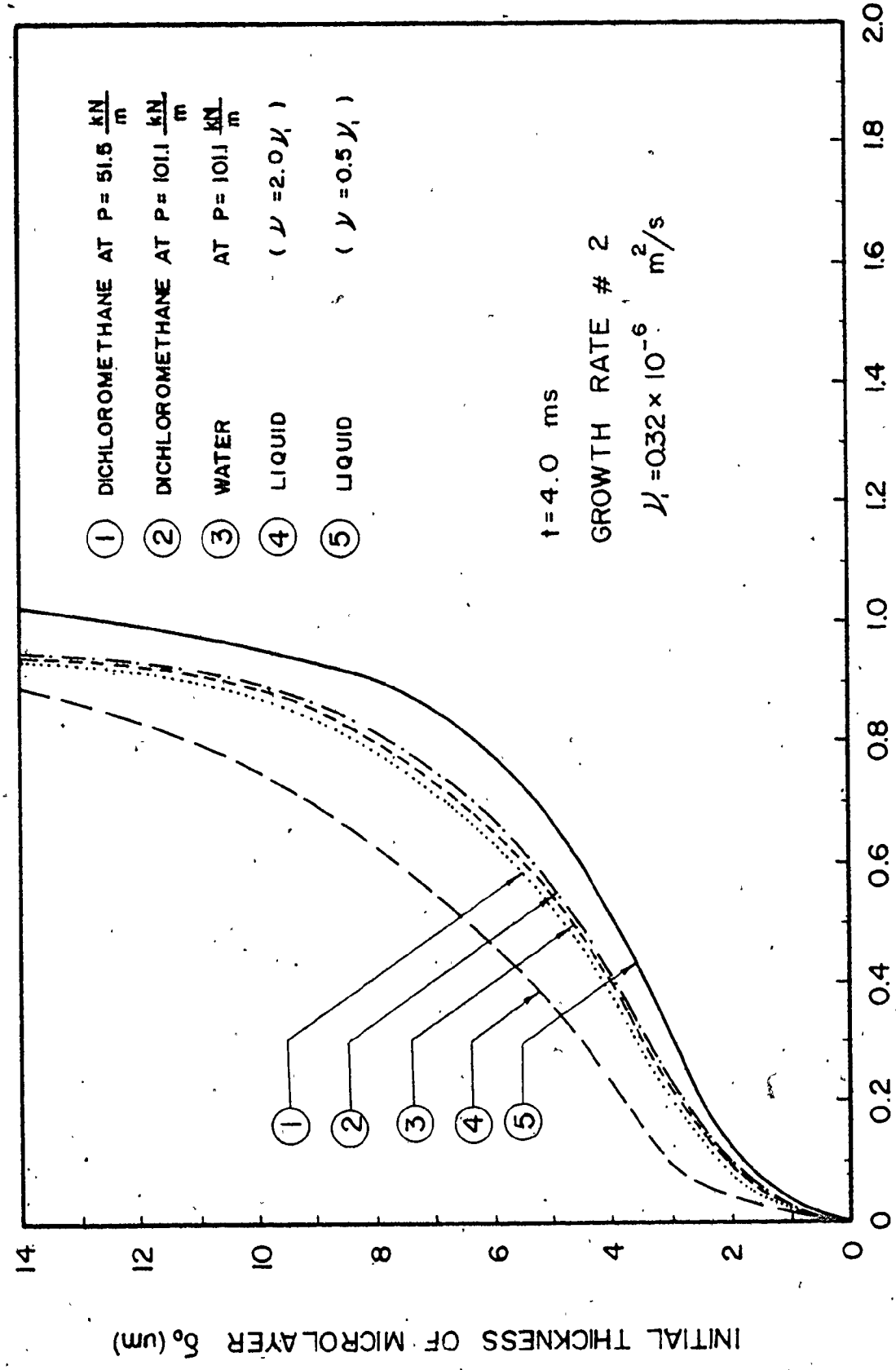

FIGURE (4.13) EFFECT OF LIQUID PHYSICAL PROPERTIES

negligible since its effect on the properties is very small. For different liquids the effect is also small if the liquid's properties are close (water and dichloromethane at P = 101.3 kN/m^2 are shown). However for liquids of greater viscosity, the residual flow ceases faster leaving behind a thicker microlayer. For less viscous liquids, liquid resistance will be less and a thinner microlayer will be obtained.

4.5.4 Application of an Existing Growth Rate Model

From the previous sections one can see that once the fluid properties (mainly μ and ρ) as well as the growth relationship $\dot{R}(t)$ for a bubble are specified, the initial thickness of the microlayer under the bubble can be obtained. One of the many existing models to predict the bubble growth rate is that of Mikic et al. [7] (MRG model). The growth rate formula is given as:

$$\dot{R}(t) = A\left[\frac{A^2}{B^2}\, t+1 - \theta\left[\frac{t}{t+t_w}\right]^{1/2}\right]^{1/2} - \frac{A^2}{B^2}\, t^{1/2} \qquad (4.42)$$

where

$$A = \left(\frac{\pi\, h_{fg}\, \rho_v\, \Delta T_{sup}}{7\, \rho_\ell\, T_{sat}}\right)^{1/2}$$

$$B = \left(\frac{1.2\, \alpha_\ell}{\pi}\right)^{1/2} Ja$$

$$Ja = \left(\frac{\Delta T_{sup}\, \rho_\ell\, C_\ell}{h_{fg}\, \rho_v}\right)$$

$$\theta = \frac{T_B - T_w}{T_{sat} - T_w}$$

This model was incorporated to test the computer program for dichloromethane at t_w = 5.0 ms and ΔT_{sup} = 30°C. Figure (4.14) illustrates the growth rate adapted to include an assumed initial growth rate relationship since MRG [7] model neglected it. The resultant microlayer profile is shown in figure (4.15).

4.6 Discussion of the Initial Microlayer Results

The advantages of the numerical study presented in this chapter are associated with the simplicity of the computer program and its capability in handling any specified bubble growth rate relationship (experimental or analytical) which is an advantage over almost all the existing analyses which approximate the growth rate as $R(t) \propto t^n$. The numerical results presented show that the initial microlayer thickness is of the order of 0-5 μm, which is consistent with the experimental data (as discussed in section 2.3.2).

To the best of the author's knowledge, there is no experimental data available for the isothermal microlayer. However, the instantaneous microlayer profiles $\delta(r,t)$ of the experimental data of Fath [1], and Voutsinos and Judd [26] could give an indication of the initial microlayer thickness as a function of the bubble radius. If the initial microlayer thickness $\delta_o(r)$ is considered as the locus of points at which the gradient $\frac{\partial \delta(r,t)}{\partial r}$ goes to infinity, it can be seen that the present solution gives a good prediction for

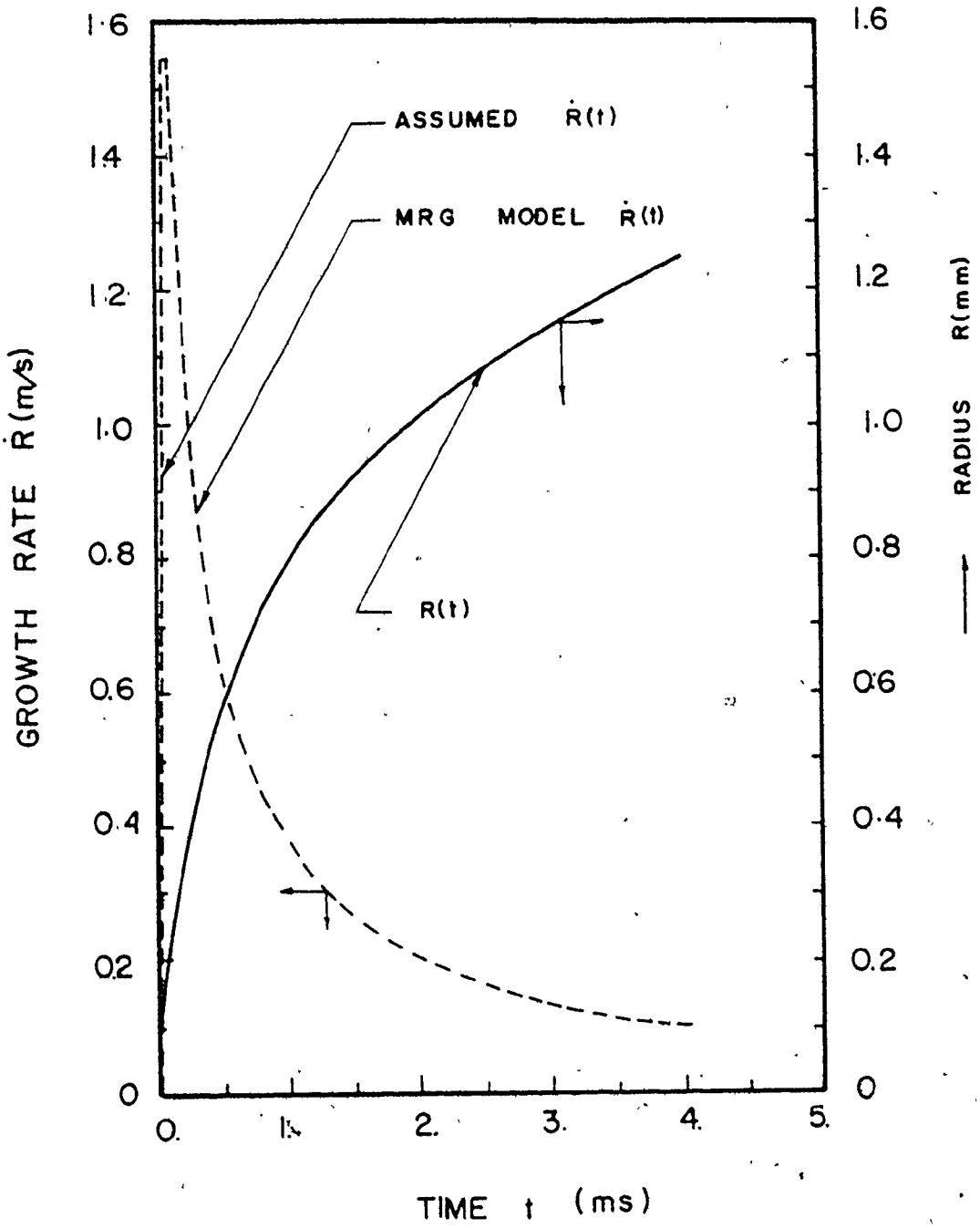

FIGURE (4.14) MRG [7] MODEL (Growth Rate)

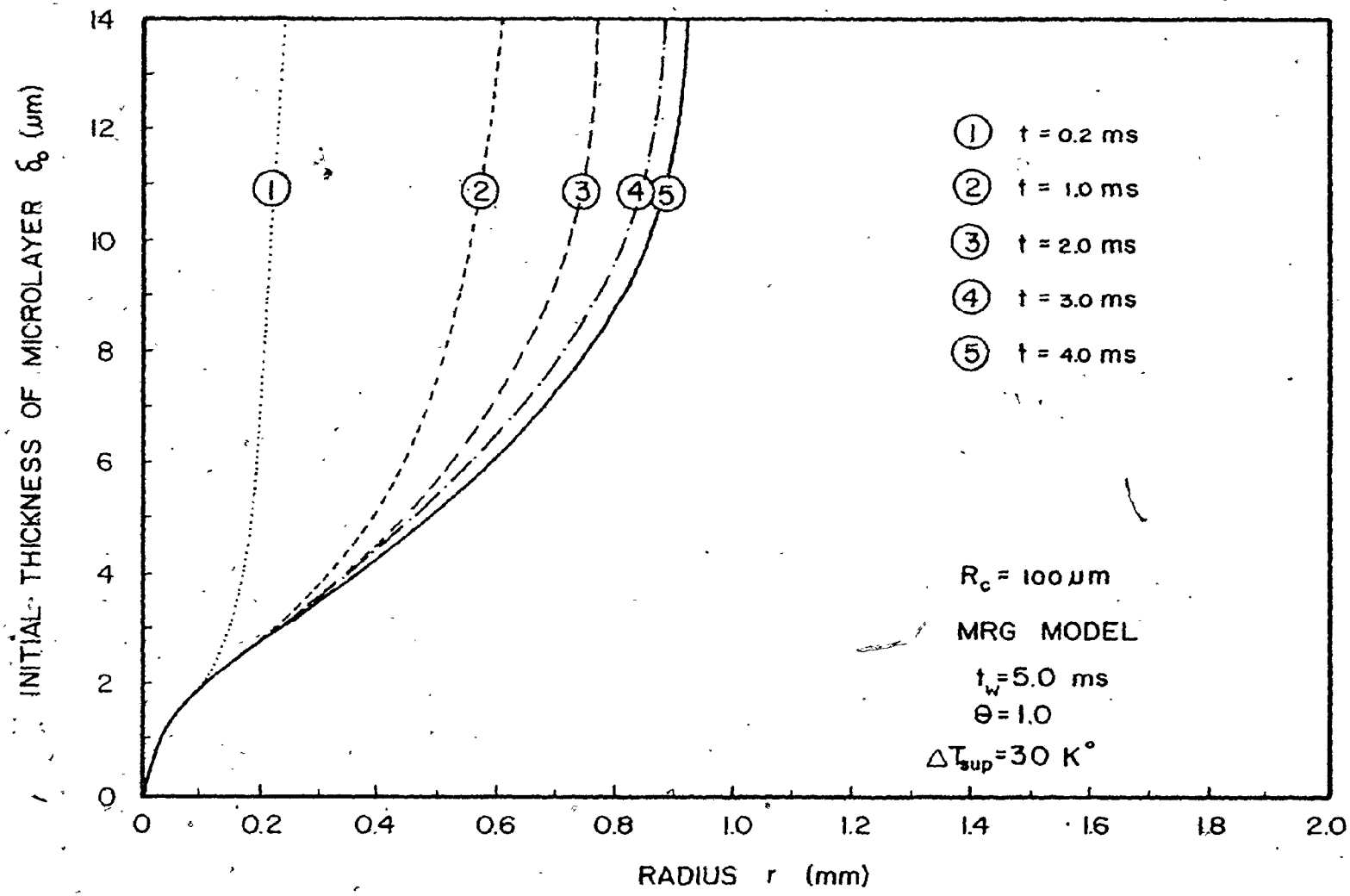

FIGURE (4.15) MRG [7] MODEL (Microlayer Formation)

the initial microlayer thickness. Figure (4.16) shows the locus of points at which the gradient $\frac{\partial \delta(r,t)}{\partial r} \to \infty$ for some experimental data [1] obtained for selected bubbles which have a growth relationship R(t) close to the arbitrary growth indicated in the figure. The experimental data and the present numerical model show good agreement. Nevertheless, it will be shown in the next chapter that the instantaneous microlayer thickness $\delta(r,t)$ gives better proof of the good predictability of the present numerical solution. Figure (4.16) shows also the experimental data of Voutsinos and Judd [26] which shows good agreement with the present numerical solution as well as two theoretical models of different approaches for the sake of comparison.

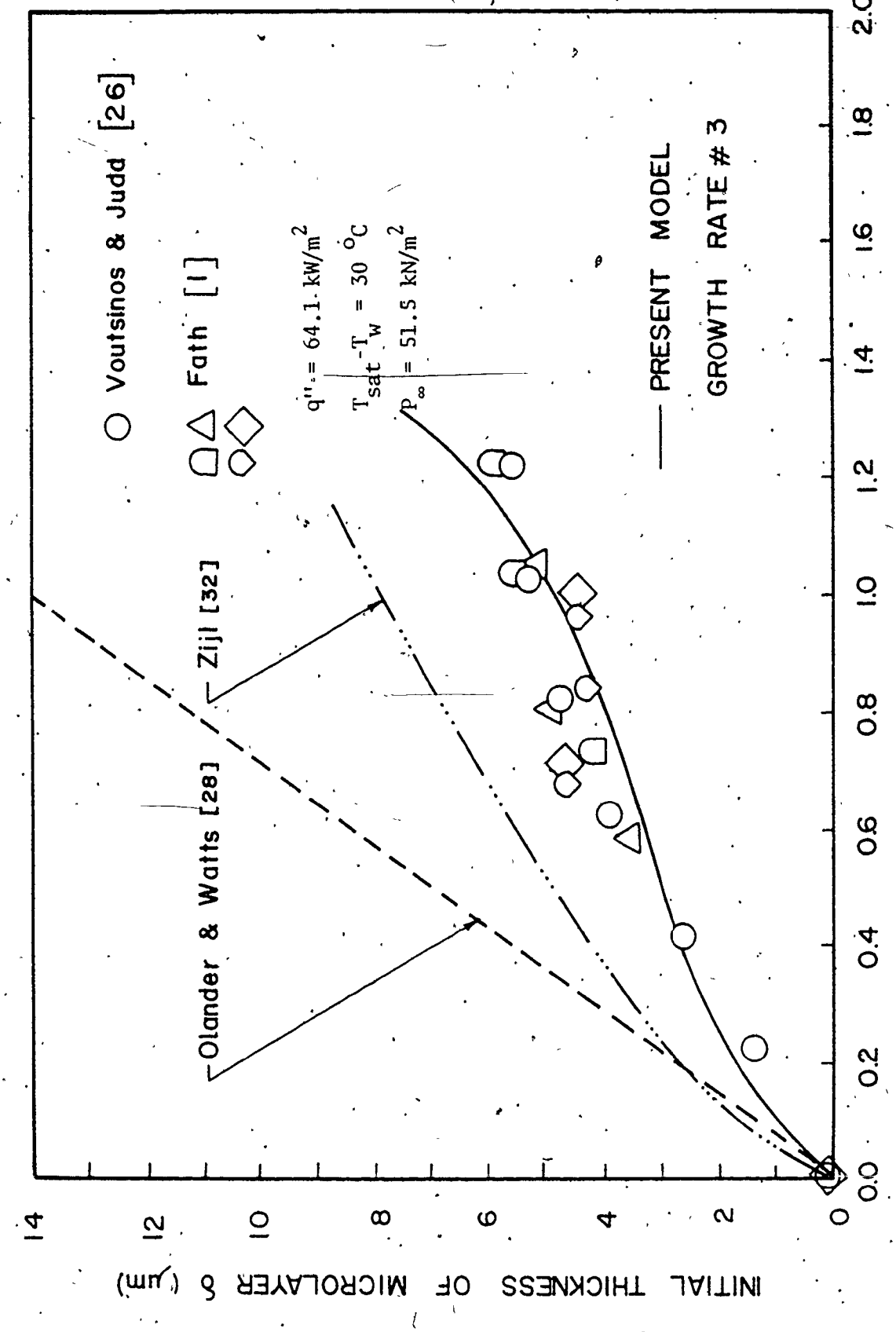

FIGURE (4.16) COMPARISON BETWEEN THE PRESENT MODEL & OTHERS

CHAPTER 5

MICROLAYER EVAPORATION

5.1 Introduction

In boiling, during the growth of a bubble on a heated surface, the formation and evaporation of the microlayer occurs simultaneously and a varying microlayer thickness $\delta(r,t)$ would actually be present under the bubble with a dry area at its center.

The present chapter discusses microlayer evaporation, the instantaneous thickness of the microlayer and its contribution to the total mass of the bubble. Specifically, the following sections present a general background of microlayer evaporation, a theoretical analysis of the transient cooling of a liquid layer on a heating surface as it affects the rate of the microlayer evaporation, a numerical representation of the evaporation process, the results of the microlayer evaporation model, and finally a discussion of the present model and comparison with some experimental results.

5.2 Microlayer Evaporation (General Background)

Between the nucleation of two successive bubbles, there is a waiting period during which the heat supplied by the external source will be partially accummulated in the solid (replacing the heat lost to the preceding bubble) and

partially conducted into the liquid. Only when the energy deficit is completely replaced and the wall temperature becomes uniform at T_w will the external heat be totally conducted to the liquid. Obviously the liquid layer adjacent to the wall will have the same wall temperature and a temperature variation will be found with increasing distance from the wall. Considering the temperature gradient from the heat conduction equation $\frac{\partial T}{\partial y} = - \frac{1}{k_\ell} \left(\frac{Q}{A}\right)$ one could assume that the temperature drop across a distance of the order of the extremely small microlayer (≈ 5 μm) could be neglected and the microlayer temperature can be approximated by T_w at the beginning of evaporation, decreasing towards T_{sat} as time goes on.

The major part of the vapour production comes from the outer regions of the liquid microlayer as a consequence of its large area and of the short time elapsed there since the beginning of transient cooling and evaporation. In this region the thermal properties of the solid do not have much influence on the evaporation at the beginning when $\delta_o > \sqrt{\alpha_\ell t}$. The evaporation in this region will depend on the solid only after a period of time $\tau \geq \delta_o^2/\alpha_\ell$. On the other hand evaporation near the dry area will depend on the thermal properties of the solid since the transient cooling involves the solid here. As a consequence, a combination of both liquid and solid cooling effects must be considered.

The effect of the external heat input (constant in the present situation) could be accounted for by adding a

constant rate of microlayer evaporation superimposed on the transient cooling, figure (5.1).

5.3 Transient Cooling and Microlayer Evaporation

Different theoretical analyses of the microlayer evaporation were presented in the literature. The analysis of the general case of a finite liquid layer on a semi-infinite heating surface will be considered below, [40].

Assume a liquid layer of thickness δ_o initially at temperature T_{sup} on a semi-infinite solid wall, figure (5.2). The differential equations for liquid and solid temperatures could be written as:

$$\frac{\partial T_\ell(y,t)}{\partial t} = \alpha_\ell \frac{\partial^2 T_\ell(y,t)}{\partial y^2} \tag{5.1}$$

$$\frac{\partial T_s(y,t)}{\partial t} = \alpha_s \frac{\partial^2 T_s(y,t)}{\partial y^2} \tag{5.2}$$

The initial conditions are:

$$T_\ell(y,0) = T_s(y,0) = T_{sup} \tag{5.3}$$

$$\delta(r,0) = \delta_o \tag{5.4}$$

The boundary conditions are:

$$T_\ell(\delta_o,t) = T_v \tag{5.5}$$

$$T_\ell(0,t) = T_s(0,t) \tag{5.6}$$

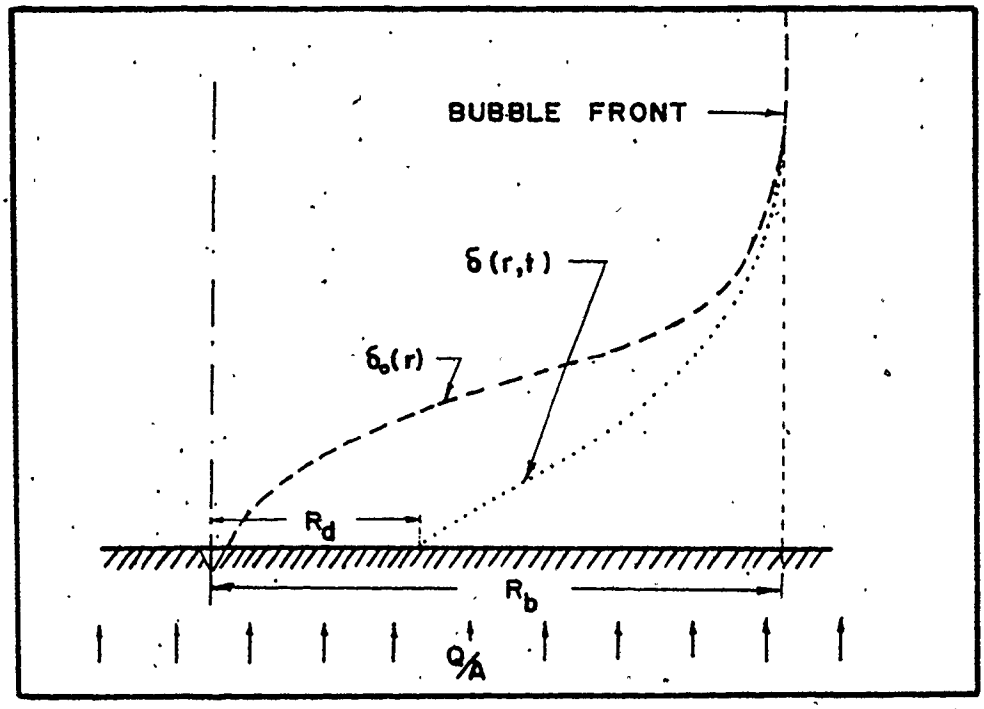

FIGURE(5.1) REPRESENTATION OF INITIAL AND INSTANTANEOUS MICROLAYERS

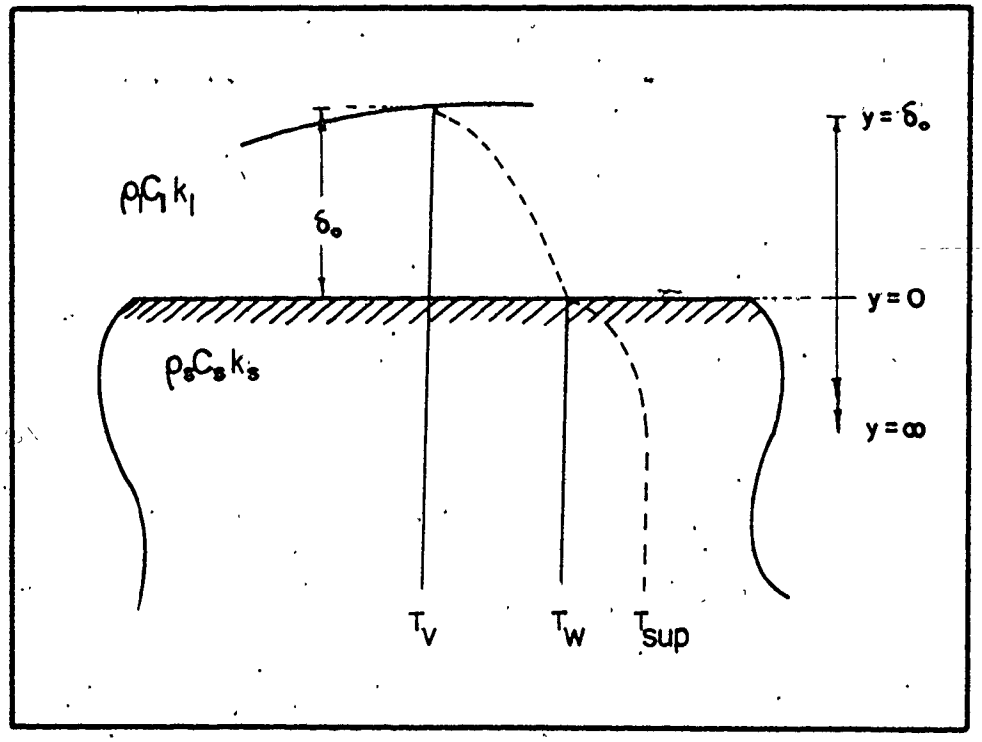

FIGURE (5.2) TEMPERATURE DISTRIBUTION IN THE MICROLAYER & HEATING SURFACE

$$- k_\ell \frac{\partial T_\ell(0,t)}{\partial y} = - k_s \frac{\partial T_s(0,t)}{\partial y} \qquad (5.7)$$

$$T_s(-\infty,t) = T_{sup} \qquad (5.8)$$

Equations (5.1) and (5.2) can be solved with the aid of the initial conditions (5.3) and (5.4) and the boundary conditions (5.5) to (5.8) for the liquid and solid temperatures $T_\ell(y,t)$ and $T_s(y,t)$ respectively. The rate of liquid microlayer evaporation can be evaluated by:

$$\left(\frac{Q}{A}\right)_{evap} = \rho_\ell \, h_{fg} \frac{\partial \delta(r,t)}{\partial t} = - k_\ell \frac{\partial T_\ell(\delta_o,t)}{\partial y} \qquad (5.9)$$

If it is assumed that the liquid layer thickness change is negligible (i.e., δ_o is assumed constant), the analysis can be simplified as indicated in Carslaw [40]. Evaporation with changing thickness was studied by Knuth [49]. His theoretical analysis indicated that for a reasonable superheated wall (i.e., $C_p (T_{sup}-T_v)/h_{fg} \leq 0.1$) the difference in results from a constant thickness is negligible. Accordingly, the heat flux across the liquid vapour interface is given by [40]:

$$\left(\frac{Q}{A}\right)_{evap} = \frac{\Delta T_{sup} \, k_\ell}{\sqrt{\pi \, \alpha_\ell \, t}} \left[1 + 2 \sum_{m=1}^{\infty} \left(\frac{\gamma-1}{\gamma+1}\right)^m e^{-\frac{m^2 \delta_o}{\alpha_\ell t}} \right] \qquad (5.10)$$

where

$$\gamma = \left[\frac{k_s \, \rho_s \, C_s}{k_\ell \, \rho_\ell \, C_\ell}\right]^{1/2}$$

This general equation can be simplified for two-extreme cases, the THICK and the THIN microlayer. For a thick microlayer corresponding to a short time since evaporation (approximating evaporation in the outer region of the microlayer), the exponential factor in equation (5.10) approaches zero and the heat flux will be governed by the properties of a semi-infinite liquid, i.e.:

$$\left(\frac{Q}{A}\right)_{evap} = \frac{\Delta T_{sup}\, k_\ell}{\sqrt{\pi\, \alpha_\ell\, t}} \tag{5.12}$$

For a thin microlayer (approximating evaporation near the dry area), the exponential factor in equation (5.10) approaches unity and the heat flux will be governed by the properties of a semi infinite solid, i.e.:

$$\left(\frac{Q}{A}\right)_{evap} = \frac{\Delta T_{sup}\, k_\ell}{\sqrt{\pi\, \alpha_\ell\, t}}\,(\gamma) = \frac{\Delta T_{sup} k_s}{\sqrt{\pi\, \alpha_s\, t}} \tag{5.13}$$

In dimensionless form equation (5.10) can be written as [41]:

$$\left(\frac{Q}{A}\right)_{evap} \left(\frac{\delta_o}{k_\ell}\right) \left(\frac{1}{\Delta T_{sup}}\right) = \frac{1}{\gamma\sqrt{\pi Y}} \left[1+2 \sum_{m=1}^{\infty} \left(\frac{\gamma-1}{\gamma+1}\right)^m \exp\left(\frac{m^2}{\gamma^2 Y}\right)\right] \tag{5.14}$$

where

$$Y = \left[\frac{k_\ell \sqrt{\alpha_s\, t}}{k_s\, \delta_o}\right]^2$$

Similarly equation (5.12) can be written as:

$$\left(\frac{\dot{Q}}{A}\right)_{evap} \left(\frac{\delta_o}{k_\ell}\right) \frac{1}{\Delta T_{sup}} = \frac{\frac{1}{\sqrt{\pi}} \sqrt{\frac{\rho_\ell C_\ell k_\ell}{\rho_s C_s k_s}}}{\sqrt{Y}} = \frac{1}{\gamma\sqrt{\pi Y}} \qquad (5.15)$$

and equation (5.13) can be written as:

$$\left(\frac{\dot{Q}}{A}\right)_{evap} \left(\frac{\delta_o}{k_\ell}\right)\left(\frac{1}{\Delta T_{sup}}\right) = \frac{1}{\sqrt{\pi Y}} \qquad (5.16)$$

The dimensionless heat flux equations (5.14) to (5.16) are plotted against the dimensionless time factor $\sqrt{Y}$ in figure (5.3), for the case of the dichloromethane/glass combination. It is evident from the figure that the finite liquid layer on a semi infinite solid solution (equation (5.14)) approaches the thick and thin microlayer equations (5.15) and (5.16) respectively at the two extremes i.e., evaporation heat flux starts as thick microlayer behaviour and gradually approaches thin microlayer behaviour .

From equations (5.9) to (5.13) one can evaluate the microlayer evaporation rate $\frac{\partial \delta(r,t)}{\partial t}$ for the three cases thick, thin and intermediate initial microlayer thickness as follows:

Thick microlayer evaporation rate:

$$\frac{\partial \delta(r,t)}{\partial t} = - \frac{\Delta T_{sup}\, k_\ell}{\rho_\ell\, h_{fg} \sqrt{\pi \alpha_\ell}} \frac{1}{\sqrt{t}} \qquad (5.17)$$

Thin microlayer evaporation rate:

$$\frac{\partial \delta(r,t)}{\partial t} = - \frac{\Delta T_{sup}\, k_s}{\rho_\ell\, h_{fg} \sqrt{\pi \alpha_s}} \frac{1}{\sqrt{t}} \qquad (5.18)$$

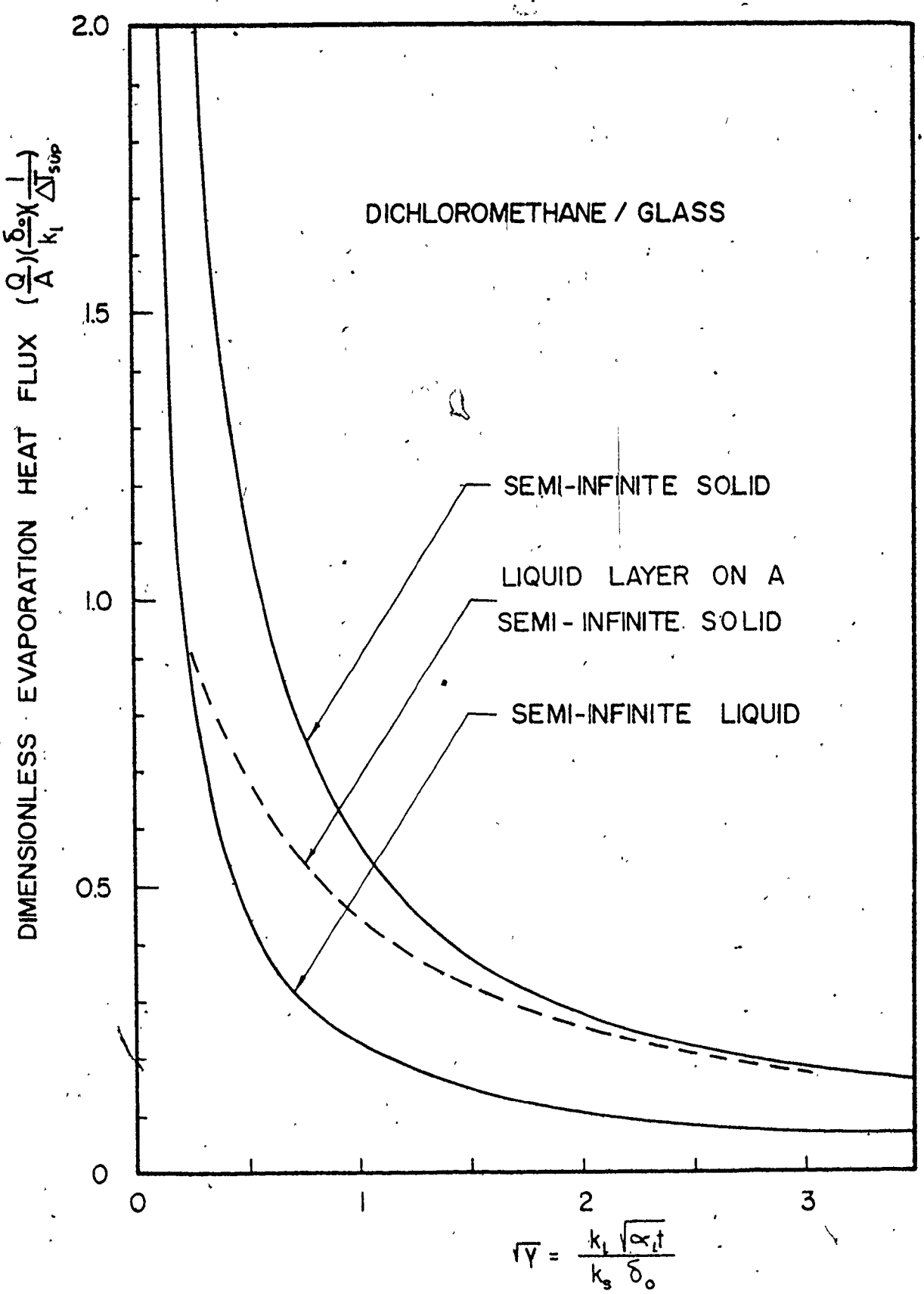

FIGURE (5.3) HEAT FLUX TO AN EVAPORATING LIQUID BOUNDED BY A HEATING SURFACE

Intermediate microlayer evaporation rate:

$$\frac{\partial \delta(r,t)}{\partial t} = - \frac{\Delta T_{sup} \, k_\ell}{\rho_\ell \, h_{fg} \sqrt{\pi \alpha_\ell t}} \left[1+2 \sum_{m=1}^{\infty} \left(\frac{\gamma-1}{\gamma+1}\right)^m e^{-\frac{m^2 \delta_o^2}{\alpha_\ell t}}\right] \qquad (5.19)$$

The evaporation rate $\frac{\partial \delta(r,t)}{\partial t}$ for the three cases (equations (5.17) to (5.19)) are shown in figure (5.4) for the dichloromethane/glass combination.

The external heat flux input $(Q/A)_{input}$ will have the effect of adding a constant C_1 to the evaporation rate $\frac{\partial \delta(r,t)}{\partial t}$. This constant can be calculated as,

$$C_1 = \frac{\partial \delta(r,t)}{\partial t}\Big|_{input} = - \frac{(Q/A)_{input}}{\rho_\ell \, h_{fg}} \qquad (5.20)$$

5.4 Numerical Representation of the Microlayer Evaporation

5.4.1 Instantaneous Microlayer Profile

The bubble front moves over the heating surface leaving the superheated microlayer. As soon as this layer comes under the bubble and in touch with the vapour (i.e., i = IBL-1, see figure (5.5)), evaporation starts at column i with a rate of:

$$\frac{\partial \delta(r,t)}{\partial t} = - \frac{\Delta T_{sup} \, k_\ell}{\rho_\ell h_{fg} \sqrt{\pi \alpha_\ell}} \frac{1}{\sqrt{t-TBL(i)}} \left[1+2\left(Be^{-\tau/t} + B^2 e^{-4\tau/t} + B^3 e^{-9\tau/t} + \ldots\right)\right] - \frac{(Q/A)_{input}}{\rho_\ell \, h_{fg}} \qquad (5.21)$$

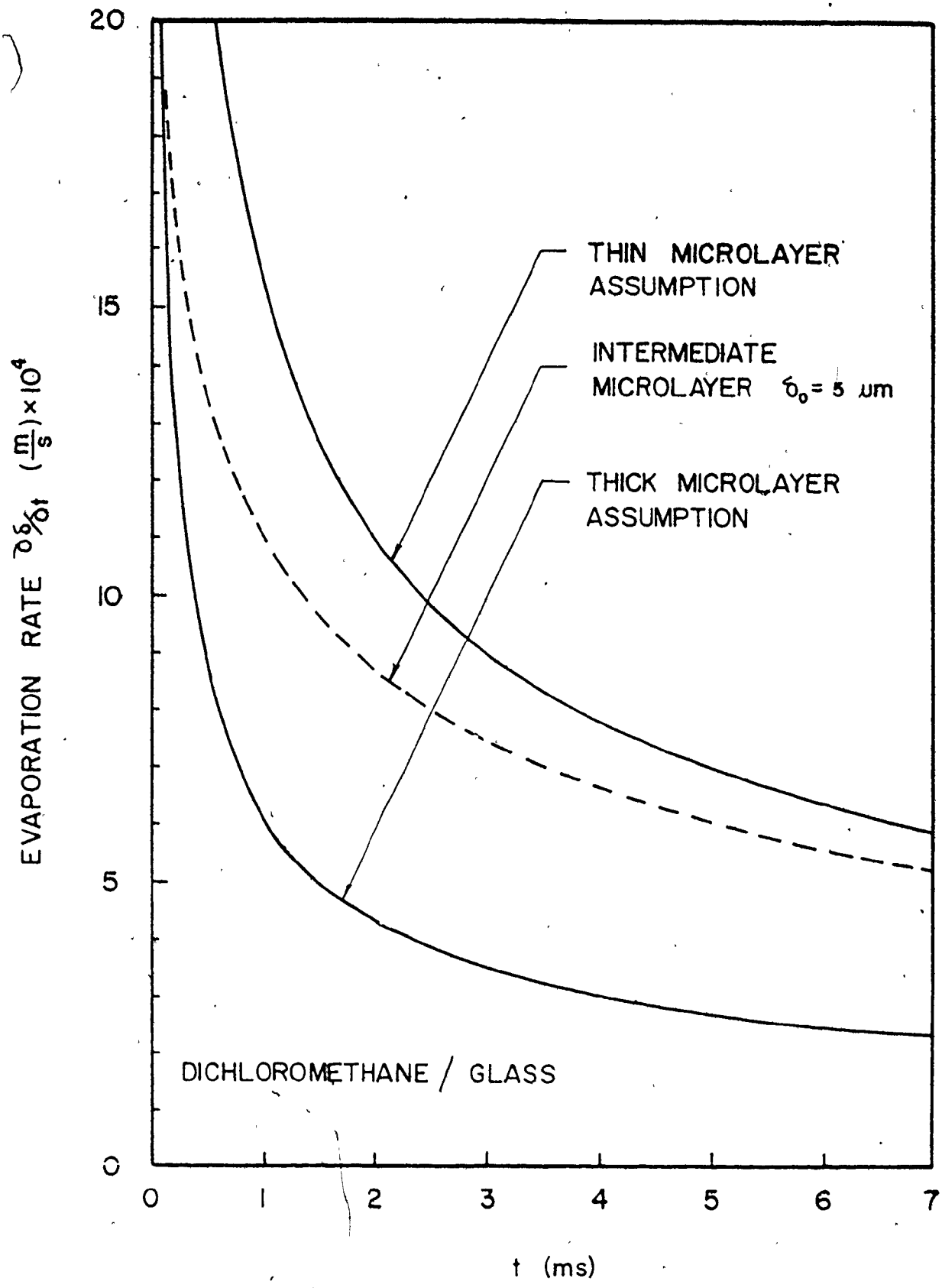

FIGURE (5.4) RATE OF CHANGE OF MICROLAYER THICKNESS

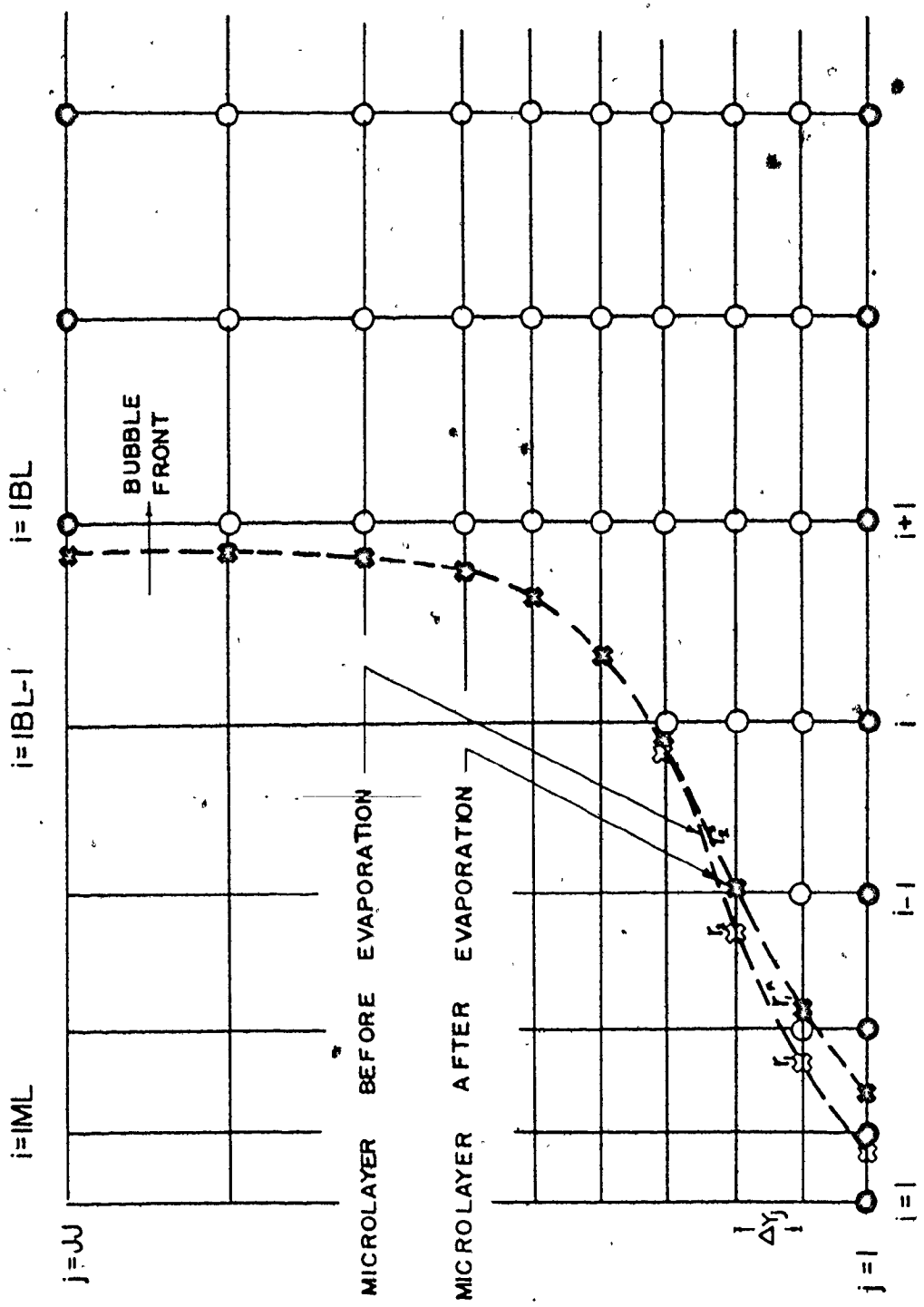

FIGURE(5.5) EVAPORATION NUMERICAL REPRESENTATION

where

$$\tau = \delta_o^2/\alpha_\ell \qquad B = \left(\frac{\gamma-1}{\gamma+1}\right)$$

TBL(i) is the time elapsed until the bubble front passes over the column i. The value of the penetration time τ depends on δ_o which varies from one bubble to another as discussed in Chapter 4.

The effect of evaporation will cause the liquid vapour interface, represented by the massless markers, to move in the radial direction by an incremental distance Δr so that:

$$\Delta r = \Delta t \left(\frac{\partial \delta}{\partial t}\right)_K \left(\frac{\Delta r}{\Delta y}\right)_K \tag{5.22}$$

where

Δt = time step

$\left(\frac{\partial \delta}{\partial t}\right)_K$ = evaporation rate for marker K, linearly interpolated between the two columns i and i-1 so that $r_i < r_k < r_{i-1}$

and $$\left(\frac{\Delta r}{\Delta y}\right)_K = \frac{1}{2}\left[\frac{r_K - r_{K-1}}{y_K - y_{K-1}} + \frac{r_{K+1} - r_K}{y_{K+1} - y_K}\right]$$

5.4.2 Mass Evaporated from the Microlayer

In order to answer the question of how much evaporation from the microlayer contributes to the total bubble mass, the mass evaporated from the microlayer was evaluated numerically. By assuming straight line segments connecting

the markers, the vapour volume before evaporation V_1 and after evaporation V_2 was calculated so that the incremental mass of microlayer evaporated ΔM_{ML} could be calculated as:

$$\Delta M_{ML} = \rho_{\ell} \, (\bar{V}_2 - \bar{V}_1) \tag{5.24}$$

where according to figure (5.5)

$$\bar{V}_1 = \sum_{k=2}^{MK} \frac{\pi}{3} \Delta y_k \, (r_{k-1}^2 + r_{k-1} r_k + r_k^2) \tag{5.25}$$

$$\bar{V}_2 = \sum_{k=2}^{MK} \frac{\pi}{3} \Delta y_k \, (r_{k-1}^{*2} + r_{k-1}^{*} r_k^{*} + r_k^{*2}) \tag{5.26}$$

5.4.3 Computer Program

The same computer program used to compute the isothermal microlayer thickness, presented in Section 4.4.4, was used here with the addition of another subroutine to predict microlayer evaporation after step 8 of figure (4.4) entitled EVAPOML. In Reference [39], a listing of subroutine EVAPOML is presented.

5.5 Results of the Microlayer Evaporation Model

In the following sections, some results will be presented concerning the instantaneous microlayer profile and the mass evaporated from the microlayer. The effect of the initial microlayer thickness δ_o and the physical properties of the liquid on the solution will be discussed, as well as

the microlayer evaporation contribution to the bubble growth and the dry radius under the bubble.

5.5.1 The Effect of the Initial Microlayer Thickness

Figures (5.6a) and (5.6b) show the effect of the initial microlayer thickness δ_o at two different instants of the growth period, t = 2.0 ms and 4.0 ms respectively. The isothermal microlayer thickness is also shown for the sake of comparison. From the two figures it is clear that decreasing the initial microlayer thickness increases the evaporation rate which results in thinner instantaneous microlayer thickness with larger dry area at the center.

5.5.2 The Effect of the Liquid Physical Properties and Heating Conditions

The evaporation rate of the microlayer is given as:

$$\frac{\partial \delta(r,t)}{\partial t} = - \frac{\Delta T_{sup} \sqrt{k_\ell C_\ell}}{h_{fg} \sqrt{\pi \rho_\ell (t - TBL(i))}} \left[1 + 2\left(Be^{-\tau/t} + B^2 e^{-4\tau/t} + B^3 e^{-9\tau/t} + \ldots\right)\right] - \frac{(Q/A)_{input}}{\rho_\ell h_{fg}} \qquad (5.21)$$

From this equation it can be seen that increasing the superheat, input heat flux, liquid thermal conductivity and liquid specific heat or decreasing the latent heat of evaporation and liquid density, will increase the evaporation rate which results in thinner instantaneous microlayer thickness with larger dry area similar to the effect of the initial microlayer

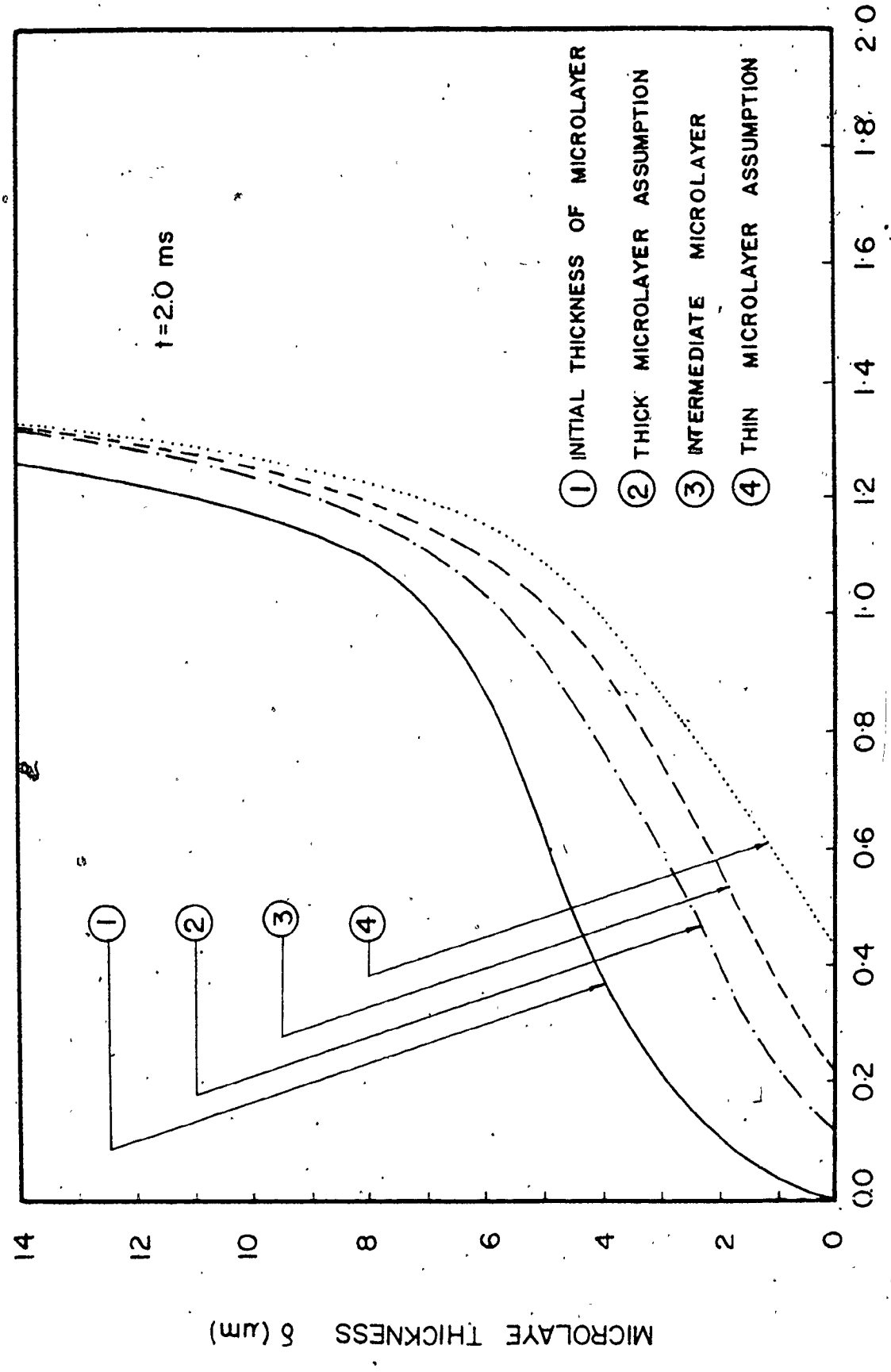

FIGURE(5.6a) EFFECT OF INITIAL MICROLAYER THICKNESS δ_o (t=2.0ms)

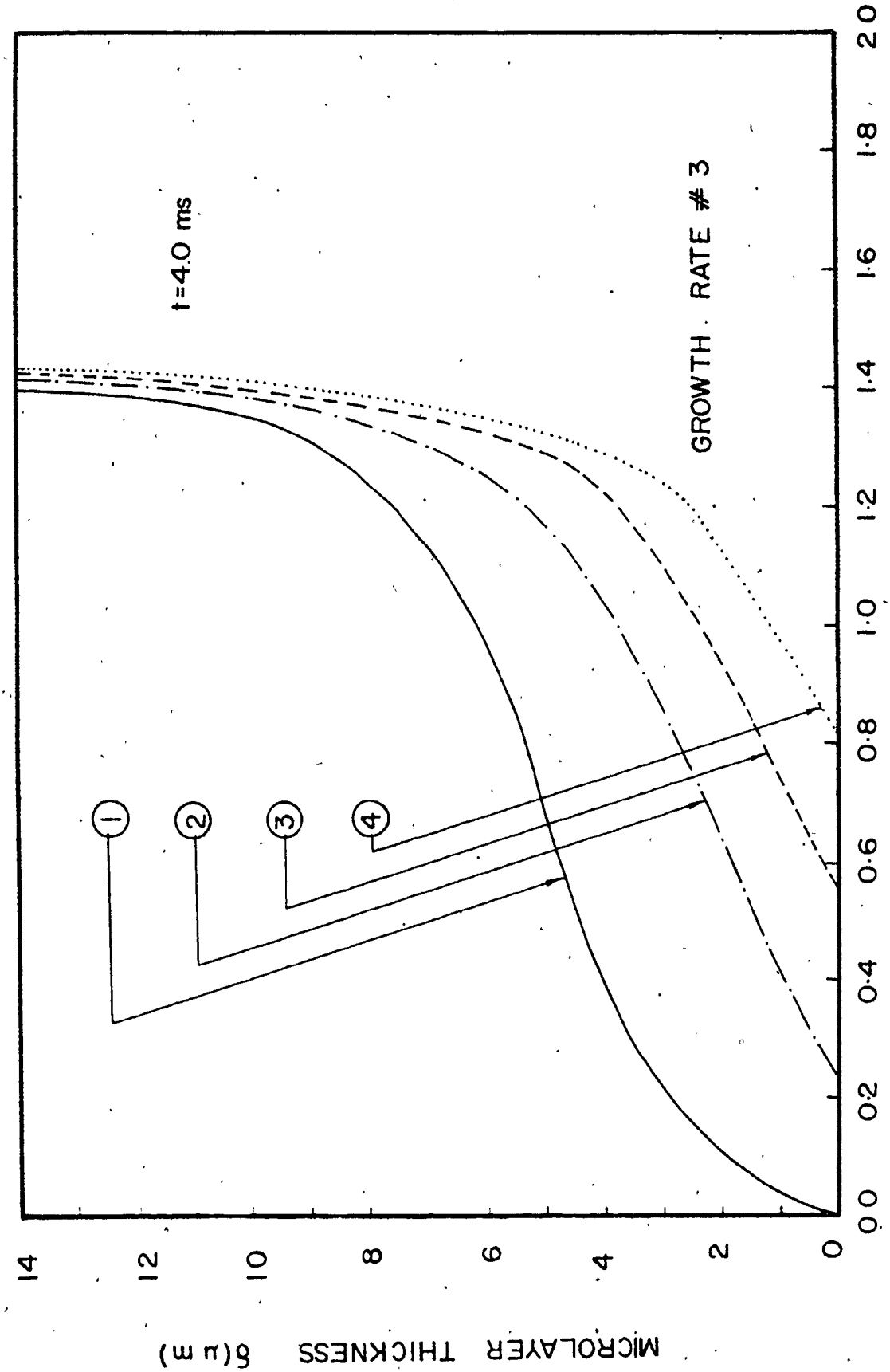

FIGURE(5.6b) EFFECT OF INITIAL MICROLAYER THICKNESS δ_o (t=4.0 ms)

thickness discussed in the previous section.

5.5.3 Temporal Variation of Microlayer Evaporation Mass

Figure (5.7) shows the temporal variation of mass evaporated from the microlayer M_{ML} (i.e., the mass contained by the bubble if microlayer evaporation were the only source of vapour) for two different assumed growth rates depicted in figure (4.6). Figure (5.8) shows the effect of the initial microlayer thickness assumption on the mass evaporated from the microlayer. From figure (5.7), one can see that increasing the growth rate, increases the amount of liquid microlayer with a larger area coming in touch with the vapour which allows for more evaporation and as a consequence more mass evaporated from the microlayer. Also, decreasing the microlayer thickness increases the evaporation rate which increases the mass evaporated from the microlayer as shown in figure (5.8).

5.5.4 Dry Area Under the Bubble

The existence of a dry area around the cavity under the growing bubble has been observed experimentally [1] and confirmed in the present numerical study for each bubble. Even for the case of thick microlayer assumption, the dry area does exist. Figures (5.9) and (5.10) show the predicted dry radius $R_d(t)$ variation with time and the ratio $R_d(t)/R_b(t)$ respectively for the bubble considered in figure (5.6). Some experimentally measured values (Film #11

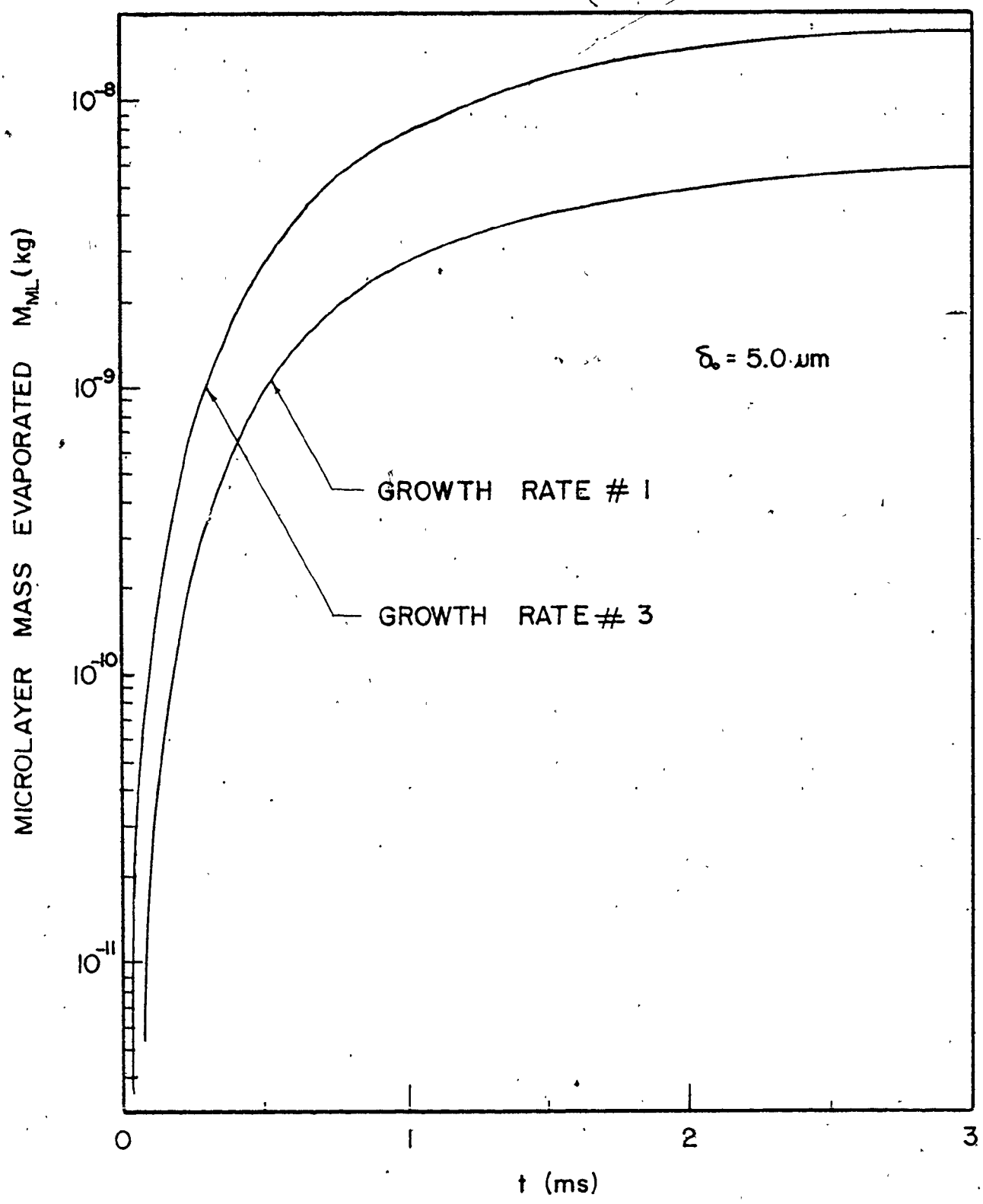

FIGURE (5.7) TEMPORAL MICROLAYER MASS EVAPORATED

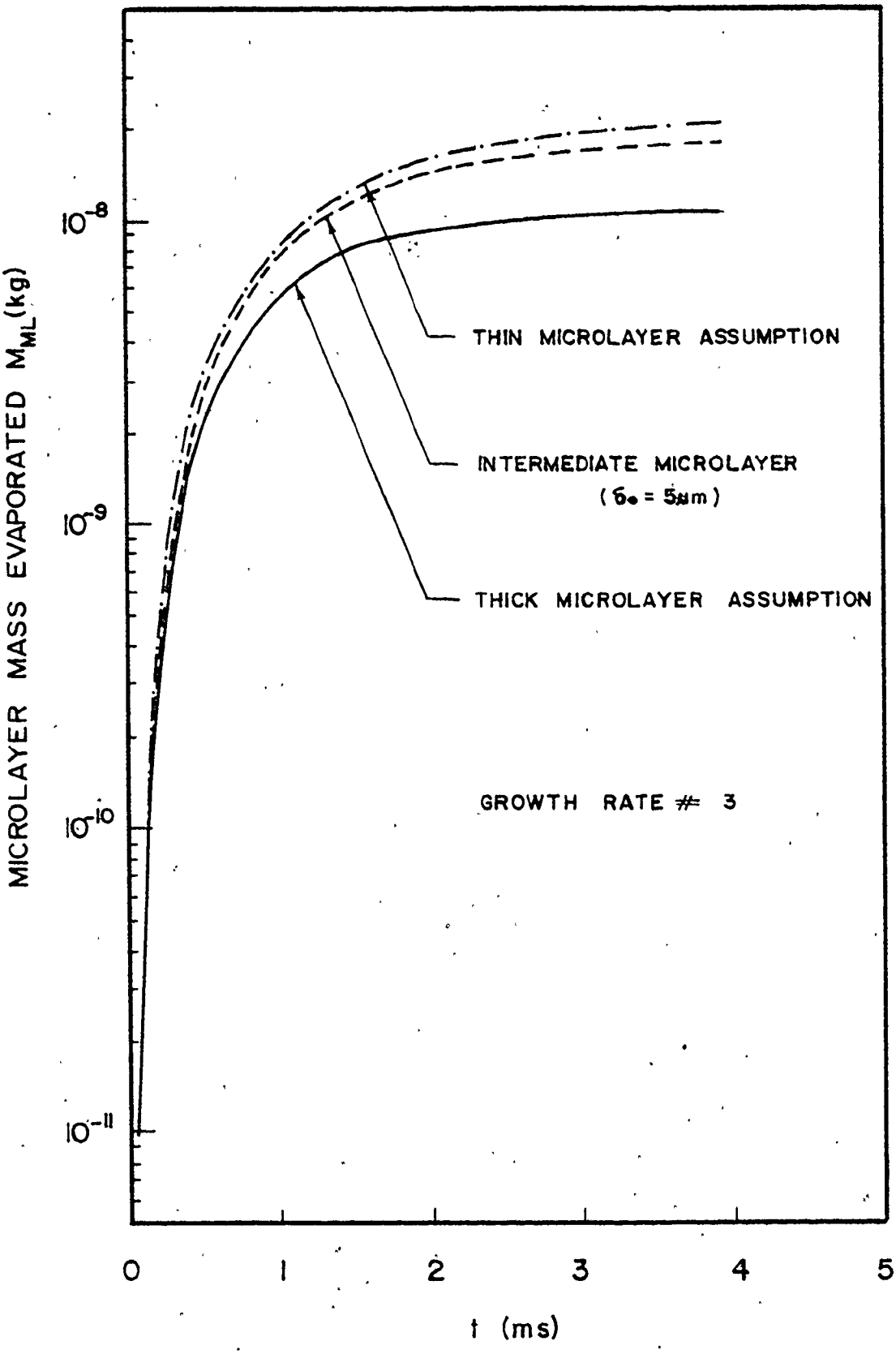

FIGURE (5.8) EFFECT OF EVAPORATION RATE ON MICROLAYER MASS EVAPORATION

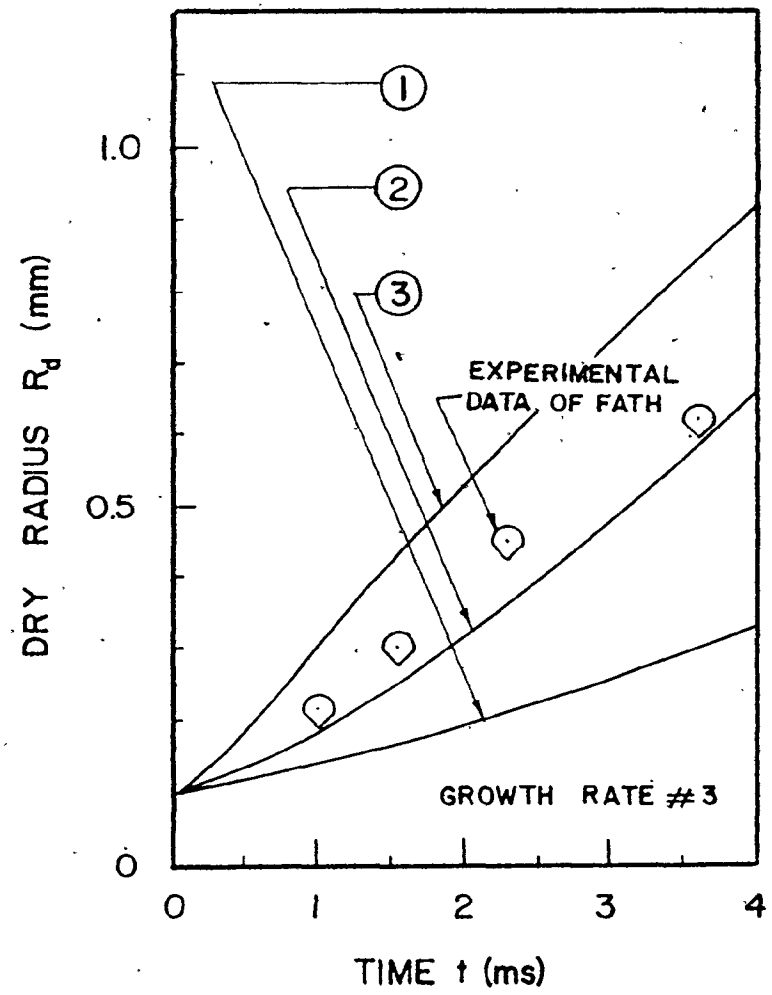

FIGURE (5.9) DRY RADIUS

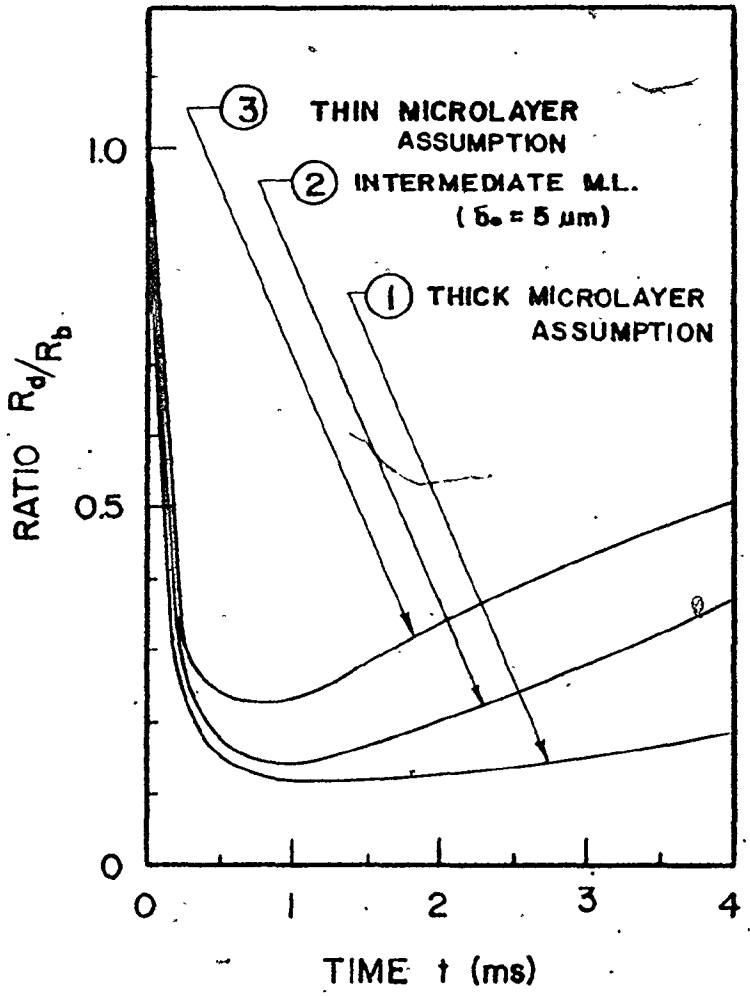

FIGUR (5.10) DRY / BUBBLE RADIUS RATIO

Bubble #4 [1]) are shown for the sake of comparison. From this figure, it is obvious that the experimental data fits the intermediate microlayer thickness better than the two extremes of thin and thick microlayer thickness.

5.6 Discussion of the Microlayer Evaporation Results

The validity of the numerical predictions of the present model was checked in two different ways. Firstly, a comparison was done between the numerical results for the instantaneous microlayer thickness $\delta(r,t)$ with some corresponding measurements for selected bubbles from [1]; secondly, a comparison was made between the assumed bubble growth relationship $R(t)$ and that predicted for a hemispherical bubble whose contained mass was set equal to the mass evaporated from the microlayer M_{ML}.

The numerical results of the instantaneous microlayer thickness $\delta(r,t)$ were compared with the experimental data of Fath [1]. Figures (5.11) and (5.12) present a comparison between the prediction of the present model for two arbitrary growth rates (Growth rate #1 and #3) and the measurements of two selected bubbles. From the figures one can see that the predicting model and the experimental profiles match well. It is significant to note that this is the first time (as far as the author's knowledge is concerned) that such comparison has been made.

A comparison between an equivalent hemispherical bubble radius $R_{eq}(t) = \left(\frac{3\, M_{ML}(t)}{2\, \pi\, \rho_v}\right)^{1/3}$ and the assumed growth

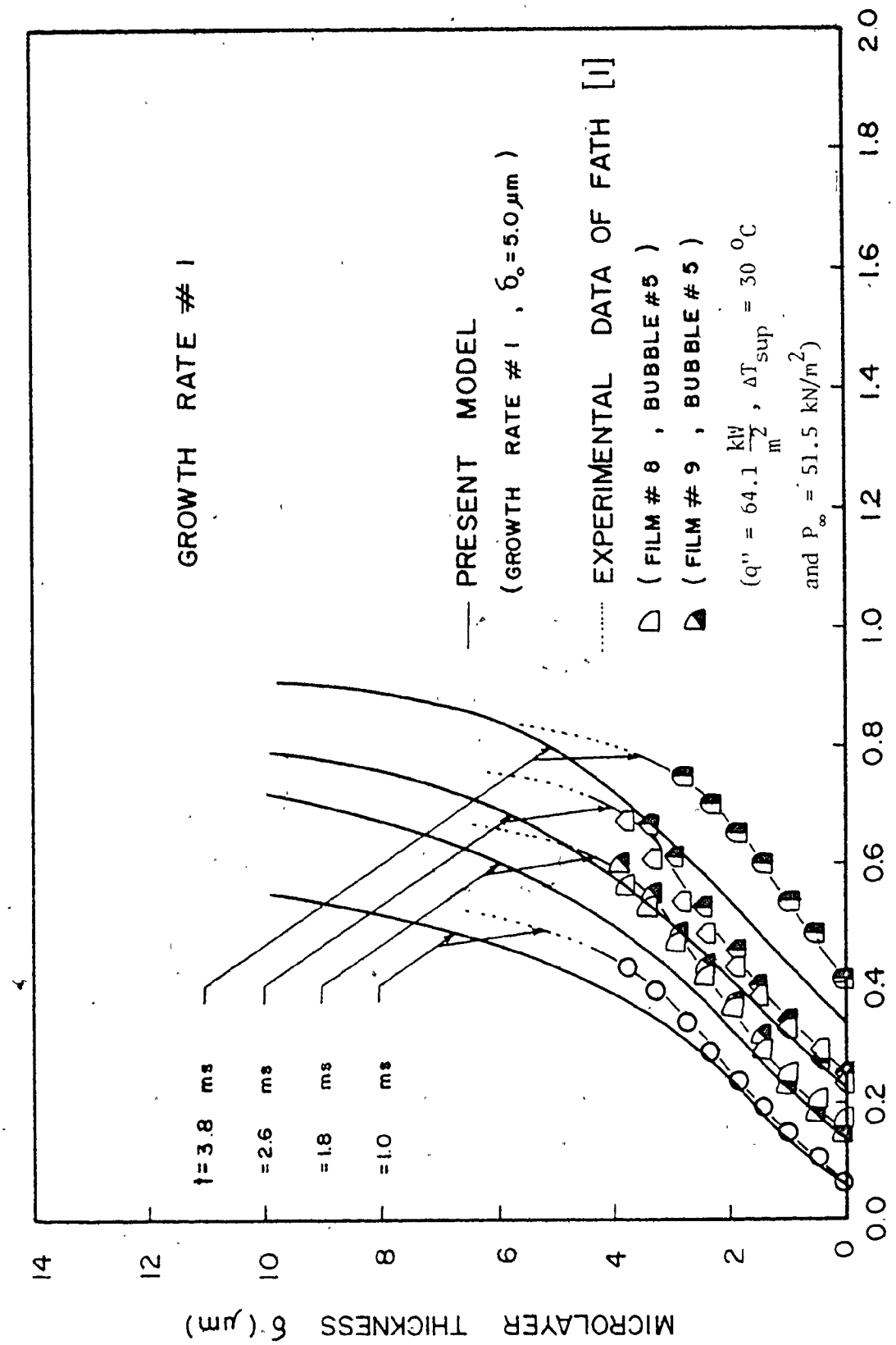

FIGURE (5.11) COMPARISON BETWEEN THE PRESENT NUMERICAL MODEL AND THE EXPERIMENTAL DATA OF FATH [1]

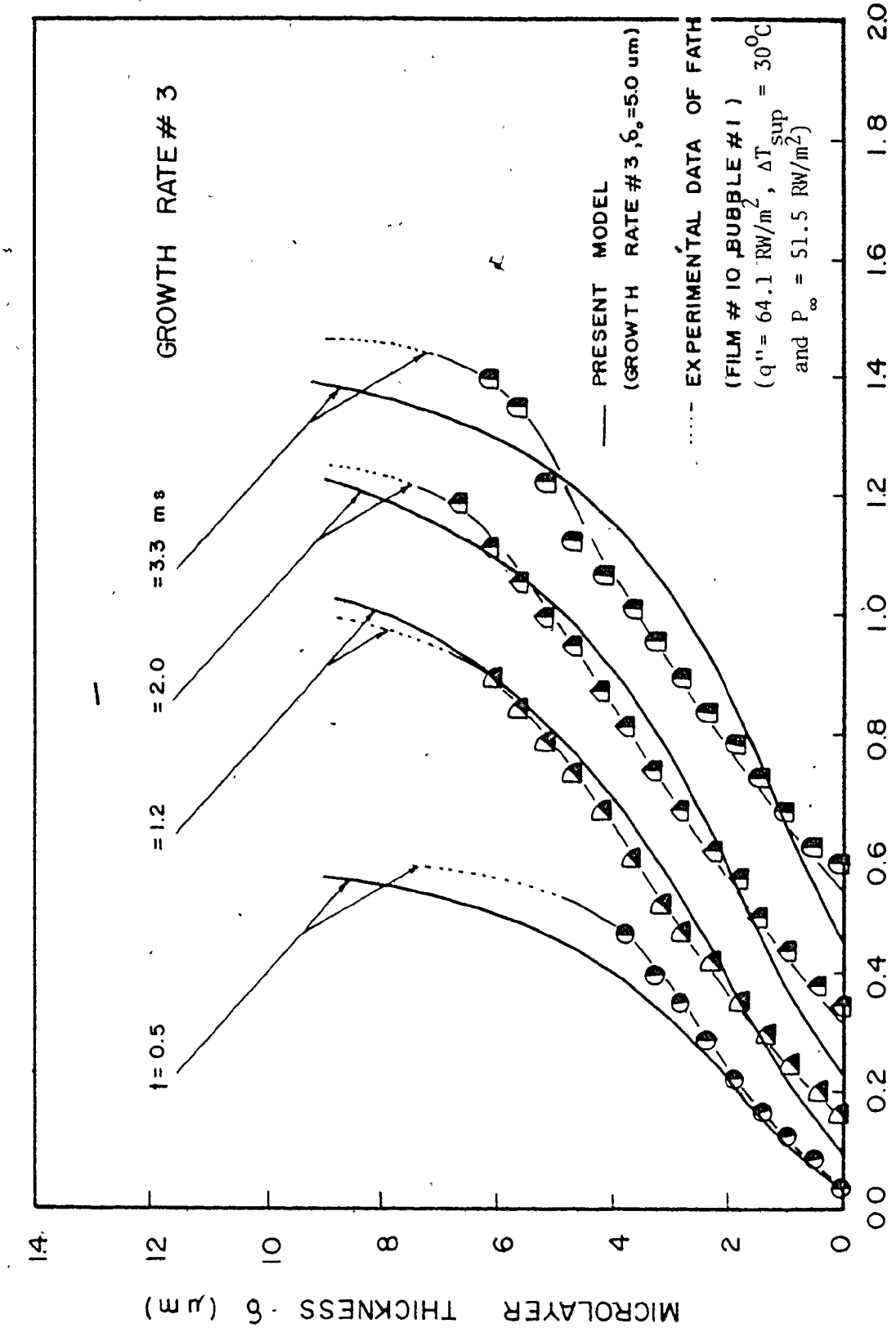

FIGURE(5.12) COMPARISON BETWEEN THE PRESENT NUMERICAL MODAL AND THE EXPERIMENTAL DATA OF FATH [1]

radius $R(t) = \int_0^\tau \dot{R}(t)\, dt$ is shown in figures (5.13) and (5.14) for the same two cases, which indicates that microlayer evaporation may contribute up to 100% of the bubble mass. These results are of a great significance to the understanding of bubble growth as will be discussed in Chapter 7.

To conclude this discussion, once a reasonable growth rate model for a bubble growing on a wall $\dot{R}(t)$ has been obtained in addition to the liquid and solid properties, one could use the present simple program to obtain a good prediction of the instantaneous microlayer thickness $\delta(r,t)$ and the temporal variation of the mass evaporated from the microlayer. This will be of use in all boiling studies especially for the cases where experimental measurements are rather difficult to obtain.

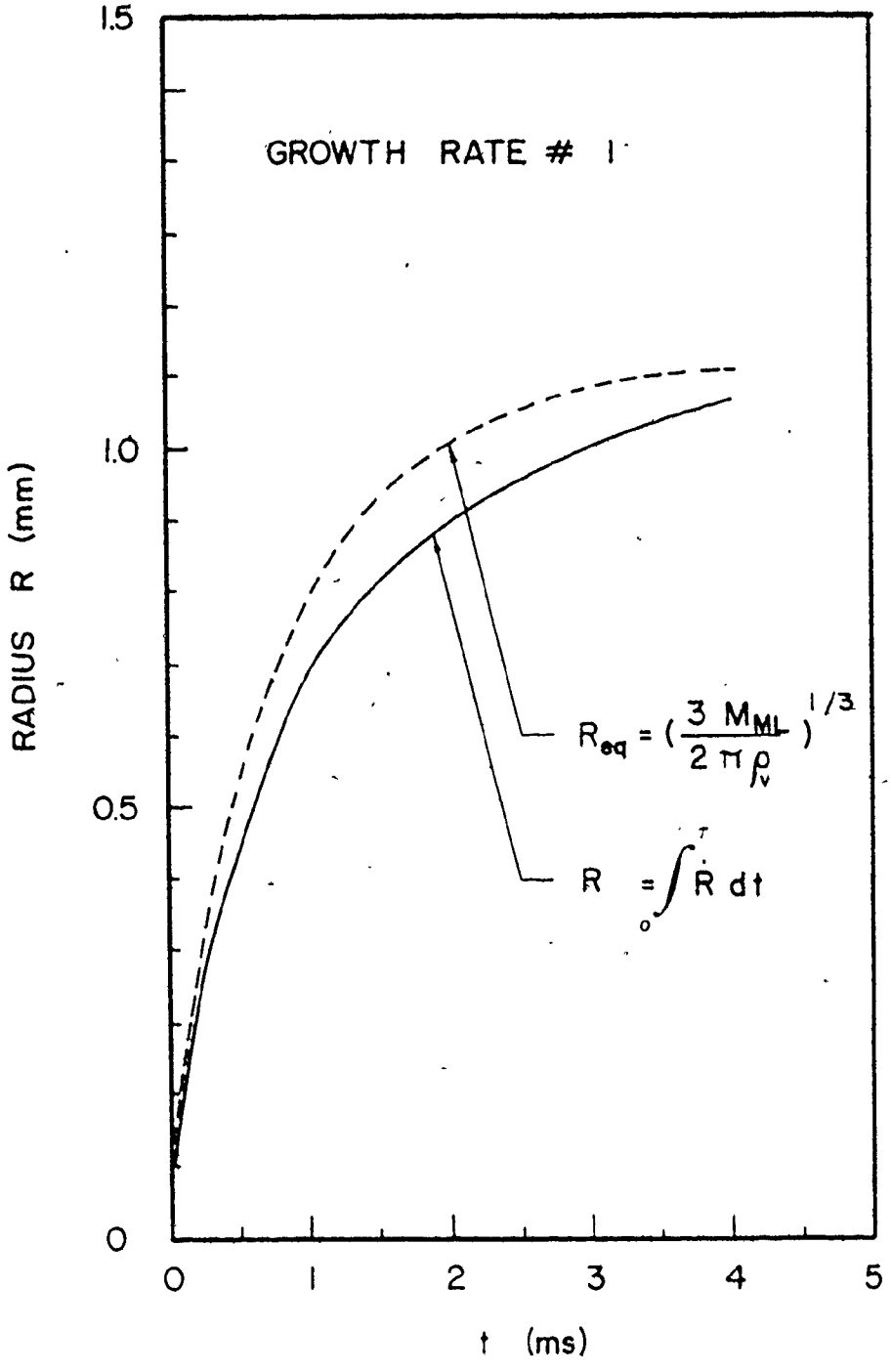

FIGURE (5.13) EQUIVALENT BUBBLE RADIUS

(GROWTH RATE # 1)

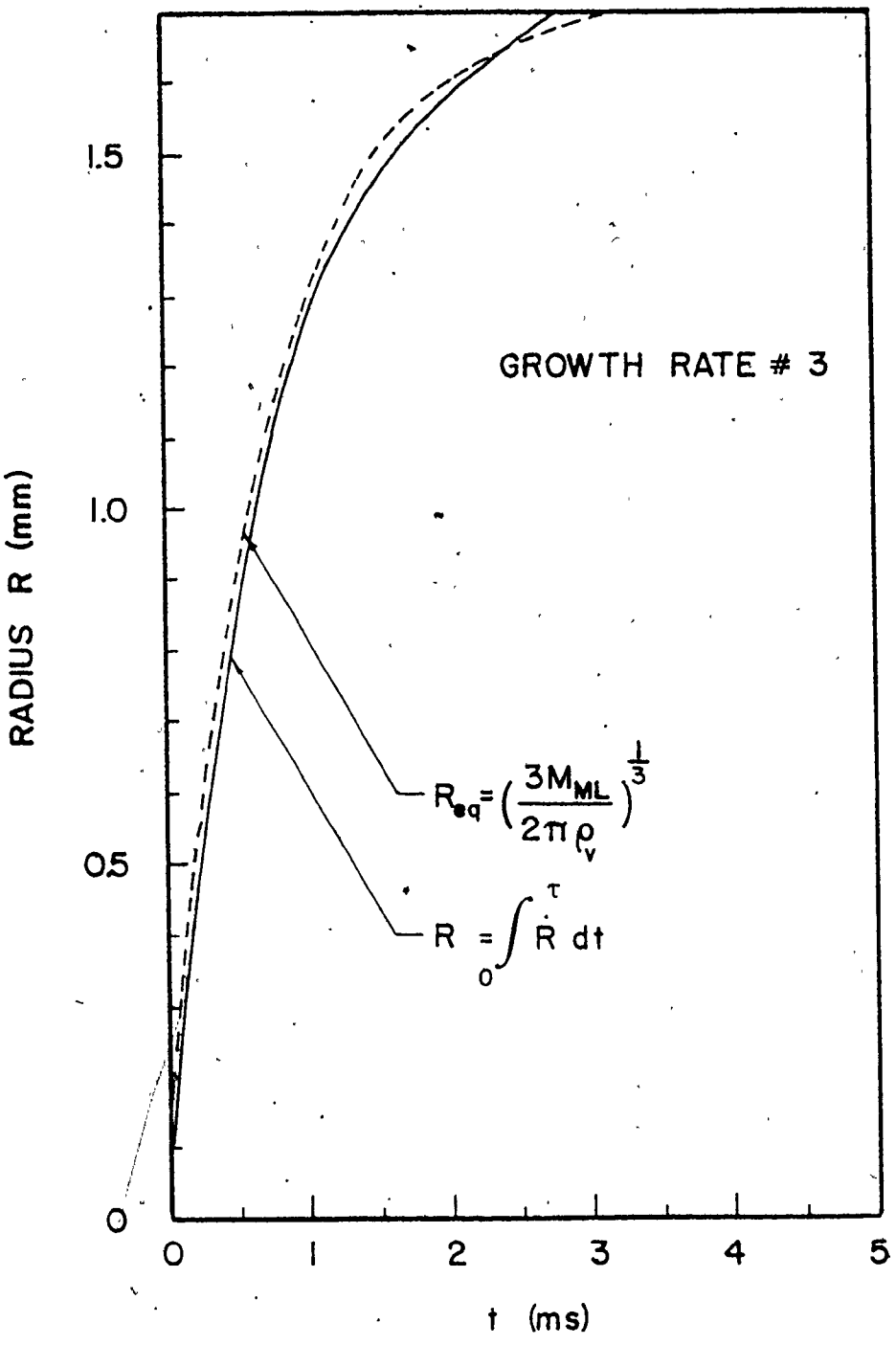

FIGURE(5.1.4) EQUIVALENT BUBBLE RADIUS (GROWTH RATE #3)

CHAPTER 6

BUBBLE GROWTH ON A HEATING SURFACE

6.1 Introduction

The appearance of a bubble implies the existence of a closed surface which divides the region of concern into two parts, each occupied by a homogeneous fluid. The dividing surface is usually called a bubble wall or interface. The purpose of the study of bubble dynamics, in general, is to determine the flow field in each separate region as well as the shape and motion of the bubble wall. A simplifying assumption, which usually is accepted, concerns the uniformity of the bubble interior. It was shown that this assumption can be justified when the velocity of the bubble wall is not very large (i.e., less than sonic speed) which is consistent with a vapour bubble in nucleate boiling. When this is the case, the only detailed flow field requiring study is that outside the bubble, while the parameters that characterize the interior of the bubble may be directly related to the corresponding values at the bubble wall. Many of the previous analyses were based on the assumption of hemispherical bubble growth on the heating surface, but it is problematical whether an initially hemispherical bubble nucleus will remain so at later stages. This question will be answered by the discussion which follows.

In this chapter, an analysis of a bubble growing on a heating surface will be discussed. In Section 6.2, the equations governing the flow field outside the bubble will be stated as well as both the initial and boundary conditions. The numerical technique chosen (The Marker And Cell -MAC-technique in its simplified version - SOLA - [42]) and the modifications performed to suit the problem of bubble growth will be covered in Section 6.3. Some results related to the bubble growth and flow field outside the bubble will be presented in Section 6.4, and finally, Section 6.5 will discuss some of the bubble growth predictions.

6.2 Theoretical Formulation

The conservation equations of momentum and continuity in terms of the primitive variables u, v and P with the appropriate initial and boundary conditions form the hydrodynamic basis for the solution of the flow field outside the bubble. These equations and conditions are presented in the following sections.

6.2.1 Continuity and Momentum Equations

For incompressible flow the momentum and continuity equations in cylindrical coordinates can be written in the form:

$$\frac{\partial u}{\partial t} = -u\frac{\partial u}{\partial r} - v\frac{\partial u}{\partial y} - \frac{\partial P^*}{\partial r} + \nu \left[\frac{\partial^2 u}{\partial r^2} + \frac{1}{r}\frac{\partial u}{\partial r} - \frac{u}{r^2} + \frac{\partial^2 u}{\partial y^2}\right] \qquad (6.1)$$

$$\frac{\partial v}{\partial t} = -u \frac{\partial v}{\partial r} - v \frac{\partial v}{\partial y} - \frac{\partial P^*}{\partial y} + \nu \left[\frac{\partial^2 v}{\partial r^2} + \frac{1}{r} \frac{\partial v}{\partial r} + \frac{\partial^2 v}{\partial y^2}\right] - g \qquad (6.2)$$

$$D \equiv \frac{\partial u}{\partial r} + \frac{u}{r} + \frac{\partial v}{\partial y} \equiv 0 \qquad (6.3)$$

where $P^* = P/\rho_\ell$ is the ratio of the pressure P to the constant liquid density ρ_ℓ.

6.2.2 Initial Conditions

For a static bubble nucleus on a wall such as that depicted in Figure (6.1), the pressure inside the bubble is initially equal to the vapour pressure $P_v(0)$, the pressure elsewhere is equal to P_∞ and the velocity components are equal to zero everywhere, i.e.:

$$u(r, y, 0) = 0 \qquad (6.4)$$

$$v(r, y, 0) = 0 \qquad (6.5)$$

6.2.3 Boundary Conditions

(i) Heating Surface (No-slip Condition)

For the no-slip wall, the radial and axial velocity components should equal zero, i.e.

$$u(r, 0, t) = 0 \qquad (6.6)$$

$$v(r, 0, t) = 0 \qquad (6.7)$$

(ii) Axis of Symmetry (Free-slip Condition)

This condition requires the normal velocity component

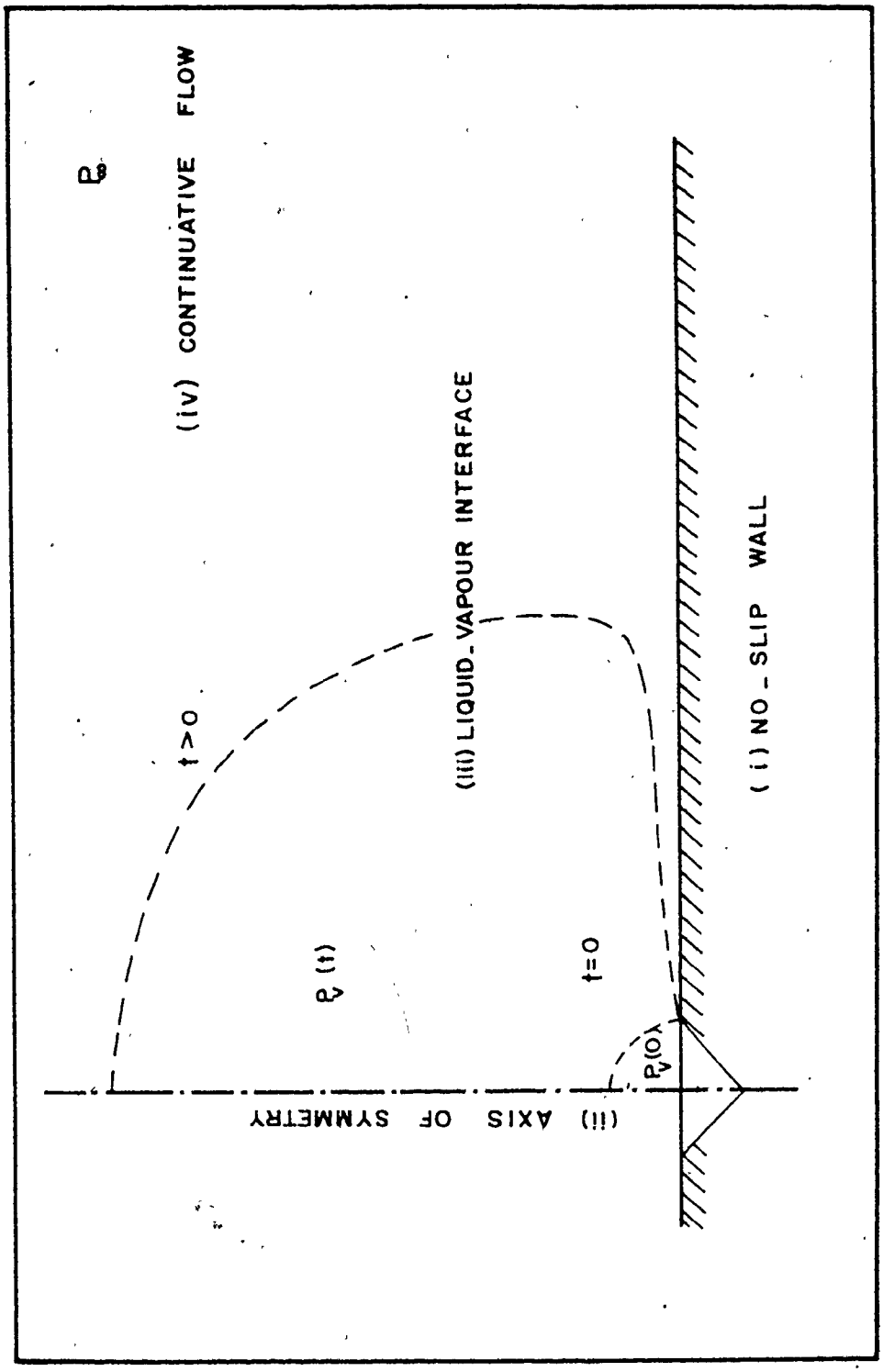

FIGURE (6.1) BUBBLE GROWTH ON A HEATING SURFACE

to be zero and the gradient of the tangential velocity to be zero, i.e.

$$u(0, y, t) = 0 \tag{6.8}$$

$$\frac{\partial v(0, y, t)}{\partial r} = 0 \tag{6.9}$$

Furthermore, the normal pressure gradient is zero,

$$\frac{\partial P}{\partial r} = 0 \tag{6.10}$$

(iii) Interface Condition

For a free surface, stress normal to the interface must balance the externally applied force and the tangential stress must balance the tangential surface tension effect. In this analysis, the vapour pressure applied was supplied as a function of time $P_v(t)$ and the surface tension effect was ignored. Hence the only forced boundary condition at the interface is:

$$P = P_v(t) \tag{6.11}$$

(iv) Continuative Flow at an Infinite Distance

It is assumed that at "infinity", far from the influence of the bubble, the velocity gradient is zero. More details will be discussed in section (6.3.5).

6.2.4 Energy Equation and Temperature Field

For an axisymmetric bubble, the energy equation in two-dimensional cylindrical coordinates can be written as:

$$\frac{\partial T}{\partial t} = -u \frac{\partial T}{\partial r} - v \frac{\partial T}{\partial y} + \alpha_\ell [\frac{\partial^2 T}{\partial r^2} + \frac{1}{r} \frac{\partial T}{\partial r} + \frac{\partial^2 T}{\partial y^2}] \qquad (6.12)$$

The initial and boundary conditions are:

6.2.5 Initial Condition

$$T(r, y, 0) = T(r,y) \qquad (6.13)$$

where T(r,y) is the instantaneous solution of the heat conduction equation

$$\frac{\partial T}{\partial t} = \alpha_\ell [\frac{\partial^2 T}{\partial r^2} + \frac{1}{r} \frac{\partial T}{\partial r} + \frac{\partial^2 T}{\partial y^2}]$$

6.2.6 Boundary Conditions

$$T(r, 0, t) = T_w \qquad (6.14)$$

$$\frac{\partial T(0,y,t)}{\partial r} = 0 \qquad (6.15)$$

$$T(r,\infty,t) = T_\infty \qquad (6.16)$$

$$T(\infty,y,t) = T(y) \qquad (6.17)$$

where T_w and T_∞ are the wall and pool temperatures respectively.

6.3 Numerical Solution

6.3.1 Introduction

The selection of an appropriate method for the solution of bubble growth on the heating surface was not a simple problem. The primary qualifications of the "right" method are:

1) Accuracy in the more important areas of bubble growth field,
2) Flexibility with regard to introduction of initial and boundary conditions,
3) Inclusion of as many fluid properties as possible and the possibility of adding or deleting other properties.

The choice of techniques is at first a matter of elimination. The non-linearity of the partial differential equations for conservation of mass and momentum in time-dependent two-dimensional axially symmetric cylindrical coordinate form, combined with the moving free surface boundary conditions excludes a direct analytical solution.

A comprehensive survey of finite difference methods for transient flows in two or more dimensions has been presented by Harlow [43] and Roache [44]. Such methods represent the primary alternative remaining among present day methods of solution of fluid flow problems.

The appropriate method to handle the bubble growth problem appeared to be the Marker And Cell (MAC) technique [45] in its simplified version SOLA [42]. This method was reported to work very well for the solution of a variety of problems involving incompressible liquids with free surfaces. The details of the SOLA method as applied to the bubble growth problem is described in the following sections. Some

of the modifications incorporated are also discussed.

6.3.2 Marker And Cell (MAC) Technique

The Marker And Cell (MAC) technique obtains the solution to a set of finite difference equations that are derived from the momentum and continuity partial differential equations and the boundary conditions of viscous fluid flow in two spatial coordinates. A straight forward differencing scheme can be used but the primary requirement imposed is that both continuity and momentum equations should be satisfied in the difference equations as they are in the original differential equations. The marker particles used in MAC are "massless" particles which move with the advection field. These markers do not participate directly in the computation. By tracing and plotting the position of the marker particles, one obtains a "streakline" picture, analagous to dye visualization photographs. Similarly, "massless" markers are identified along the free surface; these markers are advanced in each time step to new postions in accordance with a simple kinematic relation between the surface geometry and fluid velocities. These markers are initially laid out in order along the fluid interface and therefore mark the interface as they move, which is their sole function in the numerical computation.

6.3.3 Unequal Cell Size

Numerical studies of fluid dynamics problems are quite often concerned with flow near solid bodies where fairly large velocity gradients are encountered. In the vicinity of the body, it is often convenient to use a mesh system which is smaller than the mesh system imposed over the remainder of the flow field. This type of problem is of interest because the velocity can change rather abruptly and the effect of the change is more pronounced in certain regions than other regions. Therefore, it was felt that by increasing the density of the mesh cells in the region of greatest change (near the heating surface), a marked improvement in the overall accuracy of the solution could be affected without the expense of increasing the density of the grid system everywhere.

6.3.4 Cell Structure and Flagging

The MAC cell structure is shown in figure (6.2.a). The radial velocity components u are defined along the middle of the left and right hand boundary of the cell (vertical sides) as $u_{i-1/2,j}$ and $u_{i+1/2,j}$. The axial velocity components v are defined along the middle of the bottom and top boundaries (horizontal sides) as $v_{i,j-1/2}$ and $v_{i,j+1/2}$. Other variables (as pressure and temperature) are defined at the cell center as $P_{i,j}$ and $T_{i,j}$.

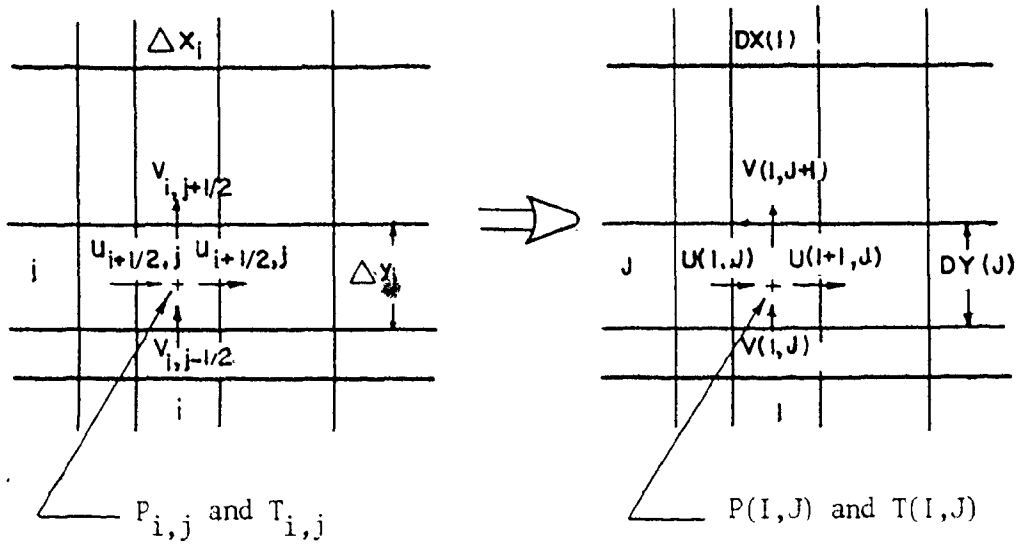

FIGURE(6.2a) CELL STRUCTURE

Each cell was flagged by a number depending upon its condition. Vapour cells were given number (1), interface cells were given number (2), fluid cells were given number (3) and boundary cells were given number (4). The interface cells are defined as soon as the interface marker(s) enter the cell, Figure (6.2b).

6.3.5 Finite Difference Representation

In order to solve the momentum and continuity equations (6.1) to (6.3) by a finite difference scheme, a computation region is specified and divided into a number of rectangular flagged cells, while the interface is defined by massless markers as shown in figure (6.2b). The present computation region is the space bounded by (i) the heating surface boundary, (ii) the axis of symmetry, (iii) the top boundary, and (iv) the right boundary. The top and right boundaries (iii) and (iv) depend on the area of interest.

In the method used, the term $\frac{\partial u}{\partial t}$ is represented by the first order approximation:

$$\frac{\partial u}{\partial t} = \frac{u^{n+1}_{i+1,j} - u^{n}_{i+1,j}}{\Delta t} \qquad (6.18)$$

where n refers to the n^{th} time step and Δt is the time increment which is determined by the numerical stability condition discussed later. The differencing scheme for the advection terms of momentum and energy equation is the

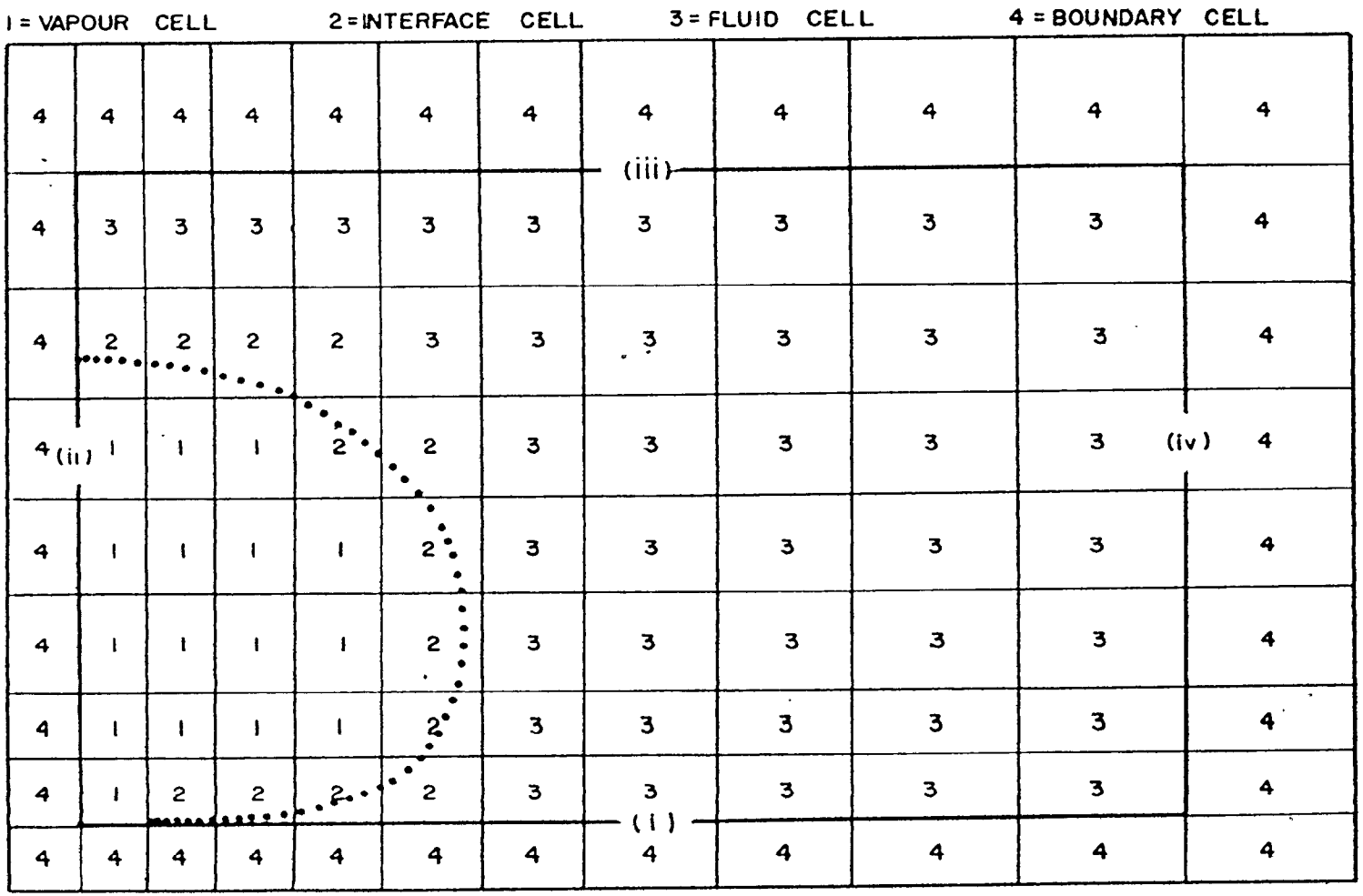

FIGURE (6 2b) COMPUTATION REGION

"donor cell" or fully upstream formulation. It is not necessary to use pure "donor cell" as other approximations could be used.

The finite difference equations for the momentum and continuity equations (6.1) to (6.3) and the energy equation (6.12) used for the present calculations can be written as:

Momentum Equations

$$u^{n+1}_{i+1,j} = u_{i+1,j} - \Delta t(FUX+FUY)_{i+1,j} - \Delta t*DPDX)_{i+1,j} + \Delta t*\nu*VISCOX)_{i+1,j} \tag{6.19}$$

$$v^{n+1}_{i,j+1} = v_{i,j+1} - \Delta t(FVX+FVY)_{i,j+1} - \Delta t*DPDY)_{i,j+1} + \Delta t*\nu*VISCOY)_{i,j+1} - \Delta t*g \tag{6.20}$$

where

FUX, FUY, DPDX, VISCOX, FVX, FVY, DPDY and VISCOY are defined in Appendix C.

Continuity Equation

$$D^{n+1}_{ij} = (u^{n+1}_{i+1,j} - u^{n+1}_{i,j})/\Delta r_i + \frac{(u^{n+1}_{i+1,j} + u^{n+1}_{i,j})}{2(\sum_{m=2}^{i} \Delta r_m - \Delta r_i/2)} + (v^{n+1}_{i,j+1} - v^{n+1}_{i,j})/\Delta y_j = 0 \tag{6.21}$$

Energy Equation

$$T_{ij}^{n+1} = T_{ij} - \Delta t[TUX+TVY] + \alpha_{\ell}*\Delta t*COND \qquad (6.22)$$

where parameters with no superscript represent n^{th} time step. TUX, TVY and COND are defined in Appendix C.

Conservation of Mass and Momentum

The momentum equtions (6.19) and (6.20) will provide the velocity components u and v if they are applied at each cell to satisfy the conservation of momentum. However, these velocity components will not necessarily satisfy the conservation of mass at each cell in the computation region. Accordingly, an iteration procedure was applied to adjust the velocity components so that the conservation of mass was satisfied at each cell. During the iteration procedure, the continuity equation (6.21) was written as:

$$D_{ij}^{k} = (u_{i+1,j}^{k} - u_{i,j}^{k})/\Delta r_i + \frac{(u_{i+1,j}^{k}+u_{i,j}^{k})}{2(\sum_{m=2}^{i} \Delta r_m - \frac{\Delta r_i}{2})} + \frac{v_{i,j+1}^{k}-v_{ij}^{k}}{\Delta y_j} \neq 0 \qquad (6.23)$$

If the divergence D_{ij}^{k} of a cell is negative, this corresponds to a net flow of mass into the cell and the cell pressure is then increased to eliminate this net "inflow". On the other hand the cell pressure is decreased to eliminate a net "outflow" if D_{ij}^{k} is positive. Changes of pressure ΔP are assumed to occur that will change the values of the velocity components at the (k+1) iteration so that D_{ij}^{k+1} is always zero.

The change in the velocity components will be:

$$u^{k+1}_{i+1,j} = u^{k}_{i+1,j} + \frac{\Delta P\ \Delta t}{\Delta r_i}$$

$$u^{k+1}_{i,j} = u^{k}_{i,j} - \frac{\Delta P\ \Delta t}{\Delta r_i} \qquad (6.24)$$

$$V^{k+1}_{i,j+1} = v^{k}_{i,j+1} + \frac{\Delta P\ \Delta t}{\Delta y_j}$$

$$v^{k+1}_{i,j} = v^{k}_{i,j} - \frac{\Delta P\ \Delta t}{\Delta y_j}$$

The new cell pressure will be

$$p^{k+1}_{ij} = P^{k}_{ij} + \Delta P \qquad (6.25)$$

The divergence at the k+1 iteration will be

$$D^{k+1}_{ij} = \frac{u^{k+1}_{i+1,j} - u^{k+1}_{i,j}}{\Delta r_i} + \frac{u^{k+1}_{i+1,j} + u^{k+1}_{i,j}}{2\left(\sum_{m=2}^{i} \Delta r_m - \frac{\Delta r_i}{2}\right)} + \frac{v^{k+1}_{i,j+1} - v^{k+1}_{i,j}}{\Delta y_j} = 0 \qquad (6.26)$$

Substituting from equations (6.24) into (6.26) and making use of equation (6.23)

$$D^{k+1}_{ij} = 0 = D^{k}_{ij} + \Delta P\ \Delta t\ \left[2\left(\frac{1}{\Delta r_i^2} + \frac{1}{\Delta y_j^2}\right)\right] \qquad (6.27a)$$

or

$$\Delta P = \frac{-\ D^{k}_{ij}}{\Delta t\left[2\left(\frac{1}{\Delta r_i^2} + \frac{1}{\Delta y_j^2}\right)\right]} = -\ \beta\ D^{k}_{ij} \qquad (6.27b)$$

Equation (6.27b) gives the pressure change required for each cell so that the divergence $D_{ij}^{k+1} = 0$. Note that if the pressure of one cell is adjusted, then the adjacent cells are also affected. Therefore, the pressure adjustment must be done iteratively. Since it is very difficult to reach the value of zero in finite difference solutions a specified accuracy value ε was introduced. It was also found from experimentation with this procedure that an accelerating coefficient ω might be used to minimize the number of iterations. The value of ω could vary from one problem to another, values between 1.5 - 1.9 were tried and the optimum value was found to be 1.85. Accordingly,

$$\Delta P = - \beta \omega D_{ij}^{k}$$

and

$$D_{ij}^{k+1} \leq \varepsilon$$

Initial Conditions

The initial conditions provide the starting values of u, v, P and T which are assumed to be:

$$u_{i+1,j}^{1} = 0 \qquad (6.28)$$

$$v_{i,j+1}^{1} = 0 \qquad (6.29)$$

$$T_{ij}^{1} = \text{steady state temperature distribution or any specified function} \qquad (6.30)$$

$$P^1_{ij} = P_\infty \tag{6.31a}$$

$$P_v = P_v(0) \tag{6.31b}$$

Boundary Conditions

To impose the necessary boundary conditions, the computation field is considered to be surrounded by a single layer of fictitious cells in which the variables are specified. The arrangement of the fictitious cells used for the present calculations is illustrated in figure (6.2b).

(a) Heating Surface

The decision as to whether to consider the heating surface boundary as no-slip or free-slip depends on the relative thickness of the boundary layer in comparison with the cell size near the wall. For the non-slip wall, with reference to figure (6.3a),

$$u_{i+\frac{1}{2},1} = - u_{i+\frac{1}{2},2} \tag{6.32}$$

$$v_{i,\frac{3}{2}} = 0 \tag{6.33}$$

$$T_{i,1} = T_w \tag{6.34}$$

The use of equation (6.32) to determine a fictitious value of $u_{i+\frac{1}{2},1}$ inside the wall gives an effective $u_{i+\frac{1}{2},\frac{3}{2}} = 0$.

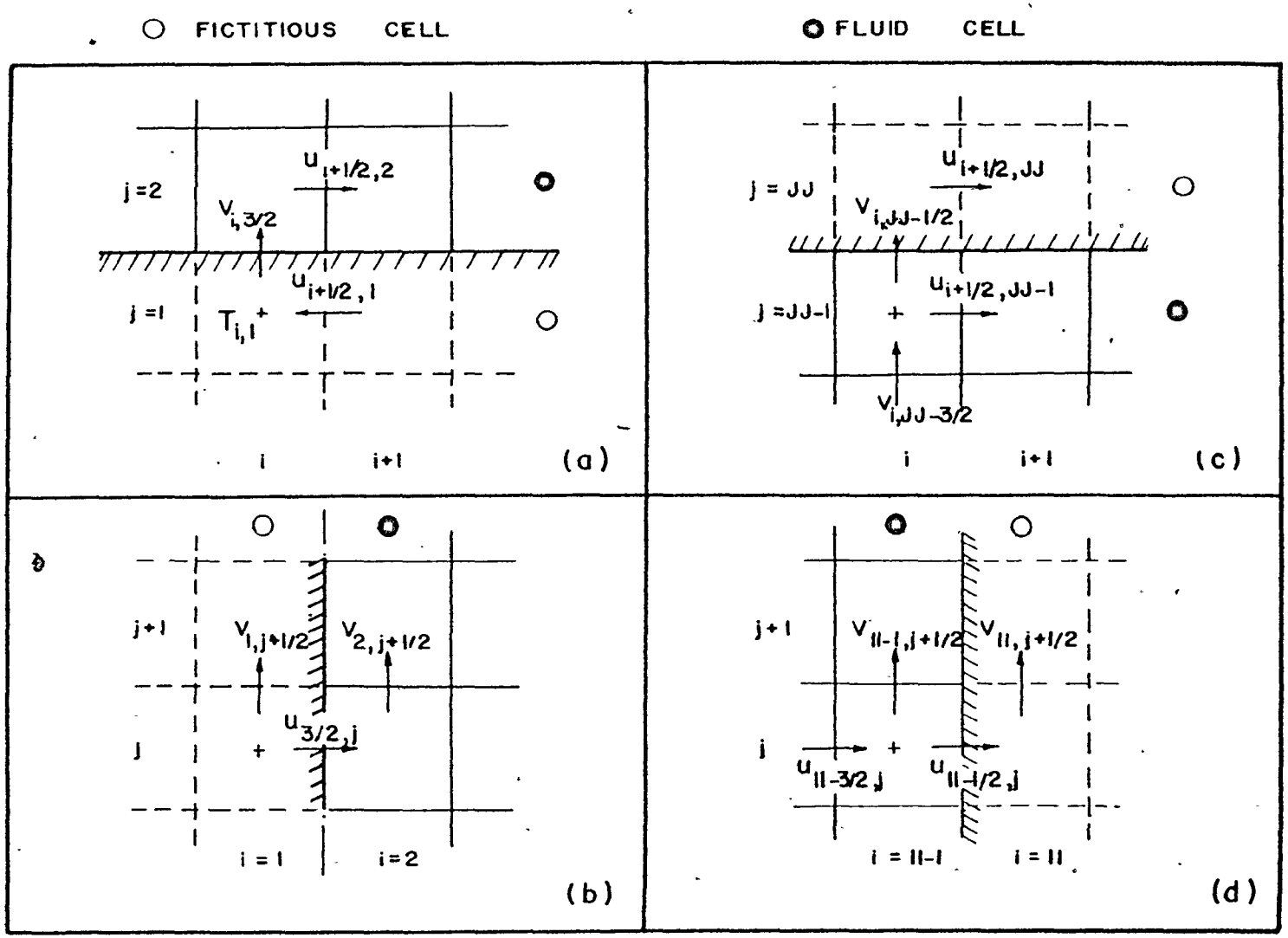

FIGURE(6.3) BOUNDARY CONDITIONS REPRESENTATIONS

For the free-slip wall, the same conditions stated above were used except that equation (6.32) was replaced by

$$u_{i+\frac{1}{2},1} = + u_{i+\frac{1}{2},2} \qquad (6.32)^*$$

(b) Axis of Symmetry

From symmetry considerations, with reference to figure (6.3b),

$$u_{\frac{3}{2},j} = 0 \qquad (6.35)$$

$$v_{1,j+\frac{1}{2}} = v_{2,j+\frac{1}{2}} \qquad (6.36)$$

$$P_{1,j} = P_{2,j} \qquad (6.37)$$

$$T_{1,j} = T_{2,j} \qquad (6.38)$$

Conditions (6.32) to (6.38) were imposed on the velocities resulting from the evaluation of the momentum equations (6.19) and (6.20), and after each pass through the mesh during the pressure iteration.

Continuative Outlet Flow

Continuative outlet flow boundaries always pose a problem for low speed calculations [42], because any prescribed condition may send signals back into the mesh that

affect the entire upstream flow. What is needed is prescribed conditions that permit fluid to flow out of the mesh with a minimum of upstream influence. In the present problem, these conditions have been specified such that the normal and tangential velocity components are equal to the upstream ones, i.e.,

Top Boundary

Referring to figure (6.3c)

$$u_{i+\frac{1}{2},JJ} = u_{i+\frac{1}{2},JJ-1} \tag{6.39}$$

$$v_{i,JJ-\frac{1}{2}} = v_{i,JJ-\frac{3}{2}} \tag{6.40}$$

$$T_{i,JJ} = T_{i,JJ-1} \tag{6.41}$$

Right Boundary

Referring to figure (6.3d)

$$u_{II-\frac{1}{2},j} = u_{II-\frac{3}{2},j} \tag{6.42}$$

$$v_{II,j+\frac{1}{2}} = v_{II-1,j+\frac{1}{2}} \tag{6.43}$$

$$T^{n+1}_{II,j} = T^{n}_{II,j} \tag{6.44}$$

These conditions (6.39) to (6.44) are only imposed after solving equations (6.19) and (6.20) and not after each

pass through the mesh in the pressure iteration. During the iterations, the normal boundary velocities can vary with changes in pressure, just as any interior velocity component so that the continuity equation is satisfied.

6.3.6 Marker Velocity Components

The markers used in the MAC method are massless particles which move with the advection field. The position of each marker r_k^n and y_k^n is obtained by numerical integration from the initial position r_k^o and y_k^o at time equal to zero, i.e.,

$$r_k^n = r_k^o + \int_o^t u_k \, dt \tag{6.45}$$

$$y_k^n = y_k^o + \int_o^t v_k \, dt \tag{6.46}$$

where u_k and v_k denote the velocity components for the k^{th} marker. Equations (6.45) and (6.46) can be written as:

$$r_k^{n+1} = r_k^n + u_k^n \, \Delta t \tag{6.47}$$

$$y_k^{n+1} = y_k^n + v_k^n \, \Delta t \tag{6.48}$$

The values of the marker velocity components u_k and v_k can be obtained by linear interpolation of the u and v field velocity components. However, a more accurate procedure which improves the accuracy near the velocity extrema is the

use of a second order Taylor series expansion, i.e.

$$u_k = u_o + h\left(\frac{\partial u}{\partial r}\right)_o + L\left(\frac{\partial u}{\partial y}\right)_o + \frac{1}{2!}\left[h^2\left(\frac{\partial^2 u}{\partial r^2}\right) + 2hL\left(\frac{\partial^2 u}{\partial r \partial y}\right) + L^2\left(\frac{\partial^2 u}{\partial y^2}\right)\right]_o \tag{6.49}$$

The value of v_k is obtained in a similar fashion. The numerical representations of u_k and v_k are given in Appendix C3.

6.3.7 Interface Modifications

The presence of an interface in unsteady incompressible flow problems complicates the solution for two reasons. Firstly, it is necessary to follow up the position and orientation of the interface in order to impose the boundary conditions. Secondly, it is necessary to be concerned with the proper application of the interface boundary conditions. The first problem was resolved by the use of the interface markers as discussed before. The second problem concerning the proper application of the interface boundary conditions used in the present analysis will be discussed in the following sections.

(i) Pressure and Temperature at the Interface Boundary

Considering $P_{ij} = P_v$ at the center of the surface cell is not accurate. Only at the interface surface, which does not necessarily coincide with the surface cell center, is $P = P_v$. This difference affects the accuracy of the solution

of the pressure field which in turn influences the calculations of the velocity fields.

Let ℓ_1, ℓ_2, ℓ_3 and ℓ_4 be the lengths of the four arms and P_1, P_2, P_3 and P_4 be the values of P at the end of the arms respectively as depicted in figure (6.4a). Using Taylor series expansion for the pressure at each end we get:

$$P_1 = P_{ij} + \ell_1 \left(\frac{\partial P}{\partial r}\right)_{ij} + O(\ell_1^2) \tag{6.50}$$

$$P_3 = P_{ij} - \ell_3 \left(\frac{\partial P}{\partial r}\right)_{ij} + O(\ell_3^2) \tag{6.51}$$

$$P_2 = P_{ij} + \ell_2 \left(\frac{\partial P}{\partial y}\right)_{ij} + O(\ell_2^2) \tag{6.52}$$

$$P_4 = P_{ij} - \ell_4 \left(\frac{\partial P}{\partial y}\right)_{ij} + O(\ell_4^2) \tag{6.53}$$

Multiplying (6.50) by ℓ_3 and (6.51) by ℓ_1 and adding

$$P_1 \ell_3 + P_3 \ell_1 = P_{ij} (\ell_1 + \ell_3) \tag{6.54}$$

Similarly, multiplying (6.52) by ℓ_4 and (6.53) by ℓ_2 and adding

$$P_2 \ell_4 + P_4 \ell_2 = P_{ij} (\ell_2 + \ell_4) \tag{6.55}$$

Adding (6.54) and (6.55) and arranging leads to

$$P_{ij} = \frac{(P_1 \ell_3 + P_3 \ell_1) + (P_2 \ell_4 + P_4 \ell_2)}{\ell_1 + \ell_2 + \ell_3 + \ell_4} \tag{6.56}$$

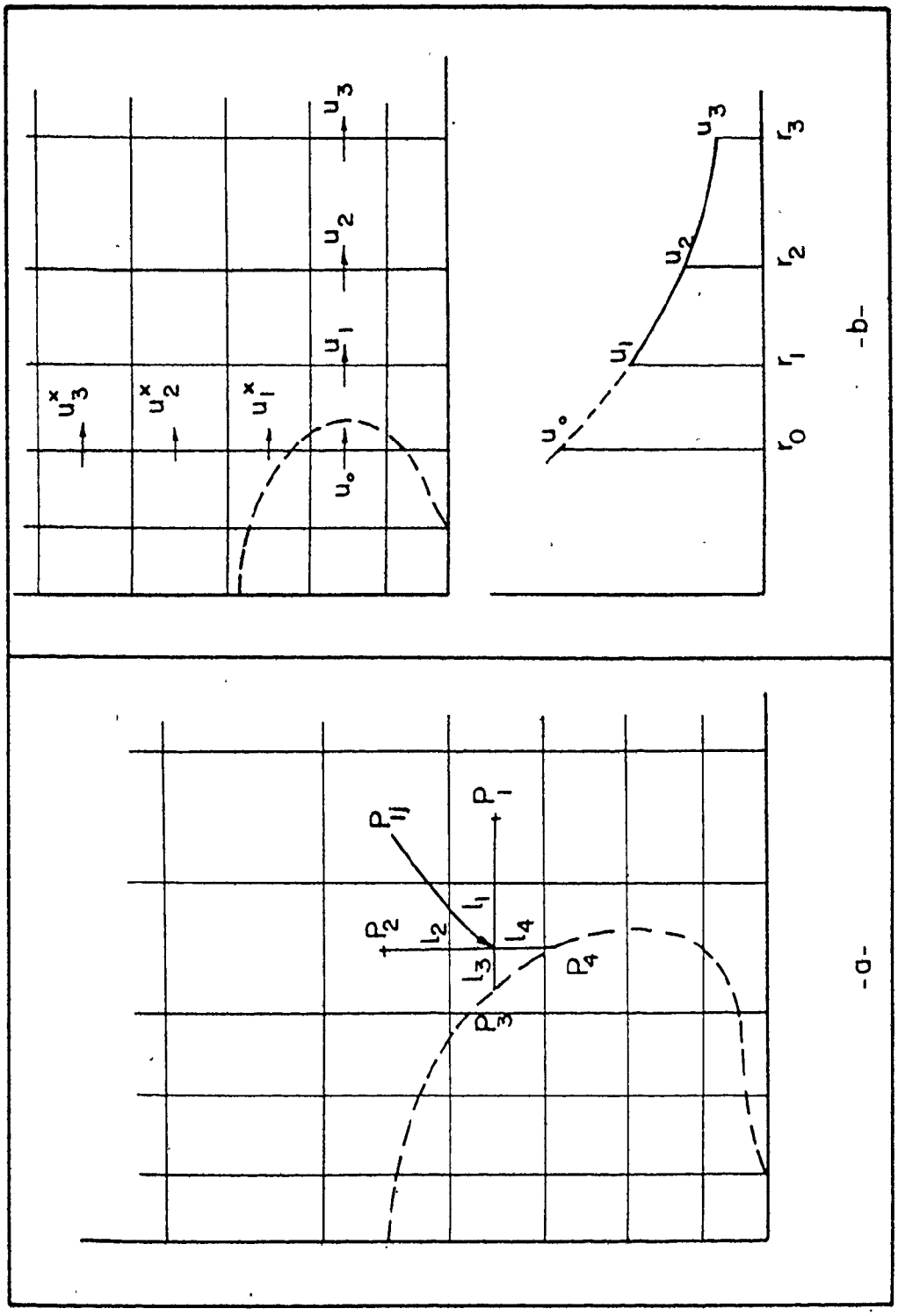

FIGURE (6.4) LIQUID_VAPOUR INTERFACE MODIFICATIONS

Equation (6.56) specifies the pressure at the surface cell centers as a boundary condition in more accurate form. Similar equations are applied for the interface temperature, i.e., for interface cells

$$T_{ij} = \frac{(T_1 \ell_3 + T_3 \ell_1) + (T_2 \ell_4 + T_4 \ell_2)}{\ell_1 + \ell_2 + \ell_3 + \ell_4} \qquad (6.56)$$

(ii) Velocity Components Outside the Fluid Region

The velocity components are not defined outside the fluid region (i.e., inside the bubble), but they are needed to carry out the computations near the bubble interface and to move the markers. These velocity components are calculated by using an extrapolation formula. Assuming that a Lagrangian quadratic polynomial passes through points 1, 2 and 3 in figure (6.4b), one can use this polynomial to determine the approximate value of the velocity components at point (0). Let the values of the velocities at r_1, r_2, and r_3 be u_1, u_2 and u_3 respectively. The second degree polynomial passing through these points will be:

$$u(r) = A_1(r)u_1 + A_2(r)u_2 + A_3(r)u_3 \qquad (6.57)$$

where

$$A_1(r) = \frac{(r-r_2)(r-r_3)}{(r_1-r_2)(r_1-r_3)}$$

$$A_2(r) = \frac{(r-r_1)(r-r_3)}{(r_2-r_1)(r_2-r_3)}$$

$$A_3(r) = \frac{(r-r_1)(r-r_2)}{(r_3-r_1)(r_3-r_2)}$$

The velocity at point (0) will be

$$u_o = A_1(r_o)\, u_1 + A_2(r_o)\, u_2 + A_3(r_o)\, u_3 \qquad (6.57)$$

An expression for v_o is obtained in a similar fashion.

The extrapolation for the velocity components u_o and v_o could be done horizontally or vertically (using the velocities u_1^*, u_2^* and u_3^*) depending on the interface cell orientation. Five different possible interface cells are shown in figure (6.5).

Cell (100) → Top side open to vapour

Cell (200) → Bottom side open to vapour

Cell (300) → Left side open to vapour

Cell (400) → Both top and left sides open to vapour

Cell (500) → Both bottom and left sides open to vapour

For interface cells (100) and (300) horizontal extrapolation was used, for interface cells (200), vertical extrapolation was used and for interface cells (400) and (500) an average obtained from both techniques was used.

6.3.8 Evaporation from the Bubble Cap

Evaporation from the bubble cap is allowed if for any interface cell, the temperature is higher than the vapour temperature T_v. The evaporation rate will be calculated by combining the heat transferred by conduction at the bubble interface with the latent heat of the liquid, i.e.,

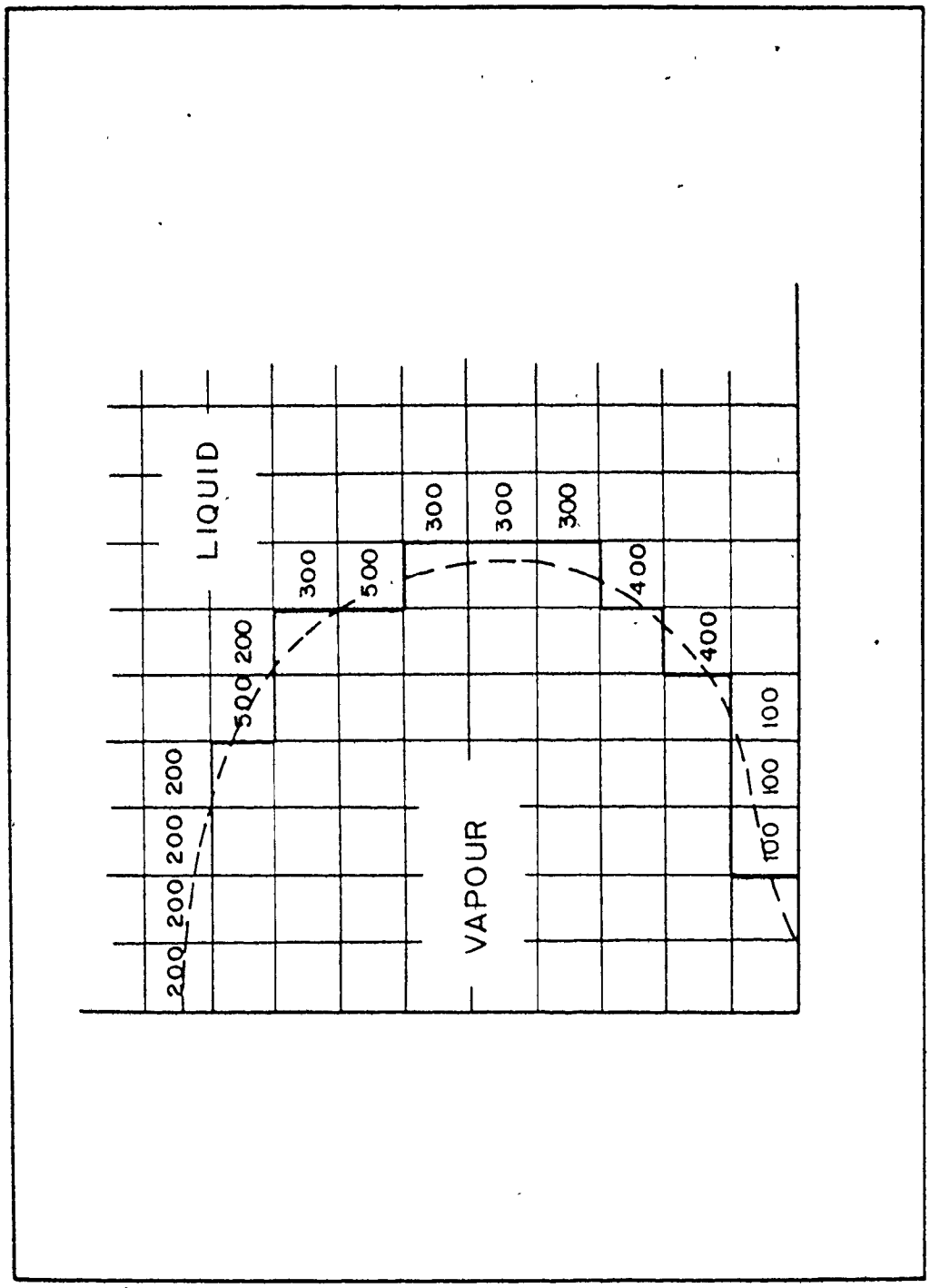

FIGURE (6·5) EXTRAPOLATION

$$\frac{d M_{cap}}{dt} = \frac{Q}{h_{fg}} \qquad (6.58)$$

where

$Q = Q_r$ for cells #300

$Q = Q_y$ for cells #100 and 200

$Q = (Q_r+Q_y)/2.0$ for cells #400 and 500

$$Q_r = \frac{k_\ell (T^n_{ij}-T_v) A_r}{\Delta r} \quad , \quad Q_y = \frac{k_\ell (T^n_{ij}-T_v) A_y}{\Delta y}$$

$A_v = 2\pi r \Delta y$ $\qquad$ $A_y = 2\pi r \Delta r$

6.3.9 Computation Procedure

Figure (6.6) depicts the flow for the computation procedure used. These steps can be summarized as follows:

1. The data needed (computation parameters such as Δt, Δr,... and physical parameters such as ρ_ℓ, ν_ℓ,... etc) are supplied (subroutine DATA).

2. The initial conditions provide the starting values of u, v, P and T while the position of the liquid-vapour interface is defined by the locations of the markers (subroutine IC).

3. The cells are reflagged according to the new interface position (subroutine FLAG).

4. The pressure and the temperature interface cells are determined using the technique discussed in Section (6.3.6) (subroutine PRESS).

5. The boundary conditions for u, v, P and T are set up.

6. Estimates for the new velocity components u^{n+1} and v^{n+1} are computed from the momentum equations (6.19) and (6.20) using the previous time step values for all quantities on the right hand side. This is done for all interface and fluid cells (subroutine NSE).

7. The numerical stability is checked in accordance with Section 6.3.9.

8. The new velocity components are adjusted to satisfy the continuity equation (6.21) by changing the cell pressure in accordance with Section 6.3.5.

9. When the divergence $D_{ij} \leq \varepsilon$ is satisfied, the velocity components are extrapolated to the interface and vapour cells (subroutine EXTRPO). Otherwise the procedure is repeated from step 8.

10. The temperature of the liquid is calculated for each cell (subroutine TEMPDIS).

11. The marker velocity components u_k and v_k are calculated by interpolation and the new position of the markers are calculated as discussed in Section 6.3.6 (subroutine MARKER).

12. The new values of u, v, P, and T are stored (subroutine ADVANCE).

13. The heat transferred at the interface cells and the mass evaporated from the bubble interface are calculated.

14. The pressure inside the bubble $P_v(t)$ is specified for the vapour cells.

15. The results are printed if needed (subroutine PRINT).

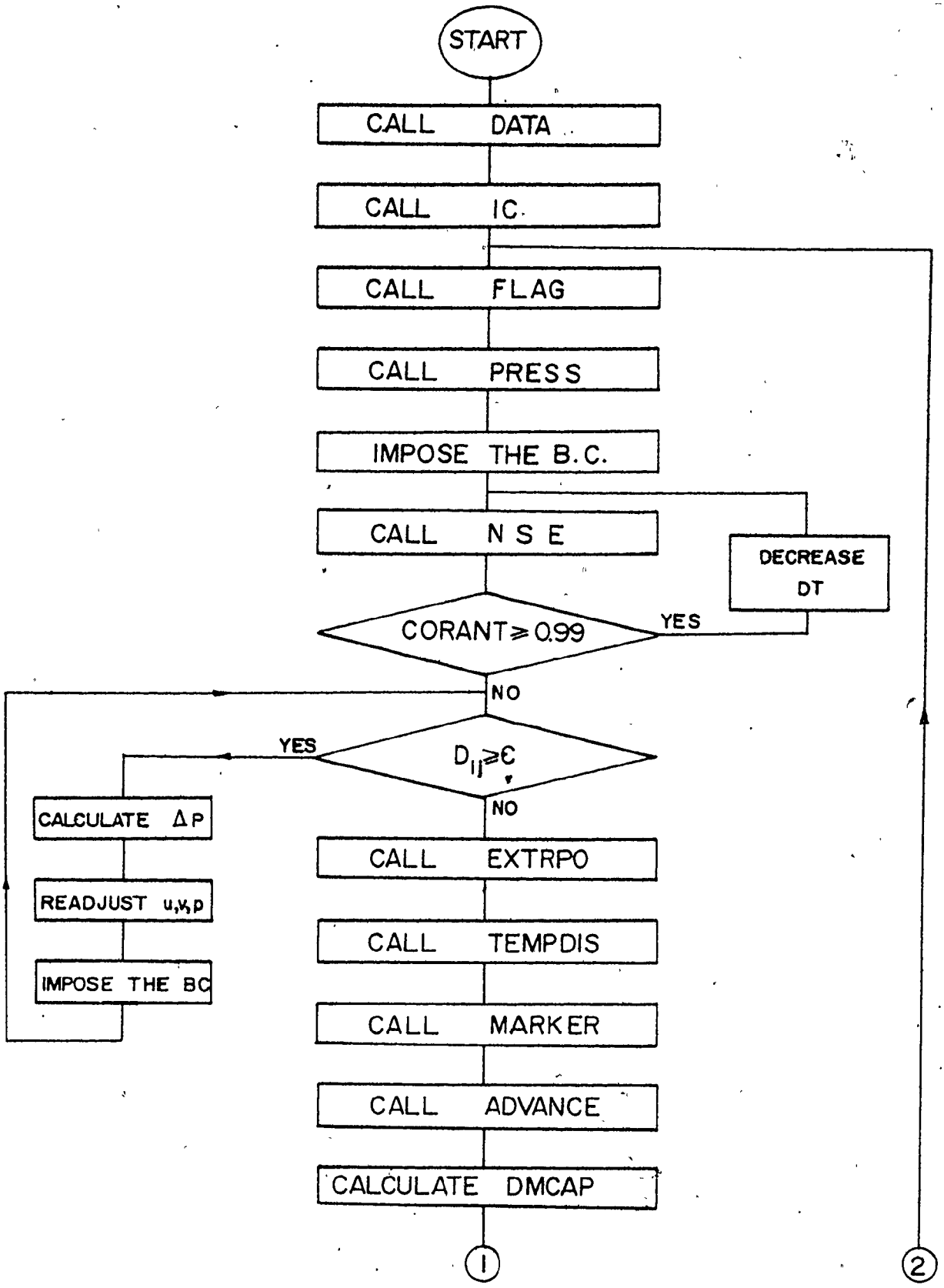
START
CALL DATA
CALL IC
CALL FLAG
CALL PRESS
IMPOSE THE B.C.
CALL N S E
DECREASE DT
CORANT ≥ 0.99
YES
NO
YES
$D_{ij} \geq \epsilon$
NO
CALCULATE ΔP
READJUST u,v,p
IMPOSE THE BC
CALL EXTRPO
CALL TEMPDIS
CALL MARKER
CALL ADVANCE
CALCULATE DMCAP
1
2

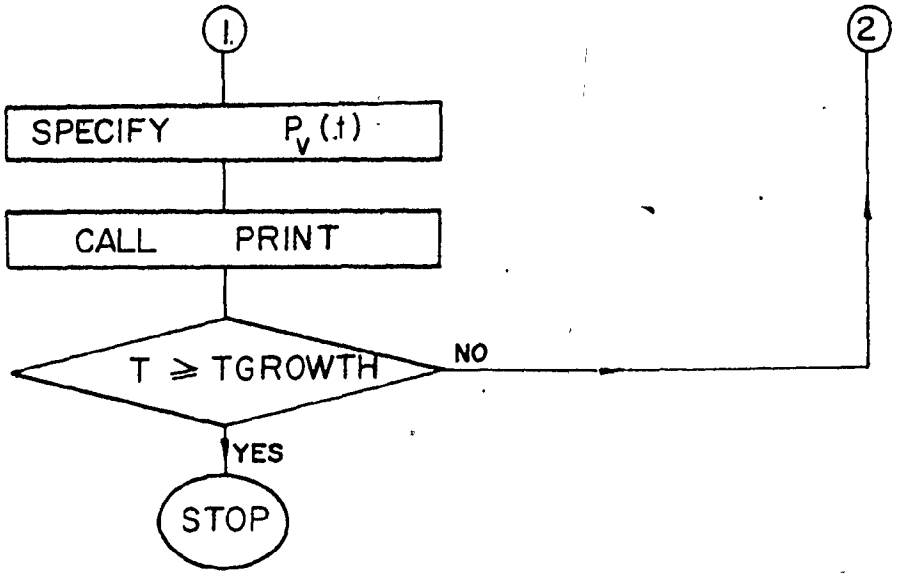

FIGURE(6.6) COMPUTATION PROCEDURE OF BUBBLE GROWTH

16. The subsequent cycles proceed from step number 3 until the elapsed time is equal to the growth time specified.

A detailed listing of the program is given in reference [39].

6.3.10 Stability of the MAC Technique

The mesh increment must be chosen small enough (depending on the problem) to obtain the most accurate results. Once the mesh size has been chosen, the choice of the time increment is governed by two restrictions as discussed in Chapter 4. Firstly, the fluid cannot move through more than one cell in one time step. This condition is known as the Courant stability condition which can be represented by

$$\text{Courant} = \max\left(\frac{u\,\Delta t}{\Delta r_i}, \frac{v\Delta t}{\Delta y_j}\right) < 1 \qquad (6.59)$$

Secondly, the momentum must not diffuse more than one cell in one time step. This condition is known as the diffusional stability condition which can be represented by

$$\Delta t \leq \frac{1}{2\nu} \frac{\Delta r_i^2 \cdot \Delta y_j^2}{\Delta r_i^2 + \Delta y_j^2} \qquad (6.60)$$

6.4 Predictions of Bubble Growth on a Heating Surface

6.4.1 Introduction

In the previous two chapters the behaviour of the

bubble base was studied for different cases with the assumption that the growth rate $\dot{R}(t)$ was specified. In the literature many experimentally and analytically based models have been proposed to predict the bubble growth rate $\dot{R}(t)$ for different combinations of surface, liquid and system conditions. The well know basic differential equation for bubble growth is the modified Rayleigh differential equation written as follows:

$$\Delta P_V^*(t) = \frac{P_V(t)-P_\infty}{\rho_\ell} = R\ddot{R} + \frac{3}{2}\dot{R}^2 + \frac{2\sigma}{\rho_\ell R} + 4\nu\frac{\dot{R}}{R} \qquad (6.61)$$

Equation (6.61) shows that the bubble expands due to the excess pressure $\Delta P_V^*(t)$ acting as the driving force. How the bubble will expand depends in fact on the function assigned to the pressure function $\Delta P_V^*(t)$.

In order to study the bubble growth behaviour, bubble shape and the thermal and fluid fields around the bubble in a more general way, one should solve the continuity, momentum and energy equations of the fluid surrounding the bubble; in which all significant forces can be accounted for. This has been done herein by adapting the (MAC) method discussed in the previous sections. The only parameter still to be supplied is the pressure function $\Delta P_V^*(t)$. This function could be obtained one of several different ways:

1. $\Delta P_V^*(t)$ function could be assumed in order to generate an arbitrary bubble growth rate.

2. Equation (6.61) could be used to obtain $\Delta P_V^*(t)$ using

the results of a model which predicts R(t).

3. The equation of state could be used to determine the vapour pressure $P_v(t)$, using a specified bubble mass function M(t) and a known initial vapour pressure $P_v(0)$.

Although the first method is the easiest, it is the longest and the most costly since one has to try many pressure functions to generate a specified growth rate. However, the pressure function $\Delta P_v^*(t)$ may be known experimentally as in barbotage or sudden depressurization systems. The second method was also found to work successfully. Figures (6.7a) and (6.7b) show the results of the pressure function $\Delta P_v^*(t)$ and the growth relationship R(t) using the growth model of Mikic et al. [7] and equation (6.61). The third method, involving the use of the equation of state, will be discussed in more detail in Chapter 7. In the following sections, the analysis of the behaviour of the bubble and its surroundings will be analyzed using the Mikic et al. [7] model and the modified Rayleigh equation (6.61) to generate the pressure function $\Delta P_v^*(t)$, figure (6.7).

6.4.2 Bubble Shape

Figures (6.8) and (6.9) show the variation in bubble growth shape with time. Figure (6.8) shows the case where the free slip condition was assumed (this condition is usually acceptable for cell sizes bigger than the boundary layer thickness), and figure (6.9) shows the case of the no slip condition at the wall. From both figures one can see that the

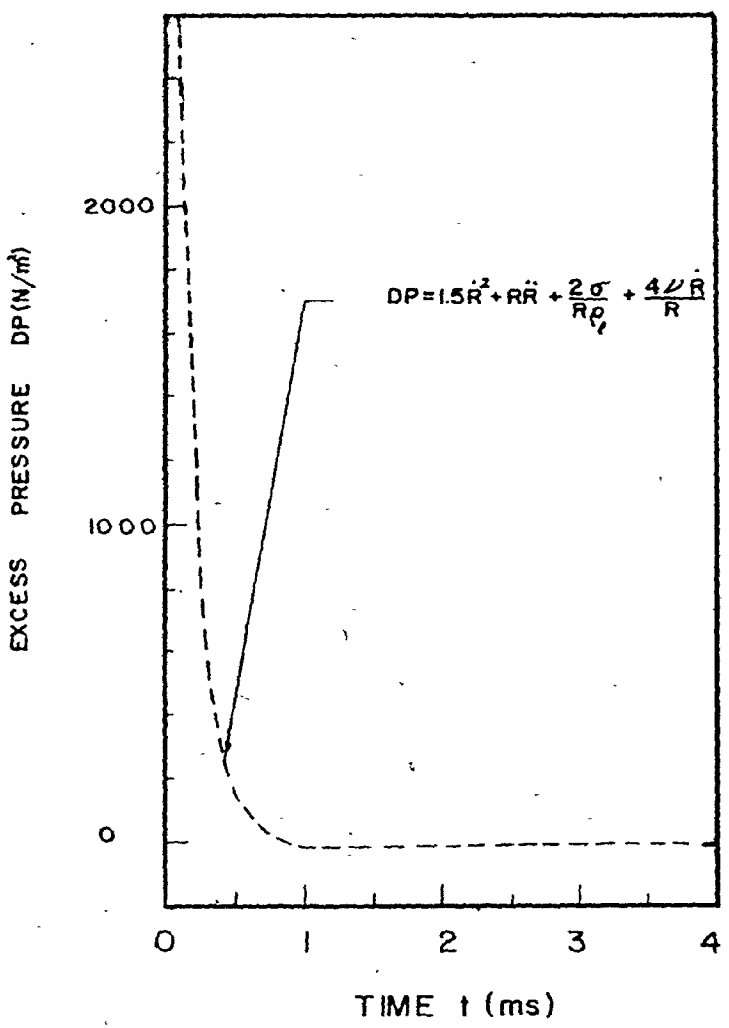

FIGURE (6.7a) PRESSURE FUNCTION OF MRG MODEL

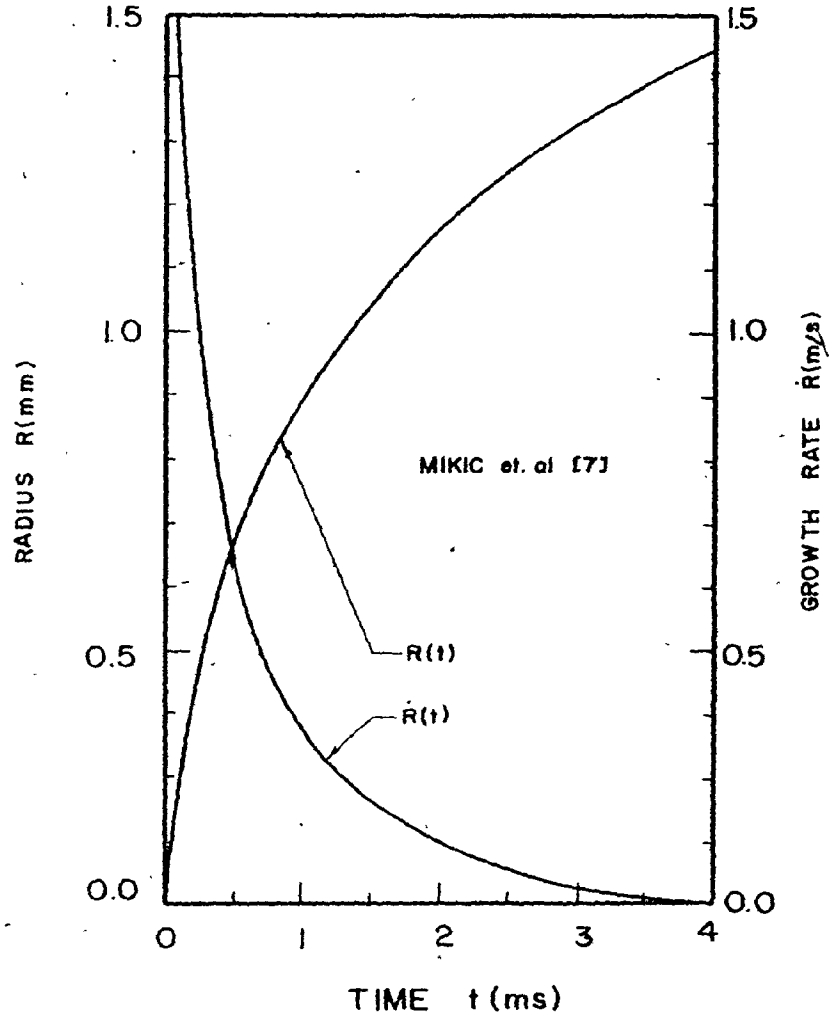

FIGURE (6.7b) GROWTH RATE OF MRG MODEL

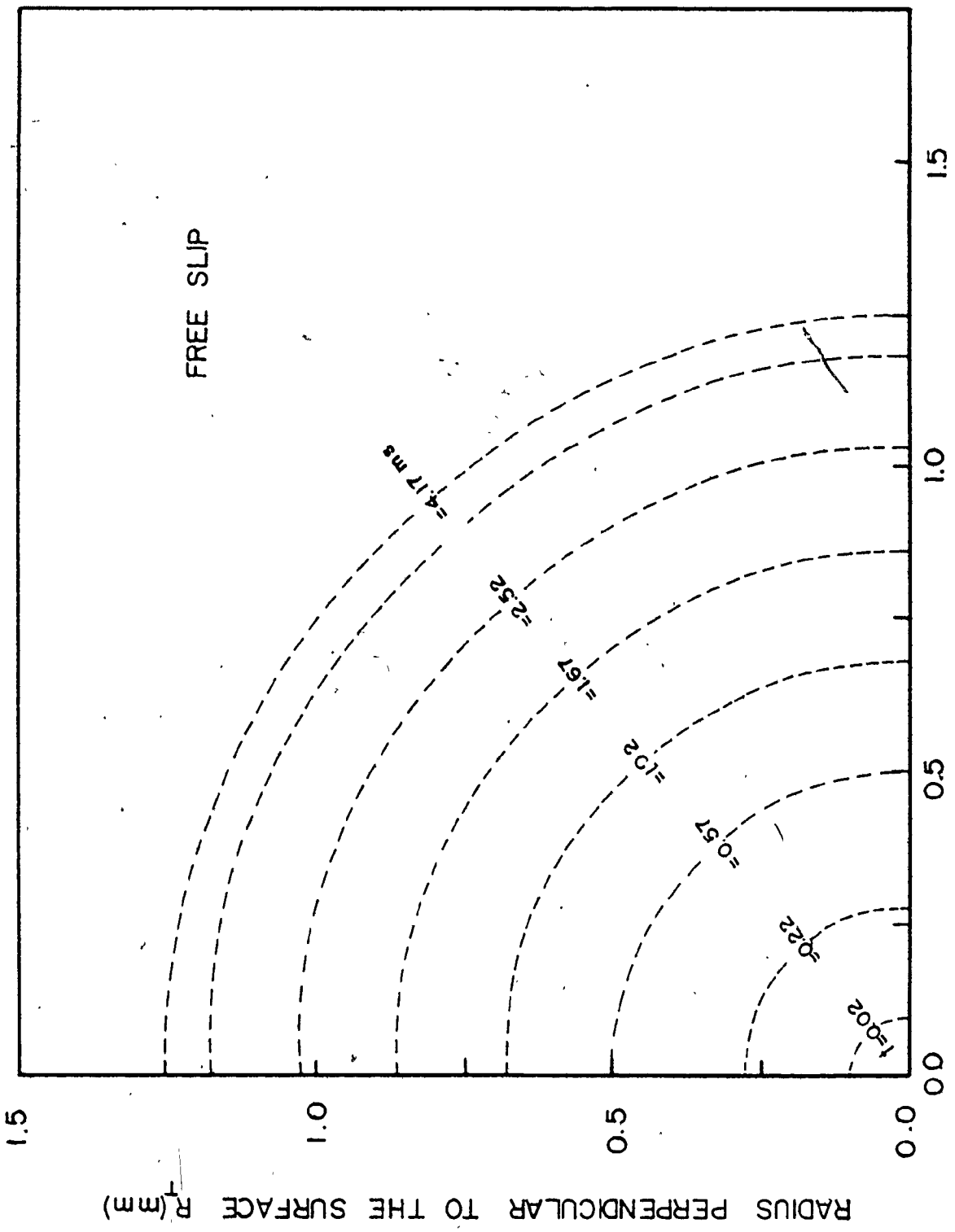

FIGURE (6.8) BUBBLE SHAPE (Free Slip)

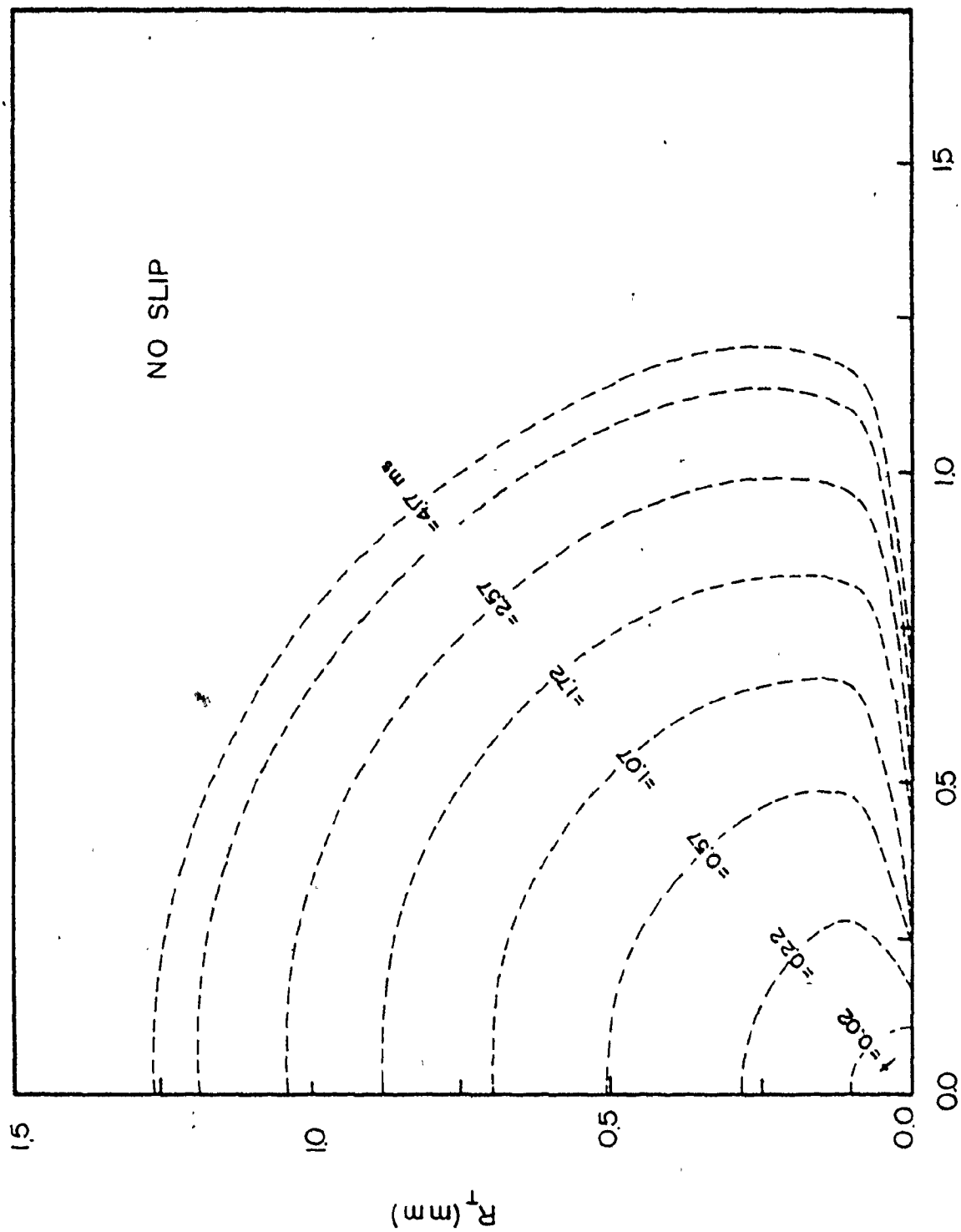

FIGURE (6.9) BUBBLE SHAPE (No Slip)

bubble grows as a hemisphere. The apparent movement of the markers in figure (6.9) at the wall is due to a numerical approximation since they should be fixed.

6.4.3 Velocity Field Around Growing Bubble

Figure (6.10) shows the dimensionless radial velocity component $u(r,y,t)/\dot{R}(t)$ against the dimensionless spatial coordinate $r/R(t)$ at the wall, for a bubble growing under the free slip condition. From the figure one can see that the radial velocity component is almost the same as that obtained analytically for potential flow velocity solution, i.e., $u = \dot{R}\, R^2/r^2$. The radial and axial velocity component distributions for the case of the non-slip condition are shown in figures (6.11) and (6.12) respectively.

6.4.4 Pressure Field Around a Growing Bubble

The pressure disturbance ΔP in the liquid outside the bubble wall ($\Delta P = P_\ell(r,t) - P_\infty$) which is associated with the bubble growth was calculated and shown in figure (6.13a) at various radial distances from the bubble center for up to 12.5 ms from the start of growth. From the figure one can observe that the pressure disturbance ΔP is associated with the vapour pressure $P_v(t)$ during the growth period t_g. The figure also shows the pressure disturbance ΔP which results when the bubble is left to grow with zero driving force ($\Delta P_v(t) = P_v(t) - P_\infty = 0$) after the initial impulse. During

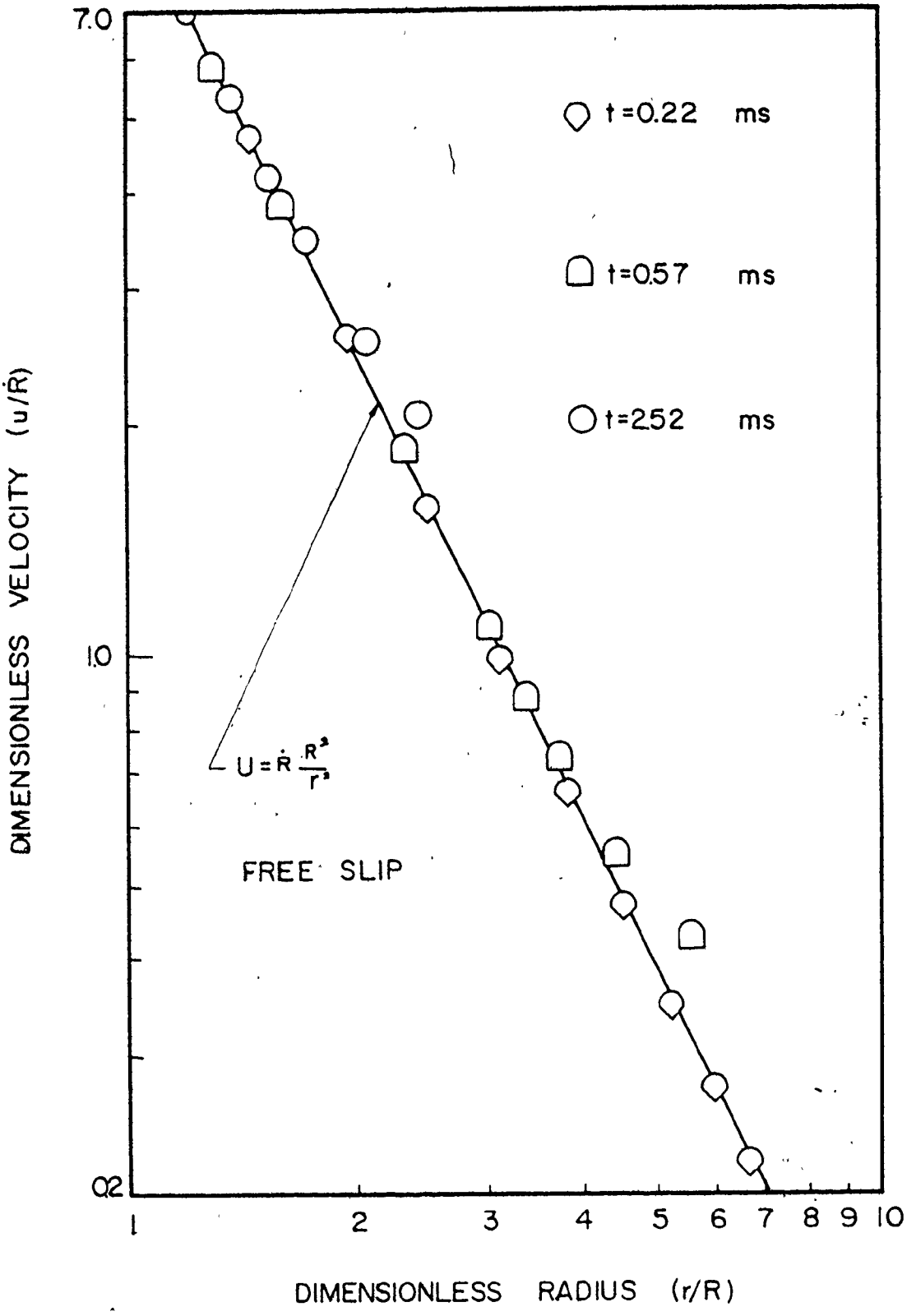

FIGURE(6.10) RADIAL VELOCITY AT THE WALL

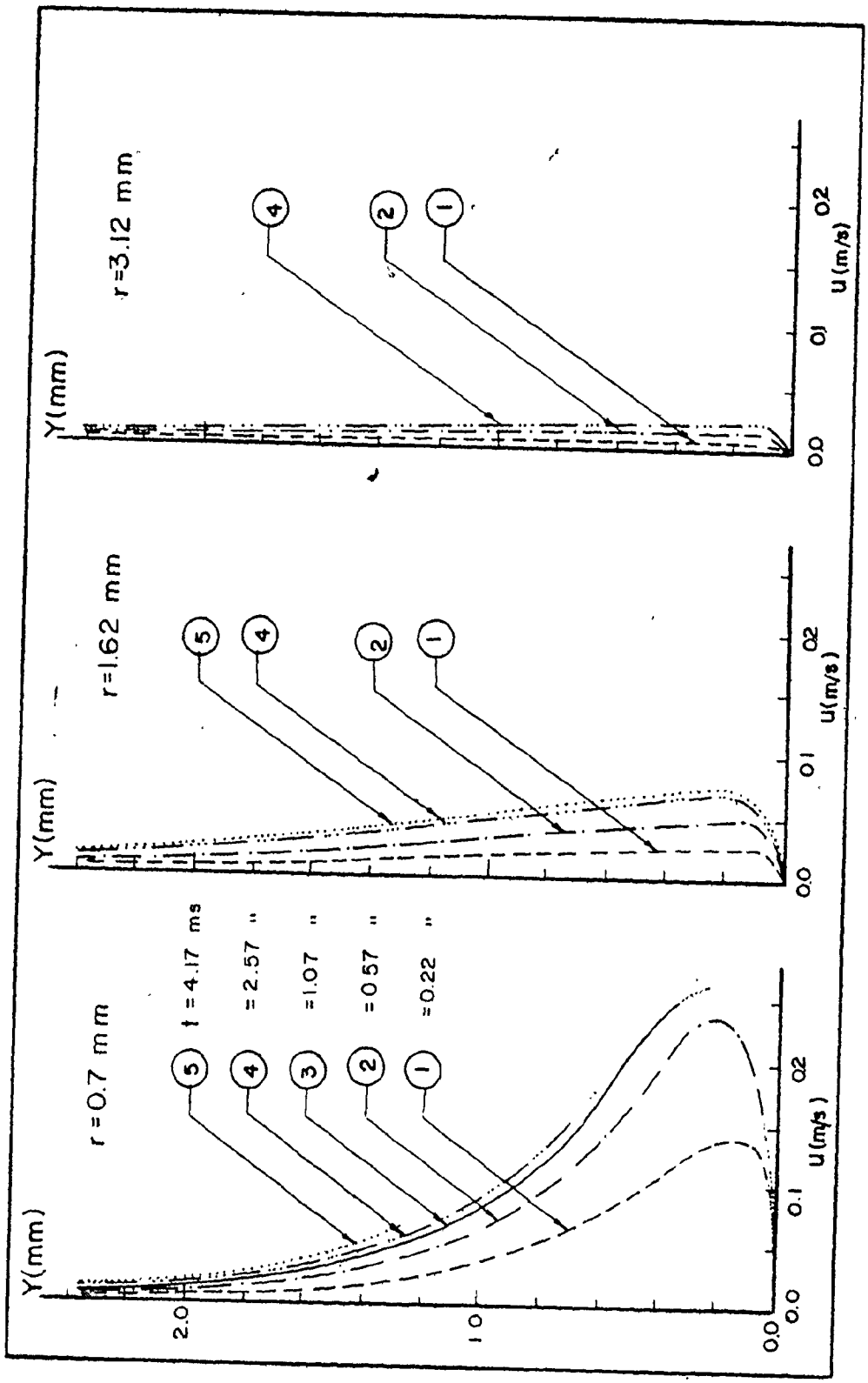

FIGURE (6.11) RADIAL VELOCITY DISTRIBUTION (No-Slip)

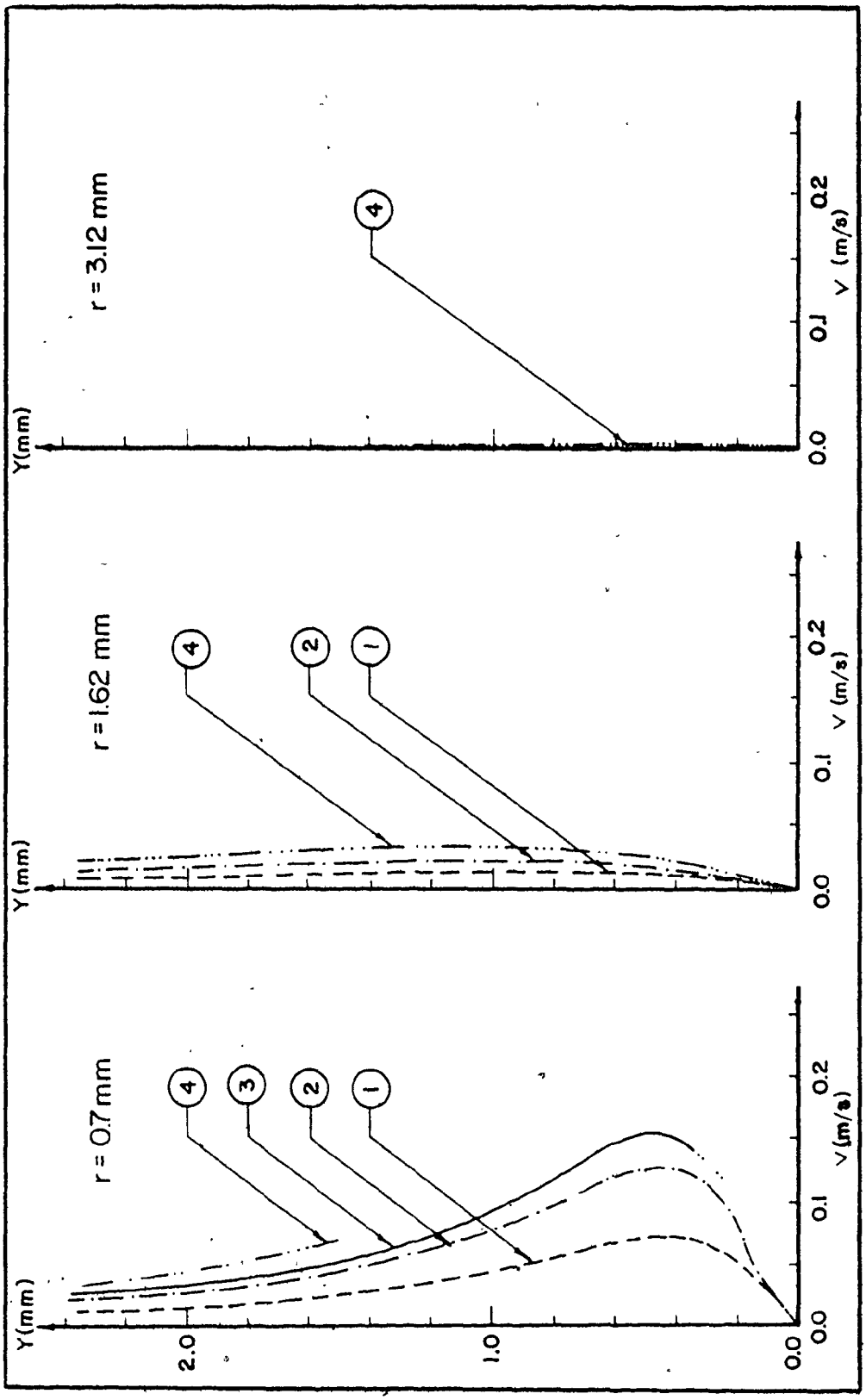

FIGURE (6.12) AXIAL VELOCITY DISTRIBUTION (No-Slip)

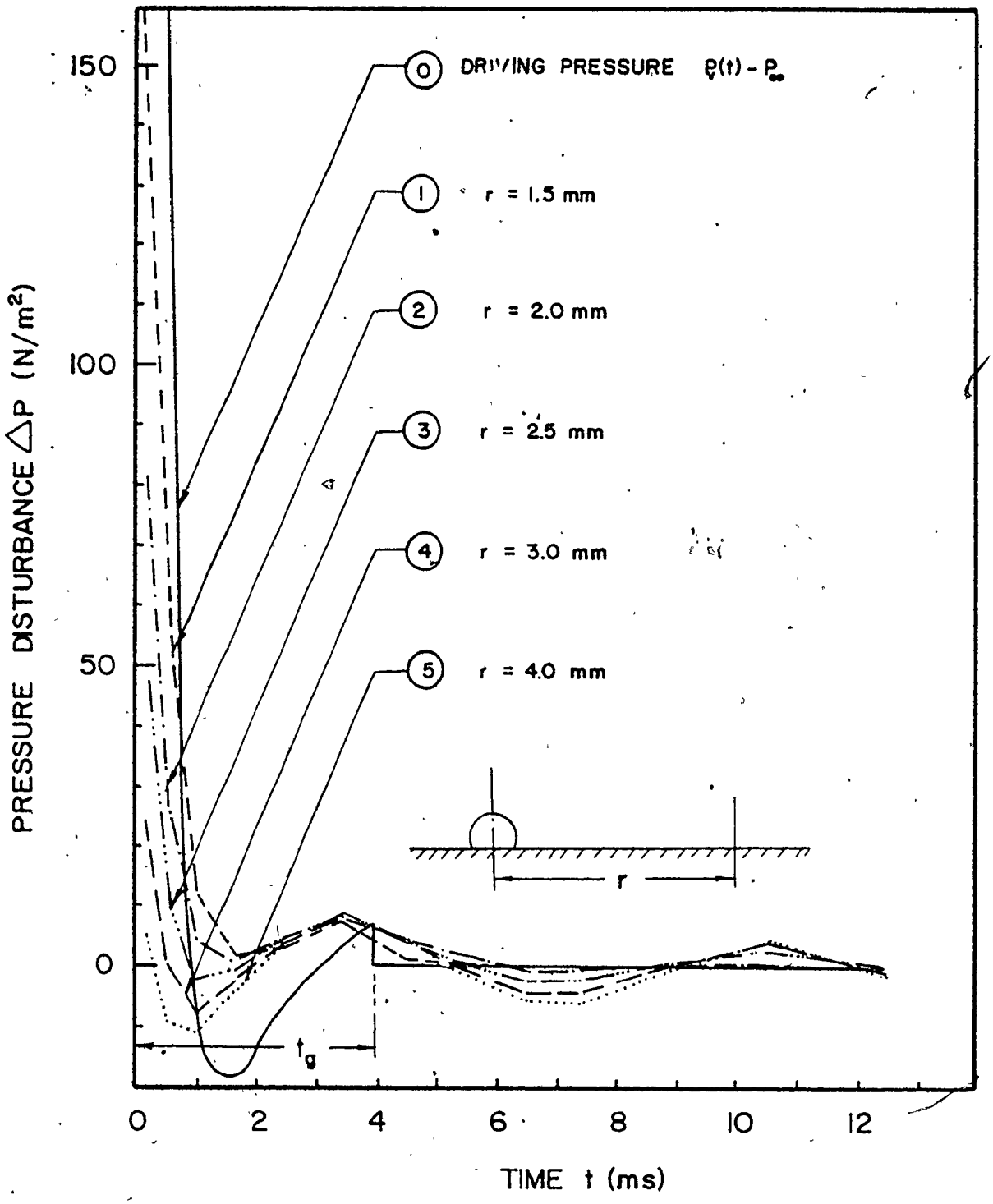

FIGURE (6.13 a) TEMPORAL PRESSURE VARIATION

this period it is observed that the pressure disturbance is composed of both positive and negative variations, oscillating around the system pressure P_∞. Figure (6.13b) shows the pressure distribution in the axial direction (perpendicular to the surface) at two different radial distances from the bubble center.

6.4.5 Temperature Field Around a Growing Bubble

A knowledge of the temperature field around a growing bubble is of great importance in order to calculate the heat transferred from the bubble surroundings to the bubble interior. This analysis can be used to calculate the amount of liquid evaporated at the bubble cap to add to or compare with that of the microlayer. Figure (6.14) depicts the temperature distribution in the radial direction at different heights from the heating surface. From the figure one can observe a peak just outside the bubble which is moving towards the surroundings with increasing amplitude. Whether this peak continues moving after bubble detachment or not depends on the direction of the flow after bubble detachment. The figure indicates also that the liquid temperature distribution in the axial direction (perpendicular to the surface) drops considerably within 1.0 to 1.5 mm. Liquid evaporation will occur in this region.

6.4.6 Evaporation from the Bubble Cap

Evaporation from the bubble cap is allowed if the

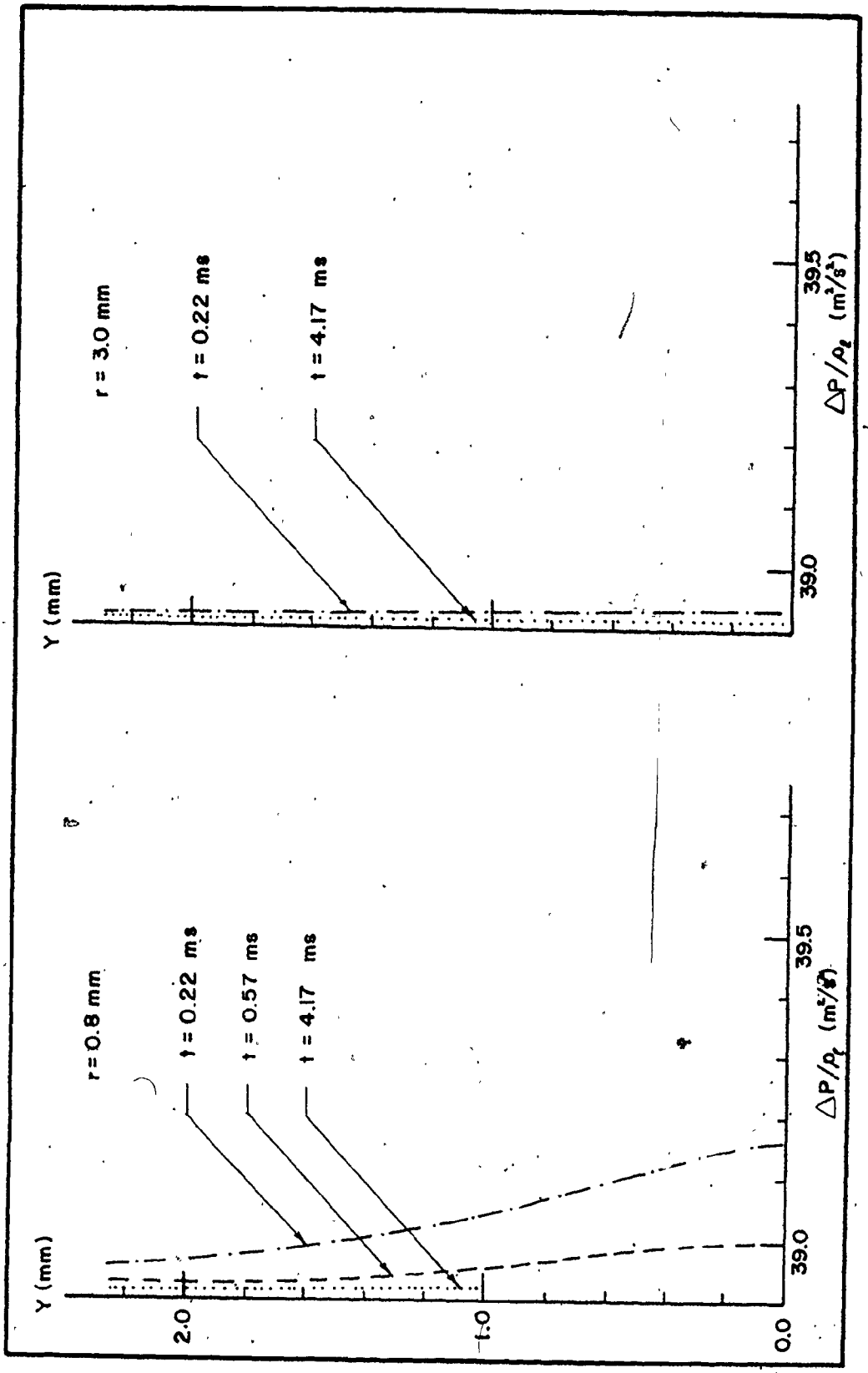

FIGURE (6.13b) SPATIAL PRESSURE VARIATION

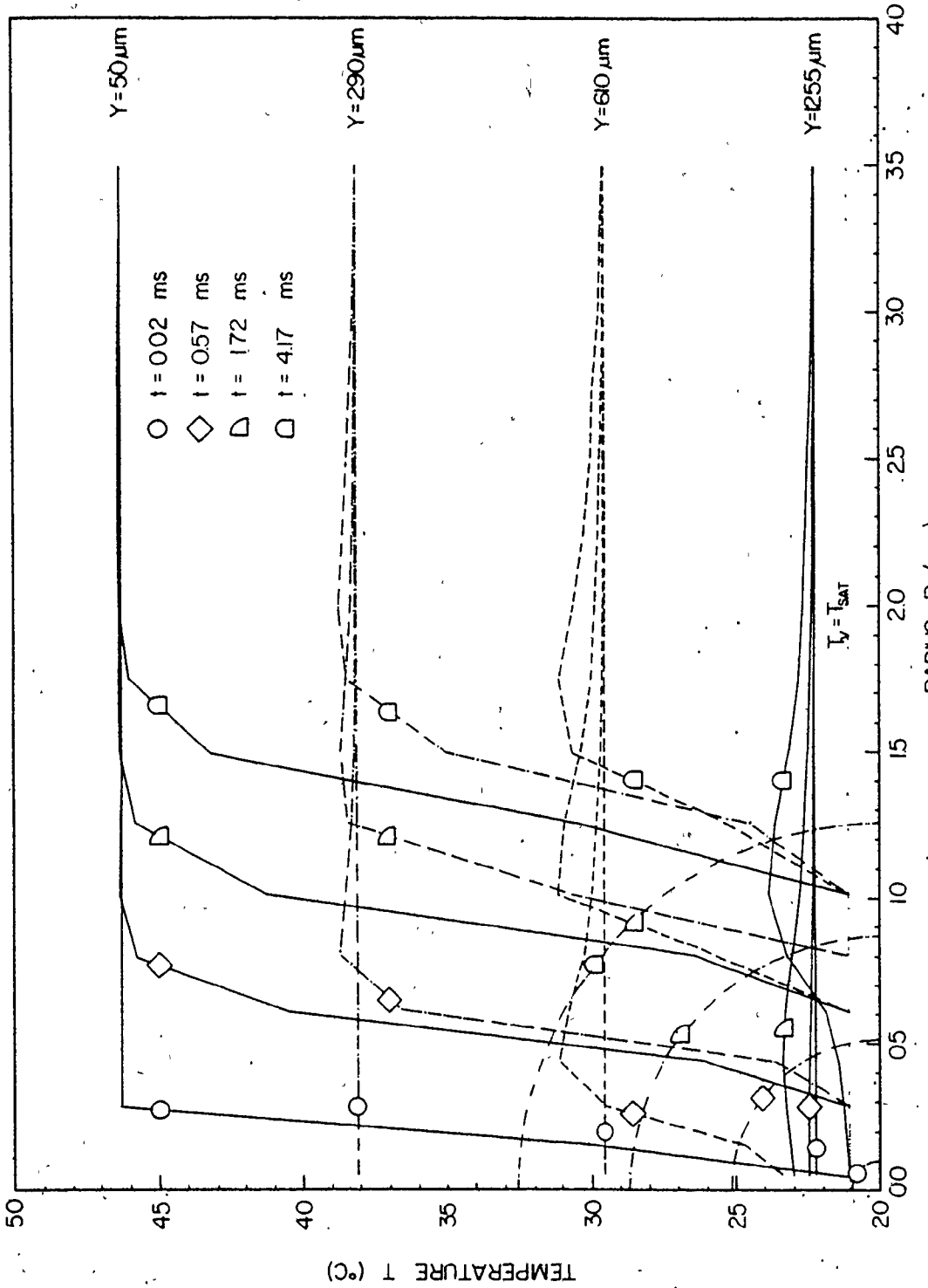

FIGURE (6.14) TEMPERATURE DISTRIBUTION IN THE LIQUID

liquid temperature adjacent to the bubble wall is higher than the vapour temperature T_v. Figure (6.15) shows the temporal variation in the liquid evaporated from the bubble cap $M_{cap}(t)$.

6.4.7 Effect of the Gravitational Field

Figure (6.16) presents a comparison of the bubble growth shape under zero gravitational field (the bubbles shown and discussed in the previous sections for the free slip wall) and at the normal gravitational ($g = 9.8\ m/s^2$) at different stages of bubble growth. The effect of the gravitational field on the bubble growth relationship R(t) is shown in figure (6.17).

6.4.8 Bubble Growth in a Confined Space

The growth of a bubble in a confined space as depicted in figure (6.18) is of some importance (for instance the narrow spaces found between the fuel rods in nuclear reactors). Figures (6.19) to (6.21) show the bubble shape for different distances D separating the two walls for a single vapour pressure function $P_v(t)$. From the figures one can observe the change of the hemispherical bubble shape to the oblate one when the separating distance decreases. The growth relationship in the two directions, parallel and perpendicular to the heating surface, decreases with decreasing distance D as shown in figures (6.22) and (6.23) respectively.

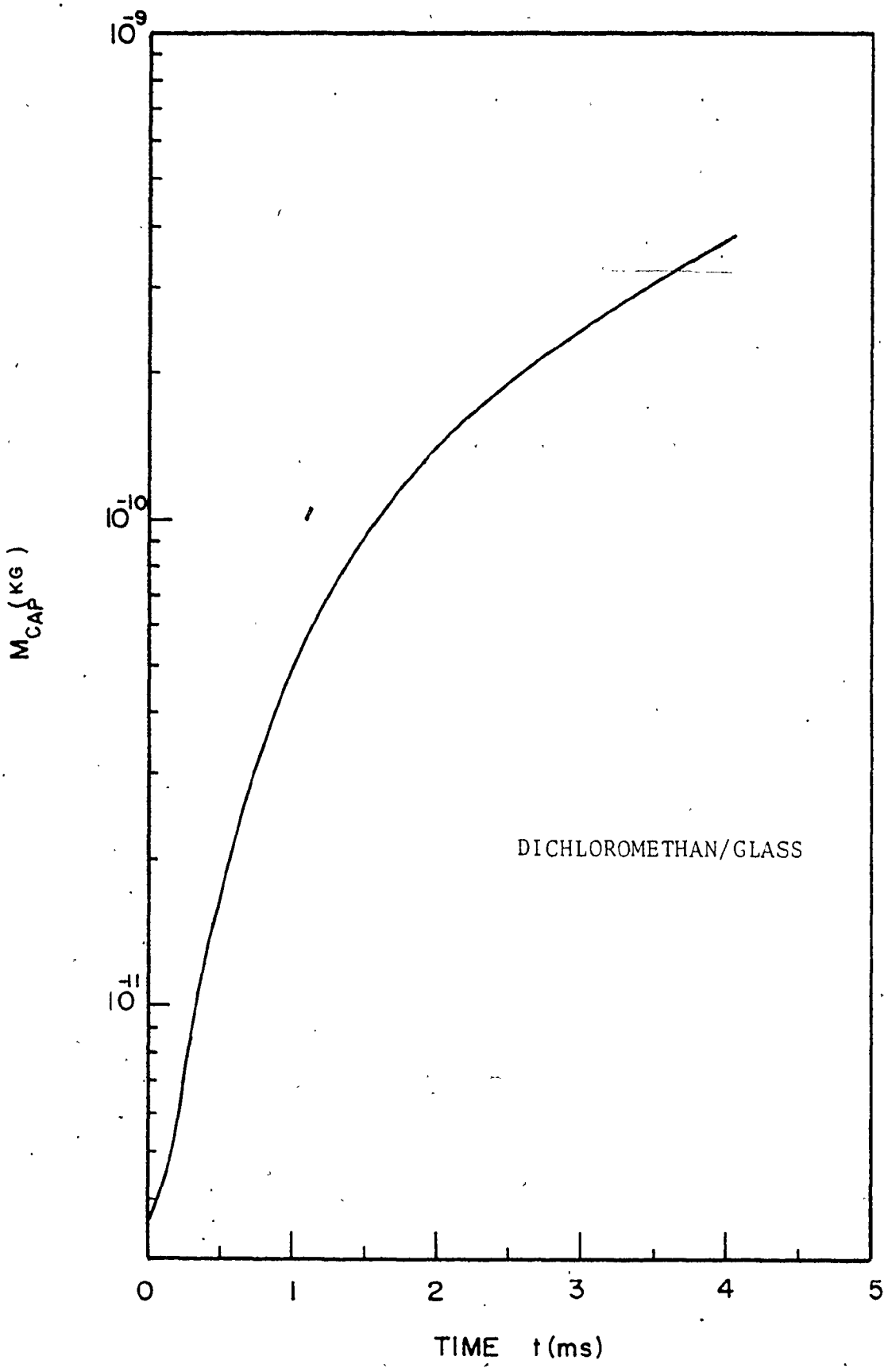

FIGURE (6.15) EVAPORATION FROM BUBBLE CAP

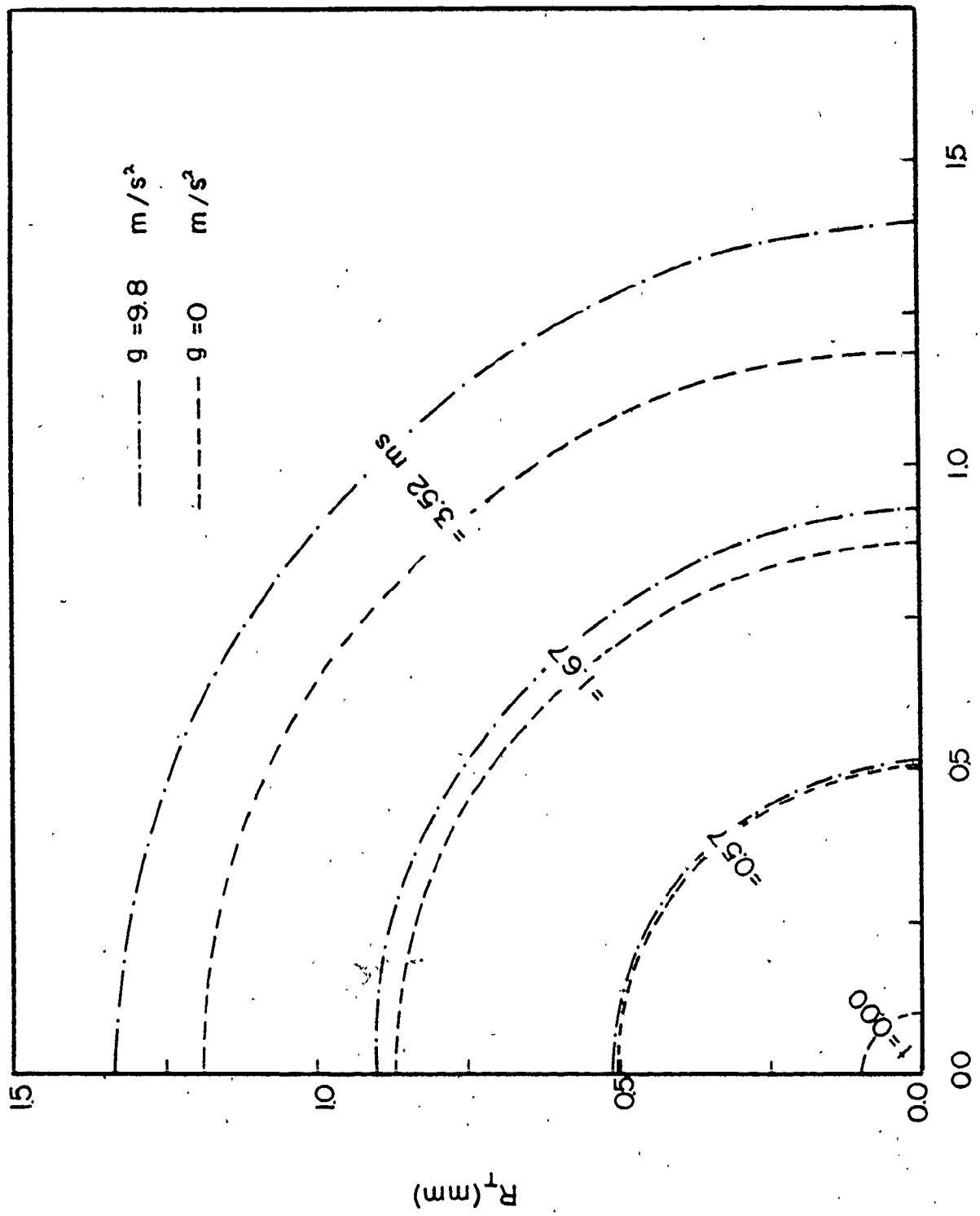

FIGURE (6.16) GRAVITATION FIELD INFLUENCE ON BUBBLE SHAPE

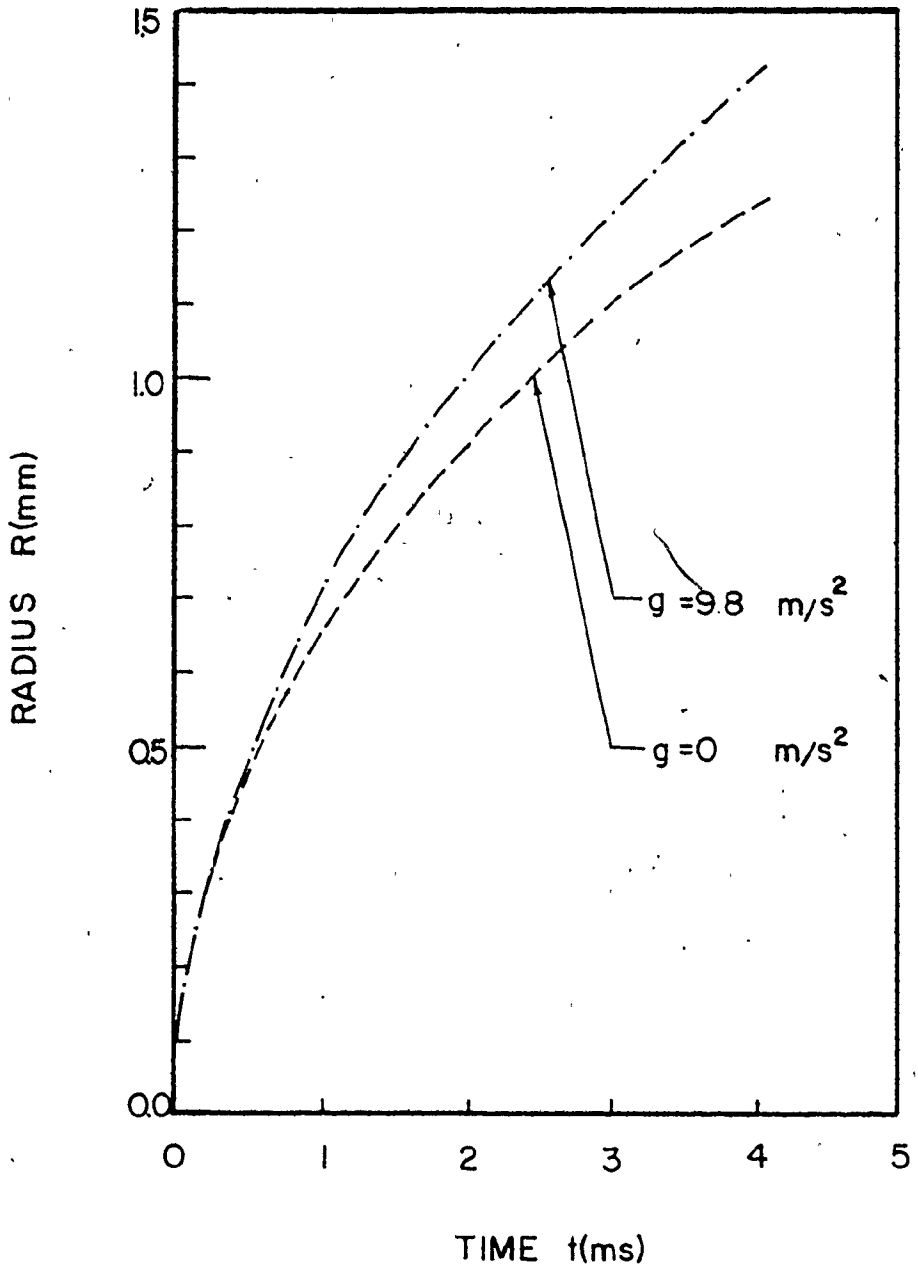

FIGURE(6.17) GRAVITATION FIELD INFLUENCE ON BUBBLE GROWTH

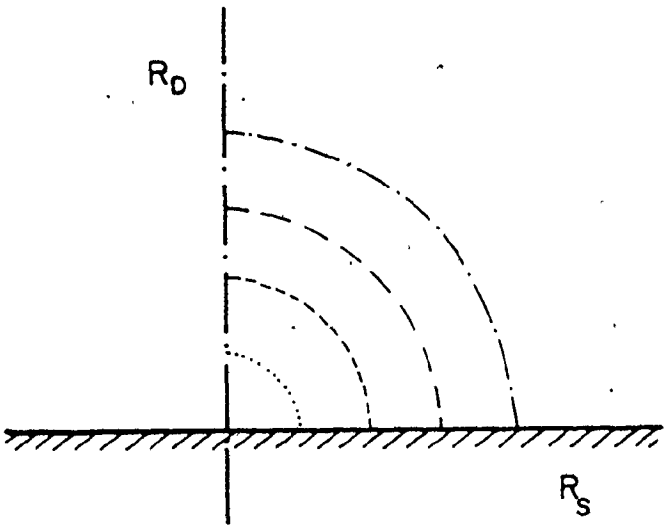

ISOLATED BUBBLE

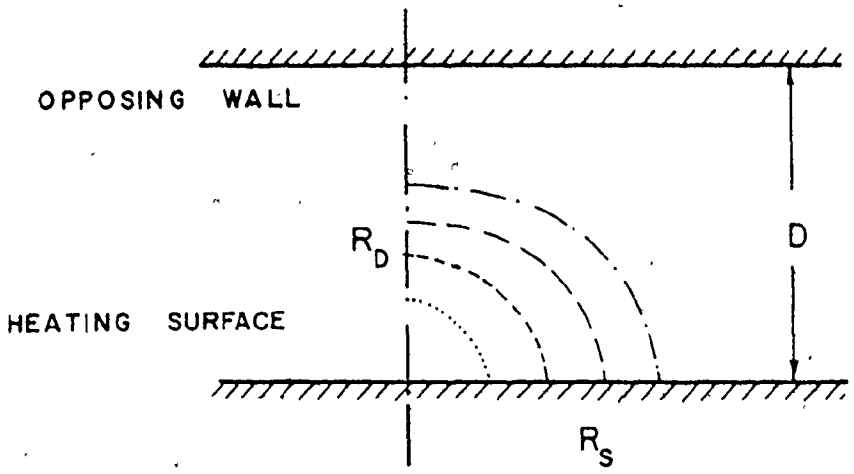

BUBBLE IN A CONFINED SPACE

FIGURE(6.18) BUBBLE GROWTH IN A CONFINED SPACE

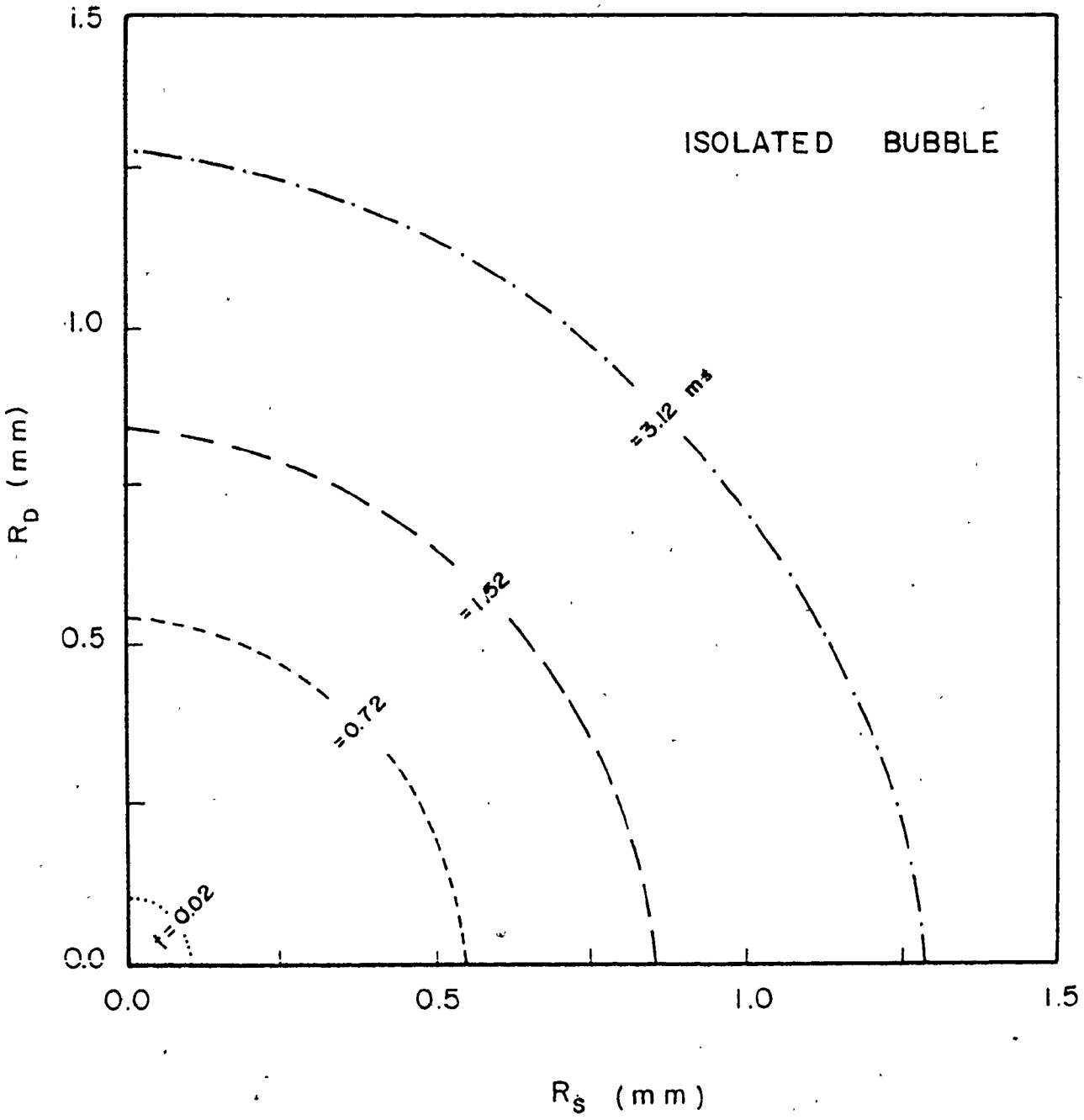

FIGURE(6.19) INVESTIGATION OF BUBBLE GROWTH IN A CONFINED SPACE

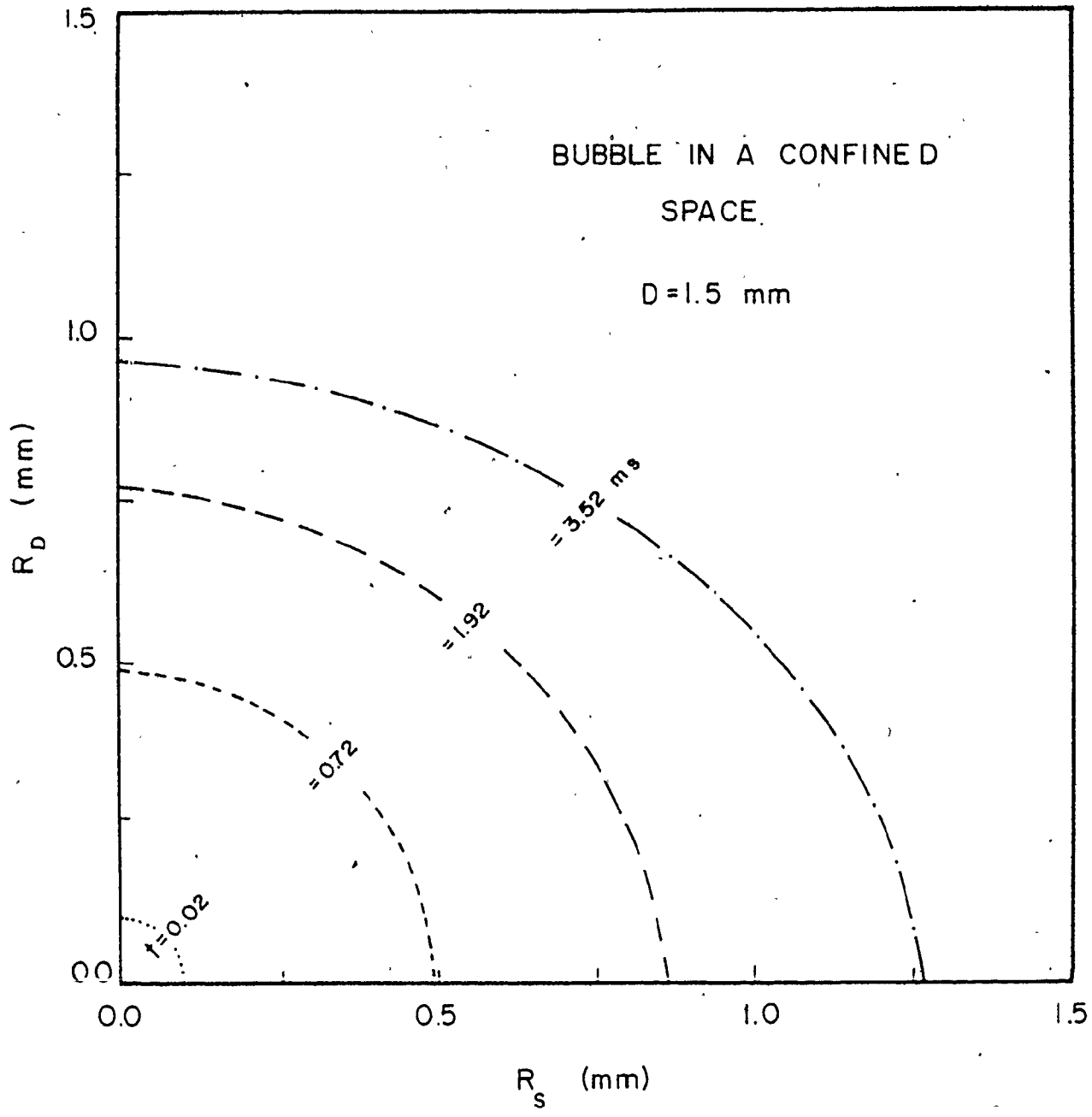

FIGURE (6.20) INVESTIGATION OF BUBBLE GROWTH IN A CONFINED SPACE

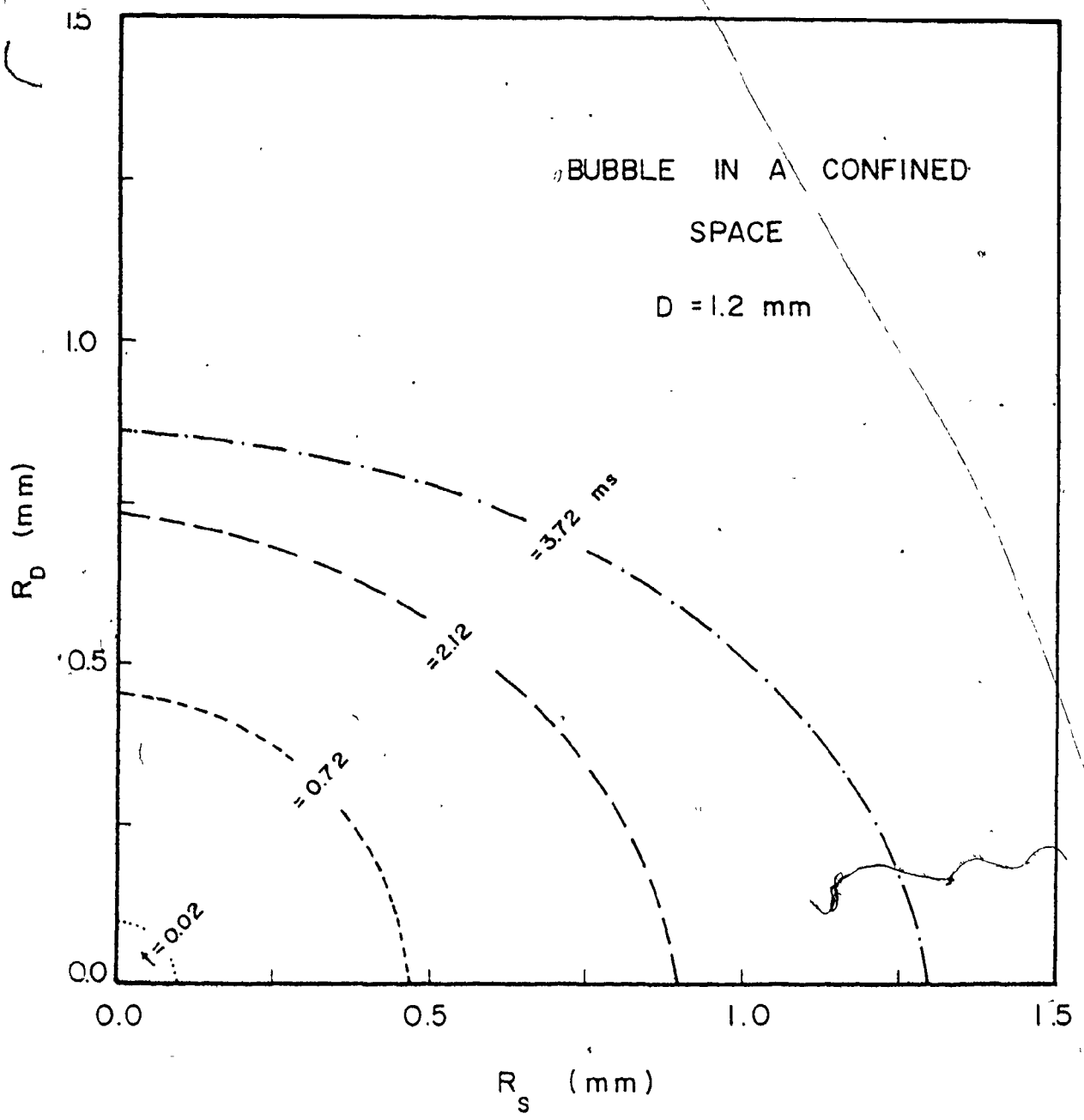

FIGURE(6.21) INVESTIGATION OF BUBBLE GROWTH IN A CONFINED SPACE

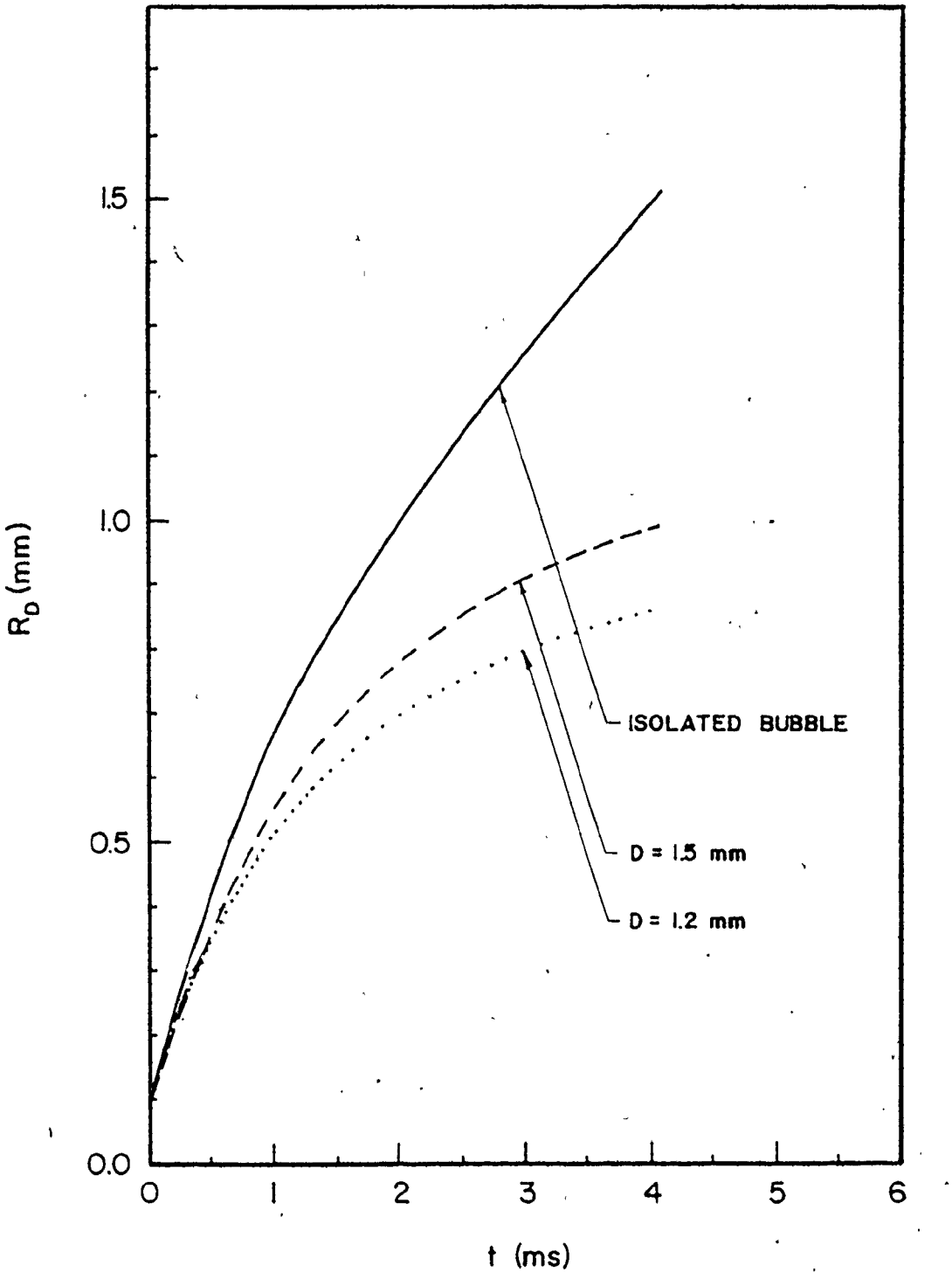

FIGURE (6.22) BUBBLE GROWTH RELATIONSHIP IN A CONFINED SPACE

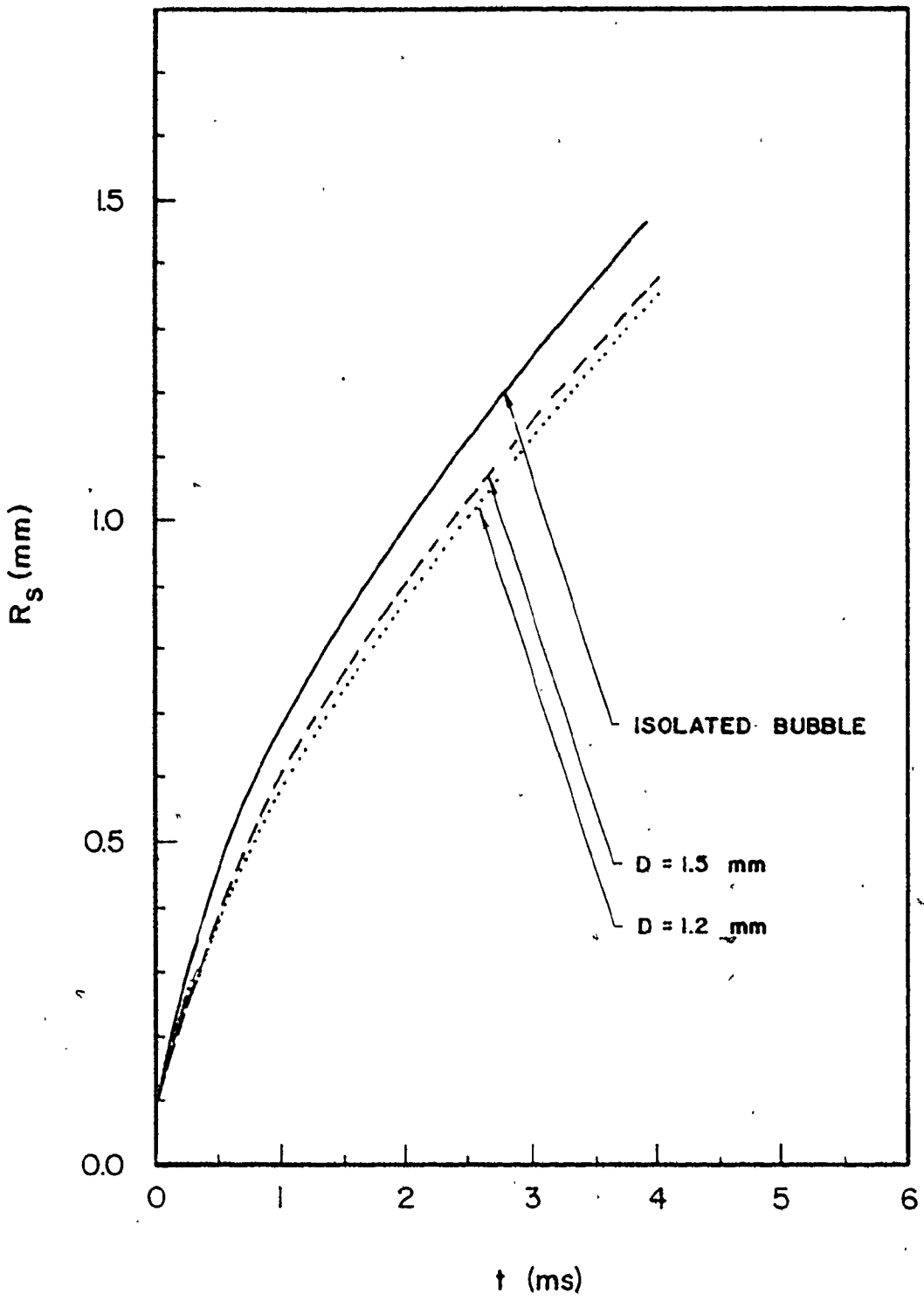

FIGURE(6.23) BUBBLE GROWTH RELATIONSHIP IN A CONFINED SPACE

6.5 Discussion of the Bubble Growth Results

The results presented in this chapter show that if one can provide the program with a vapour pressure function $P_v(t)$ or if a way of producing such a function as discussed in Section (6.4.1) could be found, the program is capable of predicting the parameters needed for characterizing the bubble growth phenomenon. Figures (6.8) and (6.9) showed that a hemispherical nucleus grows as a hemisphere. The effect of the surface tension may cause the bubble base to deform towards the spherical shape, assisting the bubble detachment as discussed by Madhavan and Mesler [11]. The agreement between the present results for the radial velocity component and that obtained analytically from the potential flow solution, in reference to figure (6.10), supports the validity of the method used and the parameters chosen. From the results of the pressure variation in the liquid shown in figure (6.13a) one might conclude in agreement with Schmidt et al. [14] that the pressure variation ΔP ($\Delta P = P_\ell(r,t) - P_\infty$) is primarily associated with the initial growth of the bubble and is comprised of both positive and negative components. The temperature distribution shown in figure (6.14) shows a peak, just outside the bubble wall, which is moving towards the surroundings with increasing amplitude. This observation agrees with the experimental measurements by Beer et al. [13] whose results are reproduced in figure (6.24). The presence of this moving peak may partially support the "enthalpy transport mechanism" during which the growing bubble is

Figure (6.24) Interference Fringe Pattern Abstracted from Reference [31].

responsible for displacing the hot liquid layer, which grew during the waiting period, and pushing its enthalpy content towards the bulk liquid. On the other hand, the temperature field results indicate that the bubble grows in a non-isothermal region and accordingly the bubble interface may be subject to a temperature gradient which in turn causes a surface tension gradient along the bubble wall. Such a surface tension gradient initiates a fluid motion along the interface causing microconvective currents, known as the "Marangoni effect". Evaporation of the liquid adjacent to the bubble occurs in the superheated region close to the heating surface. A comparison between the mass evaporated from the bubble cap, depicted in figure (6.15), M_{cap}, and the mass evaporated from the microlayer, depicted in figure (5.7), M_{ML} is shown in figure (6.25) which indicates that the mass evaporated from the microlayer exceeds the mass evaporated from the bubble cap by an order of magnitude. The gravitational field showed no significant effect on the bubble shape as depicted in figure (6.16) which agrees with the results of Madhavan and Mesler [11]. The results presented for the bubble growth in a confined space indicate the change of the bubble shape from the hemispherical to oblate with a slower growth rate for the same vapour pressure function $P_v(t)$. Considering the forces responsible for the bubble detachment one can see that both buoyancy and inertia forces will decrease due to the decrease in both bubble volume and bubble growth rate respectively. As a consequence this may delay the

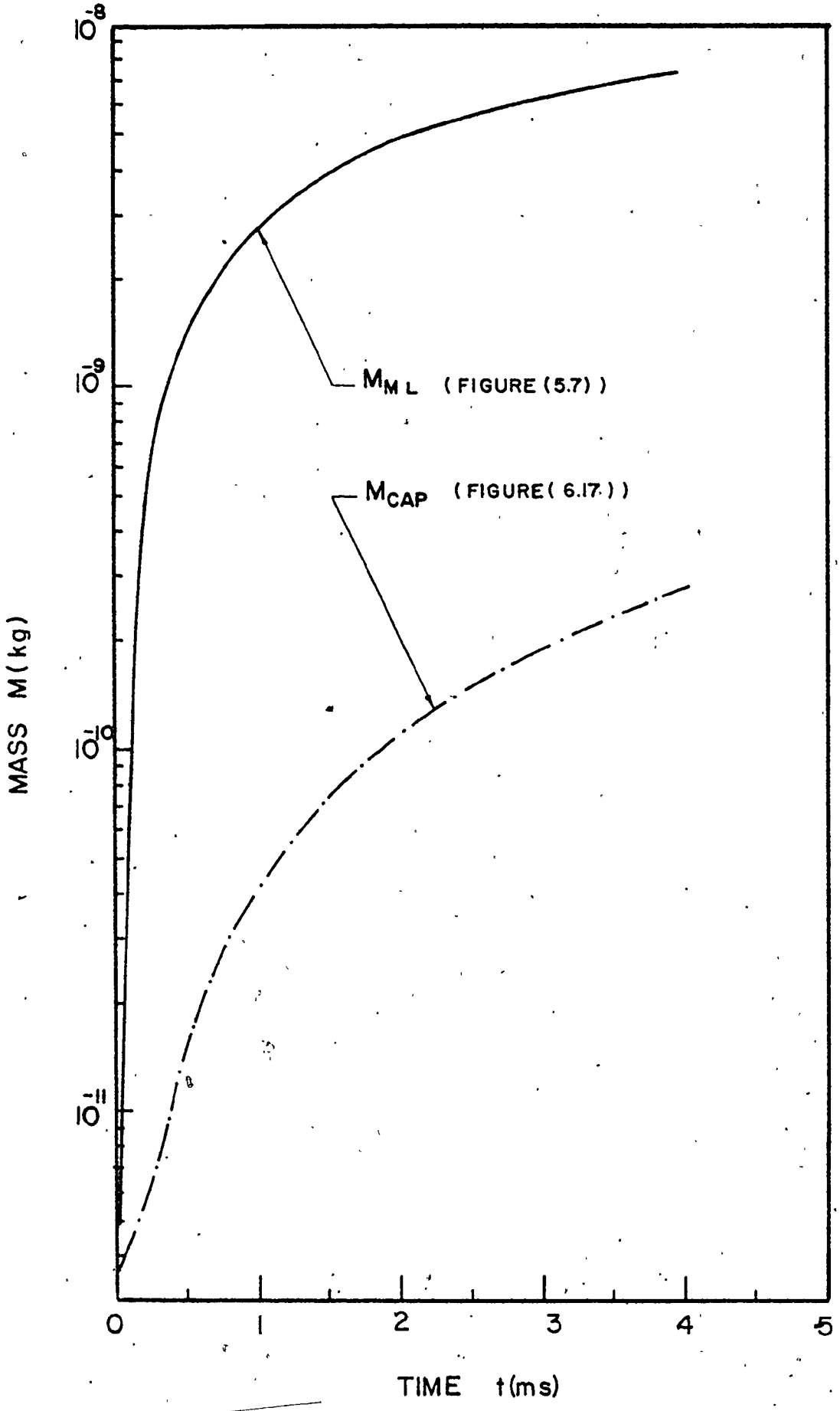
10^{-8}
10^{-9}
10^{-10}
10^{-11}
MASS M(kg)
M_{ML} (FIGURE (5.7))
M_{CAP} (FIGURE (6.17))
0
1
2
3
4
5
TIME t(ms)

bubble detachment from the heating surface. This in turn, will allow for longer existence of the dry area under the bubble which increases the possibility of overheating of the heating surface which may cause local melting at high heat flux.

CHAPTER 7

MICROLAYER EVAPORATION AND BUBBLE GROWTH

7.1 Introduction

In this chapter, the bubble growth behaviour will be discussed assuming that the mass transfer component of energy exchange across the liquid-vapour interface is the predominant mechanism causing the bubble to grow. Utilizing the results obtained from Chapter 5 for the mass contributed by the microlayer evaporation $M_{ML}(t)$ and those obtained from Chapter 6 for the mass contributed from the bubble cap $M_{CAP}(t)$, one can determine the bubble mass as a function of time $M_B(t) = M_{ML}(t) + M_{CAP}(t)$. Assuming the vapour inside the bubble to be uniform in both temperature and density and obeying the equation of state, the vapour pressure due to mass transfer can be calculated as:

$$\frac{P_v(t_2)}{P_v(t_1)} = \frac{M_B(t_2)}{M_B(t_1)} \cdot \frac{V_B(t_1)}{V_B(t_2)} \cdot \frac{T_v(t_2)}{T_v(t_1)} \qquad (7.1)$$

If it is assumed that $T_v(t_2) = T_v(t_1) = T_v$ = constant, equation (7.1) will reduce to:

$$\frac{P_v(t_2)}{P_v(t_1)} = \frac{M_B(t_2)}{M_B(t_1)} \cdot \frac{V_B(t_1)}{V_B(t_2)} \qquad (7.2)$$

For a known (or assumed) initial vapour pressure $P_v(0)$, the temporal vapour pressure function $P_v(t)$ and accordingly the driving pressure function $\Delta P_v(t) = P_v(t) - P_\infty$ can

be determined.

7.2 Mass Transfer and Bubble Growth

As a first attempt to investigate the capabilities of the program using mass transfer as the dominant controlling mechanism, an arbitrarily specified time dependent mass function $M_B(t)$ was supplied to the program described in Chapter 6 with different initial vapour pressure and time steps. Figure (7.1) shows some relationships obtained for R(t) and Figure (7.2) shows the resultant vapour pressure variation $P_V^*(t) = P_V(t)/\rho_\ell$. From figure (7.2) one can observe vapour pressure oscillations during the growth with higher amplitude in the initial growth period and a mean value which approaches the system pressure P_∞ as time goes on. This oscillation phenomenon can be simply explained as follows; for a slow growing bubble the mass supplied will be at a higher rate than the bubble volume expansion rate. According to equation (7.2), this will cause the vapour pressure to increase. Increasing the vapour pressure $P_V(t)$ causes the bubble growth rate to increase and the volume expansion rate will be higher than the mass rate supplied. Accordingly the vapour pressure $P_V(t)$ will decrease and so on. The oscillation of the vapour pressure is accompanied by an oscillation in the bubble growth rate $\dot{R}(t)$. Similar oscillations during vapour bubble growth were also observed experimentally by Zijl and Van Stralen [46]. A physical explanation advanced

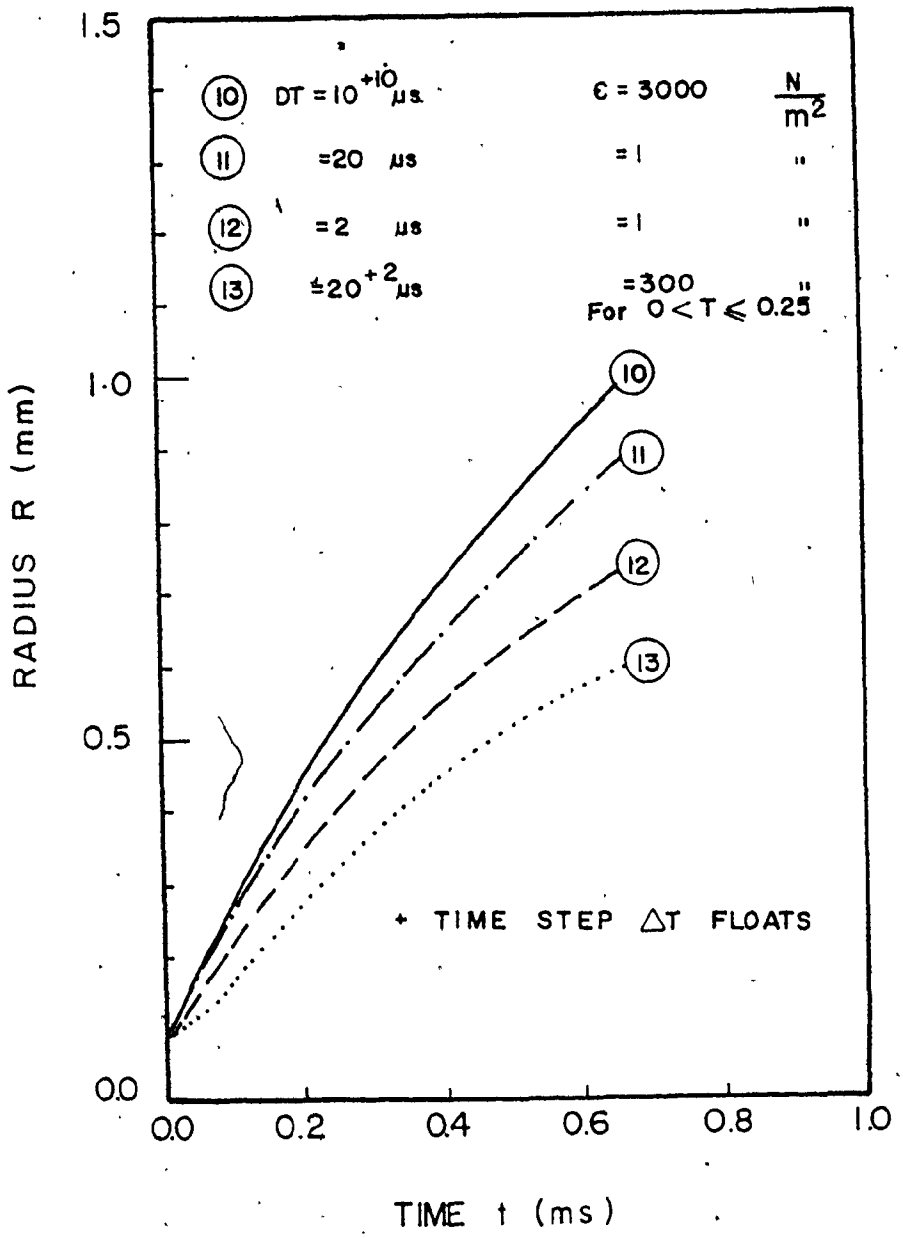

FIGURE (7.1) BUBBLE GROWTH RELATIONSHIP UNDER THE INFLUENCE OF MASS TRANSFER

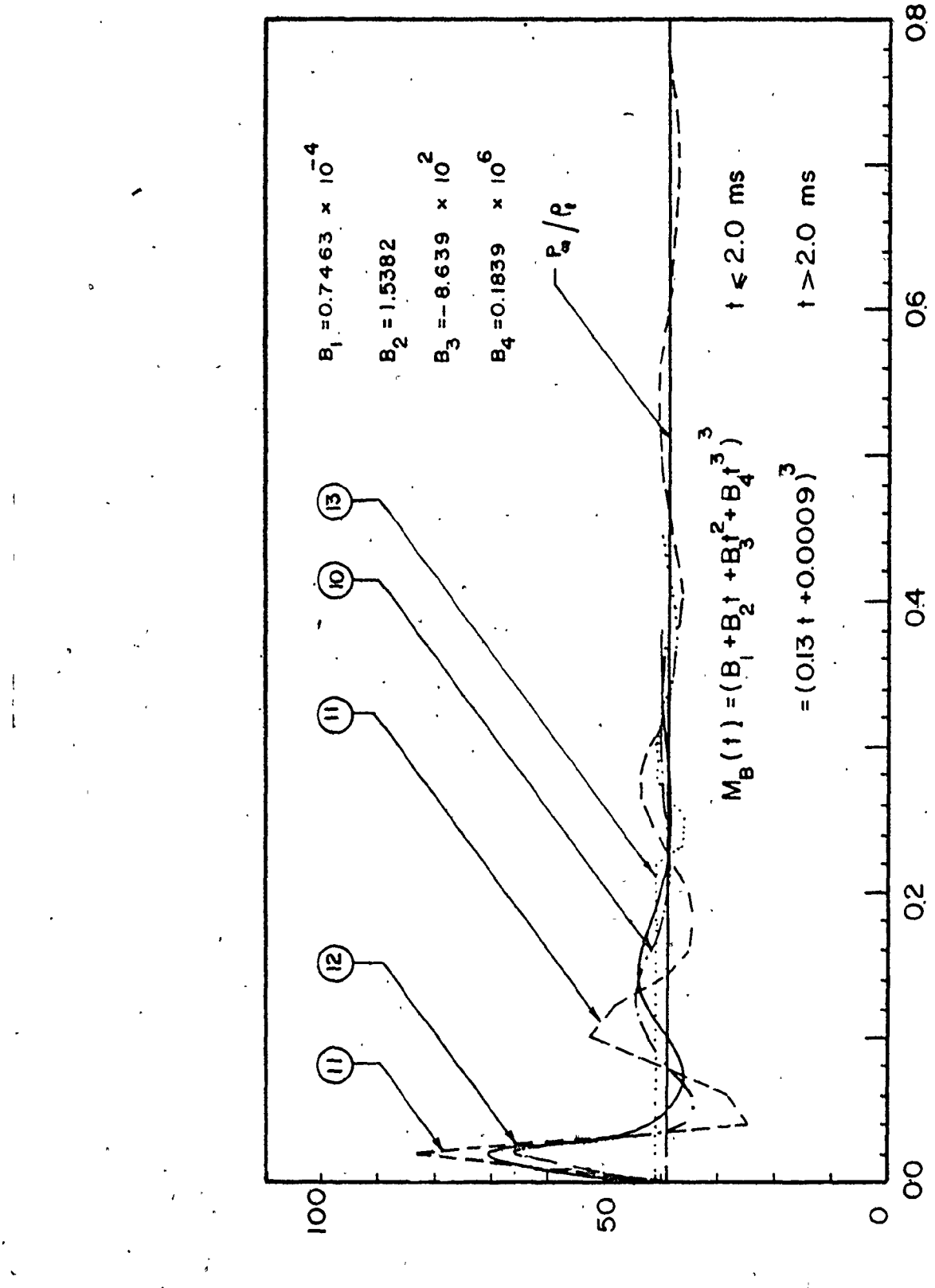

FIGURE (7.2) VAPOUR PRESSUR VARIATION

by Van Stralen claimed that during the initial growth, the bubble wall superheat decreases due to the requirement of the latent heat of vapourization. The vapour pressure difference $\Delta P_v(t)$ decreases (and may become negative) and therefore the bubble growth rate decreases (and may become zero or even negative). During the period of slow growth, more heat is supplied so that the vapour pressure increases again and the cycle repeats itself. The oscillation period was found to increase rapidly with decreasing system pressure. At higher system pressures, fast oscillations occur although bubble growth is then mainly determined by heat diffusion. The bubble oscillation damps out due to viscosity effects [41]. It has also been shown by Van Stralen, Zijl and De Vries [47], using the theory of fractional derivatives, that both the volume and the temperature of free vapour bubbles may oscillate during growth. The nature of these oscillations originates from combined liquid inertia and transient heat conduction, which causes the changes in liquid velocity to lag behind changes in excess pressure. Similar observations of the bubble volume oscillations have been presented in the theoretical study of the bubble growth in combined gravitational and nonuniform temperature fields on a horizontal surface by Joosten et al. [48].

More discussion of the oscillation phenomenon will be presented in Section 7.5.

7.3 Microlayer Evaporation and Bubble Growth

In this section the two programs discussed in Chapter 5 for the microlayer evaporation and in Chapter 6 for the bubble growth respectively are combined in order to produce a bubble growth model in which the microlayer evaporation and the evaporation from the bubble cap are incorporated. With reference to figure (7.3), at any time t during the growth period, the incremental mass evaporated from the microlayer ΔM_{ML} can be evaluated using subroutine BASE (Subroutine BASE represents the main program for the microlayer evaporation discussed in Chapter 5) and the incremental mass evaporated from the bubble cap ΔM_{CAP} can be evaluated using subroutine CAP (Subroutine CAP represents the main program for the bubble growth discussed in Chapter 6). The incremental bubble mass $\Delta M_B = \Delta M_{ML} + \Delta M_{CAP}$ will be used to evaluate the vapour pressure $P_v(t)$ using equation (7.2) for an assumed initial vapour pressure $P_v(0)$. The calculation of the vapour pressure is included in subroutine CAP. It should be noted that in this program, the bubble cap will grow on a heating surface considered as a free-slip boundary, and the growth rate $\dot{R}(t)$ needed for the microlayer formation and evaporation program (Subroutine BASE) is used as the radial velocity component of the first cap marker near the free slip boundary as depicted in figure (7.3). Figure (7.4) shows a flow chart for the combined main program.

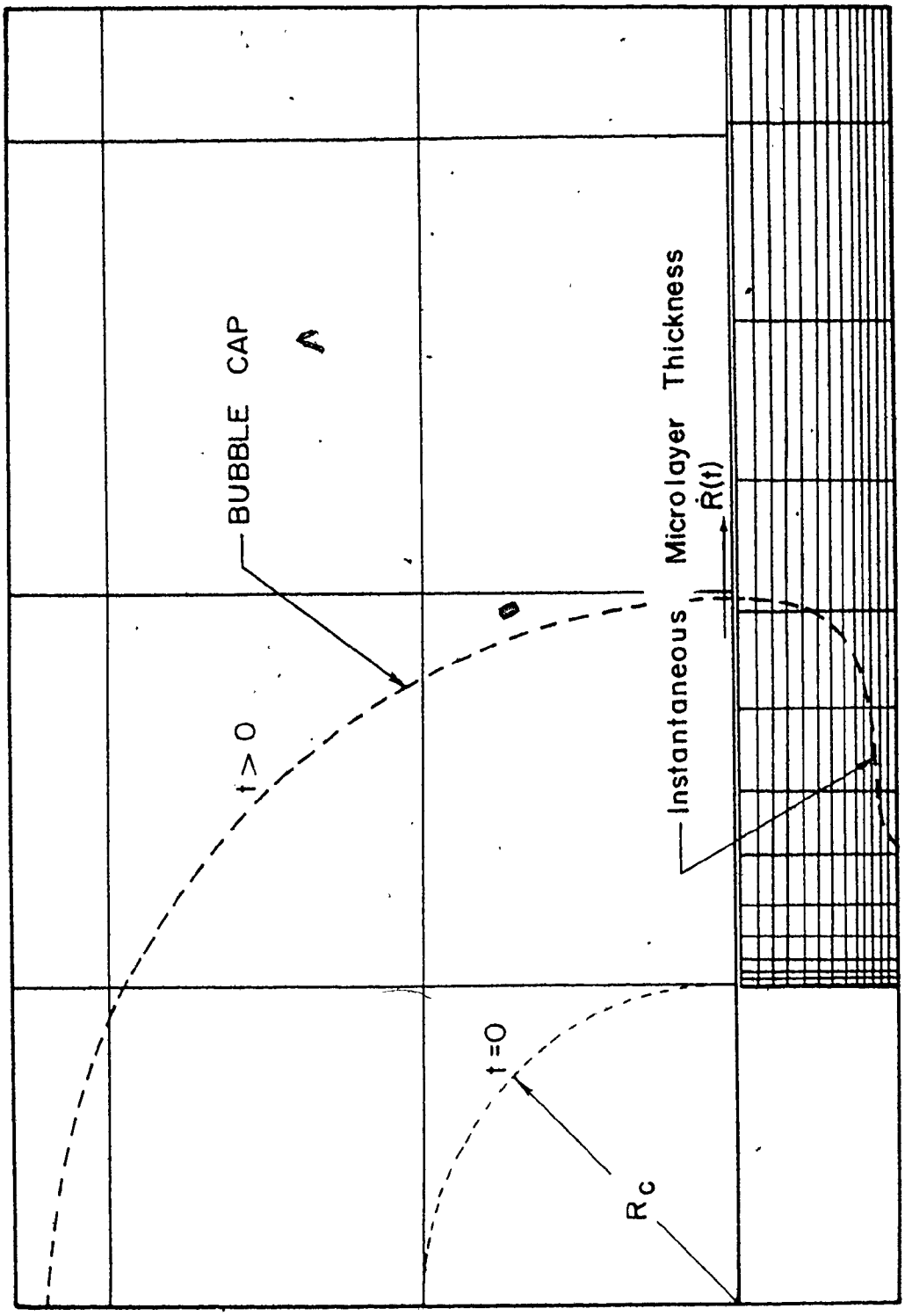

FIGURE (7.3) MICROLAYER EVAPORATION AND BUBBLE GROWTH
(Computation Representation)

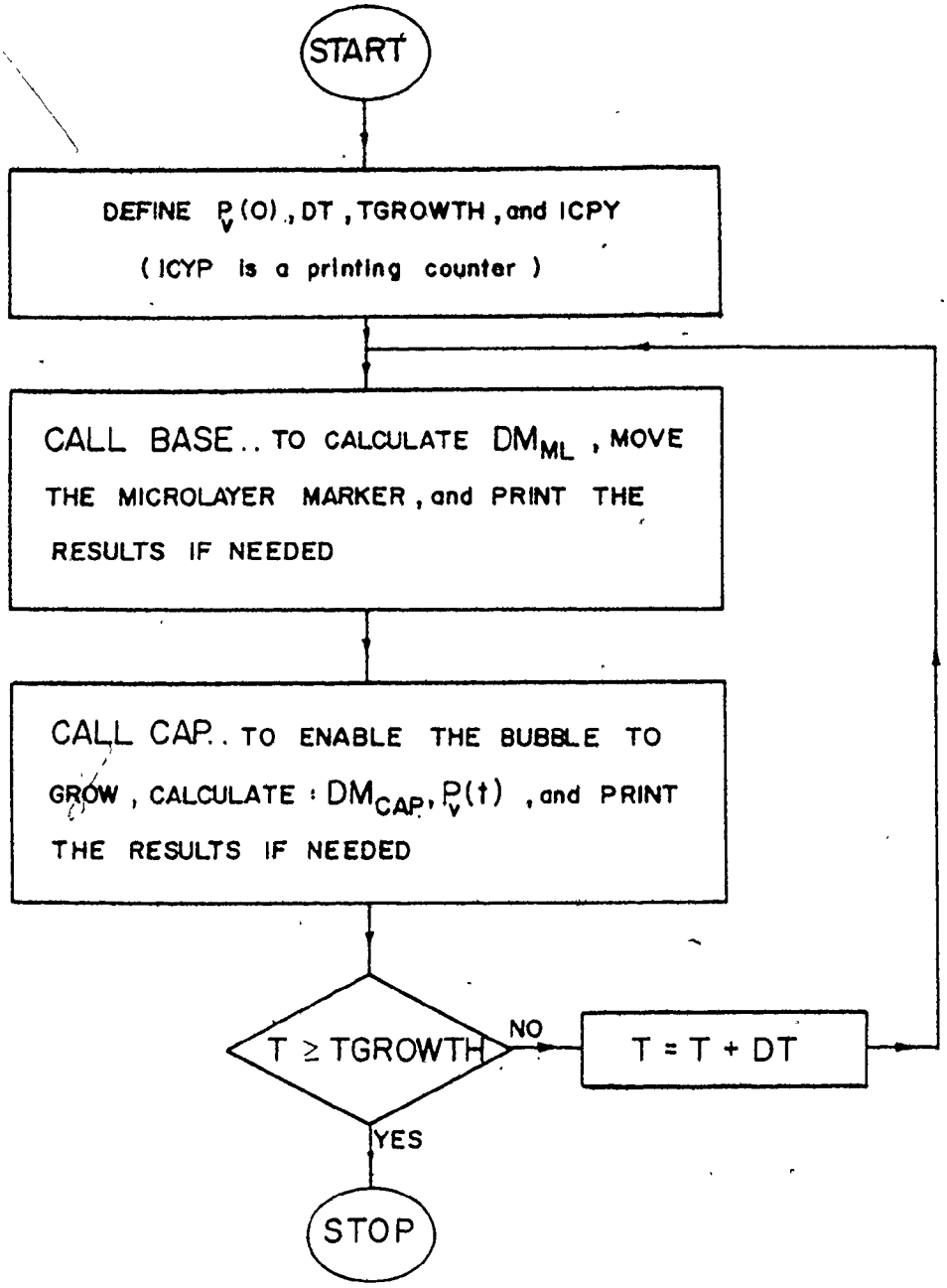

FIGURE (7.4) COMPUTATION PROCEDURE OF MICROLAYER EVAPORATION & BUBBLE GROWTH

7.4 Results of the Numerical Model

7.4.1 Introduction

It was observed that the bubble mass $M_B(t)$ increases very rapidly at the beginning of the growth period and then more slowly as shown in figure (7.5). This behaviour causes the vapour pressure $P_v(t)$ to increase more rapidly at the beginning of the growth period than later on. The vapour pressure oscillation (due to combined vapour pressure and liquid inertia) was also observed as seen in figure (7.6). The oscillation in the vapour pressure causes the bubble growth rate $\dot{R}(t)$ to oscillate as shown in figure (7.7). Figure (7.8) shows the corresponding bubble growth relationship $R(t)$.

Some computational and physical parameters which may affect the predictions of the present model were studied. The computational parameters include the step sizes Δr and Δy which are bounded by the accuracy and the computational time constraints, and the time step Δt which is bounded by the stability conditions as discussed in the previous chapters. The physical parameters include the initial vapour pressure $P_v(0)$ and the initial microlayer thickness δ_o. Changes in the initial vapour pressure $P_v(0)$, for instance, affect the initial growth rate which affects the microlayer formation and evaporation which in turn affects the bubble mass $M_B(t)$ and the vapour pressure $P_v(t)$ and so on. The result of changing the initial vapour pressure and the initial microlayer thickness will be examined below.

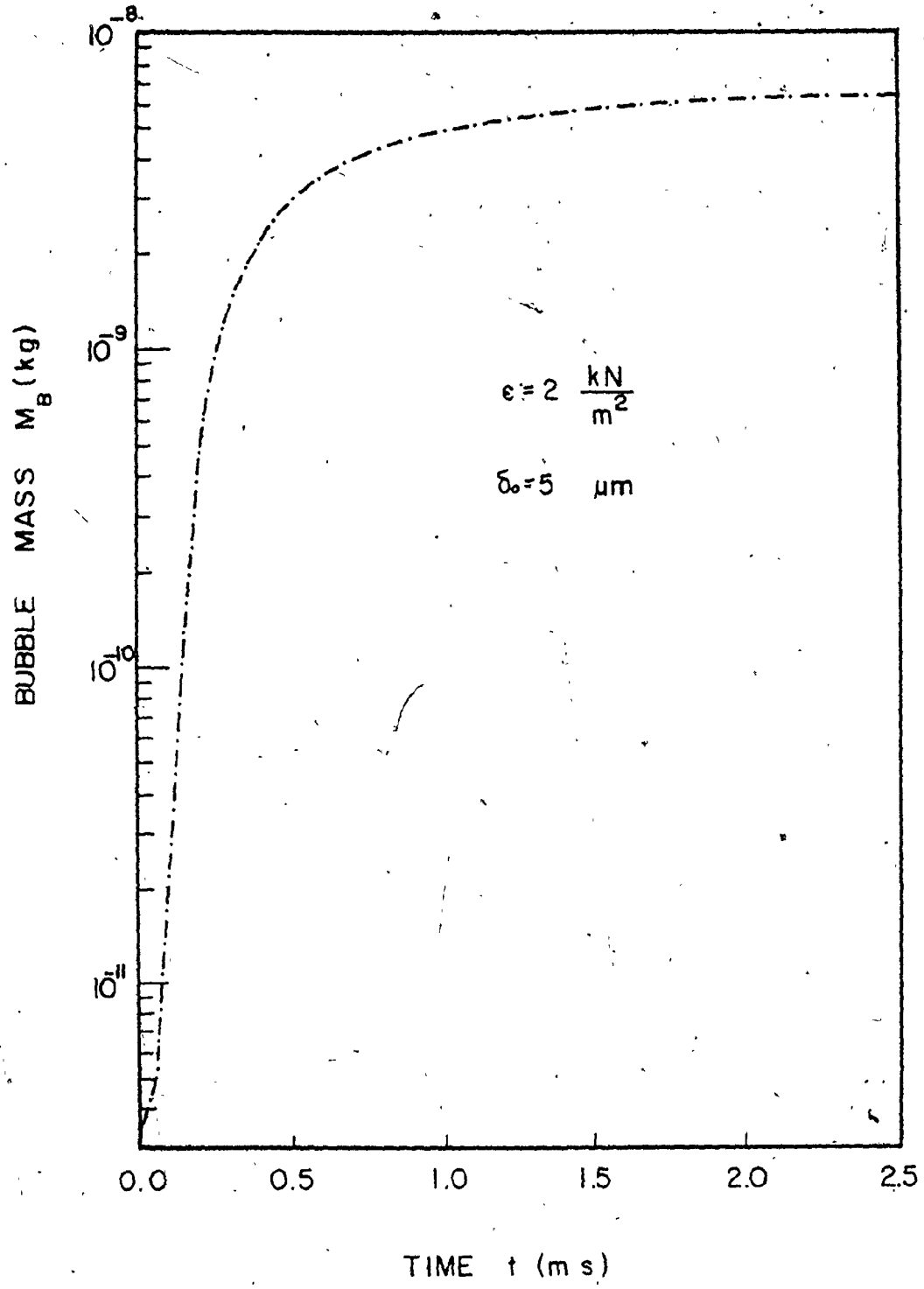

FIGURE (7.5) BUBBLE MASS VARIATION

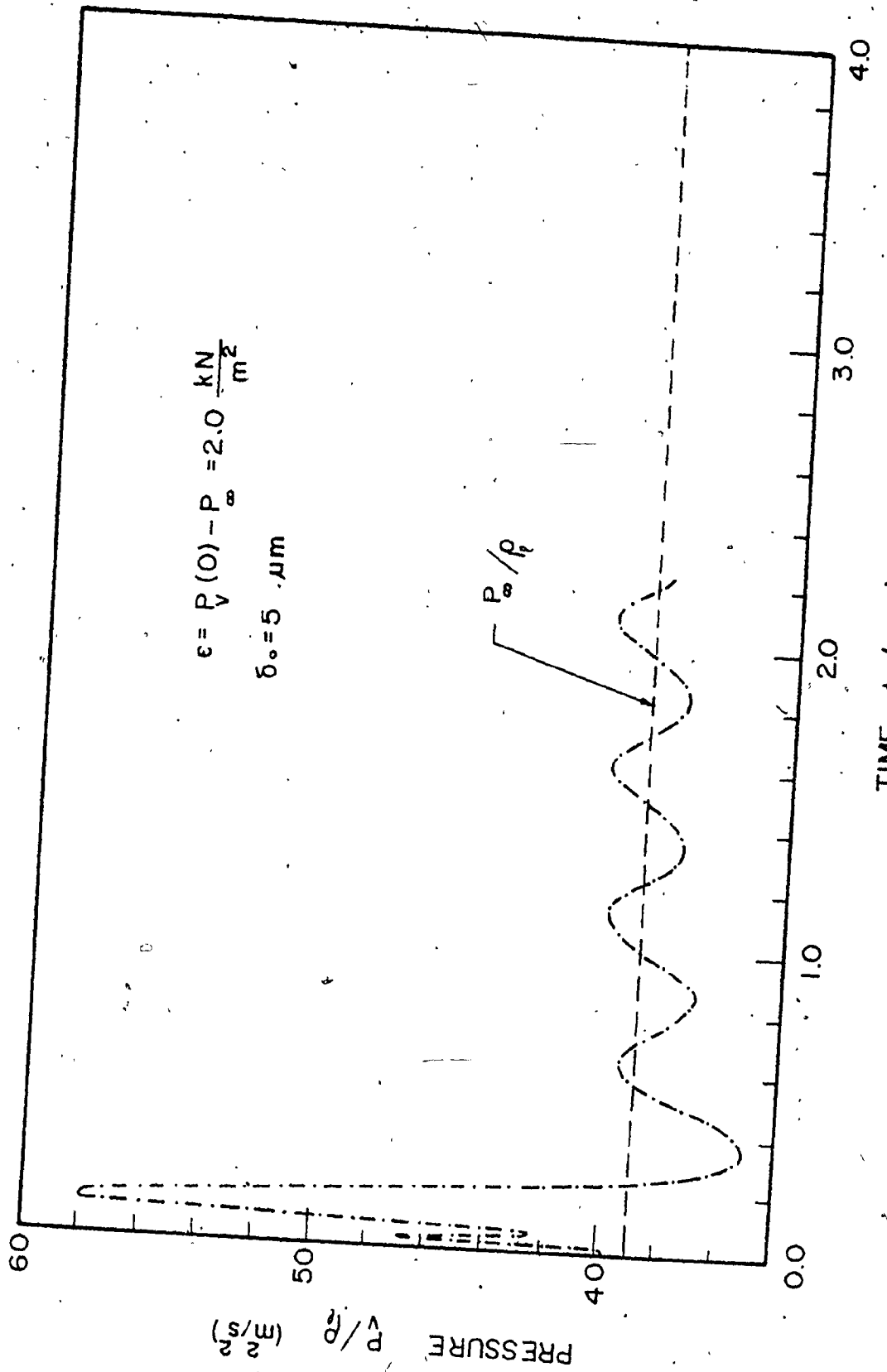

FIGURE (7.6) VAPOUR PRESSURE VARIATION

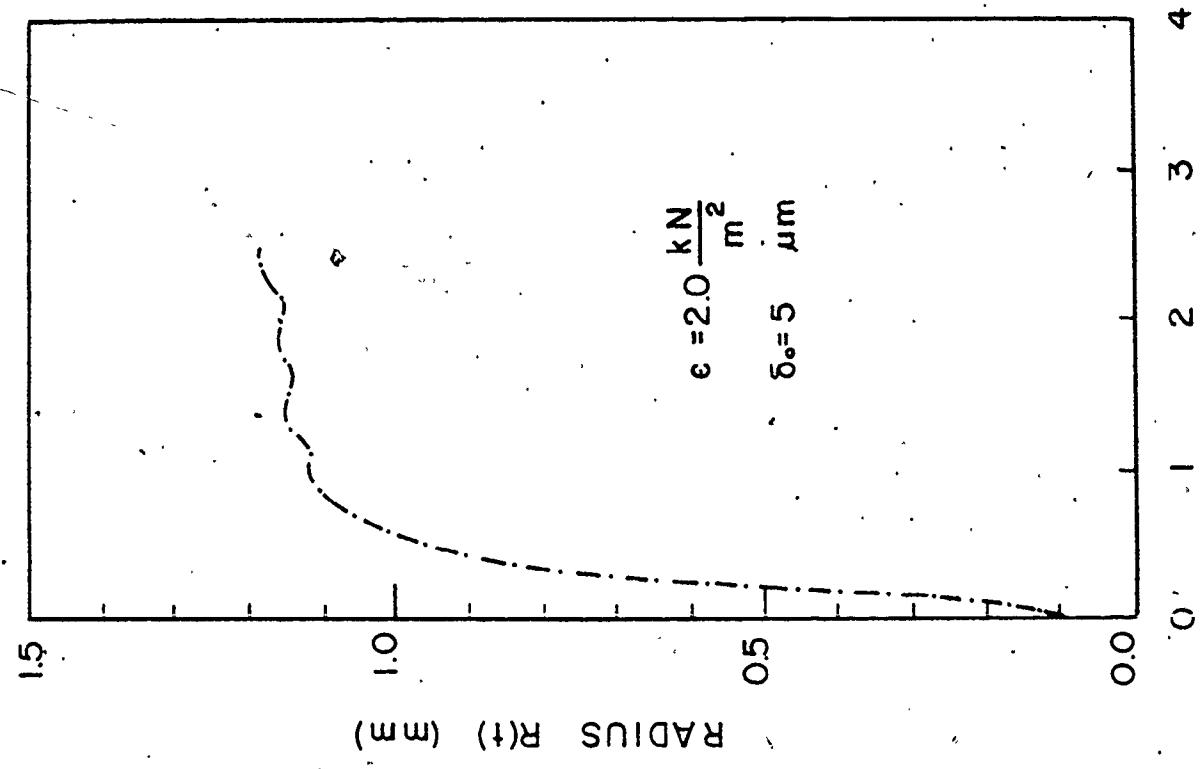

FIGURE (7.8) GROWTH RELATIONSHIP

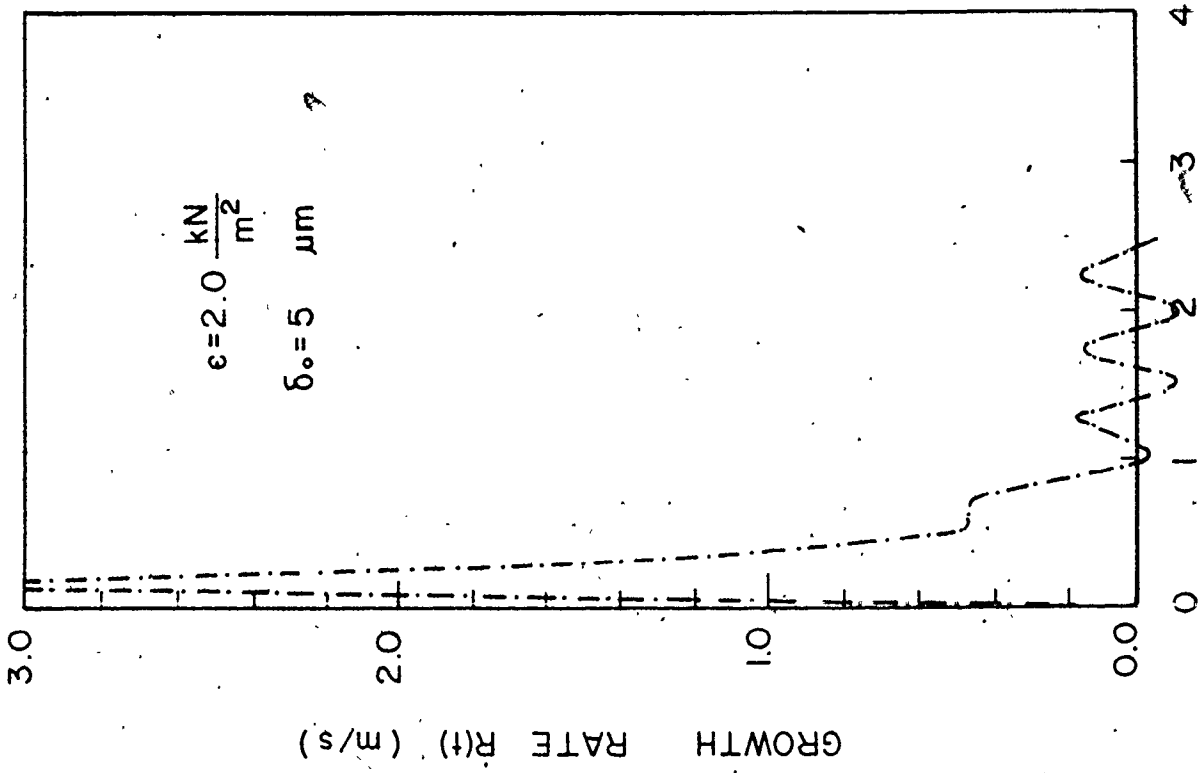

FIGURE (7.7) GROWTH RATE RELATIONSHIP

7.4.2 Effect of the Initial Vapour Pressure $P_v(0)$

It is well known from the nucleation theory that bubble nucleus is at equilibrium if the vapour pressure is balanced with the system pressure and surface tension pressure, i.e.,

$$P_v = P_\infty + \frac{2\sigma}{r_n}$$

where r_n is the radius of the nucleus. For dichloromethane $\sigma = 0.02658$ N/m and for $r_n = 100$ μm, the surface tension pressure $2\sigma/r_n$ is of the order of 500 N/m^2. If however such equilibrium condition is disturbed by a perturbation value ε, i.e.,

$$P_v' = P_\infty + \frac{2\sigma}{r_n} + \varepsilon > P_\infty + \frac{2\sigma}{r_n}$$

$$\varepsilon \equiv P_v' - P_v = [P_\infty + \frac{2\sigma}{r_n} + \varepsilon] - [P_\infty + \frac{2\sigma}{r_n}] = [P_\infty + \varepsilon] - P_\infty = P_v(0) - P_\infty$$

the bubble starts growing. The value of ε (which represents the starting driving pressure) could be very small just sufficient to perturb the static balance of the nucleus. However, since the evaporation of the microlayer in the finite difference program will not start until the bubble front moves one radial step of the computational region (see Chapter 5) at least, the perturbation parameter ε was given a higher value to fulfil this requirement. Note, however, that the perturbation parameter ε is an unknown parameter and may vary due to the pressure disturbances

created by other surrounding bubbles. A comparison between some of the results obtained for two different perturbation values (ε = 2.0 and 8.5 kN/m^2) are shown in figures (7.9) to (7.13). The influence of this parameter on the bubble mass is shown in figure (7.9), on the vapour pressure in figure (7.10), on the growth rate in figure (7.11), on the growth relationship in figure (7.12) and on the instantaneous microlayer profile $\delta(r,t)$ in figure (7.13). From these results, it is clear that apart from the initial growth period t_g > .3 ms, the difference between the two cases is small (up to 15% for bubble mass and 10% for bubble growth relationships). As far as the instantaneous microlayer thickness $\delta(r,t)$ is concerned, the perturbation value ε has more effect as shown in figure (7.13).

7.4.3 The Effect of the Initial Microlayer Thickness

The evaporation rate of the microlayer $\frac{\partial \delta(r,t)}{\partial t}$ depends on the assumed value of the initial microlayer thickness δ_o in accordance with equation (5.21). The evaporation rate affects the shape of the instantaneous microlayer thickness $\delta(r,t)$ as well as the mass evaporated from the microlayer and accordingly the vapour pressure $P_v(t)$ and the growth rate $\dot{R}(t)$. Figures (7.14) to (7.18) show this effect for two different values of δ_o (3 and 5 μm). The effect on the bubble mass is shown in figure (7.14), on the vapour pressure in figure (7.15), on bubble growth rate in figure (7.16), on bubble growth relationship in

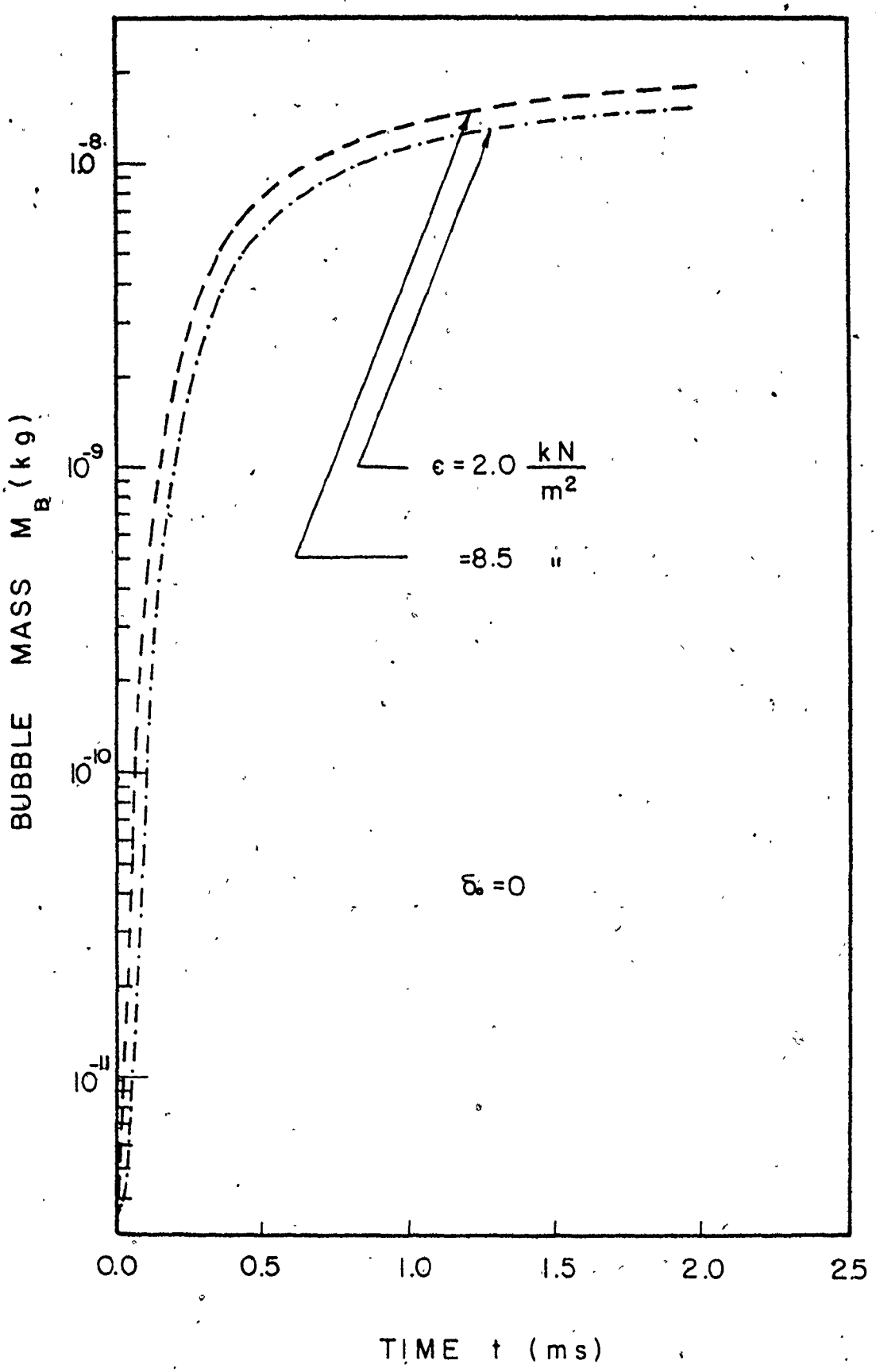

FIGURE (7.9) EFFECT OF THE PRESSURE PERTURBATION ON BUBBLE MASS $M_B(t)$

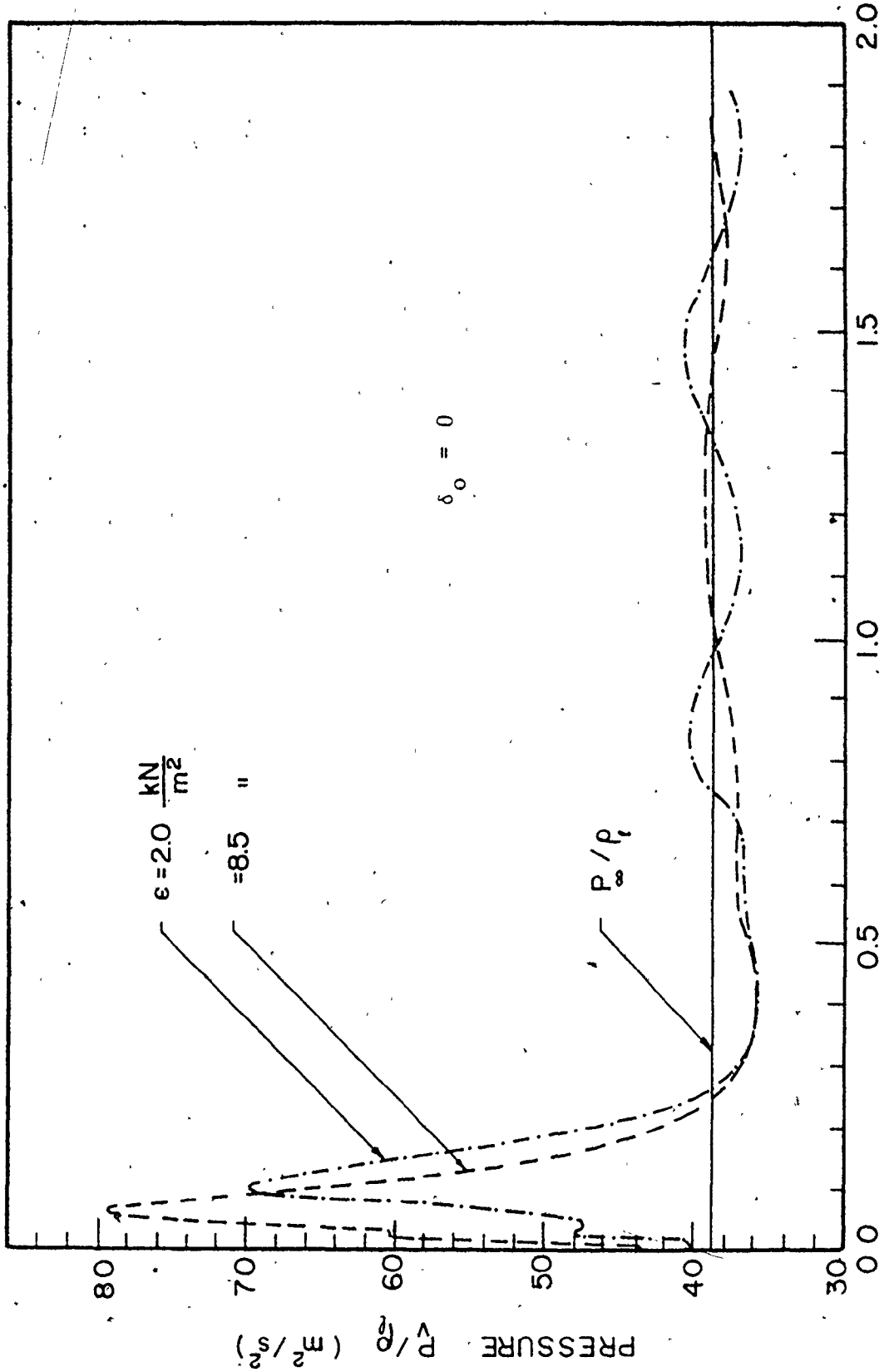

FIGURE(7.10) EFFECT OF THE PRESSURE PERTURBATION PARAMETER ON VAPOUR PRESSURE

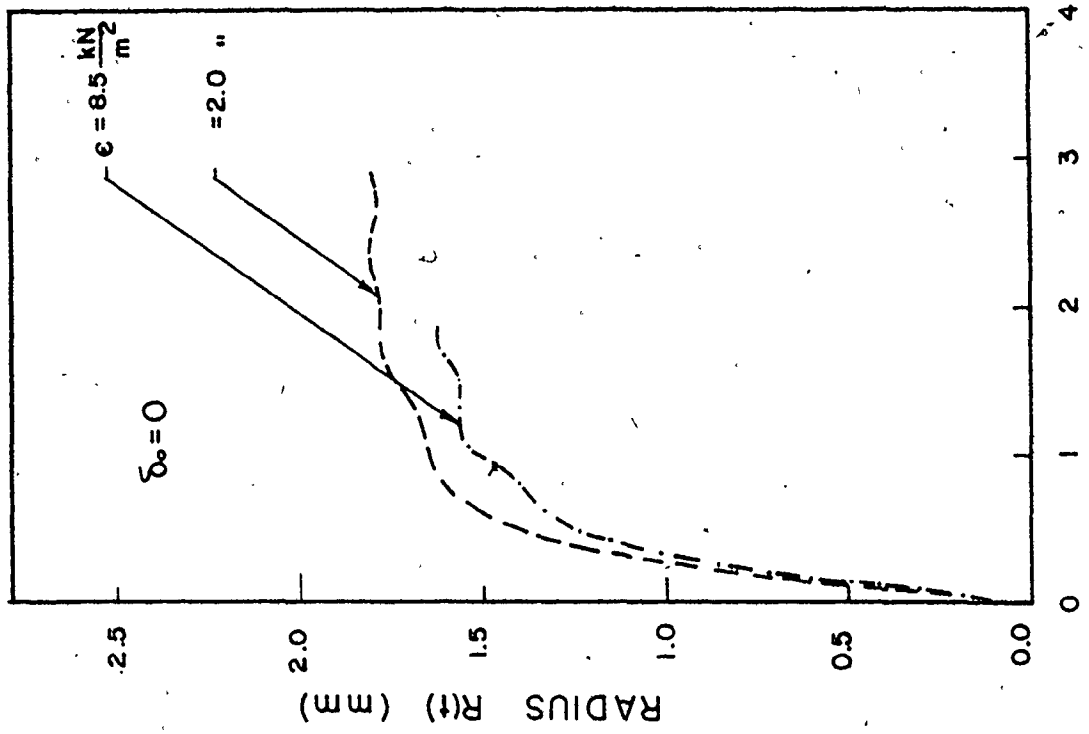

FIGURE (7.12) EFFECT OF THE PRESSURE PERTURBATION PARAMETER ON GROWTH RELATION

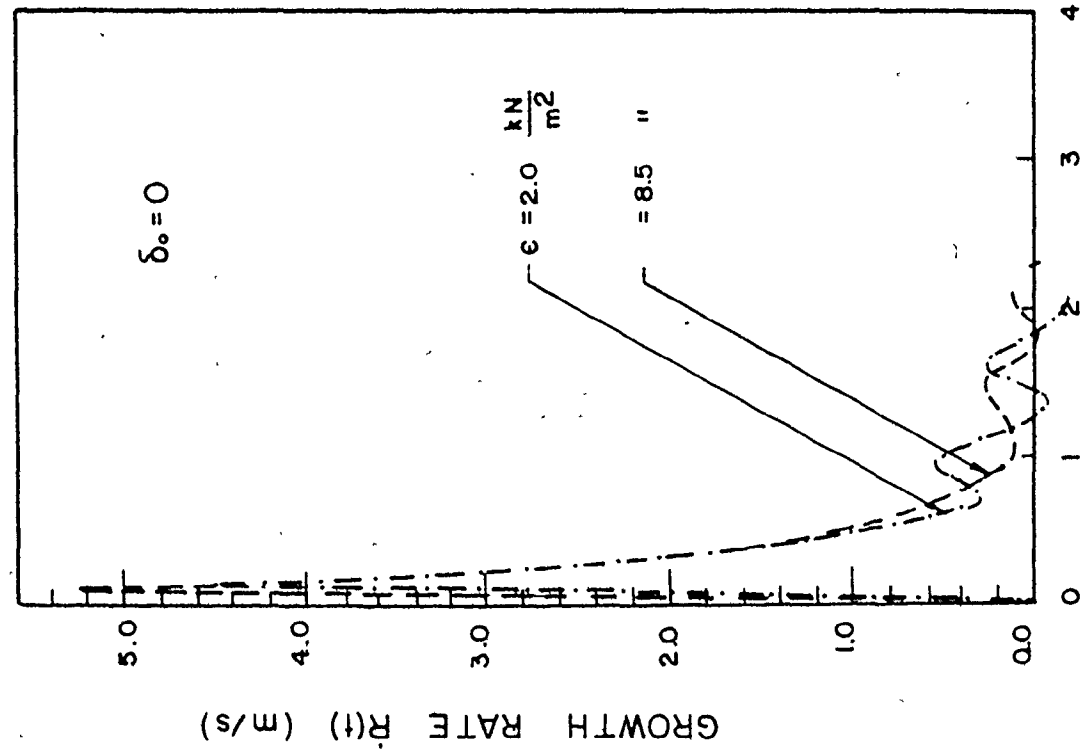

FIGURE (7.11) EFFECT OF THE PRESSURE PERTURBATION PARAMETER ON GROWTH RATE

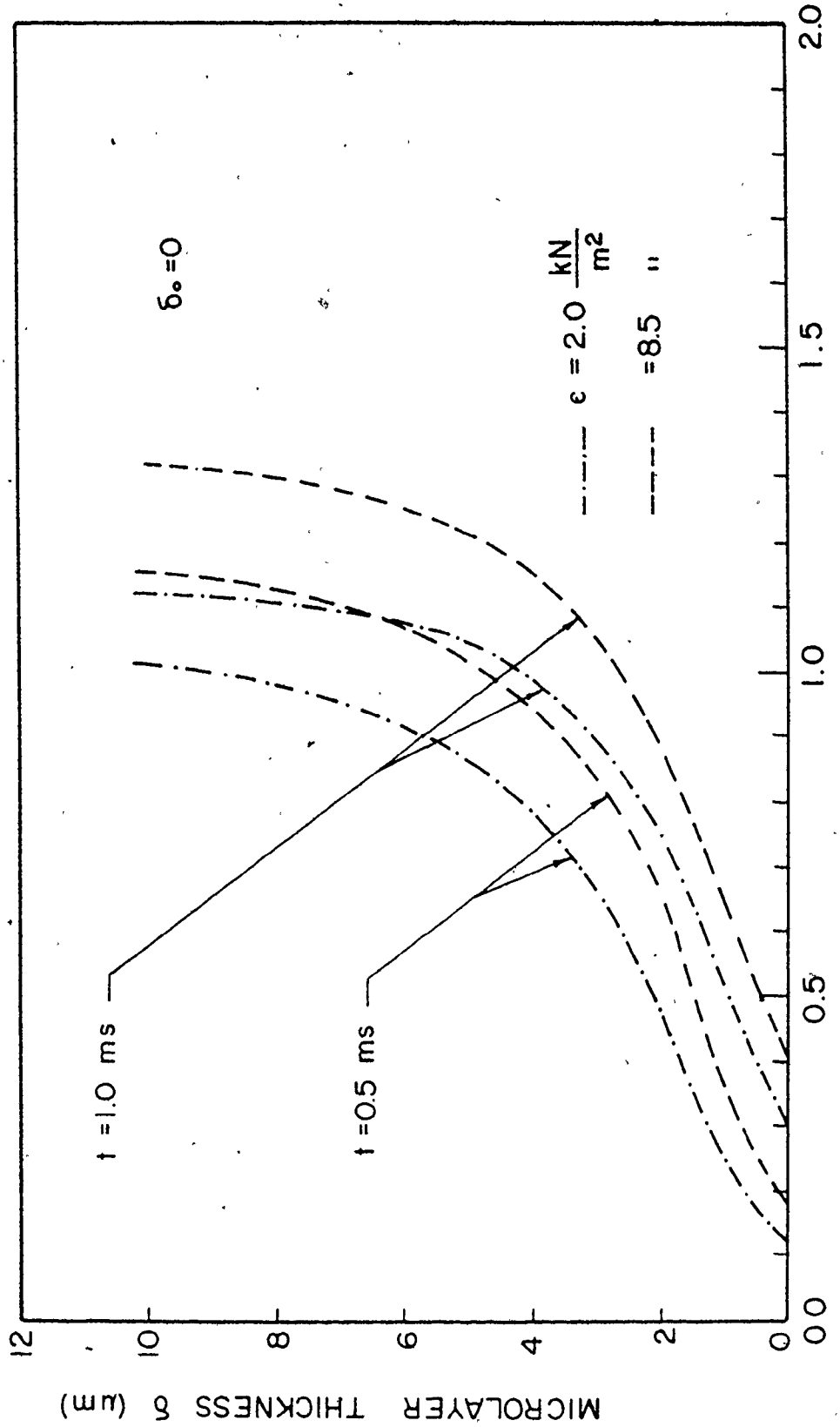

FIGURE(7.13) EFFECT OF THE PRESSURE PERTURBATION PARAMETER ON INSTANTANEOUS MICROLAYER THICKNESS

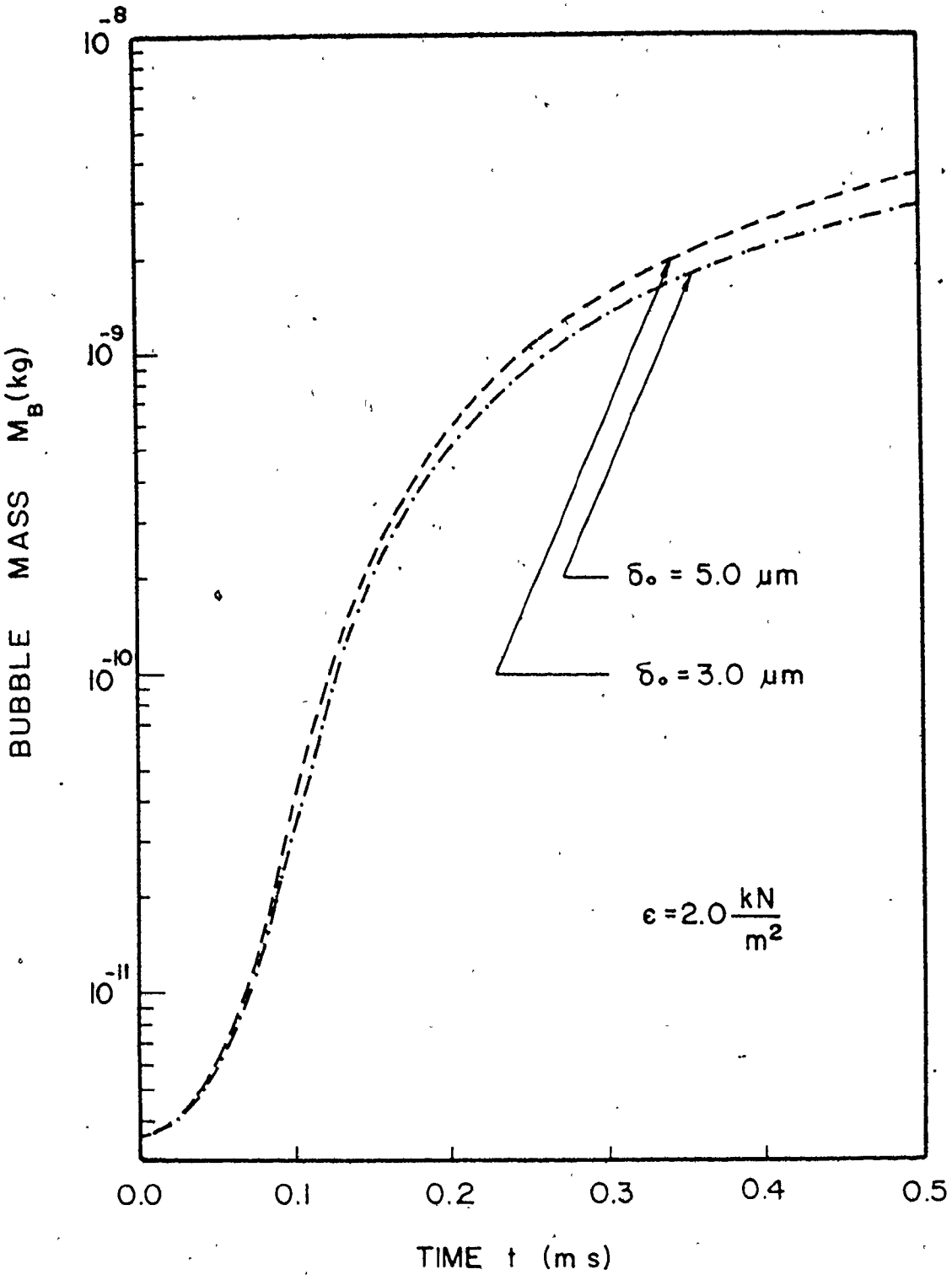

FIGURE(7.14) EFFECT OF THE INITIAL MICROLAYER THICKNESS ON BUBBLE MASS

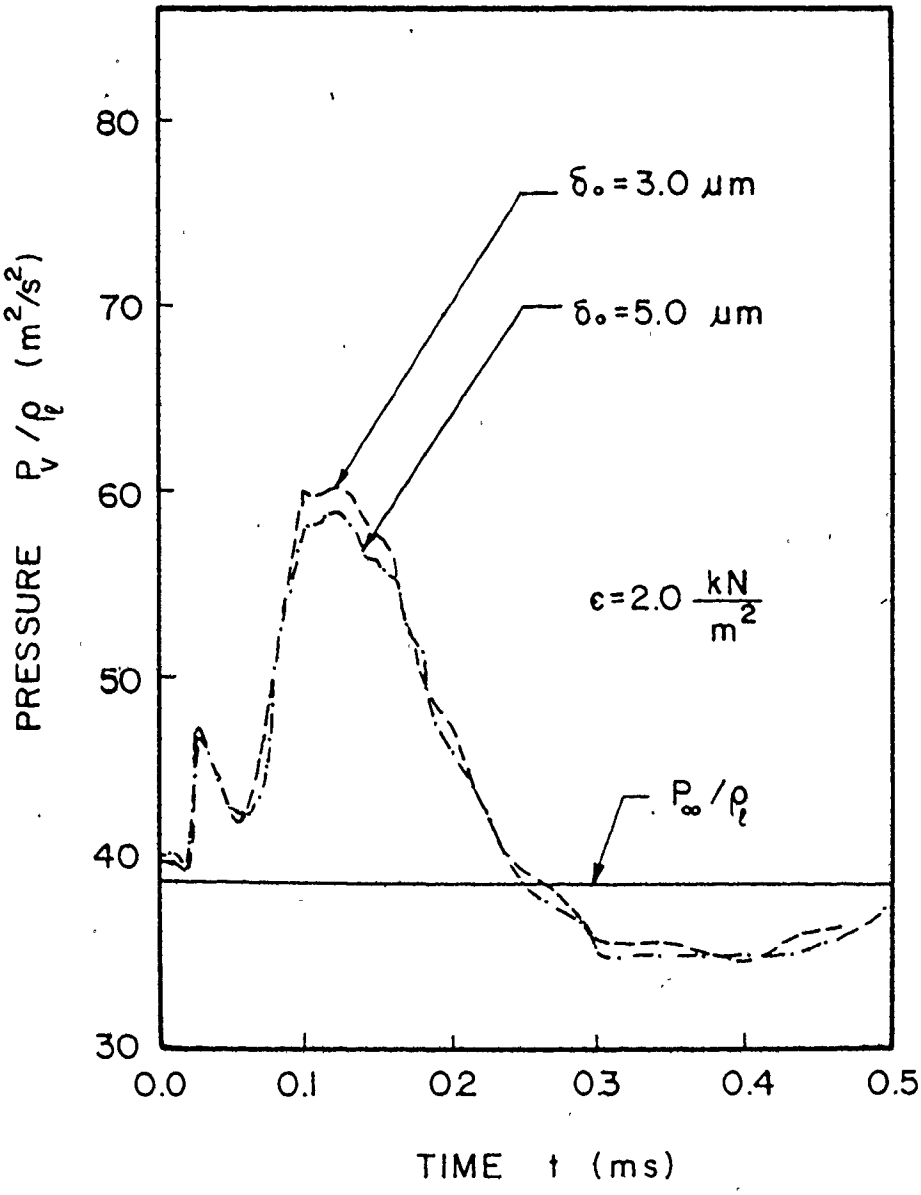

FIGURE (7.15) EFFECT OF THE INITIAL MICROLAYER THICKNESS ON VAPOUR PRESSURE

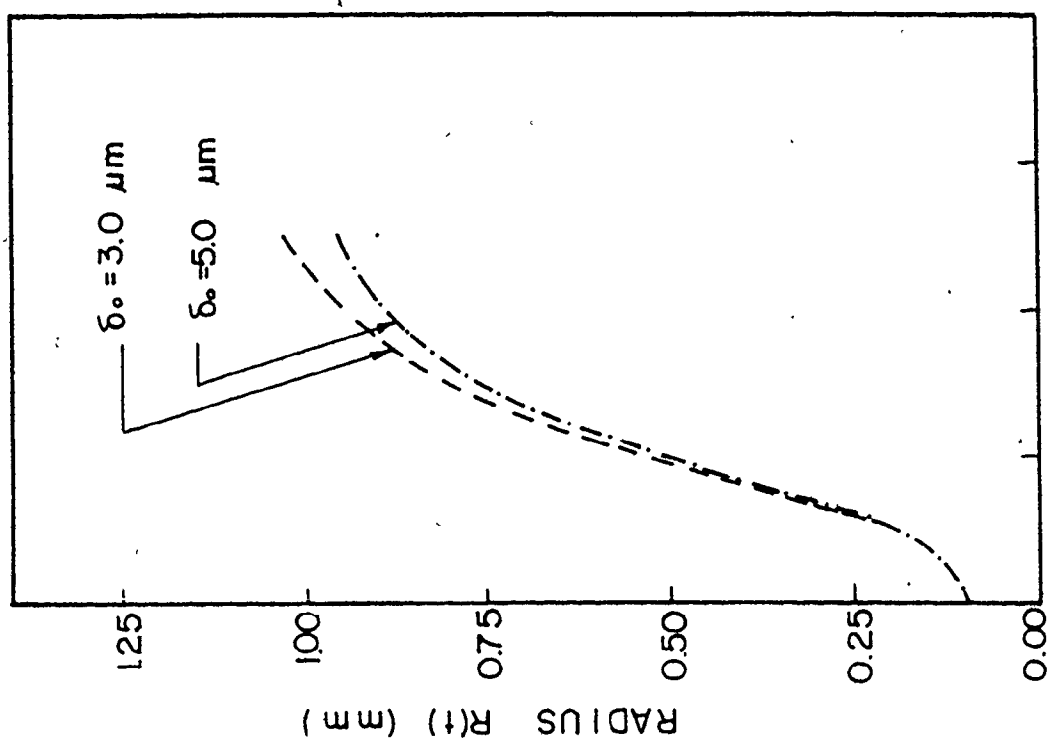

FIGURE (7.17) EFFECT OF THE INITIAL MICROLAYER THICKNESS ON GROWTH RELATIONSHIP

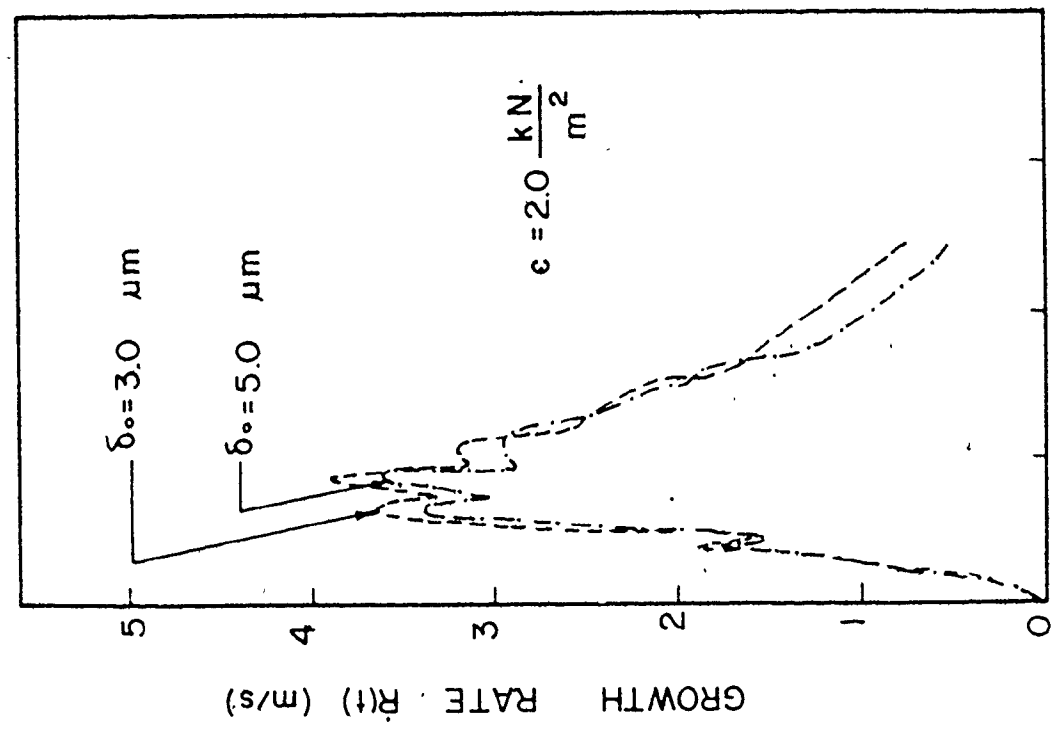

FIGURE (7.16) EFFECT OF THE INITIAL MICROLAYER THICKNESS ON GROWTH RATE

figure (7.17) and on the instantaneous microlayer thickness in figure (7.18). From these results one can conclude that the effect of changing the initial microlayer thickness (within the experimental measurement limits) is insignificant during the initial growth period with an error of the order of 10% occurring at later stages. The effect on the instantaneous microlayer thickness is also small as shown in figure (7.18).

7.5 Discussion

The oscillations of the vapour bubble shown in figures (7.6) to (7.8) for vapour pressure, growth rate and the growth relationship are replotted in figure (7.19). From this figure one can observe that the growth rate and the growth relationship oscillations lag behind the vapour pressure oscillations due to the liquid inertia. According to the numerical study of Joosten et al. [48] and the experimental results of Van Stralen [30] and [46], the oscillation period for a water bubble at system pressure P_∞ = 16.27 kN/m^2 is of the order of (8-9) ms, at P_∞ = 20.28 kN/m^2 it is of the order of (3.5-6) ms and at P_∞ = 26.72 kN/m^2 it is of the order of (2-4) ms. The effect of increasing system pressure is to rapidly decrease the oscillation period and as a consequence it is not unreasonable that the oscillation period for the present study (P_∞ = 51.5 kN/m^2) should be of the order of (0.3-0.5) ms as shown in figures (7.19) and (7.20). Accordingly it is

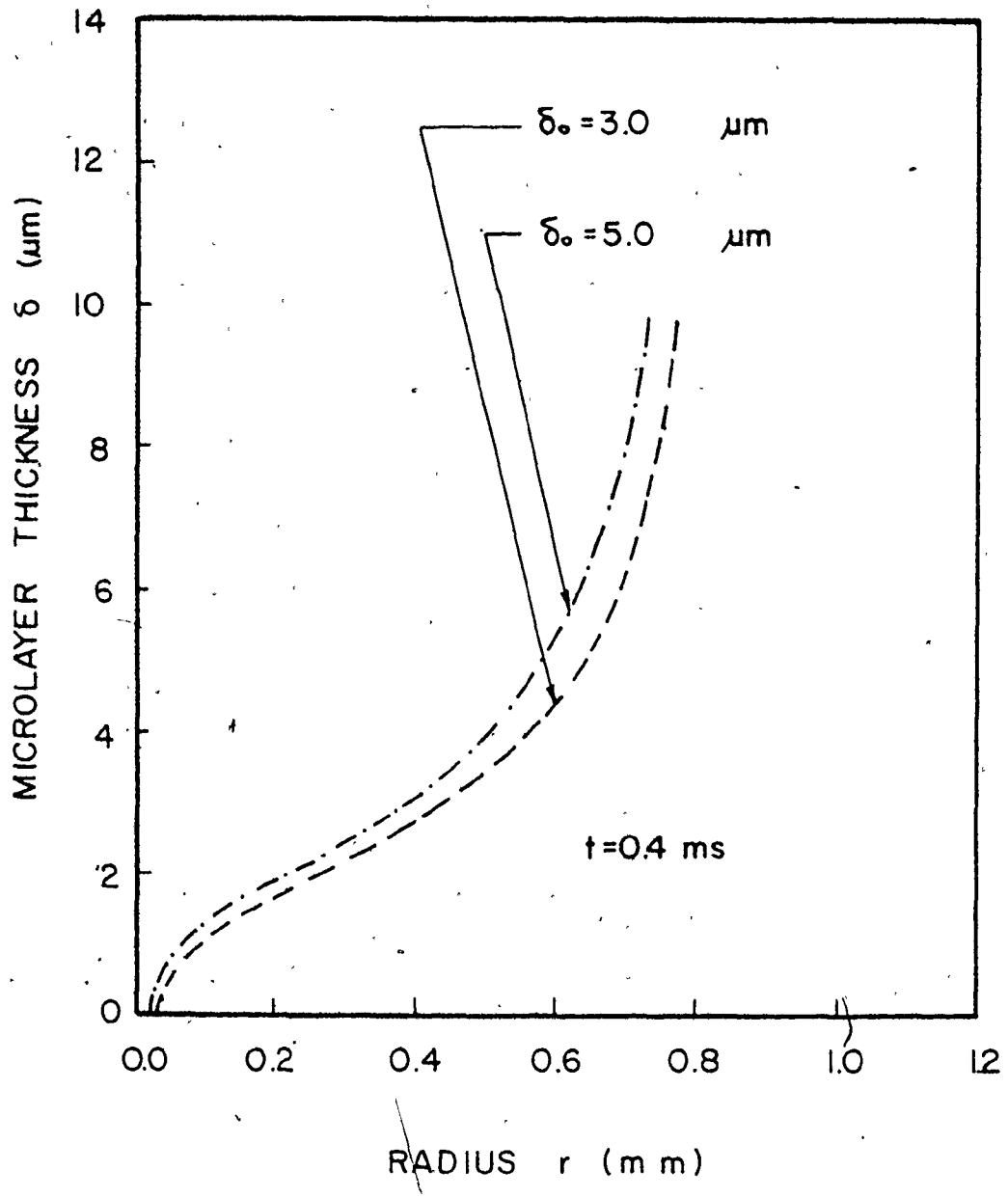

FIGURE (7.18) EFFECT OF THE INITIAL MICROLAYER THICKNESS ON THE INSTANTANEOUS MICROLAYER THICKNESS

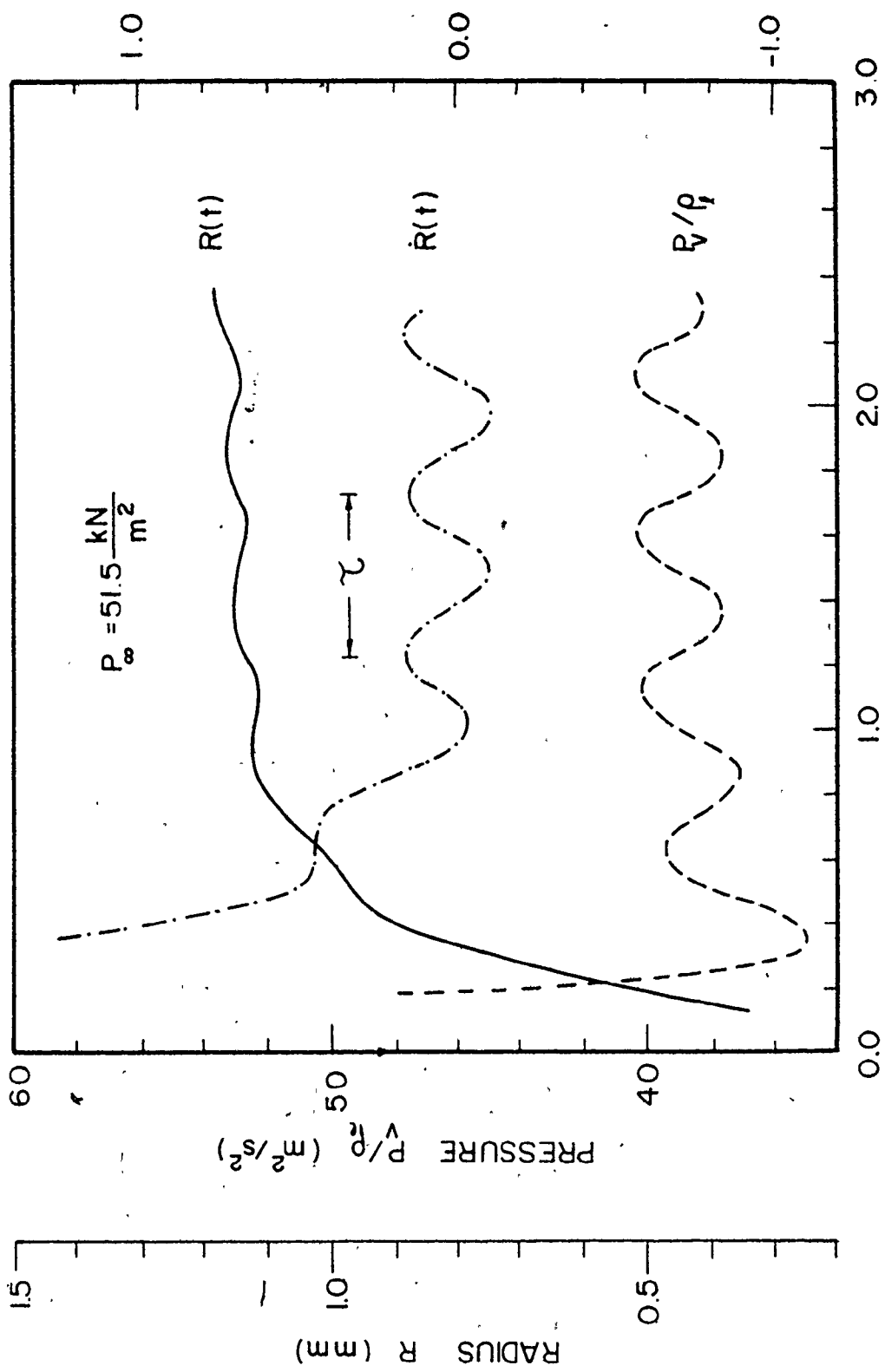

FIGURE (7.19) OSCILLATION OF BUBBLE PARAMETERS

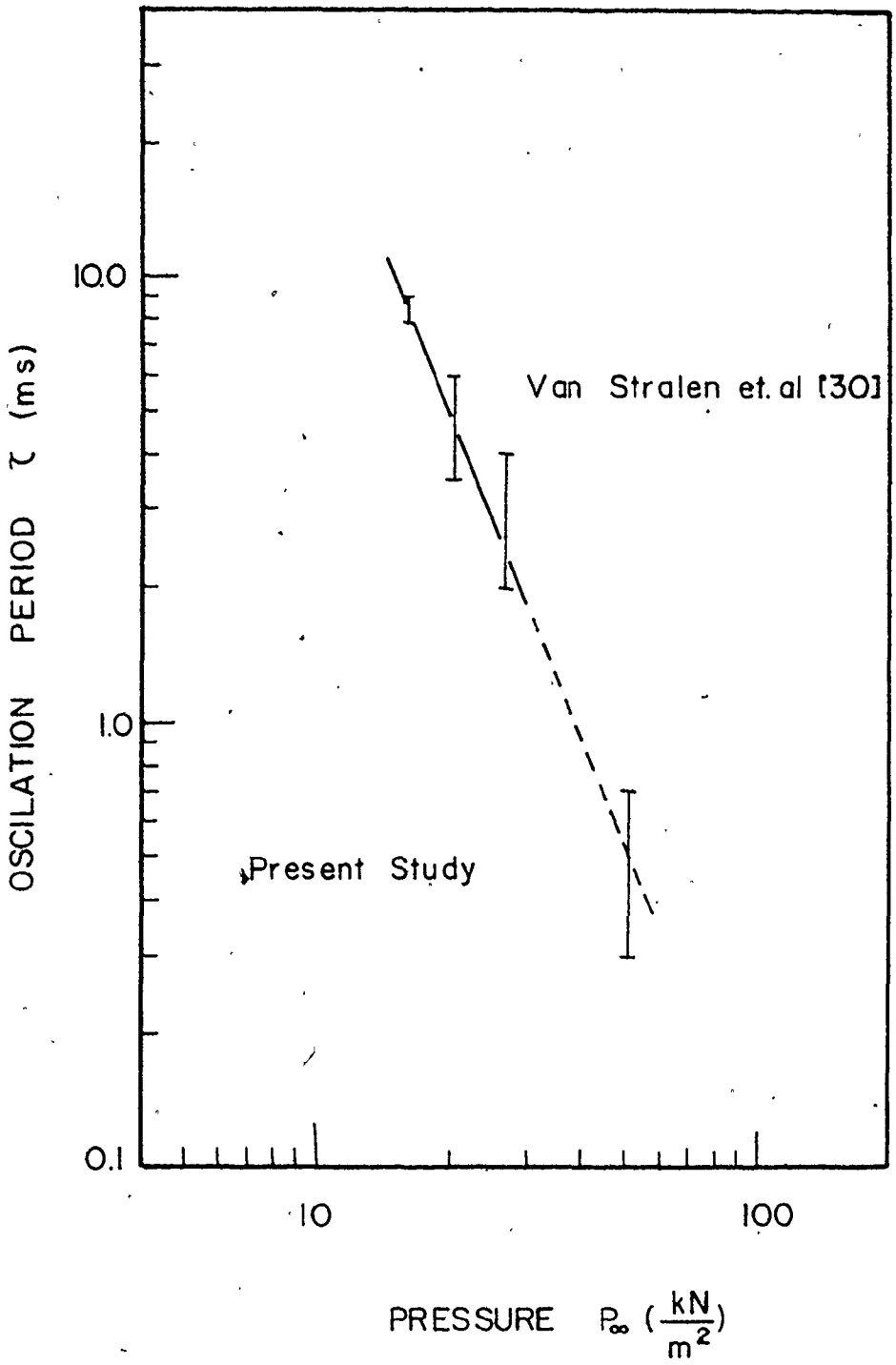

FIGURE (7.20) EFFECT OF SYSTEM PRESSURE ON THE OSCILLATION PERIOD

felt that the oscillation behaviour observed is a real phenomenon and not due to computational instability.

The effect of the perturbation parameter ε, where $\varepsilon = P_v(0) - P_\infty$, on bubble growth parameters is presented in figures (7.9) to (7.13). Increasing ε allows the microlayer to be formed and start evaporating earlier and accordingly increases the microlayer mass evaporated and consequently the bubble mass $M_B(t)$ as shown in figure (7.9). This will have the effect of increasing the vapour pressure $P_v(t)$, the bubble growth rate $\dot{R}(t)$ and the growth relationship $R(t)$ at the earlier stages as shown in figures (7.10) to (7.12) respectively. The growth rate $\dot{R}(t)$ was observed to oscillate and decrease with time, sometimes reaching a negative value due to the combined effects of liquid inertia and vapour pressure as discussed in Section (7.2), figure (7.11). Similarly, increasing ε causes the maximum vapour pressure $P_v(t)$ to increase and shift towards an earlier growth period as seen in figure (7.10). The instantaneous microlayer profile $\delta(r,t)$ is also shifted due to early evaporation and higher growth rate according to figure (7.13).

Decreasing the initial microlayer thickness δ_o increases the evaporation rate $\frac{\partial \delta(r,t)}{\partial t}$ according to equation (5.21), which increases the mass evaporation from the microlayer ΔM_{ML} and the bubble mass $M_B(t)$, figure (7.14), the vapour pressure $P_v(t)$, figure (7.15), the growth rate $\dot{R}(t)$, figure (7.16) and the bubble growth relationship $R(t)$,

figure (7.17). The instantaneous microlayer profile $\delta(r,t)$ will also be shifted due to higher growth rate, as shown in figure (7.18).

The experimental research carried out by Judd, Voutsinos and Fath [26] and [1] provides measurements of the instantaneous microlayer thickness $\delta(r,t)$. Regrettably other parameters such as the growth rate, the growth relationship and the vapour pressure are not available for these data. A comparison between the experimental instantaneous microlayer thickness measurements of Fath [1] and the predictions of the present numerical model for a selected bubble is shown in figure (7.21). From the figure it is clear that the experimental measurements and the numerical results match quite well. The predicted radius of the dry area and the bubble is shown in figure (7.22) with the experimental measurements of Fath [1] which shows a good agreement.

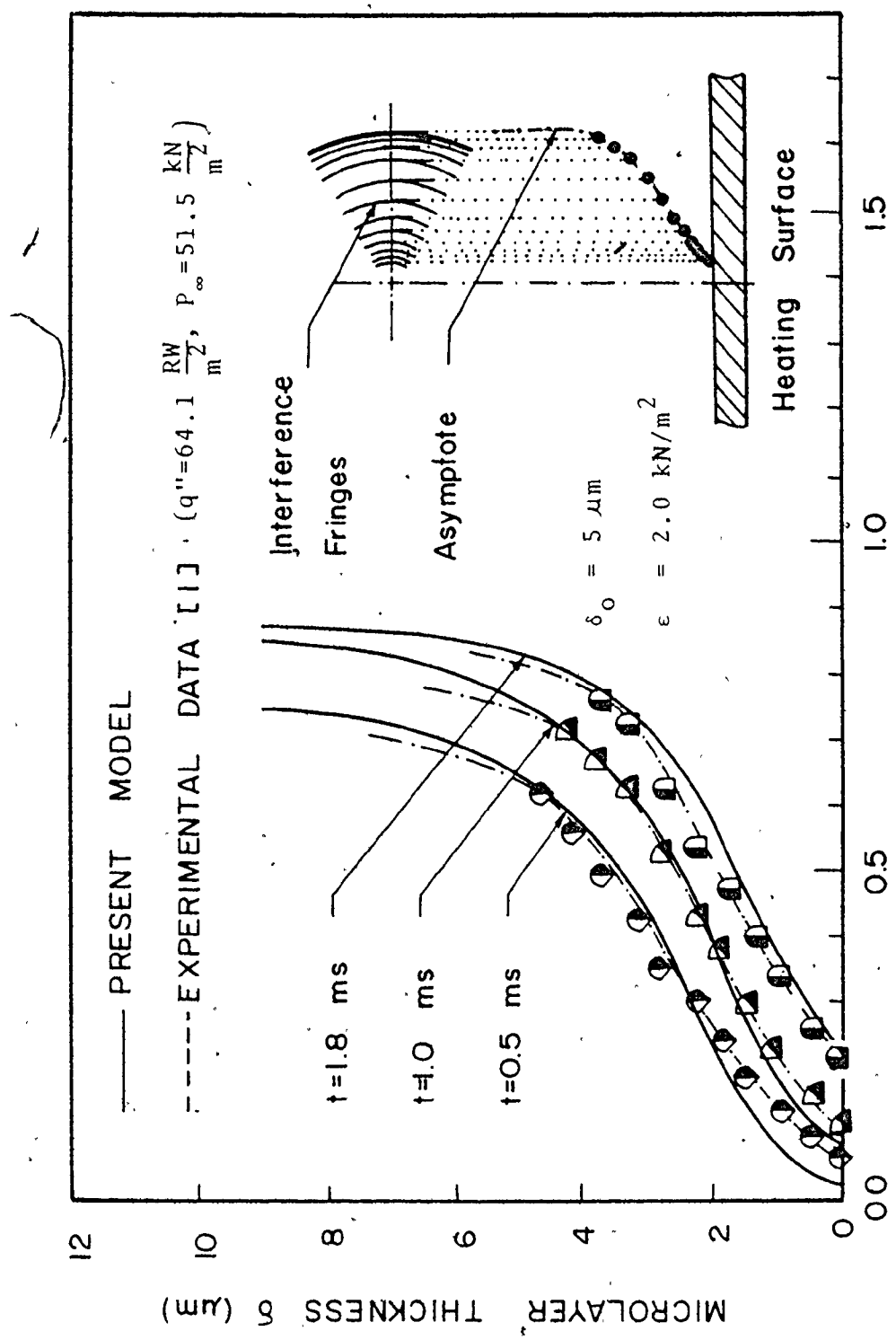

FIGURE (7.21) INSTANTANEOUS MICROLAYER THICKNESS

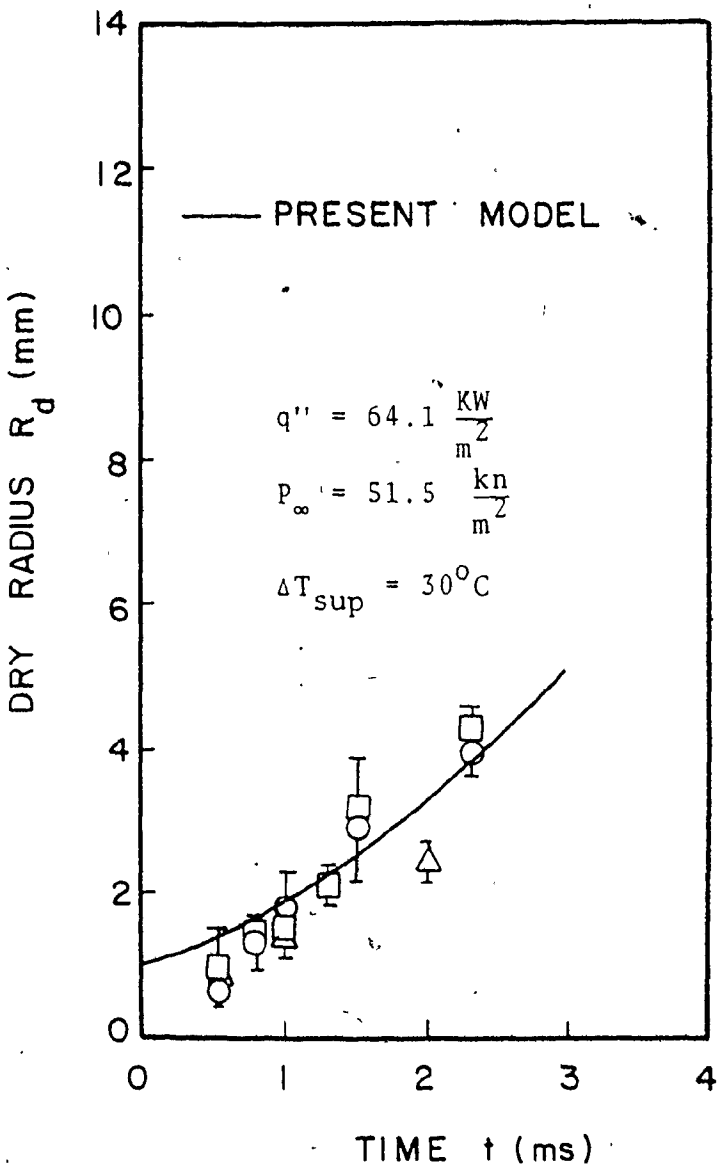

FIGURE (7.22) DRY RADIUS COMPARISON

CHAPTER 8

CONCLUSIONS, LIMITATIONS AND RECOMMENDATIONS

Conclusions

A numerical study of microlayer formation, evaporation and bubble growth has been presented in this thesis. Different finite difference techniques were adopted in order to develop computer programs capable of predicting the isothermal and the instantaneous microlayer profiles as well as the bubble growth behaviour on a heating surface for any liquid-surface combination and boiling conditions.

The predictions of the isothermal and the instantaneous microlayer profiles show good agreement with the experimental data of Fath and indicate that the microlayer evaporation may contribute up to 100% of the total bubble mass. The program developed has the advantage of being able to handle any bubble growth rate which is an original contribution as well as the ability to vary the input heat flux and the liquid and solid thermal physical properties. As a consequence, one is able to predict the microlayer behaviour associated with boiling conditions for which experimental measurements are rather difficult to obtain.

The behaviour of bubble growing on a heating surface was studied by adapting the Marker And Cell technique. The hydrodynamic and the thermodynamic fields of the liquid

surrounding the growing bubble were analysed allowing the evaporation from the bubble to be computed. The results of this analysis showed that the contribution of bubble cap evaporation to the bubble mass is small in comparison with the contribution of microlayer evaporation. The program developed was also used to study the bubble growth behaviour in a confined space which has some important applications particularly in connection with the CANDU nuclear reactor pressure tube.

Finally, a numerical model for bubble growth on a heating surface was presented in which evaporation from both the microlayer and the bubble cap was incorporated. The model assumes that the mass transfer across the liquid-vapour interface is the predominant mechanism for the bubble growth. The computer program developed was able to predict the instantaneous microlayer thickness in agreement with selected bubbles from Fath's experimental data.

Limitations

The bubble growth rate in the model presented in Chapter 7 was found to increase very quickly at the beginning of the growth period and then slow down with oscillations as time goes on, sometimes reaching negative values. After 2.5 ms, the bubble starts to collapse due to negative vapour pressure difference $\Delta P_v(t)$, ($\Delta P_v(t) = P_v(t) - P_\infty$) and the markers move in an irregular fashion. This growth time limitation was found to vary depending upon the initial vapour

pressure $P_v(0)$ and the reason may be associated with the assumption that mass transfer across the liquid vapour interface is the only mechanism causing the bubble to grow. The program accordingly does not predict properly after this limiting period of time.

All the programs developed in this thesis are limited to the initial and boundary conditions provided, but any other initial and boundary conditions could be handled easily in the subroutines provided for them. In addition, the programs assume a constant vapour temperature which might not be the case for vapour bubbles in general.

Recommendations

Throughout the course of the present investigation, it was felt that an expansion of this study would be of a great help in confirming the results and improving the prediction capabilities of the present programs.

Beside the improvements which could be done in order to overcome the limitations presented in the previous section, other studies could be performed as outlined below:

1. In order to confirm the results predicted in Chapter 4 for isothermal microlayer thickness, an experimental investigation could be performed to measure the microlayer thickness formed under a bubble growing in an isothermal field photographically (refer to the experimental study of Fath and Theofanous et al.) in which it would be important to measure the bubble growth rate simultaneously with the

microlayer formation.

2. The computer program developed in Chapter 6 for the analysis of the bubble growth could be modified to allow for bubble collapse if the bubble were to grow in a highly subcooled condition. This program allows for any vapour temperature function to be specified. The effect of the surface tension due to the liquid-vapour interface geometry and the temperature variation along the interface could be introduced as a boundary condition at the interface (refer to the paper by Daly). In addition this program could be modified to predict the three dimensional results whence the bubble behaviour under forced convection could be analysed.

3. The oscillation phenomenon observed in Chapter 7 associated with bubble growth should be investigated further under different system pressures particularly those reported by Van Stralen et al. Also, in order to reduce the running time for this program, the time step assigned to the bubble cap solution could be different from that assigned to the bubble base solution instead of using a single time step which is bounded by the bubble base stability conditions.

APPENDIX A

Dichloromethane/Glass Properties

Property (P_{sat}=51.5 kN/m^2, T_{sat}=21.1^{o}C)			Dichloromethane	Glass
Density	kg/m^3	ρ	1323.5	
Viscosity	Ns/m^2	μ	$0.43*10^{-3}$	
Kinematic Viscosity	m^2/s	ν	$0.32*10^{-6}$	
Thermal Conductivity	W/m^{o}K	k	0.15385	0.762
Specific Heat	J/kg^{o}C	C	1312.5	
Thermal Diffusivity	m^2/s	α	$0.885*10^{-7}$	$3.36*10^{-7}$
Latent Heat of Evaporation	J/kg	h_{fg}	$3.426*10^5$	

APPENDIX B

FINITE DIFFERENCE APPROXIMATION

B.1 Boundary Layer Momentum Equation (4.23)

The boundary layer momentum equation is reproduced here as:

$$\left(\frac{\partial u}{\partial t}\right)_{ij}^{n+1} = -u_{ij}^{n}\left(\frac{\partial u}{\partial r}\right)_{ij}^{n+1} - v_{ij}^{n}\left(\frac{\partial u}{\partial y}\right)_{ij}^{n+1} - \frac{1}{\rho_\ell}\left(\frac{\partial P}{\partial r}\right)_{ij}^{n+1} + \nu_\ell\left(\frac{\partial^2 u}{\partial y^2}\right)_{ij}^{n+1} \tag{4.23}$$

Each velocity derivative can be approximated by a simple finite difference representation as:

$$\left(\frac{\partial u}{\partial t}\right)_{ij}^{n+1} = \frac{u_{ij} - u_{ij}^{n}}{\Delta t} \tag{B1}$$

$$\left(\frac{\partial u}{\partial r}\right)_{ij}^{n+1} = \frac{u_{ij} - u_{i-1,j}}{\Delta r_i} \tag{B2}$$

$$\left(\frac{\partial u}{\partial y}\right)_{ij}^{n+1} = \frac{1}{(\Delta y_j + \Delta y_{j+1})}\left[\frac{u_{ij} - u_{i,j-1}}{\Delta y_j}\Delta y_{j+1} + \frac{u_{i,j+1} - u_{ij}}{\Delta y_{j+1}}\Delta y_j\right] \tag{B3}$$

$$\left(\frac{\partial^2 u}{\partial y^2}\right)_{ij}^{n+1} = \frac{2}{(\Delta y_{j+1} + \Delta y_j)}\left[\frac{u_{i,j+1} - u_{ij}}{\Delta y_{j+1}} - \frac{u_{ij} - u_{i,j-1}}{\Delta y_j}\right] \tag{B4}$$

The velocities with no superscript correspond to time (n+1). Substituting in equation (4.23) and rearranging we get:

$$u_{i,j-1}\left[\frac{-v^n_{ij}}{(\Delta y_j+\Delta y_{j+1})}\left(\frac{\Delta y_{j+1}}{\Delta y_j}\right) - \frac{\nu}{(\Delta y_j+\Delta y_{j+1})(\Delta y_j)}\right]$$

$$+ u_{ij}\left[\frac{1}{\Delta t} + \left(\frac{u^n_{ij}}{\Delta r_i}\right) + \frac{u^n_{ij}}{(\Delta y_j+\Delta y_{j+1})}\left(\frac{\Delta y_{j+1}}{\Delta y_j} - \frac{\Delta y_i}{\Delta y_{j+1}}\right) + \right.$$

$$\left.\left(\frac{\nu}{\Delta y_j+\Delta y_{j+1}}\right)\left(\frac{1}{\Delta y_{j+1}} + \frac{1}{\Delta y_i}\right)\right]$$

$$+ u_{i,j+1}\left[\frac{v^n_{ij}}{(\Delta y_j+\Delta y_{j+1})}\left(\frac{\Delta y_j}{\Delta y_{j+1}}\right) - \left(\frac{\nu}{\Delta y_j+\Delta y_{j+1}}\right)\left(\frac{1}{\Delta y_{j+1}}\right)\right]$$

$$= \frac{u^n_{ij}}{\Delta t} + u^n_{ij}\left(\frac{u_{i-1,j}}{\Delta r_i}\right) - DPDX \qquad (B5)$$

where $DPDX = \frac{1}{\rho_\ell}\frac{\partial P}{\partial r}$ is defined in equation (4.13). The resulting equation has the form,

$$A_j\, u_{i,j-1} + B_j\, u_{ij} + C_j\, u_{i,j+1} = D_j \qquad (4.24)$$

B.2 Microlayer Equation (4.34)

The microlayer equation (4.34) is reproduced as:

$$\left(\frac{\partial u}{\partial t}\right)^{n+1}_{ij} = -u^n_{ij}\left(\frac{\partial u}{\partial r}\right)^n_{ij} - v^n_{ij}\left(\frac{\partial u}{\partial y}\right)^n_{ij} - \frac{1}{\rho_\ell}\left(\frac{\partial P}{\partial r}\right)^n_{ij} + \nu\left(\frac{\partial^2 u}{\partial y^2}\right)^n_{ij} \qquad (4.34)$$

The velocity derivatives can be approximated as:

$$\left(\frac{\partial u}{\partial t}\right)^{n+1}_{ij} = \frac{u^{n+1}_{ij} - u^n_{ij}}{\Delta t} \qquad (B6)$$

$$(u_{ij}^n)\left(\frac{\partial u}{\partial r}\right)_{ij}^n = FUX = \frac{1}{2\Delta r_{i+1}}\left(u_{ij}^n - |u_{ij}^n|\right)\left(u_{i+1,j}^n - u_{ij}^n\right)$$

$$+ \frac{1}{2\Delta r_i}\left(u_{ij}^n + |u_{ij}^n|\right)\left(u_{ij}^n - u_{i-1,j}^n\right) \qquad (B7)$$

$$(v_{ij}^n)\left(\frac{\partial u}{\partial y}\right)_{ij}^n = FUY = \frac{1}{2\Delta y_{j+1}}\left(v_{ij}^n - |v_{ij}^n|\right)\left(u_{i,j+1}^n - u_{ij}^n\right)$$

$$+ \frac{1}{2\Delta y_j}\left(v_{ij}^n + |v_{ij}^n|\right)\left(u_{ij}^n - u_{i,j-1}^n\right) \qquad (B8)$$

$$\frac{1}{\rho_\ell}\left(\frac{\partial P}{\partial r}\right)_{ij}^n = DPDX$$

$$\left(\frac{\partial^2 u}{\partial y^2}\right)_{ij}^n = VISCOX = \frac{2}{(\Delta y_j + \Delta y_{j+1})}\left(\frac{u_{i,j+1}^n - u_{ij}^n}{\Delta y_{j+1}} - \frac{u_{ij}^n - u_{i,j-1}^n}{\Delta y_j}\right) \qquad (B9)$$

Substituting in equation (4.34) above and rearranging, we get:

$$u_{ij}^{n+1} = u_{ij}^n - \Delta t\,(FUX+FUY) - \Delta t * DPDX + \Delta t * \nu * VISCOX \qquad (4.3\text{[illegible]})$$

APPENDIX C

FINITE DIFFERENCE REPRESENTATION FOR THE MARKER AND CELL TECHNIQUE

C.1 Momentum Equation

The momentum equations (6.1) and (6.2) can be rewritten as,

$$\left(\frac{\partial u}{\partial t}\right)^{n+1}_{i+1,j} = -u\left(\frac{\partial u}{\partial r}\right)_{i+1,j} - v\left(\frac{\partial u}{\partial y}\right)_{i+1,j} + \nu\left(\frac{\partial^2 u}{\partial r^2} + \frac{1}{r}\frac{\partial u}{\partial r} - \frac{u}{r^2} + \frac{\partial^2 u}{\partial y^2}\right)_{i+1,j} + \left(\frac{\partial P^*}{\partial r}\right)_{i,j} \qquad (C1)$$

$$\left(\frac{\partial v}{\partial t}\right)^{n+1}_{i,j+1} = -u\left(\frac{\partial v}{\partial r}\right)_{i,j+1} - v\left(\frac{\partial v}{\partial y}\right)_{i,j+1} + \left[\nu\left(\frac{\partial^2 v}{\partial r^2} + \frac{1}{r}\frac{\partial v}{\partial r} + \frac{\partial^2 v}{\partial y^2}\right)_{i,j+1}\right] - \left(\frac{\partial P^*}{\partial y}\right)_{i,j+1} - g \qquad (C2)$$

Referring to Figure C1, each velocity derivative can be approximated by a simple finite difference representation as:

$$\left(\frac{\partial u}{\partial t}\right)^{n+1}_{i+1,j} = \frac{u^{n+1}_{i+1,j} - u_{i+1,j}}{\Delta t}$$

$$\left(u\frac{\partial u}{\partial r}\right)_{i+1,j} = (FUX)_{i+1,j} = 0.5\,(u_{i+1,j} - |u_{i+1,j}|)^* \frac{(u_{i+2,j} - u_{i+1,j})}{\Delta r_{i+1}} + 0.5\,(u_{i+1,j} + |u_{i+1,j}|)^* \frac{(u_{i+1,j} - u_{i,j})}{\Delta r_i}$$

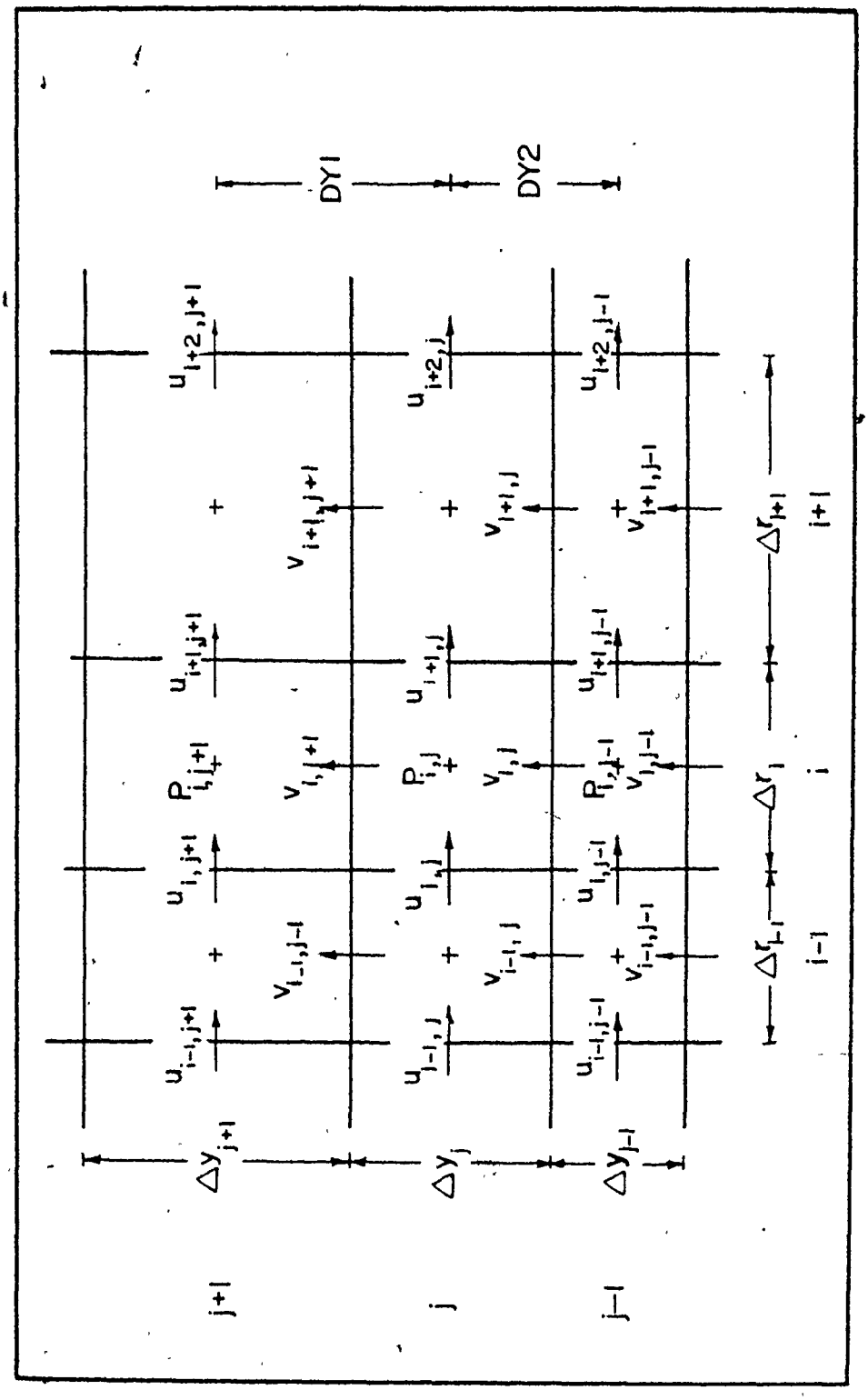

FIGURE (C1) MAC FINITE DIFFERENCE REPRESENTATION

$$\left(v\,\frac{\partial u}{\partial y}\right)_{i+1,j} = FVX)_{i+1,j} = 0.5\,(v_{i+1,j} - |v_{i+1,j}|)*\frac{u_{i+1,j+1} - u_{i+1,j}}{DY1}$$

$$+ 0.5\,(v_{i+1,j} + |v_{i+1,j}|)*\frac{u_{i+1,j} - u_{i+1,j-1}}{DY2}$$

and

$$v_{i+1,j} = 0.25[(v_{i+1,j+1} + v_{i+1,j})\,\Delta r_i + (v_{i,j+1} + v_{i,j})\,\Delta r_{i+1}]/Dr1$$

$$\frac{\partial P^*}{\partial r})_{i+1,j} = DPDX)_{i+1,j} = \frac{P^*_{i+1,j} - P^*_{i,j}}{Dr1}$$

$$\left(\frac{\partial^2 u}{\partial r^2} + \frac{1}{r}\frac{\partial u}{\partial r} - \frac{u}{r^2} + \frac{\partial^2 u}{\partial y^2}\right)_{i+1,j} = VISCOX)_{i+1,j}$$

$$= \left[\frac{u_{i+2,j} - u_{i+1,j}}{\Delta r_{i+1}} - \frac{u_{i+1,j} - u_{i,j}}{\Delta r_i}\right]/Dr1$$

$$+ \left[\frac{(u_{i+2,j} - u_{i+1,j})}{\Delta r_{i+1}} * \Delta r_i + \frac{(u_{i+1,j} - u_{i,j})}{\Delta r_i}\,\Delta r_{i+1}\right]/\left[2 * \Delta r_i * \sum_{m=2}^{i} \Delta r_m\right]$$

$$- u_{i+1,j}/\left[\sum_{m=2}^{i} \Delta r_m\right]^2$$

$$+ \left[\frac{u_{i+1,j+1} - u_{i+1,j}}{DY1} - \frac{u_{i+1,j} - u_{i+1,j-1}}{DY2}\right]$$

Similarly

$$\frac{\partial v}{\partial t})^{n+1}_{i,j+1} = \frac{v^{n+1}_{i,j+1} - v^{n}_{i,j+1}}{\Delta t}$$

$$\left(u\frac{\partial v}{\partial r}\right)_{i,j+1} = FVX)_{i,j+1} = 0.5\ (u_{i,j+1} - |u_{i,j+1}|)*\frac{v_{i+1,j+1} - v_{i,j+1}}{Dr1}$$

$$+ 0.5(u_{i,j+1} + |u_{i,j+1}|)*\frac{v_{i,j+1} - v_{i-1,j+1}}{Dr2}$$

and

$$u_{i,j+1} = 0.25[(u_{i+1,j} + u_{i,j})\Delta y_{j+1} + (u_{i+1,j+1} + u_{i,j+1})\Delta y_j]/DY1$$

$$\left(v\ \frac{\partial v}{\partial y}\right)_{i,j+1} = 0.5(v_{i,j+1} - |v_{i,j+1}|)\ *\ \frac{v_{i,j+2} - v_{i,j+1}}{\Delta y_{j+1}}$$

$$+ 0.5(v_{i,j+1} + |v_{i,j+1}|)*\ \frac{v_{i,j+1} - v_{i,j}}{\Delta y_j}$$

$$\left(\frac{\partial^2 v}{\partial r^2} + \frac{1}{r}\ \frac{\partial v}{\partial r} + \frac{\partial^2 v}{\partial y^2}\right)_{i,j+1} = VISCOY)_{i,j+1}$$

$$= \left[\frac{v_{i+1,j+1} - v_{i,j+1}}{Dr1} - \frac{v_{i,j+1} - v_{i-1,j+1}}{Dr2}\right]/\Delta r_i$$

$$+ \frac{1}{2}\left[\frac{v_{i+1,j+1} - v_{i,j+1}}{Dr1} + \frac{v_{i,j+1} - v_{i-1,j+1}}{Dr2}\right]/\left(\sum_{m=2}^{i} \Delta r_m - \Delta r_i/2\right)$$

$$+ \left[\frac{v_{i,j+2} - v_{i,j+1}}{\Delta y_{j+1}} - \frac{v_{i,j+1} - v_{i,j}}{\Delta y_j}\right]/(DY1)$$

C.2 Energy Equation

The energy equation (6.12) can be written as

$$\left(\frac{\partial T}{\partial t}\right)_{ij}^{n+1} = -\ u\ \frac{\partial T}{\partial r})_{ij} - v\ \frac{\partial T}{\partial y})_{ij} + \alpha_\ell\left[\frac{\partial^2 T}{\partial r^2} + \frac{1}{r}\ \frac{\partial T}{\partial r} + \frac{\partial^2 T}{\partial y^2}\right]_{ij} \qquad (C3)$$

Each temperature derivative of equation (C3) can be approximated by a simple finite difference as:

$$\left(\frac{\partial T}{\partial t}\right)_{ij}^{n+1} = \frac{T_{ij}^{n+1} - T_{ij}}{\Delta t}$$

$$u\left(\frac{\partial T}{\partial r}\right)_{ij} = TUX = \frac{1}{4}\left[(u_{i+1,j}+u_{i,j}) - |(u_{i+1,j}+u_{i,j})|\right]\frac{T_{i+1,j}-T_{ij}}{Dr1}$$

$$+ \frac{1}{4}\left[(u_{i+1,j}+u_{i,j}) + |(u_{i+1,j}+u_{ij})|\right]\frac{T_{ij}-T_{i-1,j}}{Dr2}$$

$$v\left(\frac{\partial T}{\partial y}\right)_{ij} = TVY = \frac{1}{4}\left[(v_{i,j+1}+v_{i,j}) - |(v_{i,j+1}+v_{i,j})|\right]\frac{T_{i,j+1}-T_{ij}}{DY1}$$

$$+ \frac{1}{4}\left[(v_{i,j+1}+v_{ij}) + |(v_{i,j+1}+v_{ij})|\right]\frac{T_{ij}-T_{i,j-1}}{DY2}$$

$$COND = \left(\frac{\partial^2 T}{\partial r^2} + \frac{1}{r}\frac{\partial^2 T}{\partial r} + \frac{\partial^2 T}{\partial y^2}\right)_{ij}$$

$$= \left[\frac{T_{i+1,j}-T_{ij}}{Dr1} - \frac{T_{ij}-T_{i-1,j}}{Dr2}\right]/\Delta r_i$$

$$+ \frac{\frac{1}{2}}{\left(\sum_{m=2}^{i} \Delta r_m - \Delta r_i/2\right)}\left[\frac{T_{i+1,j}-T_{ij}}{Dr1} + \frac{T_{i,j}-T_{i-1,j}}{Dr2}\right]$$

$$+ \left[\frac{T_{i,j+1}-T_{i,j}}{DY1} - \frac{T_{ij}-T_{i,j-1}}{DY2}\right]/\Delta Y_j$$

C.3 Marker Velocity Component

The Taylor series expansion around point (0) (Figure (C2)), equation (6.44) can be rewritten as:

$$u_k \simeq u_o + h\left(\frac{\partial u}{\partial r}\right)_o + L\left(\frac{\partial u}{\partial y}\right)_o + \frac{1}{2!}\left[h^2\left(\frac{\partial^2 u}{\partial r^2}\right) + 2hL\left(\frac{\partial^2 u}{\partial r \partial y}\right) + L^2\left(\frac{\partial^2 u}{\partial y^2}\right)_o\right] \qquad (6.49)$$

In finite difference form, equation (6.49) can be written for two cases depending on the location of the Marker with respect to the point (0) as shown in figure (C2).

CASE -1-

$$u_k = u_o + \frac{H}{Dr1}\left[\frac{(u_1 - u_o)}{\Delta r_{i+1}}\,\Delta r_i + \frac{(u_o - u_3)}{\Delta r_i}\,\Delta r_{i+1}\right]/2$$

$$+ \frac{L}{2}\left[\frac{u_2 - u_o}{DY1} + \frac{u_o - u_4}{DY2}\right]$$

$$+ \frac{1}{2}\left\{\left[\frac{H^2}{Dr1}\left(\frac{u_1 - u_o}{\Delta r_{i+1}} - \frac{u_o - u_3}{\Delta r_i}\right)\right]\right.$$

$$+ \left[\frac{L^2}{\Delta Y_j}\left(\frac{u_2 - u_o}{DY1} - \frac{u_o - u_4}{DY2}\right)\right]$$

$$\left. + \left[\frac{HL}{Dr1}\left(\frac{DUDY1 - DUDY0}{\Delta r_{i+1}}\,\Delta r_i + \frac{DUDY0 - DUDY3}{\Delta r_i}\,\Delta r_{i+1}\right)\right]\right\}$$

where:

$$DUDY1 = \left(\frac{u_5 - u_1}{DY1} + \frac{u_1 - u_8}{DY2}\right)/2$$

$$DUDY0 = \left(\frac{u_2 - u_o}{DY1} + \frac{u_o - u_4}{DY2}\right)/2$$

$$DUDY3 = \left(\frac{u_6 - u_3}{DY1} + \frac{u_3 - u_7}{DY2}\right)/2$$

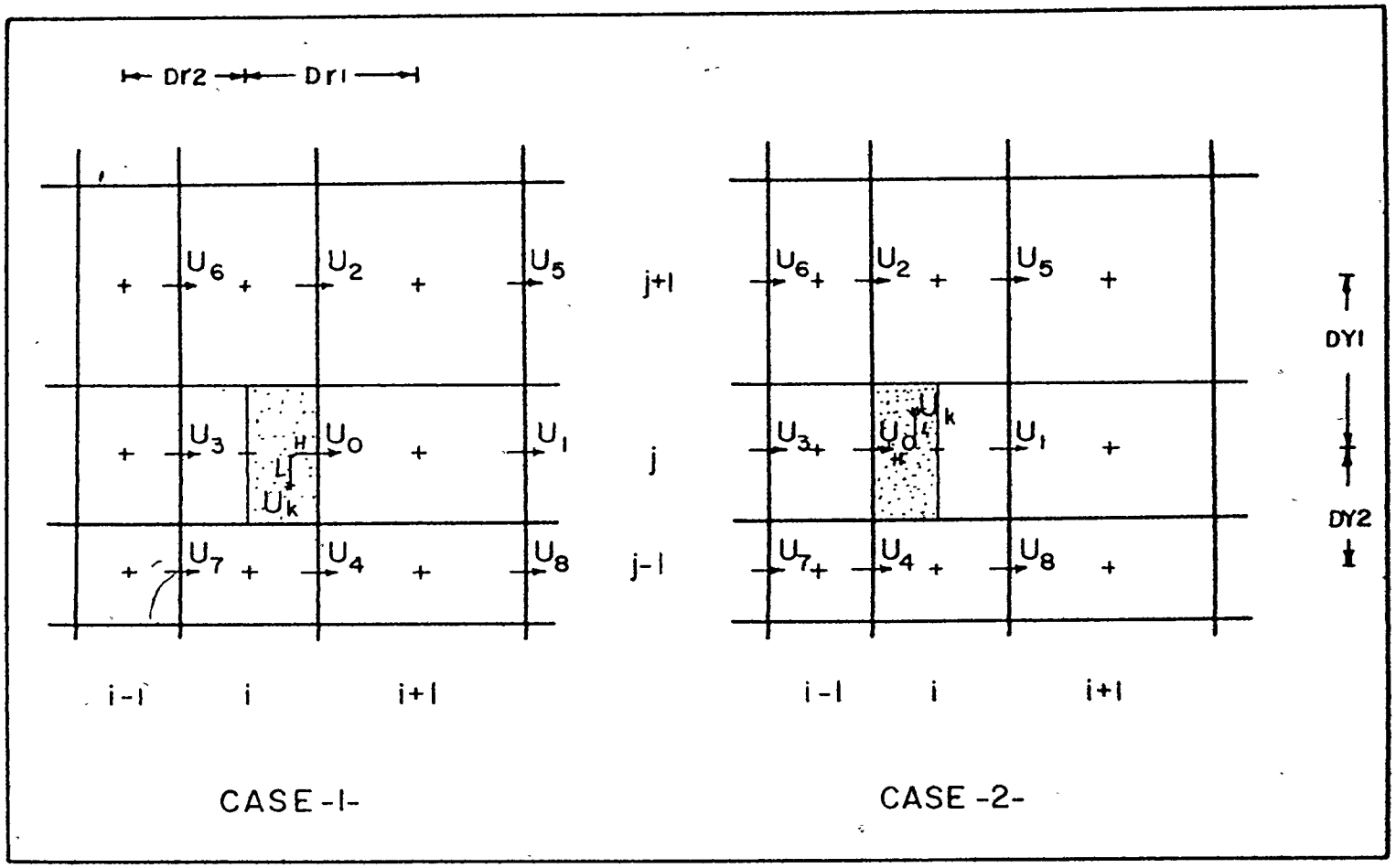

FIGURE (C2) MARKER VELOCITY COMPONENTS

CASE -2-

$$u_k = u_o + \frac{H}{Dr2}\left[\frac{u_1-u_o}{\Delta r_i}\Delta r_{i-1} + \frac{u_o-u_3}{\Delta r_{i-1}}\Delta r_i\right]/2$$

$$+ L\left[\frac{u_2-u_o}{DY1} + \frac{u_o-u_4}{DY2}\right]/2$$

$$+ \frac{1}{2}\left\{\left[\frac{H^2}{Dr2}\left(\frac{u_1-u_o}{\Delta r_i} - \frac{u_o-u_3}{\Delta r_{i-1}}\right)\right]\right.$$

$$+ \left[\frac{L^2}{\Delta Y_j}\left(\frac{u_2-u_o}{DY1} - \frac{u_o-u_4}{DY2}\right)\right]$$

$$\left. + \left[\frac{HL}{Dr2}\left(\frac{DUDY1-DUDY0}{\Delta r_i}\Delta r_{i-1} + \frac{DUDY0-DUDY3}{\Delta r_{i-1}}\Delta r_i\right)\right]\right\}$$

where:

$$DUDY1 = \left(\frac{u_5-u_1}{DY1} + \frac{u_1-u_8}{DY2}\right)/2$$

$$DUDY0 = \left(\frac{u_2-u_o}{DY1} + \frac{u_o-u_4}{DY2}\right)/2$$

$$DUDY3 = \left(\frac{u_6-u_3}{DY1} + \frac{u_3-u_7}{DY3}\right)/2$$

Similar approximations could be written for v_k

REFERENCES

1. Fath, H. S., "Influence of System Pressure on Micro-layer Evaporation Heat Transfer", M.Eng. Thesis, Mechanical Engineering, McMaster Univ. (1977).

2. Rayleigh, Lord, "On the Pressure Developed in a Liquid During the Collapse of a Spherical Cavity", Phi. Mag., 34, 94 (1917).

3. Scriven, L. E., "On the Dynamics of Phase Growth", Chem. Eng. Sci., 10, 1 (1959).

4. Plesset, M. S. and Zwick, S. A., "The Growth of Vapour Bubbles in Superheated Liquids", J. Appl. Phys., 25, 493 (1959).

5. Theofanous, T., Biasi, L. and Isbin, S., "A Theoretical Study on Bubble Growth in Constant and Time Dependent Pressure Fields", Chem. Eng. Sci., Vol. 24, pp. 885-897 (1969).

6. Board, S. and Duffey, R., "Spherical Vapour Bubble Growth in Superheated Liquids", Chem. Eng. Sci., Vol. 26, pp. 263-274 (1971).

7. Mikic, B., Rohsenow, W. and Griffith, P., "On Bubble Growth Rates", Int. J. H.M. Transf., Vol. 13, pp. 657-666 (1970).

8. Cooper, M. and Lloyd, A., "The Microlayer in Nucleate Pool Boiling", Int. J. H. M. Trans., Vol. 12, pp. 895-913 (1969).

9. Van Ouwerkerk, H., "The Rapid Growth of a Vapour Bubble at a Liquid-Solid Interface", Int. J. H. M. Transf., Vol. 14, pp. 1415-1431 (1971).

10. Guy, T. B. and Ledwidge, T. J., "Numerical Approach to Non-Spherical Vapour Bubble Dynamics", Int. J. H. M. Transf., Vol. 16, pp. 2393-2406 (1973).

11. Madhaven, S. and Mesler, R., "A Study of Vapour Bubble on Surfaces", Proc. Int. H. M. Conference (1970), B.2.6.

12. Bankoff, S. G. and Mikesell, R. D., "Bubble Growth Rate in Highly Subcooled Nucleate Boiling", Chem. Eng. Progress Symposium Series N29, Vol. 55, pp. 95-102.

13. Hahne, G., "Heat Transfer in Boiling" (1977), Chapter 2.

14. Schmidt, F. W., Robinson, G. E. and Skapura, R. J., "Experimental Study of Noise Generation in Nucleate Boiling", Proceedings Int. Heat Trans. Conference (1970) B.1.8.

15. Ganic, E. N. and Afgan, N. H., "An Analysis of Temperature Fields in the Bubble and Its Liquid Environment in Pool Boiling of Water", Int. J. H. M. Trans. , Vol. 18, pp. 301-309 (1974).

16. Wiebe, J. R. and Judd, R. L., "Superheated Layer Thickness Measurements in Saturated and Subcooled Nucleate Boiling", J. of H. T., Nov., pp. 455 (1971).

17. Johnson, M., De La Pena, J. and Mesler, R., "Bubble Shape in Nucleate Boiling", A.I.Ch.E., 12, pp. 344-348 (1966).

18. Dwyer, O., "Boiling in Liquid Metal" (1976).

19. Snyder, N. R. and Edwards, D. K., "Summary of Conference on Bubble Dynamics and Boiling Heat Transfer", Memo (20-137) Jet Prop. Lab., June 14-15 (1956).

20. Moore, F. D. and Mesler, R. B., "The Measurement of Rapid Surface Temperature Fluctuations During Nucleate Boiling of Water", A.I.Ch.E J., Vol. 7, pp. 620-624, 1961.

21. Hendricks, R. C. and Sharp, R. R., "Initiation of Cooling Due to Bubble Growth on a Heating Surface", NASA TN D2290, 1964.

22. Sharp, R. R., "The Nature of Liquid Film Evaporation During Nucleate Boiling", NASA TN D1997, 1964.

23. Jawurek, H. H., "Simultaneous Determination of Microlayer Geometry and Bubble Growth in Nucleate Boiling", Int. J. H. M. T., 12, 1969.

24. Foltz, G. E. and Mesler, R. B., "The Measurement of Surface Temperatures with Platinum Films During Nucleate Boiling of Water", A.I.Ch.E., J., 16, 44 (1970).

25. Katto, Y., Takahashi, S., and Yokoya, S., "Law of Microlayer Formation Between a Growing Bubble and a Solid with a Special Reference to Nucleate Boiling", Bulletin of JSME, pp. 1066-1075, Vol. 16, No. 97 (1973).

26. Voutsinos, C. M. and Judd, R. L., "Laser Interferometric Investigation of the Microlayer Evaporation Phenomenon", Trans. ASME, Feb., 1975.

27. Fath, H. S. and Judd, R. L., "Influence of System Pressure on Microlayer Evaporation Heat Transfer", J. H. T., Vol. 100, 49 (1978).

28. Olander, R. and Watts, R., "An Analytical Expression of Microlayer Thickness in Nucleate Boiling", ASME, JHT , Feb., pp. 178-180 (1969).

29. Dwyer, O. and Hsu, C., "Evaporation of the Microlayer in Hemispherical Bubble Growth in Nucleate Boiling of Liquid Metals", Int. J. H. M. Trans., Vol. 19, pp. 185-192 (1976).

30. Van Stralen, S., Sohal, M., Cole, R. and Sluyter, W., "Bubble Growth Rate in Pure and Binary Systems: Combined Effects of Relaxation and Evaporation Microlayers", Int. J. H. M. Trans., Vol. 18, pp. 453-467 (1975).

31. Katto, Y. and Shoji, M., "Principal Mechanism of Microlayer Formation on a Solid Surface with a Growing Bubble in Nucleate Boiling", Int. J. H. M. Trans., Vol. 13, pp. 1299-1311 (1970).

32. Zijl, W., "The Departure of Growing Bubbles Adhering to a Horizontal Wall", Ph.D. Thesis, Eindoven Univ. of Technology (1978).

33. Landau, L. and Levich, B. G., Acta Physicochimica U.R.S.S. 17, pp. 42-54 (1942) - See also Levich, B. G., "Physicochemical Hydrodynamics", Prentice-Hall, Englewood Cliffs (1962).

34. Cooper, M. G., Judd, A. M. and Pike, P. A., "Shape and Departure of Single Bubbles Growing at a Wall", Sixth Int. Heat Trans. Conference, paper PB-1 (1978).

35. Van Beek, F. and Vennekens, H., "Mikrolaag - verdamping Onder Een Groeiende Dampbel in Een Kokende Vloeistaf", Lecture presented to the "Contactgroep Warmtetransport Subgroup Tweefasenstroming". Summary at request at Koniklijke/Shell Lab., Amsterdam, Netherlands (1972) (in Dutch).

36. Judd, R. L., "Comparison of Experimental Microlayer Thickness Results", Trans. of CSME, Vol. 1, No. 3 (1972).

37. Hwang, K. S. and Judd, R. L., "A Comprehensive Model for Nucleate Pool Boiling Heat Transfer Including Microlayer Evaporation", Trans. ASME, Nov. (1976).

38. Schlichting, H., "Boundary Layer Theory", Sixth Edition (1968), McGraw-Hill Book Company.

39. Fath, H. S., "Microlayer Formation, Evaporation, and Bubble Growth - Programs Listing", Report to the Mech. Eng. Dept., McMaster Univ., Canada.

40. Carslaw, H. S. and Jaeger, J. C., "Conduction of Heat in Solids", Second Edition, pp. 322.

41. Sernas, V., "Initial Vapour Bubble Growth on a Heated Wall During Nucleate Boiling", Ph.D. Thesis, Univ. of Toronto, 1967.

42. Hirt, C. W., Nichols, B. D. and Romero, N. C., "SOLA-A Numerical Solution Algorithm for Transient Fluid Flows", LA-5852, Los Alamos, 1975.

43. Harlow, F. H., "Numerical Methods for Fluid Dynamics, an Annotated Bibliography", Los Alamos Sci. Lab., LA-4281, December 1969.

44. Roache, P. J., "Computational Fluid Dynamics", Hermosa Publishers, 1976.

45. Harlow, F. H. and Welch, J. E., "Numerical Calculation of Time-Dependent Viscous Incompressible Flow", Phys. Fluids, 8, 2182 (1965), Welch, J. C., Harlow, F. H., Shannon, J. P. and Daly, B. J., "The MAC Method; A Computing Technique for Solving Viscous Incompressible Transient Fluid Flow Problems Involving Free Surface", Los Alamos Sci. Lab. Report LA-3425, March (1966).

46. Van Stralen, S. and Cole, R., "Boiling Phenomena", Volume 2, Hemisphere Publishing, 1979.

47. Van Stralen, S., Zijl, W. and De Vries, D., "The Behaviour of Vapour Bubbles at Subatmospheric Pressures", Chem. Eng. Sci., 1977.

48. Joosten, J., Zijl, W., and Van Stralen, S., "Growth of Vapour Bubbles in Combined Gravitational and Non-Uniform Temperature Fields", Int. J. H. M. T., Vol. 12, pp. 15 (1978).

49. Knuth, E. L., "Nonstationary Phase Changes Involving a Condensed Phase and a Saturated Vapour", Phys. Fluids, 2, pp. 84 (1959).

50. Theofanous, T. G., Bohrer, T. H., Chang, M. C., Patel, P. D., "Experimental and Universal Growth Relations for Vapour Bubbles with Microlayers", J. H. T., Feb. 1978, pp. 41.

51. Daly, B. J., "A Technique for Including Surface Tension Effects in Hydrodynamic Calculations", J. of Comp. Phys., 4, pp. 97, 1969.